

**Faculty of Science and Engineering
WASM: Minerals, Energy and Chemical Engineering**

The utilisation of neoteric media technology for the development of formulations for treatment of colorectal cancer

Harikrishnan Sekar

**This thesis is presented for the Degree of
Doctor of Philosophy
of
Curtin University**

January 2021

Declaration

I declare that this thesis contains no material previously published by any other person except where due acknowledgement is made.

This thesis contains no material which has been accepted for the award of any other degree or diploma in any university.

Signature:

Date: 28/01/2021

Acknowledgment

I offer my obeisance to the almighty GOD Sri Mahaperiyava and Sri Sivan Sar for showering their mercy on me.

Firstly, I would like to express my sincere gratitude to my thesis supervisor, Emeritus Professor Neil R Foster, to believe in me and allowing me to pursue doctoral studies under his supervision. He has inspired me through his guidance, leadership, enthusiasm, analytical skills, and wisdom, which I consider a significant learning curve in my life. His constant support and advice have made me strive to give my best towards quality research. I always look upon him as a mentor for his personal and professional attributes. I am honoured to be his student and truly indebted to him all time.

I want to thank my co-supervisor, Dr. Chau Chun Beh (Jane), for her tireless and continuous support. Her unreserved help on technical and personal fronts has made my work and life at Curtin more comfortable. Her methodical approach and skills in handling challenges have shown me how to tackle problems effectively. She has always been approachable at any time and has been very kind and understanding during my difficult times. Many of the after-hour brainstormings has leveraged my thinking and research skills to a great extent. The multitasking ability and research clarity are the attributes I have always tried to learn from her supervision. I am very grateful to her in all ways.

My sincere thanks to my colleague and guide Dr. Rossen Sedev for his invaluable support during my candidature. He has been my resolute support in all my research endeavours. His friendliness and easy-to-approach quality have helped me to work closely without constraints. His close guidance on day-to-day experiments and appreciation has motivated me to continuously reach my research objective. He has always been a go-to person. I am forever thankful to him for sharing his knowledge and wisdom with me as a mentor and a friend.

A special thanks to our team collaborator Dr. Craig Priest, Australian National Fabrication Facility, University of South Australia, for showing particular interest in my research work. His timely reviews and constructive criticism has helped me in reaching perfection in my research.

With no second thoughts, I extend my thanks once again to my colleagues, who are also my friends Dr. Dimple Quyn, Dr. Rossen Sedev, Dr. Jane Beh, Ms. Deepali Arora, and Mr. Umar Khan for providing lighter moments and making me a sane and sober person despite the research rigor.

Thanks to my laboratory In-charge Mr. Araya Abera, Mr. Xiao Huo (Jimmy), and lab technicians Ms. Jennifer Wang, Ms. Roshanak Doroushi, Ms. Melina Miralles, and ex-colleague Mr. Andrew Chan for their continuous training and support in the chemical engineering laboratory procedures.

I would like to thank and acknowledge Dr. Zakaria Quadir, Ms. Elaine Miller, Ms. Veronica Avery, Dr. Matthew Rowels, and Ms. Kelly Marigot of the John de Laeter Research Centre for rendering their support and guidance in Microscopy and X-Ray diffraction analysis. I have gained expertise in microscopy and powder diffraction through their training and guidance. I thank Dr. Franca Jones of the Department of Chemistry for her support in particle analysis. A special thanks to Dr. Hussein Abid of Curtin University for his BET and surface area measurements training and advice.

I take this opportunity to thank my friends in Australia and Singapore who have been with me through all times, supporting during my ups and downs. They have been a family away from home, making my stay in Australia memorable, which I will always cherish in the memories.

Lastly, nothing is meaningful without the family. I am thankful that I have beautiful parents and family members who are my pillars of support. Their prayers, care, and encouragement have made my Ph.D. journey successful. I owe my parents all of what I am today.

Dedication

To my all, Jagath Guru Sri Sri Mahaperiyava, and Sri Sri Sivan Sar

To my Parents

To my Family

“The craving and curiosity to know why, how, when, and why not, is what a researcher must possess to make a significant and impactful contribution. Research should always be centered on social benefit.

Prof. Neil R Foster

“No experiments or circumstances are bad. Every result is meaningful, and every work teaches how nature is different from what we assume. Research with an open mind! It is what it is!”

Dr. Rossen Sedev

“Every small accomplishment is an appreciation for your effort and gets you closer to your goal- never give up and never compromise on the quality of what you do!”

Dr. Chau Chun Beh (Jane)

Abstract

Oncological medicines have growing demands due to the surge in malignancy globally. Consequently, there exists a necessity in providing continual therapies for its effective cure. The drug delivery system for cancer therapy primarily employs drugs in the form of tablets and capsules, which comes with the setback of overdose, low drug absorption, and decreased bioavailability. Micronization and formulation of Active Pharmaceutical Ingredients (API) and nanocarriers provide effective targeted drug delivery systems. Converting the drugs into micro/nanoparticles increases the absorptive capacity and hence the bioavailability. Also, micronizing and encapsulating them in suitable nanocarriers enhances the therapeutic efficacy with reduced side effects due to overdose.

Conventional methods of producing micro/nanoparticles come at the expense of excessive solvent usage, lengthy and complicated procedures, and extreme processing conditions, which affect the integrity of the APIs.

Green processing systems such as Dense gas (DG) technology and Subcritical water technology (SCW) offers a better solution for producing micro/nanoparticles and formulations in an environment-friendly manner. The current thesis focuses on researching the DG and SCW processing methods as a green alternative to formulate APIs and nanocarriers for colorectal cancer treatment. Primary drugs, 5-Fluorouracil (5FU), and Silibinin (SLB) were used as modal drugs in the current study. DG processing employs carbon dioxide in its near-critical or supercritical state to formulate drug micro/nanoparticles. The tunability of the density and solvation power of carbon dioxide at various temperatures and pressures enables the efficient processing of a broad spectrum of thermally sensitive APIs and nanocarriers. The current work studied the Gas antisolvent (GAS) process and the Atomized rapid injection for the solvent extraction (ARISE) process in detail under the DG methods.

For the first time, the thesis explored the use of naturally occurring Halloysite nanoclay/tube (HNT) in DG and SCW processes. The GAS process was employed to load 5FU onto HNT, and the effect of operating pressure, drug-nanocarrier mass ratio at an ambient temperature of 25 °C on the drug loading and encapsulation efficiency was studied. The GAS process provided a fourfold increase in the drug loading capacity compared to conventional mechanical loading. Further, an average encapsulation

efficiency of 40% of 5FU was achieved. The GAS process employs single-step processing, and significantly decreases the solvent usage compared to conventional methods.

The novel in-house built ARISE process was studied in detail in this thesis with an emphasis on understanding the micronization, encapsulation, and spray pattern analysis of the working solution. Eudragit S100 (ES100) polymer was used as the encapsulating material. The effect of solution concentration, volume of injection, and drug-nanocarrier mass ratios on the drug loading and encapsulation efficiency were examined. With the ARISE, ultra-low density (0.02 g/ml) micronized ES100 powders were produced with 90% product recovery. The process produced uniform microspheres with individual particle sizes ranging from 200 to 700 nm. About 21% drug loading and over 90% encapsulation efficiency were achieved for the ES100-SLB formulation and around 14% drug loading and less than 10% encapsulation efficiency were obtained for the ES100-5FU formulation. The work also demonstrated the ARISE capability to encapsulate both hydrophilic (5FU) and hydrophobic (SLB) drugs into ES100, confirming the versatility of the process in accommodating a wide range of materials. The pH triggered release, and improved dissolution of the formulations was further verified by performing *in vitro* drug release studies in a simulated gastrointestinal environment. The study revealed about 90% drug release in the colon condition and 30% in the gastric environment. The time-extended release of APIs from the ARISE processed samples showed 6 h of release time in the colon pH environment compared to 2 h of release time in pristine form (5FU and SLB).

Aside from the mainstream study on the formulation, the thesis also includes analyzing the effect of washing procedures on the drug loading estimation, which is less explored to date. The influence of washing time and method dramatically affects the loading estimation, hence, an optimal washing protocol has been drawn based on the observation in the current study.

One of the significant observations made was that the use of DG processes did not alter the chemical composition of the APIs and nanocarriers. Hence, the integrity of the sample is maintained without contamination and degradation, which is favourable for drug delivery applications.

Besides the DG process assisted micronization and formulation, SCW technology was adopted for the first time as an alternative to the acid etching process of HNT used in the pharmaceutical industry. HNTs are surface modified predominantly using strong

acids to increase its surface area and hence the loading capacity. The degradation due to acidic residues remains a significant drawback of this process. Water behaves as acid when it is in subcritical state and enhances drug solubility at a temperature beyond its standard boiling point. This feature was utilized for improving the surface properties of HNT. The process was carried out at a moderate pressure of 20 bar and a temperature of 170 °C under a nitrogen atmosphere. SCW was used as a replacement for the strong acid used in conventional methods. The results revealed a 25% increase in the surface area of the HNT without the use of acid and the sample is free from any acidic residues. The effect of etching time on the surface area and morphology of the HNT was analyzed using X-ray diffraction (XRD) and Transmission electron microscopy (TEM). Treatment with SCW generates crystallite growth on the surface of HNT, thereby increasing the surface area without affecting the physicochemical properties and purity of the material.

The current thesis collectively demonstrates the effectiveness of applying DG and SCW processing in the micro/nanoformulation of different genres of APIs and nanocarriers. In specific, the GAS and ARISE processes' efficiency in handling both porous materials like HNT and polymers like ES100 opens an avenue for using a broad spectrum of materials for enhanced dissolution of APIs for targeted drug delivery application. The study on the drug-nanocarrier mass ratio provides an insight into the optimum concentration suitable for producing uniform microspheres based on the application needs. The ARISE spray analysis provides a silhouette about the micronization dynamics that can be used in further re-designing and customizing the set-up based on the requirement. As a culmination, preliminary studies on the scale-up of the ARISE set-up was conducted to demonstrate its prospects towards industrial implementation. Also, the SCW process's findings open up a new avenue for acid-free etching of HNT and HNT like materials, which are highly beneficial towards realizing a green processing method with low (nearly zero) toxic discharge.

Publications

Journal Publication

1. S. Harikrishnan, R. Sedev, C.C. Beh, C. Priest, N.R. Foster, **Loading of 5-fluorouracil onto Halloysite nanotubes for targeted drug delivery using a subcritical gas antisolvent process (GAS)**, The Journal of Supercritical Fluids 159 (2020) 104756.

In Preparation

1. S. Harikrishnan, R. Sedev, C. Priest, N.R. Foster, C.C. Beh, **Non-toxic Surface Modification of Halloysite Nanotube using Subcritical Water treatment.**
2. S. Harikrishnan, R. Sedev, C. Priest, N.R. Foster, C.C. Beh, **Green processing of Halloysite nanoclay for colon targeted drug delivery system.**
3. S. Harikrishnan, R. Sedev, C. Priest, N.R. Foster, C.C. Beh, **Micronization of pH sensitive Eudragit S100 polymer through Atomized Rapid Injection for Solvent Extraction (ARISE) process.**
4. S. Harikrishnan, R. Sedev, C. Priest, N.R. Foster, C.C. Beh, **Formulation of hydrophobic and hydrophilic drug in Eudragit S100 using Atomized rapid injection for solvent extraction (ARISE) process.**

Table of Contents

CHAPTER 1	1
<hr/>	
INTRODUCTION	1
1.1 BACKGROUND AND INSPIRATION	2
1.2 RESEARCH SCOPE	5
1.3 THESIS OUTLINE	6
CHAPTER 2	9
<hr/>	
LITERATURE REVIEW	9
2.0 INTRODUCTION	10
2.1 COLORECTAL CANCER THERAPY	10
2.1.1 5-FLUOROURACIL AS AN ANTI-CANCER AGENT	11
2.1.2 SILIBININ AS AN ANTI-CANCER AGENT	12
2.2 MICRO/NANO DRUG FORMULATION	14
2.3 DENSE GAS FORMULATION METHODS	18
2.3.1 DG AS A SOLVENT	23
2.3.2 DG AS AN ANTISOLVENT	25
2.3.2.1 ATOMIZED RAPID INJECTION FOR SOLVENT EXTRACTION (ARISE).	33
2.3.3 DG AS CO-SOLVENT	41
2.3.4 DG AS AN AID IN EMULSION	42
2.4 EUDRAGIT AS AN EXCIPIENT FOR FORMULATION	46
2.5 HALLOYSITE NANOTUBES-A GREEN MATERIAL FOR NANOFORMULATION.	54
2.5.1 HALLOYSITE NANOTUBES AS DRUG NANO-CARRIERS	56
2.5.2. SURFACE MODIFICATION OF HALLOYSITE NANOTUBES	62
2.5.2.1 ACID AND ALKALINE ETCHING	64
2.6 SUBCRITICAL WATER AS A GREEN ETCHANT	67
2.7 CONCLUSION	70
CHAPTER 3	72
<hr/>	
MATERIALS AND METHODS	72
3.1 ENCAPSULATION OF 5-FLUOROURACIL ONTO HALLOYSITE NANOTUBE USING GAS ANTISOLVENT PROCESS.	73
	XI

3.1.1 SAMPLE PREPARATION	73
3.1.2 GAS PROCESS	74
3.1.3 REMOVAL OF CO-PRECIPTATE	76
3.1.4 PARTICLE CHARACTERIZATION	77
3.1.5 FTIR CHARACTERIZATION	77
3.1.6 THERMOGRAVIMETRIC ANALYSIS	78
3.1.7 IN VITRO DRUG RELEASE	79
3.2 MICRONIZATION AND SPRAY CHARACTERIZATION IN ATOMIZED RAPID INJECTION FOR SOLVENT EXTRACTION (ARISE) PROCESS	81
3.2.1 SAMPLE PREPARATION	81
3.2.2 ARISE SET-UP	81
3.2.3 SPRAY ATOMIZATION SETUP	84
3.2.4 VISCOSITY MEASUREMENT	86
3.2.5 BULK DENSITY MEASUREMENT	86
3.2.6 PARTICLE CHARACTERIZATION	86
3.2.7 FTIR CHARACTERIZATION	87
3.3 ARISE ASSISTED ENCAPSULATION OF HYDROPHOBIC AND HYDROPHILIC DRUG IN EUDRAGIT S-100	87
3.3.1 SAMPLE PREPARATION	87
3.3.2 ENCAPSULATION USING ARISE PROCESS	87
3.3.3 BULK DENSITY MEASUREMENT	88
3.3.4 REMOVAL OF CO-PRECIPTATE	88
3.3.5 PARTICLE CHARACTERIZATION	88
3.3.6 XRD CHARACTERIZATION	89
3.3.7 DRUG LOADING ESTIMATION	89
3.3.8 IN VITRO DRUG RELEASE	89
3.4 COMPARISON STUDY ON ENCAPSULATION OF 5-FLUOROURACIL ONTO HALLOYSITE THROUGH THE GAS, ARISE, AND MECHANICAL PROCESS	90
3.4.1 SAMPLE PREPARATION	90
3.4.2 MECHANICAL LOADING	90
3.4.3 REMOVAL OF CO-PRECIPTATE	91
3.4.4 PARTICLE CHARACTERIZATION	91
3.4.5 FTIR CHARACTERIZATION	91
3.4.6 DRUG LOADING ESTIMATION	92

3.5 SUBCRITICAL WATER TREATMENT OF HALLOYSITE NANOTUBE-GREEN ALTERNATIVE TO CHEMICAL ETCHING	92
3.5.1 SAMPLE PREPARATION	92
3.5.2 SUBCRITICAL WATER TREATMENT	92
3.5.3 THERMAL TREATMENT OF HALLOYSITE	93
3.5.3 SURFACE AREA MEASUREMENT	94
3.5.4 FTIR CHARACTERIZATION	94
3.5.5 XRD CHARACTERIZATION	95
3.5.6 PARTICLE CHARACTERIZATION	95
<u>CHAPTER 4</u>	<u>96</u>
GAS ANTISOLVENT PROCESS (GAS) ASSISTED LOADING OF 5-FLUOROURACIL ONTO HALLOYSITE NANOCLAY	96
RESULTS AND DISCUSSION	97
4.1 REMOVAL OF CO-PRECIPTATES	98
4.2 PARTICLE CHARACTERIZATION	100
4.2.1 ELECTRON MICROSCOPY	100
4.2.2 FTIR SPECTROSCOPY	103
4.2.3 BET SURFACE AREA	104
4.2.4 DRUG LOADING	105
4.3 IN-VITRO DRUG RELEASE	110
4.4 CONCLUSION	114
<u>CHAPTER 5</u>	<u>115</u>
ATOMIZED RAPID INJECTION FOR SOLVENT EXTRACTION (ARISE)- MICRONIZATION AND SPRAY CHARACTERIZATION OF ES100 POLYMER	115
RESULTS AND DISCUSSIONS	116
5.1 POLYMER SOLUTION VISCOSITY	116
5.2 PRODUCT RECOVERY	117
5.3 BULK DENSITY	120
5.4 PARTICLE CHARACTERIZATION	123
5.4.1 PARTICLE SIZE DISTRIBUTION	123
5.4.2 FTIR CHARACTERIZATION	130

5.5 SPRAY ATOMIZATION	132
5.5.1 SPRAY PROFILE ANALYSIS	132
5.5.2 EFFECT OF ES100 CONCENTRATION ON SPRAY ANGLE	141
5.5.3 EFFECT OF ES100 CONCENTRATION ON SPRAY WIDTH	143
5.5.4 VARIATION IN SPRAY TIME WITH THE CHANGE IN ES100 CONCENTRATION	144
5.6 CONCLUSION	146

CHAPTER 6 147

FORMULATION OF HYDROPHOBIC AND HYDROPHILIC DRUGS IN ES100 USING ATOMIZED RAPID INJECTION FOR SOLVENT EXTRACTION (ARISE) PROCESS	147
RESULTS AND DISCUSSION	148
6.1 PRODUCT RECOVERY	152
6.2 BULK DENSITY	153
6.3 REMOVAL OF CO-PRECIPIRATE	154
6.3.1 EFFECT OF THE WASHING PROCEDURE	155
6.3.2 EFFECT OF WASHING TIME	158
6.4 PARTICLE CHARACTERIZATION	160
6.4.1 SCANNING ELECTRON MICROSCOPY (SEM)	160
6.4.1.1 IMAGE ANALYSIS ON MICRONIZED ES100 FROM MeOH SOLUTION	160
6.4.1.2 IMAGE ANALYSIS ON MICRONIZED ES100-5FU FROM MeOH SOLUTION	165
6.4.1.3 IMAGE ANALYSIS ON MICRONIZED ES100-SLB FROM EtOH SOLUTION	176
6.4.2 DYNAMIC LIGHT SCATTERING MEASUREMENT	179
6.5 DRUG LOADING	181
6.5.2 EFFECT OF WASHING ON DRUG LOADING	183
6.6 ENCAPSULATION EFFICIENCY	184
6.7 X-RAY DIFFRACTION STUDY	185
6.8 ZETA POTENTIAL	188
6.9 IN VITRO DRUG RELEASE STUDY	189
6.10 CONCLUSION	194

CHAPTER 7 196

EVALUATION OF ARISE PROCESS FOR HALLOYSITE NANOCCLAY-5-FLUOROURACIL FORMULATION	196
---	-----

RESULTS AND DISCUSSION	197
7.1 REMOVAL OF CO-PRECIPIRATE	197
7.2 DRUG LOADING	199
7.3 PARTICLE CHARACTERIZATION	206
7.4 CONCLUSION	207
<u>CHAPTER 8</u>	<u>208</u>
GREEN PROCESSING OF HALLOYSITE NANOCCLAY USING SUBCRITICAL WATER TREATMENT	208
RESULTS AND DISCUSSION	209
8.1 BET SURFACE AREA	210
8.2 FTIR SPECTROSCOPY	217
8.3 X-RAY DIFFRACTION ANALYSIS	220
8.4 TRANSMISSION ELECTRON MICROSCOPY	224
8.5 ZETA POTENTIAL MEASUREMENT	228
8.6 CONCLUSION	229
<u>CHAPTER 9</u>	<u>230</u>
CONCLUSION AND FUTURE WORK	230
9.1 CONCLUSION	231
9.2. FUTURE WORK	233
<u>APPENDIX-A</u>	<u>235</u>
A1. CALIBRATION CURVES	236
A1.1 CALIBRATION CURVE OF 5FU IN MeOH	236
A1.2 CALIBRATION CURVE OF 5FU IN pH 7.4-PHOSPHATE BUFFERED SALINE (PBS)	236
A1.3 CALIBRATION CURVE OF 5FU IN pH 1.2-0.1M HCL	237
A1.4 CALIBRATION CURVE OF 5FU IN DEIONIZED WATER	238
A1.5 CALIBRATION CURVE OF SLB IN ETHANOL	240
A1.6 CALIBRATION CURVE OF SLB IN pH 7.4, 1.2, AND DEIONIZED WATER	240
A2. WASHING OF 5FU LOADED IN HNT BY THE GAS PROCESS USING ACETONE	242

APPENDIX B 243

B1.1. SPRAY ATOMIZATION DUE TO THE GRADUAL OPENING OF THE INJECTION VALVE IN
ARISE 244

B1.2 INFLUENCE OF ADDITIVES IN ES100 ON SPRAY PROFILE 248

B1.3. ARISE ASSISTED COAT OF ES100 ON HNT 249

APPENDIX C 251

C1. PRELIMINARY SCALE-UP STUDY ON ARISE 252

C1.1 INTRODUCTION 252

C1.2 MATERIALS AND METHODS 252

C1.3. RESULTS AND DISCUSSION. 256

C1.3.1 ANTISOLVENT EFFECT 256

C1.3.2. BULK DENSITY 257

C1.3.2 SCANNING ELECTRON MICROSCOPY 258

C1.3.3. PARTICLE SIZE DISTRIBUTION 266

C1.3.4. PRODUCT YIELD 266

C1.3.5. LOADING ESTIMATION 268

C1.4. SCALE-UP CHALLENGES 268

C1.5 CONCLUSION 269

REFERENCES 270

STATEMENT OF ATTRIBUTION 304

List of Figures

Figure 1.1 Illustration of the dose-response curve. The green line indicates the drug dosage, and the red line indicates the corresponding side effects. (Modified from Craig, and Stitzel et al [9] and Muller, and Milton et al[10]).	3
Figure 2.1 Chemical Structure of 5-Fluorouracil	12
Figure 2.2 Chemical structure of Silibinin	13
Figure 2.3 Scheme on the classification of drug micro/nano formulation. (Gas expanded liquids: GXL, and Supercritical fluid system: SCF).	15
Figure 2.4 Schematic of the Top-down and Bottom-up methods of nanoformulation.	16
Figure 2.5 Pressure (P)-Temperature (T) equilibrium curve. T _c : Critical temperature, P _c : Critical pressure, (a): Sublimation curve, (b): Vaporization curve, (1): Triple point, and (2): Critical point. (Adapted from Halder et al.[98] and Rabemanolontsoa et al.[99]).	19
Figure 2.6 (a) Change in the volumetric expansion (ΔV) of the organic solvents-CO ₂ mixture with CO ₂ pressure (P) at 40 °C. (b) Change in solvent polarity (π^*) with CO ₂ pressure (P) at 40 °C. (adapted from Jessop et al [105], Denardina et al [108], and Wyatt et al [109]).	22
Figure 2.7 Schematic of RESS process. 1: Mixing chamber, 2: Precipitation chamber with a micro-capillary nozzle on top.	24
Figure 2.8 Schematic diagram of the DG antisolvent processes. 1: Gas expanded solvent with precipitates, 2: Nozzle for passing API solution and DG-CO ₂ , a: Coaxial nozzle. (adapted from Foster et al[94]).	27
Figure 2.9 Schematic of the ARISE process. (1): Injection chamber, (2) Rapid opening valve, and (3): Precipitation chamber filled with atomized jet and particles formed.	34
Figure 2.10 The dependency of precipitation on solute concentration-C _s . S: is the temperature [°C] or Solvent composition for a given system. (adapted from Ende et al. [165]).	36
Figure 2.11 Schematic of the DELOS process. 1: High-pressure chamber, 2: one-way valve, and 3: precipitation chamber maintained at ambient condition. (Adapted from Ventosa et al [177], and Foster et al [94]).	42

Figure 2.12 Schematic diagram of the CAN-BD and SAA process. (1): Mixing-tee, (2): Precipitation chamber with nitrogen flux, (3): Thin wall injector. (adapted from Foster et al [94]).	44
Figure 2.13 Categories of polymers/excipients used in colon targeted therapy. (Adapted from Zang et al [201]).	46
Figure 2.14 Chemical structure of ES100. (Adapted from Yoo et al [206]).	47
Figure 2.15 Schematic of Halloysite nanoclay and its chemical structure. (Adapted from Leporatti [243], and Satish et al [246]).	55
Figure 2.16 TEM image of Halloysite nanotubes.	55
Figure 2.17 Zeta potential (ζ) of HNT, Alumina, and Silica. (Adapted from Leporatti et al [243]).	56
Figure 2.18 Illustration of organosilation of HNT surface. (adapted from Tharmavaram et al [284]).	64
Figure 2.19 Illustration of acid etching of inner alumina layers. (adapted from Abdullayev et al [245]).	66
Figure 2.20 Pressure (P)-Temperature (T) equilibrium curve. Tc: Critical temperature-3740C, Pc: Critical pressure-220 bar, (C): Critical point. (adapted from Okajima et al [305]).	68
Figure 3.1 (a) Schematic of the rig used to perform the GAS process, (b) Experimental set-up. Precipitation of HNT clay loaded with 5FU: (c) Suspension loaded in the Jerguson cell at atmospheric pressure; (d) Early expansion stage; (e) Late expansion state; (f) Final precipitated product.	75
Figure 3.2 (a) Dialysis set-up with donor and acceptor compartment, (b) Cassette filled with 5FU-nanoclay suspension before dialysis, (c) Nanoclay suspension after dialysis.	80
Figure 3.3 (a) Schematic of the ARISE rig used. 1: CO ₂ supply, 2: Syringe Pump, 3: Heating coil, 4: Precipitation Chamber, 5: Re-circulating heater, 6: Injection chamber, 7: Pressure indicator, 8: Back-pressure chamber, 9: Argon supply, 10: Solvent trap, 11: Injection conduit, Vn: Ball valve, CVn: Check Valve; (b) ARISE assembly; (c) parts of ARISE setup.	83
Figure 3.4 (a) Schematic of the Spray setup. 1: Argon supply, 2: Injection chamber, 3: Injection conduit, 4: Water bath, Vn: Ball valve, CVn: Check valve; (b) Image of the Injection chamber, ball valve, and the injection conduit used in the experiment; (b) Assembled spray setup.	85

Figure 3.5 Setup for mechanical mixing of HNT and 5FU.....	91
Figure 3.6 Schematic diagram of the Subcritical Water-HNT Treatment set-up. (1) Furnace, (2) Temperature and pressure controller, (3) Pressure vessel, (4) magnetic stirrer, (5) Heating fan, (6) T-junction connector, (7, 8, 11) check valve, (9) ISCO high-pressure pump, (10) Nitrogen supply, (12) Exhaust sample collection, and (13) Drive motor; (b) Assembled setup; (c) Assembly of parts inside the furnace.....	93
Figure 3.7 Thermal treatment of HNT using Soxhlet apparatus.....	94
Figure 4.1 Mass fraction of free drug α_F ($=m_{\text{free}}/m_{\text{tot}}$, where m_{free} is the mass of the free drug and m_{tot} is the total mass of drug used), washed with MeOH as a function of the mass ratio R ($=m_{\text{HNT}}/m_{\text{tot}}$, where m_{HNT} is the mass of the HNT). Inset: Mass fraction of free drug as a function of the inverse mass ratio.	99
Figure 4.2 TEM images of HNT. (a) Pristine, and (b) Elemental mapping of Alumina (red) and Silica (green) from TEM-EDS analysis.....	101
Figure 4.3 TEM images of HNT (a) Pristine, (b) after loading 5FU.	101
Figure 4.4 EDS spectra and SEM images of (a) pristine HNT, (b) 5FU, and (c) HNT loaded with 5FU.	103
Figure 4.5 FTIR spectra of pristine HNT, 5FU, and 5FU loaded HNT.....	104
Figure 4.6 Nitrogen adsorption-desorption isotherm of pristine HNT (blue) and GAS processed HNT (red).	105
Figure 4.7 (a) TGA mass loss curve of sample (M_{sample}) of pristine HNT and 5FU, (b) first derivative of M_{sample} of pristine HNT and 5FU, and (c) Mass loss curve of 5FU encapsulated HNT.	106
Figure 4.8 (a) Drug loading, L (mass of loaded drug relative to total mass of the precipitation product), of the washed product as a function of the mass ratio R ($=m_{\text{HNT}}/m_{\text{tot}}$, where m_{HNT} is the mass of the HNT and m_{tot} is the total mass of drug used). Inset: Adsorption, Γ (mass of drug adsorbed per mass HNT), as a function of the solution concentration of free drug, c_F [g/L]. (b) Encapsulating efficiency, E (mass of loaded drug relative to the total mass of drug used), as a function of the mass ratio R	107
Figure 4.9 (a) Qualitative sketch of the stages of the GAS process: amount of dissolved drug (5FU) – red line, amount of HNT – blue line, and amount of carbon dioxide – black line. See text for description. (b) \bigcirc – Decrease of the relative viscosity,	

μ_ε/μ_0 (μ_ε is viscosity at expansion ε and μ_0 is viscosity at expansion $\varepsilon=0$), and ∇ – Decrease of the relative polarity parameter, $\pi_\varepsilon^*/\pi_0^*$, (π_ε^* is the polarity parameter at expansion ε and π_0^* is the polarity parameter at expansion $\varepsilon=0$), as functions of the volumetric expansion.....	108
Figure 4.10 Cumulative drug release, R_D (ratio of amount of drug released and total amount of loaded drug), from the 5FU-loaded HNT in aqueous environment as a function of time at pH = 7.4 (\square) and pH = 1.2 (\circ).....	111
Figure 4.11 Dependence of (a) the final cumulative release, R_D^∞ at pH =7.4 (\square) and pH = 1.2 (\circ), and (b) characteristic time, τ [min], at pH = 7.4 (\square) and pH = 1.2 (\circ), on the mass ratio R ($=m_{\text{HNT}}/m_{\text{tot}}$, where m_{HNT} is the mass of the HNT and m_{tot} is the total mass of drug used).	112
Figure 4.12 Electrokinetic potential, ζ [mV], of HNT dispersed in water (\square – Ref.[366]; \bullet – this work) as a function of pH of the aqueous solution. The pK of 5FU is shown with a vertical dashed line.	113
Figure 5.1 Graph of change in viscosity (η) with the concentration of ES100. Shear rate (μ_s at 0.02 s^{-1} , 25° C , solution in Ethanol).	117
Figure 5.2 Samples of pristine ES100 and the ARISE processed ES100 from different injection volumes for different ES100 concentration.....	120
Figure 5.3 Bulk density (ρ_{bulk}) of product from the ARISE process measured at various ES100 concentration.....	121
Figure 5.4 Illustration of volumetric particle distribution in (a) solid particles in ES100, (b) freely settled particles from ARISE processed ES100.	122
Figure 5.5 Samples of ES100 from the ARISE process performed at 40° C . (1) Conduit surface in C_{ES100} : 3 %, (2) Conduit surface in C_{ES100} : 5 %, and (3) Bottom filter of the precipitation vessel.	122
Figure 5.6 SEM micrograph of (a) pristine ES100, (b) magnified view of ES100..	124
Figure 5.7 SEM micrograph of C_{ES100} : 3 % (a) at low magnification, (b) magnified view.	124
Figure 5.8 SEM micrograph of C_{ES100} : 5 % (a) at low magnification, (b) magnified view.	124
Figure 5.9 SEM micrograph of C_{ES100} : 10 % (a) at low magnification, (b) magnified view.	125

Figure 5.10 SEM micrograph of C_{ES100} : 15 % (a) at low magnification, (b) magnified view.	125
Figure 5.11 (a, b) SEM micrograph of high concentration (10 %, 15 % C_{ES100}), 10 ml injection, (c, d) irregular precipitates from the ARISE at high concentration. .	126
Figure 5.12 (a) Graph displaying the effect of suspension volume Z_{avg} of ARISE products, (b) Z_{avg} measured for C_{ES100} produced from ARIS. (Error is SD of 3 trials).....	127
Figure 5.13 An estimate of flow velocity (v) and Reynolds number (Re) of the feed solution inside the conduit at the onset of valve opening.....	128
Figure 5.14 FTIR spectrum of (a) pristine ES100, (b) C_{ES100} : 3%, (c) C_{ES100} : 5%, (d) C_{ES100} : 10%, and (e) C_{ES100} : 15%, processed from ARISE.	131
Figure 5.15 Dimensions of pressure vessel used in the ARISE process.....	133
Figure 5.16 Spray propagation of ES100 in (top) air, and (bottom) water medium. (a) The initial phase of jet propagation, (b) Fully developed phase of jet propagation.	134
Figure 5.17 Illustration of the spray pattern in ARISE process. (1): Pre expansion region-injection chamber, (2): Conduit, and (3): Expansion region (precipitation chamber).....	135
Figure 5.18 Spray width as a function of spray time for different concentrations of ES100 in air.....	136
Figure 5.19 Spray width as a function of spray time for different concentrations of ES100 in water.	137
Figure 5.20 Illustration of the pressure-temperature dynamics in the ARISE process.	140
Figure 5.21 Spray angle variation with change in ES100 concentration in air and water medium.....	141
Figure 5.22 Variation of theoretical spray width “C” with ES100 concentration in air and water medium.	143
Figure 5.23 Time lag (Δt) as a function of ES100 concentration in both air and water as a medium.....	145
Figure 6.1 Samples of pristine ES100 and ARISE processed ES100, ES100-5FU, and ES100-SLB for different ES100 concentrations.	150

Figure 6.2 Images of the parts of ARISE after the micronization process. (a) Tip of the conduit, (b) Bottom filter of the precipitation chamber while using 10 % ES100 solution.	152
Figure 6.3 Bulk density of ES100, ES100-5FU, and ES100-5FU processed by the ARISE at 50 bar (ΔP) and 25°C, as a function of the concentration of ES100.	153
Figure 6.4 Illustration of various forms of formulations within the ARISE process. (The images are for illustration purpose and not to the scale).	156
Figure 6.5 Illustration of the washing mechanism of the ARISE produce. Harsh washing results in the extraction of free and encapsulated drugs and moderate conditions retain a major portion of encapsulated drugs. (The images are for illustration purpose and not to the scale).	157
Figure 6.6 Graph showing the trend of harsh and moderately washed product from the ARISE process as a function of Eudragit S100 concentration. (Errors are SD of 3 trials).	158
Figure 6.7 Graph showing the variation of the fraction of drug washed (α_d) as a function of wash time (t) of the ARISE processed samples. (Errors are SD of 3 trials).	159
Figure 6.8 SEM images of ARISE processed ES100 from MeOH, (a) 3% conc, (b) 3% conc –magnified view.	161
Figure 6.9 SEM images of ARISE processed ES100 from MeOH, (a) 5% conc, (b) 5% conc –magnified view.	162
Figure 6.10 SEM images of ARISE processed ES100 from MeOH (a) 10% conc, (b) 10% conc –magnified view.	163
Figure 6.11 SEM images of ARISE processed ES100 from MeOH, (a) unprocessed ES100, (b) 10 % conc-formation of chunks and microspheres.	164
Figure 6.12 SEM images of unwashed-5FU encapsulated ES100 by the ARISE process. (a) 3 % conc (ES100), (b) magnified image showing individually crystallized 5FU on top of the surface of ES100.	166
Figure 6.13 SEM images of unwashed-5FU encapsulated ES100 by the ARISE process. (a) 5 % conc (ES100), (b) magnified image showing individually crystallized 5FU on top of the surface of ES100.	167
Figure 6.14 SEM images of unwashed-5FU encapsulated ES100 by the ARISE process. (a) 10 % conc (ES100), (b) magnified image showing individually crystallized 5FU on top of the surface of ES100.	168

Figure 6.15 SEM image of (a) pristine 5FU, and (b) re-crystallized 5FU by the ARISE process.	169
Figure 6.16 Illustration of formation of craters on ES100 microspheres because of washing. (Drawings are for illustration purpose and not to the scale).	170
Figure 6.17 SEM images of washed 5FU encapsulated ES100 from ARISE. 3 % conc (ES100) before wash.	170
Figure 6.18 SEM images of washed 5FU encapsulated ES100 from ARISE. (a) 3 % conc (ES100) after 1 min, (b) 3 % conc after 8 min.	171
Figure 6.19 SEM images of washed 5FU encapsulated ES100 from ARISE. (a) 5 % conc (ES100) after 1 min, (b) 5 % conc after 8 min.	172
Figure 6.20 SEM images of washed 5FU encapsulated ES100 from ARISE, (a) 10 % conc (ES100) after 1 min, and (b) 10 % conc after 10 min washing in deionized water.	173
Figure 6.21 Energy-dispersive X-ray Spectroscopy (EDS) of 5FU encapsulated ES100 from ARISE. (a) Unwashed sample, (b) After washing.	175
Figure 6.22 SEM image of pristine SLB.	176
Figure 6.23 SEM image of washed samples of SLB encapsulated ES100 from ARISE. (a) 3 % conc (ES100), (b) 5 % conc.	177
Figure 6.24 SEM image of washed samples of SLB encapsulated ES100 from ARISE. (a, b) 10 % conc (ES100).	178
Figure 6.25 SEM image of the individual microsphere of SLB encapsulated ES100 from ARISE. The inset includes the magnified image of the microsphere surface.	179
Figure 6.26 Average hydrodynamic diameter (Z_{avg}) of ARISE processed samples of ES100, ES100-5FU, and ES100-SLB microparticles. (Error is SD of 3 experimental trials).	180
Figure 6.27 Drug loading, L, as a function of Concentration of ES100 (C_{ES100}).	181
Figure 6.28 Illustration of encapsulation of drug in the polymer in a DG environment. (1) Homogenous drug-polymer solution, (2) Expansion of solvent under DG environment and segmentation of polymer chain for the diffusion of drug molecules into the polymer matrix, (3) Solvent extracted drug encapsulated microsphere. (Drawings are for illustration and not to the scale).	182
Figure 6.29 Variation of loading, L with washing time, t for 3 % conc ES100-5FU system. (Error is SD of 3 trials). Inset graph from Figure 6.7 in Section 6.3.2.	183

Figure 6.30 Encapsulation efficiency (E) as a function of ES100 concentration. ...	184
Figure 6.31 XRD pattern of pristine 5FU with crystalline phase at 2θ : (1) 19.01° , (2) 24.50° , and (3) 28.62°	185
Figure 6.32 XRD patterns of pristine ES100 and 5FU encapsulated ES100 from ARISE process for all concentrations.	186
Figure 6.33 XRD pattern of pristine SLB and SLB loaded ES100 samples from ARISE process for all concentrations.	187
Figure 6.34 (a) The stable suspension formed after the addition of 0.5 % (v/v) Tween 20, (b) Zeta potential of ARISE processed SLB-ES100 sample dispersed in distilled water.	189
Figure 6.35 Cumulative release of (a) 5FU from ES100 microsphere, and (b) SLB from ES100 microsphere in simulated gastric pH 1.2 and Intestinal pH 7.4 at 37°C	190
Figure 6.36 Residual suspension of ES100 after 24 h dialysis in pH 1.2, and in pH 7.4.	193
Figure 7.1 Variation in αF with R for all the processes. (Error are SD of 3 trials)..	198
Figure 7.2 (a) Mass loss (vs) time “t” curve from TGA analysis, (1) mass loss due to decomposition of 5FU, (2) mass loss due to decomposition of HNT, comparison graph of (b) Drug loading, L, for different mass ratio R, and (c) Encapsulation efficiency, E. (The individual decomposition curves of HNT and 5FU can be found in Chapter 4, Section 4.2.4, and Figure 4.7).	200
Figure 7.3 (a): SEM image of GAS processed HNT-5FU sample (b): EDS profile of the sample shown in (a).	203
Figure 7.4 (a): SEM image of ARISE processed HNT-5FU sample, (b): EDS profile of the sample shown in (a).	204
Figure 7.5 (a): SEM image of mechanically processed HNT-5FU sample, (b): EDS profile of the sample shown in (a).	205
Figure 7.6 FTIR spectrum of unprocessed and DG processed samples. The imprints of 5FU in HNT is seen in all the encapsulated samples.	206
Figure 8.1 (a) Nitrogen absorption-desorption isotherm of HNT for various SCW treatment time (t), P/P_0 is the relative pressure, (b) Graph of BET surface area (A_{BET}) of HNT for various SCW processing time (t), the black and red line are the average BET surface area measured for untreated and thermally treated (at	

ambient condition) HNT respectively, and (c) Pore size distribution curve of untreated and SCW treated HNT, (Errors are SD of 3 trials).....	212
Figure 8.2 (a) Variation in dielectric constant ($\frac{\epsilon_m}{\epsilon_0}$) and Ion dissociation constant (K_w) of SCW with temperature (T) [481], and (b) Schematic of SCW etching process for HNT. (1) HNT suspended in water, (2) Etching of alumina layers in protonated SCW, and (3) Formation of new crystallite sites on HNT from saturated SCW.	214
Figure 8.3 A plot of total pore volume and average pore diameter (vs) SCW treatment time for HNT. Line (i) and (ii) represents the total pore volume, and the average pore diameter of HNT after thermal treatment at 170°C for 7 h at ambient pressure condition, respectively. (Errors are SD of 3 trials).....	216
Figure 8.4 Image of severely exfoliated HNT after etching in sulphuric acid. (Image from Gaaz et al [292]).	217
Figure 8.5 (a) FTIR spectrum of HNT before and after SCW process at a various treatment time, (b) Comparison of FT-IR spectrum of HNT processed from (1) SCW treatment (7 h), (2) after 21 h H ₂ SO ₄ treatment (adapted from Gaaz et al [292]), and (3) after 50 % alumina etching in H ₂ SO ₄ (adapted from Abdullayev et al[245]).	218
Figure 8.6 (a) X-ray diffraction spectrum of untreated and SCW treated HNT at various treatment times (Sample mass and parameters are fixed for comparison reason), (b) Sample of the model fit of the peak at 12.11° 2θ showing peak position and full-width at half maximum (FWHM), and, (c) Plot of change in peak area (A_{peak}) and crystallite size of HNT at various SCW treatment time.	221
Figure 8.7 Transmission electron microscopy (TEM) image of (1) untreated HNT showing hollow lumen, (2) interlayers of alumina-silicate under magnified view, and (3) SAD patterns of untreated HNT showing the multiple bright spots due to polycrystalline phase.	225
Figure 8.8 Transmission electron microscopy (TEM) image of (1) HNT after 7 h treatment, (2) formation of closed tip and deformed surface after 12 h treatment, and (3) SAD patterns of HNT after 7 h treatment showing formation of isotropic halo at position 1 and 2 indicating the amorphous phase and formation of new crystallite sites.	226

Figure 8.9 (a) TOP-Image of HNT retrieved after 10 h and 12 h of SCW treatment, BOTTOM-water samples collected from the pressure vessel after 10 h and 12 h, (b) Graph of change in pH of the water collected after SCW treatment.	227
Figure 8.10 Graph showing variation in Zetapotential (ξ) of HNT dispersed in water with treatment time (t), ξ at t=0 corresponds to untreated HNT.	228
Figure 10.1 Calibration curve of 5FU in MeOH.	236
Figure 10.2 Calibration curve of 5FU in PBS.	237
Figure 10.3 Calibration curve of 5FU in 0.1M HCl.	238
Figure 10.4 Calibration curve of 5FU in deionised water.	239
Figure 10.5 Characteristic absorbance peak of 5FU at 266nm.	239
Figure 10.6 Calibration curve of SLB in EtOH.	240
Figure 10.7 Calibration curve of SLB in deionized water, pH:7.4, and pH 1.2 solution. (Concentration of the solutions: 0.0065 mg/ml).	241
Figure 10.8 Characteristic absorbance peak of SLB at 288nm.	241
Figure 10.9 Graph of the fraction of 5FU washed (α_F) and Loading (L) of 5FU in HNT after washing with acetone and MeOH.	242
Figure 11.1 Spray propagation of ES100 in air through the gradual opening of the injection valve in the ARISE process.	245
Figure 11.2 Initial jet phase of spray propagation of ES100 in water through the gradual opening of the injection valve in the ARISE process.	246
Figure 11.3 Fully developed phase of spray propagation of ES100 in water through the gradual opening of the injection valve in the ARISE process.	247
Figure 11.4 Spray width as a function of spray time for 5% w/w pristine ES100 and ES100-pCA combination sprayed in the air.	248
Figure 11.5 Spray width as a function of spray time for 5% w/w pristine ES100 and ES100-pCA combination sprayed in water.	249
Figure 11.6 (a) ES100-HNT sample retrieved from ARISE process, (b) Illustration of ES100 coating on the HNT surface, (c, d) ES100 coated HNT from ARISE.	250
Figure 12.1 Assembly parts of SC-4 ARISE set-up. Left: (1) Injection chamber, (2) Tapper sealed fittings, and (3) Precipitation chamber, Right: integrated conduit in the precipitation chamber (ID 4mm).	254
Figure 12.2 Assembly parts of SC-4 ARISE set-up operation with a varying volume of precipitation chamber (V_p), SC-1: 60 mL, SC-2: 150mL, SC-3: 300 mL, and SC-4: 1.4 L).	255

Figure 12.3 The antisolvent-solvent volumetric ratio for different scales of ARISE operation.	257
Figure 12.4 Bulk density (ρ_{bulk}) vs volume of precipitation chamber (V_p) for 5% ES100 and 5% ES100-SLB retrieved from scale-up ARISE process. (Inset figure are samples from-1: pristine ES100, 2: SC-1 (60ml), 3: SC-2 (150ml), 4: SC-3 (300ml), 5: SC-4 (1.4L), and 6: SC-4 (ES100-SLB).....	258
Figure 12.5 ARISE processed ES100 from SC-1 at, (a): 5 μm scale bar, and (b): 2 μm scale bar-magnified view.....	260
Figure 12.6 ARISE processed ES100 from SC-3 at, (a): 5 μm scale bar, and (b): 2 μm scale bar-magnified view.....	261
Figure 12.7 ARISE processed ES100 from SC-4 at, (a): 5 μm scale bar, and (b): 1 μm scale bar-magnified view.....	262
Figure 12.8 ARISE processed ES100 from SC-4 at, (a): 5 μm scale bar, and (b): 2 μm scale bar-magnified view.....	263
Figure 12.9 ARISE processed ES100-SLB from SC-4 at, (a): 2 μm scale bar, and (b): 1 μm scale bar-magnified view.	264
Figure 12.10 ARISE processed ES100-SLB from SC-4 at, (c): 5 μm scale bar, and (d): 2 μm scale bar-magnified view.	265
Figure 12.11 Average particle size (Z_{avg}) of ES100 from ARISE scale-up operations.	266
Figure 12.12 The product yield of micronized ES100 and ES100-SLB as a function of the volume of the precipitation chamber (scales of operation).	267

List of Tables

Table 2.1 Widely used APIs and their combinations in the treatment of colorectal cancer (CRC) [3, 36-38].	11
Table 2.2 Commonly used Dense Gas solvents and their properties [100-104].	20
Table 2.3 Properties of CO ₂ in gas, liquid, DG, and SCF phase. SI units.	20
Table 2.4 Classification of DG process [79, 94, 103, 110].	23
Table 2.5 List of anti-cancer drugs processed using DG antisolvent processes.	28
Table 2.6 List of influential parameters in the Supercritical fluid/DG process.	37
Table 2.7 List of ARISE processed APIs and excipients.	38
Table 2.8 Patented DG assisted drug formulation.	45
Table 2.9 List of anti-cancer drug formulation with ES100.	48
Table 2.10 List of SLB formulations.	53
Table 2.11 List of drugs encapsulated in HNT.	58
Table 2.12 Surface modification of HNT using acid/alkaline etching.	64
Table 3.1 Amounts of drug, m_{tot} , and HNT, m_{HNT} , used and their mass ratio, $R = m_{HNT}/m_{tot}$.	74
Table 3.2 TGA parameter for determining decomposition temperature of pristine HNT and 5-FU.	78
Table 3.3 TGA parameter for determining drug loading.	79
Table 3.4 Parameters used in the ARISE process for micronizing ES-100.	84
Table 3.5 Parameters used in ARISE for encapsulation of 5FU and SLB in ES100.	88
Table 5.1 Experimental conditions for the micronization of ES100 using ARISE process.	119
Table 5.2 FTIR spectrum peak identification [389, 390].	131
Table 6.1 Experimental conditions for the encapsulation studies of 5FU and SLB in ES100 by the ARISE process.	151
Table 6.2 Correlation coefficient (r^2), Korsmeyer-Peppas rate constant (K), and release exponent (n) of ES100-SLB system at pH 1.2 and 7.4.	192
Table 8.1 FTIR spectrum of HNT and characteristic peak positions.	219
Table 11.1 Spray time variation between rapid and gradual valve opening.	244

Abbreviation

General	
API	Active Pharmaceutical Ingredients
DG	Dense gas
SCW	Subcritical water
GXL	Gas expanded liquids
CRC	Colorectal cancer
GI	Gastrointestinal tract
SCF	Supercritical fluid
HPH	high-pressure homogenization
CXL	CO ₂ expanded liquid
BBD	Box Behneken Design
RSM	Response surface methodology
FPF	Fine particle fraction
LCD	Liquid crystal display
IUPAC	International Union of Pure and Applied Chemistry
FDA	Food and Drug Administration
SD	Standard deviation
FWHM	Full width at half maximum
PID	Proportional, Integral, and derivative
UV	Ultraviolet
Conc	Concentration
PI	Process Intensification
SC	Scale
ID	Internal diameter
cGMP	Current good manufacturing practice
SUPAC	Scale-up and post-approval changes
EPA	Environmental Protection Agency

Materials	
5FU	5-Fluorouracil
SLB	Silibinin

HNT	Halloysite nanoclay
ES100	Eudragit S100
PLGA	Poly (lactic-co-glycolic acid)
PLA	Poly(lactic acid)
PEG	Polyethylene glycol
PLLA	Poly(L-lactide)
PVP	Poly Vinylpyrrolidone
DSPC	Daistearoyl-sn-glycero-3-phosphatidyl- choline
DCM	Dichloromethane
HP- β -CD	Hydroxypropyl- β -cyclodextrin
PCA	Para-coumaric acid
HPMC	Hydroxypropyl methylcellulose
EC	Ethyl cellulose
HB	Berberine hydrochloride
CM-CNT	Carboxylated multiwalled carbon nano- tube,
IBU	Ibuprofen
AEAPTES	N-(β -aminoethyl)- γ -aminopropyl tri- methoxysilane
DMSO	Dimethyl sulfoxide
APTES	3-Aminopropyltriethoxysilane
MPTS	Mercaptonpropyltrimethoxysilane
CPTS	3-Chloropropyltrimethoxysilane
PVC	Polyvinyl chloride
PBA	Phosphate buffered Silane

Characterization

HPLC	High pressure liquid chromatography
FTIR	Fourier transform infrared
EDS	Energy Dispersive X-RAY spectroscopy
BET	Brunauer-Emmett -Teller
TGA	Thermogravimetric analysis
SAD	Selected area diffraction

TEM	Transmission electron microscopy
SEM	Scanning electron microscopy
XRD	X-ray diffraction
DLS	Dynamic light scattering

Process

GAS	Gas Antisolvent Process
ARISE	Atomized rapid injection for solvent extraction
RESS	Rapid expansion of supercritical solution
RESS-SC	Rapid expansion of supercritical solution with a solid solvent
RESS-N	Rapid expansion of supercritical solution with a nonsolvent
PGSS	Particles from gas-saturated solution
ASES	Aerosol solvent extraction system
PCA	Precipitation with compressed fluid antisolvent
SEDS	Solution enhanced dispersion by supercritical fluids
SEDS-EM	Solution enhanced dispersion with enhanced mass transfer using ultrasound in supercritical fluids
SAS	Supercritical antisolvent process
SAS-EM	Supercritical antisolvent process enhanced mass transfer method
DELOS	Depressurisation of an expanded liquid organic solvent
CAN-BD	Carbon dioxide assisted nebulization or aerosolization of liquid solution
SAA	Supercritical fluid assisted atomization
SFEE	Supercritical fluid extraction and emulsion process

Nomenclature

C_a	Saturation solubility of solute
C_a^0	Solubility of large solute particle
v_a	Molar volume of solute (m ³ /mol)
σ_a	Interfacial energy between solute and solvent (J/m ³)
R	Universal gas constant
T	Temperature in °C
r_a	Radius of microparticle
P	Pressure (bar)
T_c	Critical temperature in °C
P_c	Critical pressure (bar)
$\Delta V, \varepsilon$	Volumetric expansion (%)
π^*	Solvent polarity (dimensionless)
L	Drug loading (%)
E	Drug encapsulation efficiency (%)
C_s	Solute concentration
P_g	Nucleation growth rate (nucleus/Vt)
t	Time (s)
V	Volume (mL)
K_{ss}	Nucleation rate constant
ΔC	Degree of supersaturation
n	Order of nucleation
ζ	Zeta potential (mV)
m_{tot}	Mass of drug (mg)
m_{HNT}	Mass of HNT (mg)
m_o	Initial mass of sample (mg)
m_l	Mass after drug decomposition (mg)
V_n	Ball valves
CV_n	Check valves
ρ_{bulk}	Bulk density (g/m ³)
$M_r, m_s,$	Mass of retrieved sample (mg)
M_{sample}	

V_r	Uncompacted volume occupied by the sample (mm ³)
ΔP	Pressure differential (bar)
m_{drug}	Mass of loaded drug (mg)
αF	Mass fraction of loosely attached drug (dimensionless)
m_{free}, W_{drug}	Mass of free drug (mg)
V_m	Molecular volume of drug (m ³ /mol)
Q_{abs}	Volumetric absorbance of Nitrogen (cm ³ /g)
Γ	Absorption of drug (dimensionless)
C_F	Free drug concentration (g/L)
μ, η	Viscosity of the solution (mPa.s)
R_D	Cumulative drug release (%)
R_D^∞	Maximum drug release (%)
τ	Characteristic time constant (dimensionless)
K_H	Huggins parameter
η_{sp}	Specific viscosity
C_{ES100}	Concentration of ES100 (wt%)
μ_S	Shear rate (s ⁻¹)
Z_{avg}	Average particle size (μm)
S	Supersaturation ratio (dimensionless)
y_{mix}	Solute concentration (g/L)
y_{eq}	Saturation concentration of solution (g/L)
Q	Flow rate (m ³ /s)
v	Flow velocity (m/s)
A_c	Conduit cross-sectional area (mm ²)
r	Conduit radius (mm)
L_c	Characteristic length (mm)
Re	Reynolds number (dimensionless)
We	Weber number (dimensionless)
σ	Surface tension (Nm)
W_d	Spray width (mm)

C_a	Curved spray width (mm)
C_t	Spray width (mm)
P_p	Internal pressure (bar)
P_{gxl}	GXL pressure (bar)
P_s	Surface tension pressure (bar)
d	Diameter of microparticle (μm)
θ	Spray angle ($^\circ$)
q	Flow rate constant
G_{sol}	Specific gravity of solution (g/mL)
G_{medium}	Specific gravity of solvent (g/mL)
D	Spray length (mm)
φ	Momentum flux (kg.m/s)
Δt	Time lag (ms)
α_d	Fraction of washed drug (%)
K	Krosmeier-Peppas rate constant (min^{-1})
A_{BET}	BET surface area (m^2/g STP)
V_g	Total volume of gas adsorbed (m^3)
V_m	Volume of monolayer gas adsorbed (m^3)
P/P_0	Relative pressure
ϵ_m	Dielectric constant of medium (F/m)
ϵ_0	Dielectric constant of vacuum(F/m)
K_w	Ion dissociation constant
2θ	Angular peak position ($^\circ$)
A_{peak}	Peak area (a.u/mg)
B	Integral breadth (rad)
λ	Incident X-ray wavelength (nm)
f_L	Lorentzian function (dimensionless)
γ_L	FWHM value of Lorentzian function
p	Position variable
f_G	Gaussian function
γ_G	FWHM value of Gaussian function
f_{pV}	Pseudo-Voigt function
η	Integration constant

CHAPTER 1

INTRODUCTION

1.1 BACKGROUND AND INSPIRATION

The pharmaceutical industry has seen a drastic expansion in developing new APIs and treatment procedures in cancer drug research over the last two decades [1]. The evolution in diagnosis and treatment procedures help in thwarting the malignant mutation and improve the survival rate of individuals [2]. Statistics of 2019 from *Cancer Australia, Government of Australia*, and *Cassidy et al* [3] show that colorectal cancer is the third most common cancer type and has the highest mortality rate [4, 5]. The treatments involve invasive surgical resection and non-invasive methods such as radiation therapy and chemotherapy by ingestion of the Food and Drug Administration (FDA) approved primary drugs and drug combinations. The development of new drugs and drug formulations are time-consuming and tedious due to the extensive regulatory demands and high cost of capital for uncertain returns [6].

The route of administration for drug delivery includes intravenous, intramuscular, topical, and intravascular as invasive means and oral routes in the form of tablets as a non-invasive way. The convenience in administering drugs orally makes the oral administration, the preferred route, which will be explained in Chapter 2, Section 2.1[7]. However, oral administration in the form of tablets reduces the drug efficacy due to the premature release in the non-targeted sites inside the body. The premature release results in decreased absorption in the target sites requiring repeated dosage crossing toxicity limits[8]. The illustration in Figure 1.1 presents the relationship between drug dosage and therapeutic response. The allowable therapeutic dose and a lethal dose of drugs based on the therapeutic dose effect can be understood from the window between the dosage (green line) and side effect (red line) curves[9, 10]. Customarily, an increase in drug dosage increases the response and hence the therapeutic effect of the drug. However, drug response benefits are accompanied by the side effects due to overdose, negating the therapeutic efficiency of the treatment. Cancer drugs have a narrow therapeutic dose level, implying that a slight increase in dosage results in a significant increase in side effects (upward arrow in Figure 1.1) crossing allowable limits [11, 12]. Although the above treatment provides a cure and long survival of patients, if not for complete normalcy in life, the problem of drug toxicity due to overdose remains, necessitating a significant improvement of oral drug administration [13].

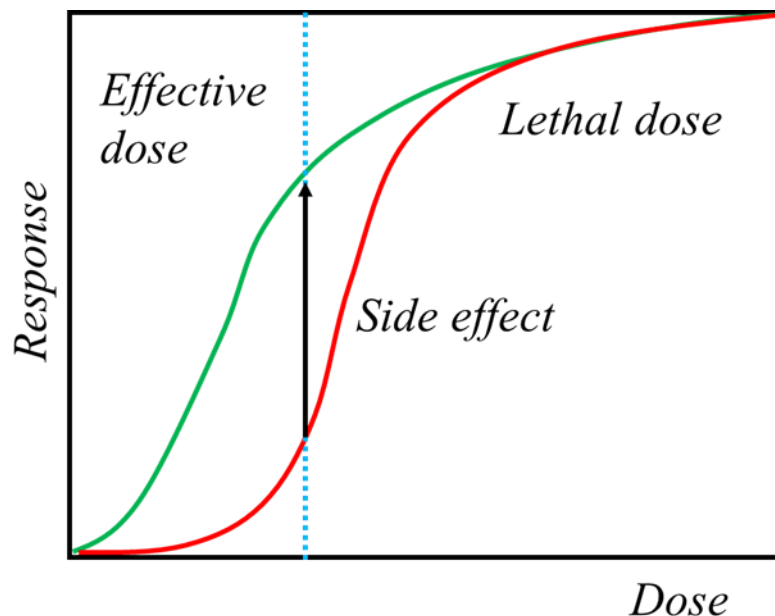


Figure 1.1 Illustration of the dose-response curve. The green line indicates the drug dosage, and the red line indicates the corresponding side effects. (Modified from *Craig*, and *Stitzel et al* [9] and *Muller*, and *Milton et al*[10]).

From a chemical engineering perspective, micronization and micro/nanoformulation of existing drugs are the most promising solution to overcome the issue mentioned above. The drug's decreased particle size increases the flowability, surface-to-volume ratio, and enhances the absorption into the target sites, hence improving the therapeutic effect (Chapter 2, Section 2.2). Micronizing the drugs and further encapsulating them into a nanocarrier protects them from getting metabolized in the gastric tract and liver. A significant portion of the drug is preserved for the target site (colon environment in the current study). Further, the slow release of drugs from nanocarriers maintain constant drug concentration over an extended period, avoiding fluctuations due to repetitive dosage as detailed in Chapter 2, Section 2.2[8]. Drug formulation through encapsulation in various nanocarriers such as polymers, liposomes, porous materials, dendrimers, to name a few, prevent premature release of drugs, otherwise released from tablets in non-specific locations in the body[14]. The bioavailability of the encapsulated drugs increases by site-specific absorptive endocytosis by preventing premature metabolism in non-specific sites [15]. As a whole, micronization and micro/nanoformulation of the existing drugs improves the targeted delivery, bioavailability, time extended-release, and reduced toxicity significantly[16-19].

Finally, the time, cost, and difficulty in synthesizing new drugs are avoided, saving the pharmaceutical industries from the lengthy and expensive process [20].

Conventional micronization and formulation methods such as jet milling, spray drying, emulsion technique, and electrostatic extrusion are used in producing micro/nanoparticles. The operation involves either breaking down large particles into smaller ones or mixing constituent compounds in solution followed by crystallization[21]. Although some of these methods are successful in producing particles with narrow size distributions, they suffer many limitations as listed:

- Process induced shear mechanical strain that can affect the microparticles.
- Thermal induced stress on the particles due to harsh operating conditions. This affects the quality of the product, specifically on thermally sensitive APIs and excipients.
- High inter-batch variation.
- Use of large volumes of solvents and chemicals in the process resulting in the release of toxic wastes.
- Costly removal of residual solvents.
- Multiple processing steps.

Green technologies aim to reduce the cost of processing and the amount of waste produced. Dense gas (DG) processing and the use of subcritical water (SCW) are viable alternatives to traditional methods. DG processes use carbon dioxide as a solvent, co-solvent, or antisolvent because of its non-toxic, non-flammable, and sterile properties[22]. The uniqueness of DG is that they exhibit liquid-like densities but gas-like diffusivities and viscosities[23]. The DG system is highly sensitive to temperature and pressure near the critical point, which allows tunability of its density and diffusivity and, hence, the fluid's solvation power.

Most of the API and nanocarriers are insoluble in carbon dioxide and soluble in organic solvents and aqueous solutions. When the dense carbon dioxide is mixed with the organic solution containing the solubilized API, the solution engenders volumetric expansion of the solvent resulting in a change in the solution's solubility. The increase in miscibility of DG and organic phase of the solution decreases the solubility of the solute phase and saturates, thereby precipitating the API as micro/nanoparticles. In this way, DG (dense carbon dioxide) acts as an anti-solvent in drug formulation (details of various processes are explained in Chapter 2, Section 2.3). The DG-solution mixture

is also called as Gas Expanded Liquids (GXL) system. By employing GXL system, a large spectrum of nanocarriers and API which are thermally sensitive and have low solubility in organic solvents can be processed. The Implementation of the DG/GXL process brings about the following advantages over the conventional approach as en-listed:

- Process tunability.
- Particles of uniform size and morphology.
- Moderate operating temperature favourable for thermally sensitive APIs and excipients.
- A single-step batch process with less processing time.
- Less use of solvent and minimal toxic wastes.
- High product yield per batch operation.

Analogous to the DG system, SCW has been used extensively as a tuneable solvent for processing API and nanomaterials. The water polarity decreases at elevated temperature (100 °C and 300 °C, moderate pressure) and is utilized to micronize hydrophobic or lipophilic materials. SCW processing also brings equivalent green advantages like DG compared to conventional techniques.

1.2 RESEARCH SCOPE

The inspiration for this thesis is on accomplishing micronization and micro/nanoencapsulation of APIs and excipients by exploring various DG processing for targeted drug delivery systems in colon cancer therapy. Further, attempts have been made to demonstrate SCW processing's effectiveness as an alternative to conventional acidic etching for surface modification in nanomaterials. By employing DG and SCW processing methods, efforts were made to subdue some of the issues faced in traditional processing.

Halloysite nanoclay/nanotube (HNT), and Eudragit S100 (ES100) polymer were used as excipients in this work. The first-line drugs for colorectal cancer treatment such as 5-Fluorouracil (5FU) and Silibinin (SLB) were used as model drugs in the study. SLB is lipophilic and it is a natural extract from milk thistle seeds while 5FU is a hydrophilic drug. The research focuses on two main DG processes: The Gas antisolvent process (GAS), and in-house developed novel Atomized rapid injection for solvent extraction

(ARISE) process in micronizing and encapsulating API. A customized SCW processing system has been developed in-house for surface treatment of HNT nano-material. In a gist, the specific research objective of this thesis is as follows:

- To demonstrate effective micronization and encapsulation of API in HNT and ES100 using GAS and ARISE process.
- Understanding the drug loading mechanism in excipients used in the current work.
- To study the effect of the drug-nanocarrier mass ratio and washing technique on the process's loading efficiency.
- To study the influence of polymer concentration on particle size and morphology of the product obtained from the ARISE process.
- To examine the pH triggered release of drugs in colonic conditions, evincing the advantage of micronization and encapsulation.
- To explore SCW processing as an alternative to acid etching of HNT nano-material.
- To analyze the effect of SCW processing time on surface morphology and physicochemical properties of HNT.

1.3 THESIS OUTLINE

This thesis consists of nine chapters. Chapter 2 presents an overview of different DG methods for the formulation of APIs. It also gives a detailed description of the various colon cancer drugs that are in the current treatment regime and excipients. The review follows the discussion on various research works in the API formulation through conventional and DG approach. The demand for micronization and micro/nanoformulation, the downside of conventional formulation techniques, and the advantages of DG processing were discussed in detail with illustrations. The credibility of the DG process such as Gas antisolvent (GAS) and Atomized rapid injection for solvent extraction (ARISE) processes in colon cancer drug formulation was discussed. The application of SCW processing as an alternative to conventional chemical etching of nanocarriers was delineated, comprehending the research objectives.

Chapter 3 describes the materials and methods used in the DG and SCW processing in this thesis. The details about the sample preparation, experimental set-up, and characterization techniques in the research projects are explained in detail.

In Chapter 4, the loading of an anti-cancer drug, 5-Fluorouracil (5FU), onto Halloysite nanoclay (HNT) using the GAS technique is discussed. The effect of the drug-nanocarrier mass ratio on loading characteristics is explored. The process efficiency on 5FU-HNT formulation is analyzed based on microscopic analysis and empirical estimation. The targeted delivery of the 5FU in the colon is discussed in detail using the *in-vitro* pH triggered release study in the simulated colon conditions.

Synthetic biopolymer ES100 was micronized using a novel ARISE process. The application of the ARISE process towards effective micronization of ES100 is detailed in Chapter 5. The effect of polymer concentration and spray pattern on the particle size and morphology are studied in detail. The rapid atomization mechanism in the ARISE was investigated by performing a spray atomization study. The spray pattern and its effects on particle formations are elaborated. The micronization and spray atomization study was conducted as a precursor in determining the viability of using the ARISE process to encapsulate APIs in ES100 polymer further.

Chapter 6 encompasses the encapsulation study of a hydrophilic drug, 5FU, and a hydrophobic drug, SLB, in ES100 using the ARISE process. The influence of the drug's intrinsic properties, such as solubility and drug-excipient compatibility, is examined and discussed. The effect of the drug-ES100 mass ratio on the loading behaviour is analyzed. The pH triggered release of the drugs in colonic conditions is investigated using the *In-vitro* dialysis method to ascertain the effectiveness of ES100 towards preserving pharmaceuticals from gastric degradation and further release in colonic conditions.

A comparative study on the loading of 5FU onto HNT using the GAS, ARISE, and conventional mechanical loading methods are discussed in Chapter 7. It is an extension to Chapter 4 and compares the processes based on the drug loading estimation. The credibility of using DG processes over conventional loading techniques are evaluated and discussed.

Besides the APIs' micronization and encapsulation using DG techniques, surface modification of HNT using SCW treatment is demonstrated in Chapter 8. SCW is used as a green alternative to acid/alkaline etching. The effect of treatment time on surface area and porosity of the HNT is explored. A detailed narrative of the mechanism of

acid/alkaline etching and advantages of SCW towards eliminating toxic residues are discussed in detail in Chapter 8.

Chapter 9 provides the conclusion of the current studies and the recommendations for future work in this genre.

Altogether, this thesis constitutes a concerted presentation of green processing techniques such as DG and SCW processes in micronization, formulation, and surface modification of the APIs and excipients. Two DG processes (GAS and ARISE) were employed to formulate colon cancer drugs (5FU and SLB) with natural nanocarrier (HNT) and synthetic polymer (ES100). The materials of interest in the current study constitute hydrophobic and hydrophilic drugs, naturally occurring nanocarriers, and synthetic polymers covering broad categories of APIs and excipients. The loading capacity and process efficiency were investigated in the ambient temperature condition based on the drug-nanocarrier concentration gradient. The benefits of the formulation towards colon targeted delivery were confirmed through *in-vitro* dialysis studies. Alongside the micro/nanoformulation and encapsulation study, the SCW processing was explored as an alternative method for surface modification of HNT. The green advantages and physicochemical property modification on the HNT were assessed based on the SCW processing time. The SCW processing is a nascent study on exploring an alternative chemical-free method, which has future potential in the surface enhancement of HNT and HNT like nanocarriers. Both the DG and SCW processing methods were studied with the intention of developing laboratory to industrial scale-up systems for drug formulations and surface enhancement.

Preliminary trials on the scale-up operation of the ARISE process was demonstrated as a culmination towards realizing industrial implementation. The study was conducted in 4 stages with an increased capacity of the precipitation chamber. The experimental procedures and results are discussed in Appendix-C.

CHAPTER 2

LITERATURE REVIEW

2.0 INTRODUCTION

The epidemiology of cancer diagnosis and treatment are pharmacologically improving over the decades towards achieving increased survival rates[24]. The World Health Organization articulates that cancer remains the archetypical and fatal disease worldwide [25]. Their prevalent in all age groups is due to the increased life expectancy of the average population. Cancers are of several types based on the place of the growth of the tumor. Amongst them, colorectal cancer remains the most common cancer with a high fatality rate [24, 25]. The evolution of cancer therapy dates back to the early 1900s with the advent of using animal models for treating malignancies [26]. The development in oncological studies in late 1900 paved the way towards the discovery of several effective anti-cancer drugs such as antifolates, thiopurines, and methotrexate, around the 1950s-1960s, which marked the milestone in cancer therapy with the possibility of internal medication than surgery[26]. Researches and clinical practices are still underway in cancer therapy to provide effective treatment and reduce mortality rates [27].

2.1 COLORECTAL CANCER THERAPY

Colorectal malignancy affects mostly middle-aged to elderly populations worldwide [28]. The stages of colorectal cancer (CRC) growth can be divided into four, with the first three stages non-metastatic and the fourth stage metastatic. The early CRC stages are treated with surgery, radiation, and chemotherapy using first-line drugs [29]. The metastatic CRC stage is treated with systemic chemotherapy with different drug combinations based on the malignant growth severity [3]. Surgical resection is the removal of tumors and lymph nodes from the affected colon part [30]. Radiation therapy involves the use of X-rays in affected colon locations to destroy the tumor cells. The systemic treatment, on the other hand, includes administrating anti-cancer drugs via intravenous (IV) tubes or in the form of tablets/capsules orally. Among the above therapies, oral administration is the most commonly followed method due to the relative ease of treatment, non-invasive factors, cost-effectiveness, and less traumatic nature to the patient [31-35]. The types of drugs for oral administration includes:

- Immunotherapy
- Chemotherapy
- Targeted therapy

The first-line drugs (APIs) used for CRC treatment are listed in Table 2.1. The combination and dosage vary based on cancer cells' mutational growth and the patient's overall health.

Table 2.1 Widely used APIs and their combinations in the treatment of colorectal cancer (CRC) [3, 36-38].

API	API combinations with the brand name
Capecitabine (orally active fluorouracil)	Leucovorin-5FU
Irinotecan	Leucovorin-oxaliplatin-5FU (FOLFOX)
Oxaliplatin	Leucovorin-Irinotecan-5FU (FOLFIRI)
5-Fluorouracil (5FU)	Capecitabine-irinotecan (CAPIRI)
Trifluridine	Capecitabine-oxaliplatin (CAPEOX)
	Cetuximab and any of the API
	Bevacizumab (Avastin)
	Panitumumab and any of the API
	Ziv-aflibercept - FOLFIRI
	Ramucirumab - FOLFIRI

2.1.1 5-FLUOROURACIL AS AN ANTI-CANCER AGENT

The development of 5-Fluorouracil (5FU) and its anti-cancer activity dates back to 1957 [39]. 5FU is used as a first-line drug in treating several malignancies such as colorectal, breast, gastric, ovarian, liver, and bladder cancers [40]. The role of 5FU in CRC therapy is critical. The treatment includes 5FU as a monotherapeutic agent or in combination with other APIs as seen from Table 2.1.[41].

5FU (Chemical formula: C₄H₃FN₂O₂) is a fluoropyrimidine derived from uracil with fluorine in position 5 on the pyrimidine block (Figure 2.1) (PubChem CID 3385). It is an antineoplastic agent, which prevents the growth of tumors by inhibiting DNA synthesis (antimetabolite property).

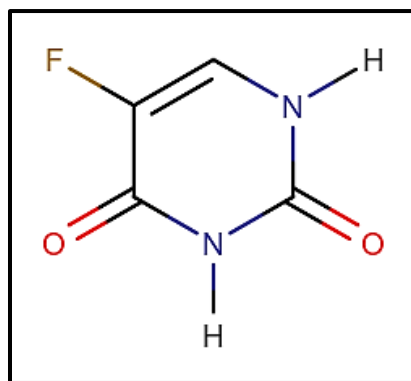


Figure 2.1 Chemical Structure of 5-Fluorouracil

The water-soluble 5FU (> 10 mg/ml [42]) has variable bioavailability due to low absorption and enzymatic degradation in the gastrointestinal (GI) tract resulting in low concentration in the colon environment [43-45]. Moreover, patients with tumors require continuous 5FU concentration in blood in systemic therapy for improved healing [31, 43]. However, continual 5FU concentration cannot be maintained with the current infusion and oral methods due to the premature drug release in the GI tract [43, 46, 47]. The overall pharmacokinetic imbalance due to variation in 5FU concentration results in decreased efficacy and increased toxic effects in cardiac, neural, and GI tracts [40, 41, 43, 48].

The dosage problem associated with 5FU was demonstrated by *Wasif Saif et al.* [38] who showed that when treating patients with 5FU through infusion and oral methods, about 40% to 60% of the patients are underdosed, and about 10%-20% of patients have overdosed. Hence, an alternate form of administration or formulation is necessary for improving the 5FU efficacy.

2.1.2 SILIBININ AS AN ANTI-CANCER AGENT

Silibinin (SLB), also called Silymarin is a natural flavonoid extract from milk thistle seeds (*Silybum marianum*) used for treating chronic liver diseases [49]. The molecular formula of SLB is $C_{25}H_{22}O_{10}$ constituting two diastomers of flavonolignan silibinin (Silybin A and Silybin B) in equimolar ratio as shown in Figure 2.2.

Recent research revealed the anti-neoplastic potential of SLB towards various anti-cancer therapies, specifically in CRC treatment [50-52]. SLB is less toxic and inhibits the cancer cell growth cycle by its anti-angiogenic activity, thereby reducing the proliferation of tumor blood vessels [53-55]. As mentioned in Section 2.1.1, standard

drugs used for CRC treatment possess high cytotoxicity, and the use of natural compounds like SLB in synergy with standard drugs reduces the toxic level in chemotherapy [49, 56].

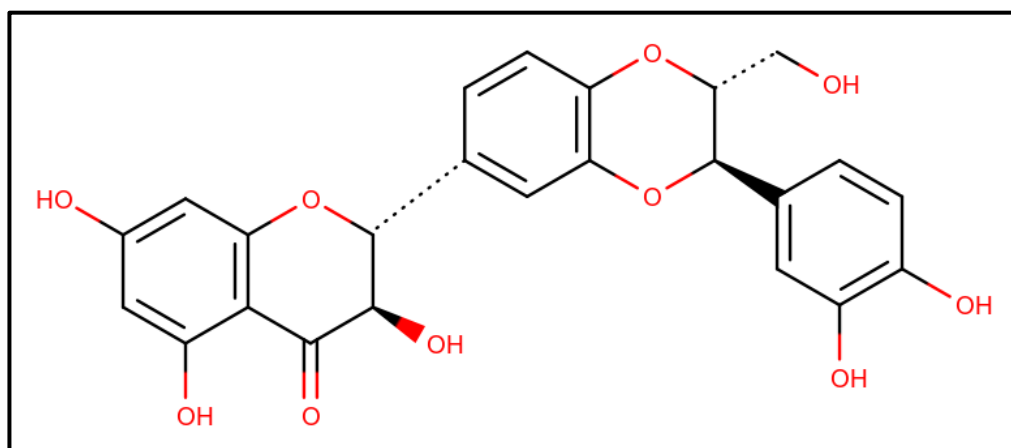


Figure 2.2 Chemical structure of Silibinin.

SLB is a hydrophobic flavonoid with low water solubility (less than 0.4 mg/ml) compared to standard anti-cancer drugs which are majorly hydrophilic [52, 57-59]. The increased membrane permeability and retention effect of SLB to the tissues due to its hydrophobicity favours its usage in the targeted delivery applications [60-62]. However, the low water solubility of SLB leads to poor bioavailability and hence poor intestinal absorption, restricting the use of SLB as a preferred drug for CRC treatment [49, 63, 64].

Undeniably, there is a challenge in oral administration of hydrophilic and hydrophobic drugs due to the premature release in the GI tract (hydrophilic drug) and poor bioavailability (hydrophobic drug), reducing their clinical effectiveness.

The above discussion stipulates that developing alternative drug formulation methods could improve the bioavailability of the drugs for achieving augmented therapeutic performance with reduced side effects. Thusly, in the current work, 5FU and SLB are used as model drugs as representatives of hydrophilic and hydrophobic APIs. The viability of drug-nano carrier combination and formulation methods are explored based on DG techniques, as explained in the following chapters.

2.2 MICRO/NANO DRUG FORMULATION

The drugs' oral bioavailability depends on intrinsic properties such as drug permeability, aqueous solubility, and presystemic metabolism, which can be enhanced through micronization and/or encapsulation in bio-compatible materials [65]. *Khadka et al*[66]. classified pharmaceutical particle processing methods based on the micronization and formulation capabilities. Micronization is the reduction of the particle size of the drugs. According to the *Ostwald-Freundlich* equation (equation 2.1), the reduced size increases the surface area available for dissolution and hence, the solubility of the drug [66, 67].

$$\ln \frac{C_a}{C_a^0} = \frac{2v_a\sigma_a}{RT r_a} \quad (2.1)$$

Where C_a is the saturation solubility of solute, C_a^0 is the solubility of the large solute particle, v_a is the solute molar volume (m^3/mol), σ_a is the interfacial energy between solute and solvent (J/m^2), R is the universal gas constant, T is the temperature in (K) and r_a is the radius of the micronized particle.

Further, the size reduction of drugs improves the particles' flowability, which in-turn shortens the risk of tissue ischemia caused by the blockage of blood flow due to large drug aggregates in parenteral administration [68, 69]. The optimal particle size differs based on the mode of administration. Parenteral delivery requires particle size below $100 \mu\text{m}$, delivery through the nasal/inhalation route requires size within $45 \mu\text{m}$ and $1 \mu\text{m}$ - $5 \mu\text{m}$ for pulmonary routes [32, 70]. Oral administration requires a particle size below $10 \mu\text{m}$ for improved dissolution and absorption [71]. Studies by *Patterson et al* [72] suggest that micronization and encapsulation of APIs with polymers convert the crystalline phase of hydrophobic drugs into an amorphous form. The dissolution properties of the formulated APIs improve due to the increase in Gibb's free energy in the amorphous phase [66]. The encapsulation of drugs into bio-compatible nano-carriers provides an external protective layer to the drug molecules, preventing them from degradation and premature release at non-targeted sites. Alongside the other benefits, encapsulation also aids in providing time-extended release at a targeted location by maintaining the continual drug concentration and improving therapeutic efficacy [73].

Drug formulation can be classified as a top-down and bottom-up approach based on the processing methods employed (Figure 2.3).

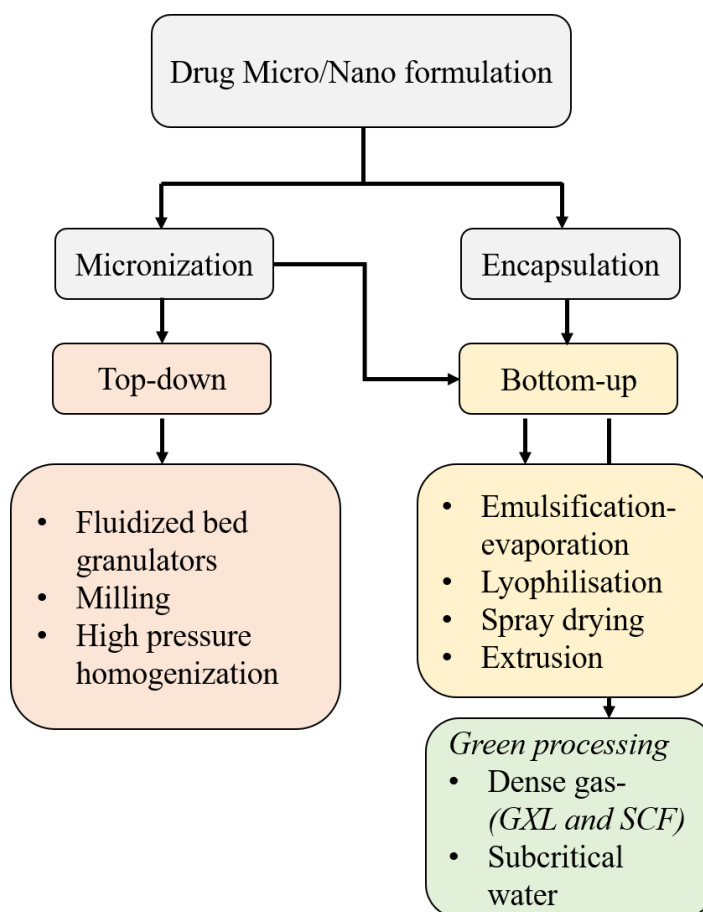


Figure 2.3 Scheme on the classification of drug micro/nano formulation. (Gas expanded liquids: GXL, and Supercritical fluid system: SCF).

The top-down method focuses on the size reduction of pristine drugs by techniques in which large particles are pulverized into finer ones by subjecting to external pressure or mechanical stress-Figure 2.4 [21, 66, 74]. The process can produce nano-sized particles with a narrow size distribution of about 100 nm to 200 nm [65]. Top-down processing involves the repetition of several steps: blending, crushing, granulating, and sieving. For example, milling, granulating, and extruding techniques use external mechanical stress to break big particles to form nanoparticles.

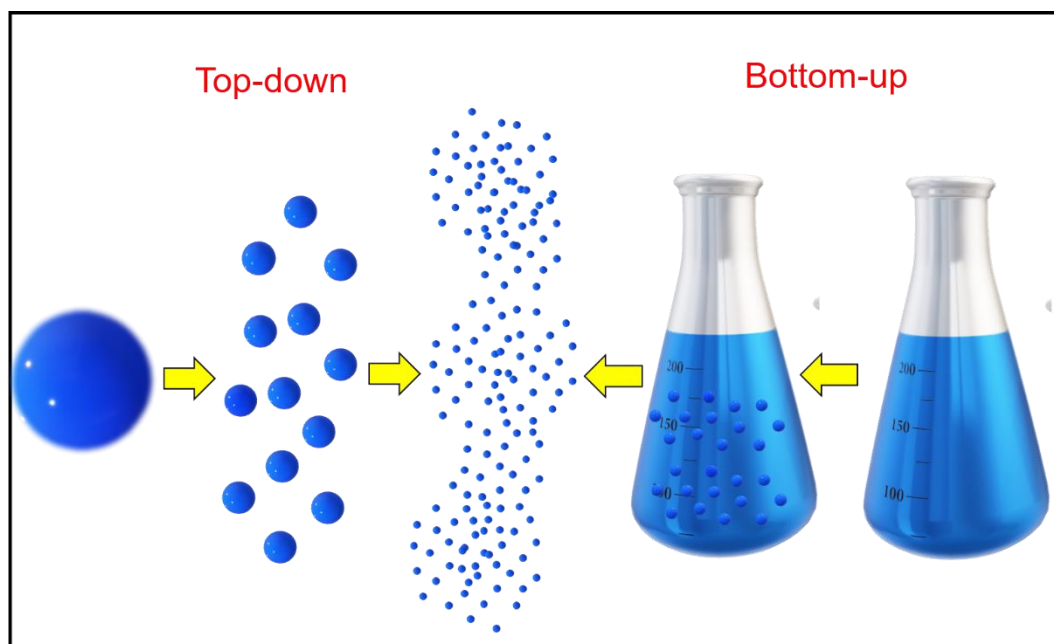


Figure 2.4 Schematic of the Top-down and Bottom-up methods of nanoformulation.

Drugs with low water solubility are widely micronized using milling and high-pressure homogenization processes (HPH). The process can handle drugs in large quantities (≈ 400 mg/ml concentration) with high yield [75]. Milling methods such as jet milling and ball milling use moderate pressure between 3 and 10 bar to generate a high shear environment. The drug particles are deformed to small size within the range of $5 \mu\text{m}$ - $40 \mu\text{m}$ [76, 77]. The process is repeated for several cycles to achieve the desired particle size. In milling, compressed air, stabilizers, and buffers are used to reduce agglomeration and dust formation [74]. The particles thus formed are within $5 \mu\text{m}$ suitable for pulmonary and oral delivery [74, 78].

The milled particles are further reduced to a narrow size distribution by high-pressure homogenization (HPH) process. As the name suggests, in the HPH process, the milled drug particles below $25 \mu\text{m}$ are suspended in the aqueous phase and passed through a narrow opening through a high pressure (100-2000 bar) induced jet [79]. The particles are broken to nano-size by the cavitation force. High suspension concentration (10-20 wt %) can be processed using HPH technique [74, 75]. For instance, particle size in the range of 75 nm-103 nm was achieved using the HPH technique in micronizing 5FU loaded PLGA nanoparticle [80].

The top-down process main drawback is that the operation involves randomly distributed shear force, which causes particle size variations within a batch operation. The process is energy-inefficient and it requires long operating hours for achieving narrow

particle size distribution, consuming substantial energy [76, 78, 79, 81]. The harsh thermal conditions and the erosion of grinding materials also pose the risk of degradation, thus lowering thermally sensitive drugs quality.

The bottom-up approach produces particles through precipitation from solution-Figure 2.4 [21]. The particles produced can be in the form of suspension or solid powders. The process is highly sensitive to operating parameters which in turn assists in tuning particle size and morphology [79]. The paramount advantage of the bottom-up approach is that the process is efficient and involves fewer operation steps compared to top-down methods [82]. The precipitation of solute from a highly miscible solution can produce nano-sized particles and eschew the issues associated with the mechanical degradation of drugs [83].

Several bottom-up methods such as emulsification, spray drying, using gas-expanded liquids, and SCW (Figure 2.3) formulate microparticles either by micronization of APIs in pristine form or by their encapsulation into a biocompatible nano-carriers. In methods such as spray drying and cryogenic spray freeze drying, the particles are micronized by spraying the solution through a nozzle in the stream of hot air (or) cold air (-60 °C). The solvent from the atomized particles evaporates and the product is collected from the filters [74, 84]. However, the process suffers the drawback of high operating temperature, affecting the thermally sensitive APIs and excipients [85]. For instance, *Insulin* micronized through spray drying, degraded due to the high temperature of the inlet, outlet, and surface of the dryer [70]. Moreover, the degradation effect due to the particles' extended resident time in the high-temperature environment cannot be neglected.

On the other hand, the emulsion evaporation method produces particles by mixing the API solution with the dispersion medium wherein the organic solvent evaporates, leaving behind solute particles dispersed in the immiscible medium [86, 87]. The process is capable of producing particles in the micrometer and nanometer range. As an example, micronization and encapsulation of *Hydrocortisone*, an anti-inflammatory drug, in polylactic acid using water-in-oil emulsion technique produced particle size in the range of 145 μm – 390 μm , whereas, *Vincristine sulfate* (anti-cancer drug) and *quercetin* (an anti-inflammatory drug) encapsulated in PLGA using oil-in-water emulsion displayed particle size of about 140 nm [88]. These observations indicate that the process produces a wide particle size distribution. Also, the particles formed from emulsion techniques are further required to be lyophilized to obtain a powdered product.

Several APIs are formulated using various emulsion evaporation techniques. Still, their purity is affected due to the incomplete evaporation of solvent from the emulsion and contamination of particles by the emulsifier coating [86, 89]. Additionally, drugs formulated by these processes can be unstable as the particles recrystallize from an amorphous state upon storage, setting significant drawbacks to its solubility [90]. Further, the entrapped solvent in the formulations reduces the dissolution rate of the APIs and produces toxic effects [65].

The use of green processing techniques such as DG and SCW process eliminates some of the disadvantages associated with conventional techniques. DG processes such as gas expanded liquids and supercritical fluid processes are versatile in formulating various drugs due to the ability to vary the solvation power of the solution and reduce the amount of organic solvents used compared to conventional processes [91]. The benefits of DG techniques and their role in drug formulation are discussed below.

2.3 DENSE GAS FORMULATION METHODS

The adaptation of DG processes as green alternatives in pharmaceutical manufacturing has been ongoing over two decades [92]. According to the report by *Ashcroft et al.*, about 56% of all raw materials in pharmaceutical processing are solvents [93]. DG scales down solvent consumption significantly and removes some of the limitations of conventional processing. The term DG refers to the state of the fluid in the vicinity of its critical point. The fluid's critical point is the temperature and pressure beyond which the liquid and gaseous phase become indistinguishable. Beyond the critical point, the system reaches supercritical fluid (SCF) conditions. DG includes fluids under both subcritical and supercritical conditions [32]. The properties of DGs are intermediate between the liquid and gas phases. The pressure-temperature phase diagram for a pure fluid is shown in Figure 2.5. In the vicinity of DG, the density and dielectric constant increases sharply with the increase in pressure along the critical point. The fluid possesses liquid-like density and gas-like diffusivity and viscosity [94]. The rise in density enhances the solvation power of the solution, improving the solubility of drugs in organic solvent. These properties can be tuned by manipulating the operating temperature and pressure. Working in moderate temperature and pressure produces significant variation in the DG density and solvation power of the solution, favouring the processing of thermosensitive APIs [94]. The combined liquid and gas-like behaviour in-

stitute exceptional capabilities for processing a vast span of APIs and excipients, minimizing the dependency on using a large volume of toxic organic solvents. The increase in mass transfer properties and low surface tension of the DG promotes molecular level mixing of solutes in solution, which are advantageous in extractions and drug formulation processes [95]. The advantages of using DG can be condensed as follows [96]

- Improved diffusion coefficient.
- Low viscosity.
- Low dielectric constant.
- Liquid-like density.
- High thermal diffusivity.
- High heat capacity.
- High thermal conductivity.

Pure gases or substances are used as DG in various applications. Table 2.2 details the list of substances that are used as DG with their critical properties. Amongst them, carbon dioxide (CO_2) is the most commonly used due to its properties: non-toxic, non-flammable, non-corrosive, cheap, and sterile [22, 32, 94, 97]., Table 2.3 lists the solvation properties of CO_2 .

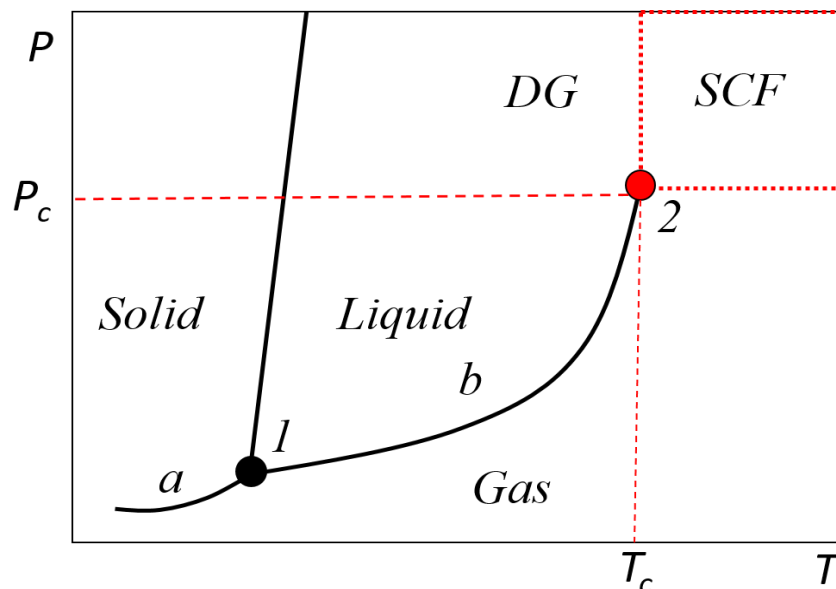


Figure 2.5 Pressure (P)-Temperature (T) equilibrium curve. T_c: Critical temperature, P_c: Critical pressure, (a): Sublimation curve, (b): Vaporization curve, (1): Triple point, and (2): Critical point. (Adapted from Halder *et al.*[98] and Rabemanolontsoa *et al.*[99]).

Table 2.2 Commonly used Dense Gas solvents and their properties [100-104].

Solvent	Critical properties		
	T _c (°C)	P _c (bar)	Density (g/cm ³)
Methane	-83	46.0	0.16
Ethylene	9	50.4	0.22
Chlorotrifluoromethane	29	39.2	0.58
Carbon dioxide	31	73.8	0.47
Ethane	32	48.8	0.20
Difluoromethane	78.5	58.73	0.424
Propylene	92	46.2	0.23
Propane	97	42.4	0.22
Ammonia	133	112.7	0.24
n-pentane	197	33.7	0.24
Trichlorofluoromethane	198	44.1	0.55
n-hexane	234	29.7	0.23
Isopropanol	235.2	47.6	0.272
Ethanol	243	63.8	0.28
Benzene	289	48.9	0.304
Toluene	318.6	41.1	0.292
Water	374	220.6	0.32

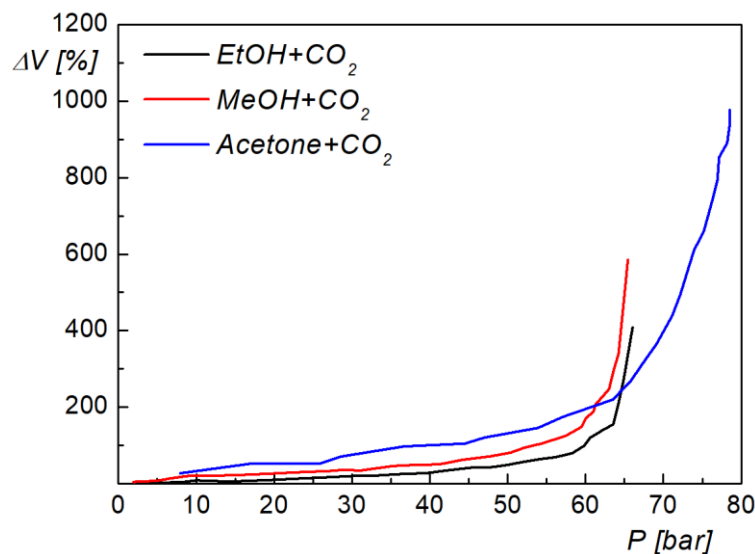
Table 2.3 Properties of CO₂ in gas, liquid, DG, and SCF phase. SI units.

Phase	Temperature (°C)	Pressure (bar)	Density (g/cm ³)	Diffusivity (cm ² /s)	Viscosity (cP)
Gas	25	1	1.78x10 ⁻³	10 ⁻¹	0.015
Liquid	5	100	0.948	5x10 ⁻⁶	0.105
DG	25	80	0.776	10 ⁻⁴ -10 ⁻³	0.069
SCF	50	150	0.699		0.056

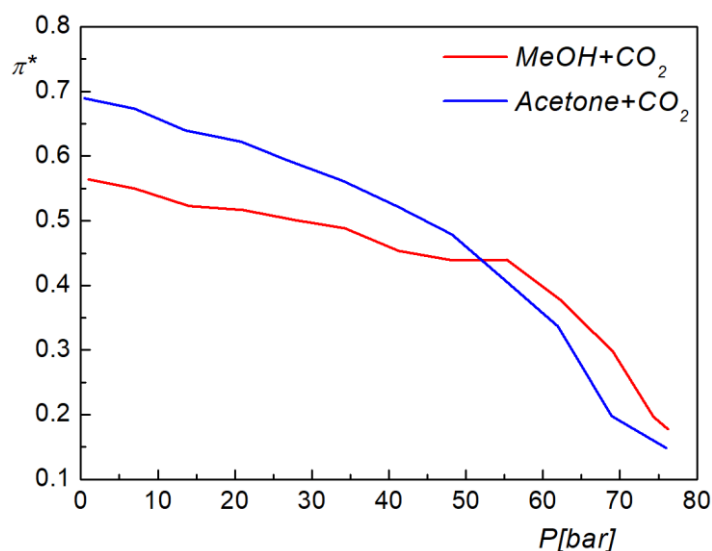
Most of the solids and liquids have high solubility in the DG phase. When a miscible organic solvent is mixed with CO₂, the volume of the solvent expands due to the complete dissolution of CO₂ within the liquid phase. Such a system is called gas-expanded liquids (GXL) or CO₂-expanded liquids (CXL)[105]. Depending upon the fraction of CO₂ in the mixture, the properties of the solution can be varied. The GXL system provides the combined advantage of the enhanced mass transfer of the dense CO₂ and improved solubility of solutes in the solvent [23]. The benefits of employing GXL as a choice over SCF systems are:

- Moderate operating pressure (low-pressure range-tens of bars) and temperature (within ambient conditions).
- Improved mass transportation rate due to CO₂-solvent mixture than that of pure organic solvents.

Based on solvents' affinity towards dense CO₂, the liquids are classified as Class I, II, and III. The majority of the organic solvents belong to Class II liquids, which show high miscibility in CO₂ with significant volumetric expansion, excepting polar organic solvents, which are less soluble due to low vapour pressure [23, 106, 107].



(a)



(b)

Figure 2.6 (a) Change in the volumetric expansion (ΔV) of the organic solvents-CO₂ mixture with CO₂ pressure (P) at 40 °C. (b) Change in solvent polarity (π^*) with CO₂ pressure (P) at 40 °C. (adapted from *Jessop et al* [105], *Denardina et al* [108], and *Wyatt et al* [109]).

Figure 2.6 (a) shows the dependency of volumetric expansion of common organic solvents with CO₂ pressure. The GXL system exhibits about 3 folds increment in volume within a moderate pressure range of 20-80 bar. The volumetric expansion is also affected by the change in temperature. Working at ambient temperature improves the solubility of CO₂ in the organic phase and increases the expansion capacity [108]. Further, the effectiveness of the micronization of solute in the GXL system depends on the solubility of the solute in the solution. The solvent polarity measured by the Kamlet-Taft parameter (π^*) indicates the solubilizing power of solvents. The polarity of the solvent reduces significantly with an increase in CO₂ pressure, thereby decreasing the solvation power of the solvent-CO₂ system as shown in Figure 2.6 (b). The change in the solvation power in the GXL system facilitates supersaturation and precipitation of solute particles within moderately high-pressure [105].

The role of DG as a processing medium in the formulation of APIs has been investigated extensively [103]. DGs can be categorized based on their role in the process - Table 2.4.

Table 2.4 Classification of DG process [79, 94, 103, 110].

DG as solvent*	DG as antisolvent*	DG as co-solvent*	DG as an aid in emulsion*
RESS RESS-SC RESS-N PGSS	GAS ASES PCA SEDS SEDS-EM SAS SAS-EM ARISE	DELOS	CAN-BD SAA SFEE DESAM

*Refer to the list of abbreviation.

Since the working mechanisms for all the processes under each category are similar, a generic overview is provided for all the processes. GAS and ARISE processes are the foci of the current study, which will be described in detail in the following sections.

2.3.1 DG AS A SOLVENT

DG can be used as a solvent to solubilize the solute molecules. The rapid expansion of supercritical solution (RESS) process is the most commonly used method to micronize particles by dissolving APIs and excipients in DG and rapidly expanding the solution through a micro-capillary nozzle - Figure 2.7. The expansion is of the order of (10^5 - 10^6 m/s), creating a supersonic jet from the nozzle [79]. The rapid depressurization decreases the density and the solvation power of the DG, thus causing supersaturation and precipitation of the dissolved material [111, 112]. The rapid expansion rate favours homogenous nucleation, thereby producing particles with narrow size distributions [113]. Non-polar and volatile polar compounds which are soluble in supercritical fluids can be processed through this technique [114].

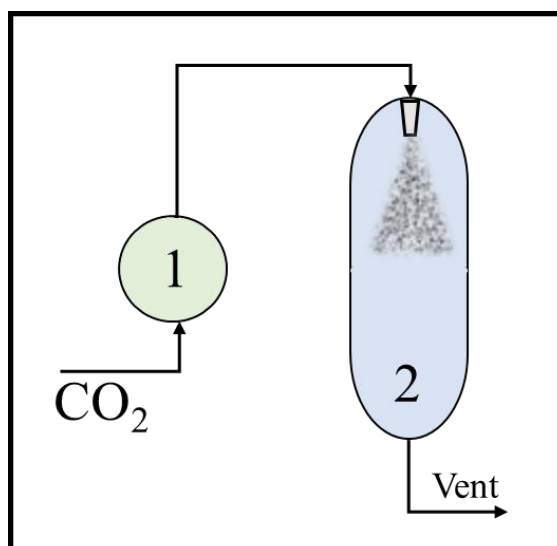


Figure 2.7 Schematic of RESS process. 1: Mixing chamber, 2: Precipitation chamber with a micro-capillary nozzle on top.

The factors governing the process are pre- and post-expansion temperature, pressure, solute concentration, and nozzle aspect ratio (length-to-diameter). They influence particle size, morphology, and also drug loading when an API is co-precipitated with an excipient. Succinctly, an increase in pre-expansion temperature for a given pressure increases the particle size and drug loading. Also, moderate pressure and increased nozzle aspect ratio affect the particle morphology. RESS process was adopted by *Sharma et al.* [115] in micronizing Cisplatin, an anti-cancer drug. The process produced particles irregular size and shape (200-300 nm) for the pre-expansion condition of 300 bar and 40° C. The study suggested that micronization using RESS increased the solubility of *Cisplatin* over 15 folds [115] The increase in solubility increased the bioavailability of Cisplatin and reduced cytotoxicity. However, the effect of post-expansion conditions on the particle size had varying trends [94]. The increase in post-expansion temperature did not directly influence particle morphology, but accelerated DG's evaporation in the expansion phase, speeding up the processing time [79].

The limiting factor for the RESS process is that most of the APIs and excipients are not very soluble in DG (solubility $\leq 10^{-3}$ g/g DG), restricting its utility in the formulation [94]. To solubilize them in DG, the temperature of the process must be increased over 80°-130° C, which is unsuitable for thermo-labile materials. *Naproxen* was encapsulated in polylactic acid (PLA) using the RESS technique at 200-400 bar, and 50 °C-70 °C, producing rod-like 120-200 nm encapsulates [116]. However, raising the temperature beyond 80 °C degraded the drug molecules, rendering them unsuitable for

consumption [117]. Further, the high operating pressure and temperature increased energy consumption, which is a concern for scale-up [94].

The RESS process was further modified to form a ternary system that includes solid solvents (RESS-SC), non-solvents (RESS-N), or gas saturated solution (PGSS), which enhances the solubility of the drugs and excipients. Several non-cancer drugs have been formulated through RESS processes [94]. However, limited work has been accomplished in formulating anti-cancer drugs. For instance, the anti-cancer drugs *Letrozole* and *Aprepitant* were formulated with the RESS-SC process to increase their solubility in ternary systems 7-8 times [118, 119]. The particle size was reduced from 30 nm to 19 nm for *Letrozole*, and from 25.6 μm to (23 ± 1.6) nm for *Aprepitant*.

The PGSS process is similar to the RESS process with the modification in the solubility of DG with solids. In the RESS process, the solid matrix is dissolved in the DG continuum. On the contrary, in the PGSS process, the DG is dissolved in the solid matrix thereby decreasing the viscosity of the solid melt. The rapid depressurization of the gas-saturated melt effectuates the vaporization of the DG and crystallization of solid particles. PGSS process is used in processing polymer materials such as PLGA and PEG due to the advantage of lowering glass transition temperature in the polymer-DG mixture. *Ibuprofen* was encapsulated in Poloxamer, Glucire, and Glyceryl monostearate using the PGSS process at 35 °C-60 °C and 100-200 bar to produce particles with increased aqueous solubility. The process produced 50-200 μm polymer microspheres with a 23° C reduction in their melting point [120]. The positive aspect of this process is that it requires less volume of CO₂ compared to the RESS process. However, the high operating pressure is a drawback for implementation [97].

2.3.2 DG AS AN ANTISOLVENT

In these processes, the DG is used as an antisolvent. Materials which are insoluble in DG can be micronized using these techniques. The APIs and excipients are solubilized in organic solvents, and the solution is expanded using DG-CO₂. The density and hence the dissolution power of the solution decrease due to the phase transfer between the solvent and CO₂ leading to supersaturation and precipitation of solute. Further, the isobaric addition of CO₂ removes solvent traces from the precipitates, producing solvent-free dry particles [94]. The operating concept for all the DG antisolvent processes such as GAS, SAS, PCA, ASES, and SEDS are similar but they differ only based on how the contact between the solution phase and the DG phase is initiated [103].

In the GAS process, the sub/supercritical fluid is introduced into the solution of interest, and the mixture is expanded at a specific pressure and temperature. The entire process is carried out in a single step inside the pressure vessel. In SAS, ASES, SEDS, and PCA processes, the solution of interest is introduced into DG, maintained at a specific pressure and temperature. These processes evolved over time by introducing different devices and methods of injection [102]. Henceforth, in further discussions, SAS, PCA, and ASES are addressed as ASES process for convenience. The schematic of the GAS, ASES, and SEDS processes are shown in Figure 2.8. The GAS process is a batch operation (fixed volume of solution-processed at a given time) while the ASES and SEDS processes are semi-continuous [94]. In the ASES and SEDS processes, the precipitation chamber is initially filled with DG similar to the GAS process.

Further, the drug solution and DG-CO₂ are concurrently delivered into the precipitation vessel through a concentric nozzle to maximize the supersaturation and precipitation shown in Figure 2.8 (ASES) [110]. The difference between ASES and SEDS process is that the SEDS incorporates a coaxial nozzle to generate turbulent flow. The high flow turbulence initiates fast mixing in the coaxial nozzle, improving the mass transfer rate and nucleation near the nozzle tip. The combined effect of high fluid velocity and turbulence-induced mass transfer generates fine particles[121]. While the GAS process is slow due to the gradual addition of DG-CO₂ to the solution, ASES and SEDS processes are rapid with large antisolvent-to-solute ratio, effecting fine particle production.

Several drugs and polymers have been processed using the GAS, ASES, and SEDS processes. *Foster et al* [94], *Yeo et al* [122], and *Padrela et al* [123] provided a comprehensive list of drugs and excipients processed using DG antisolvent methods, which includes various drug formulations. As the current work pivots on drug formulation of CRC treatment, Table 2.4 lists anti-cancer drugs processed by DG antisolvent methods.

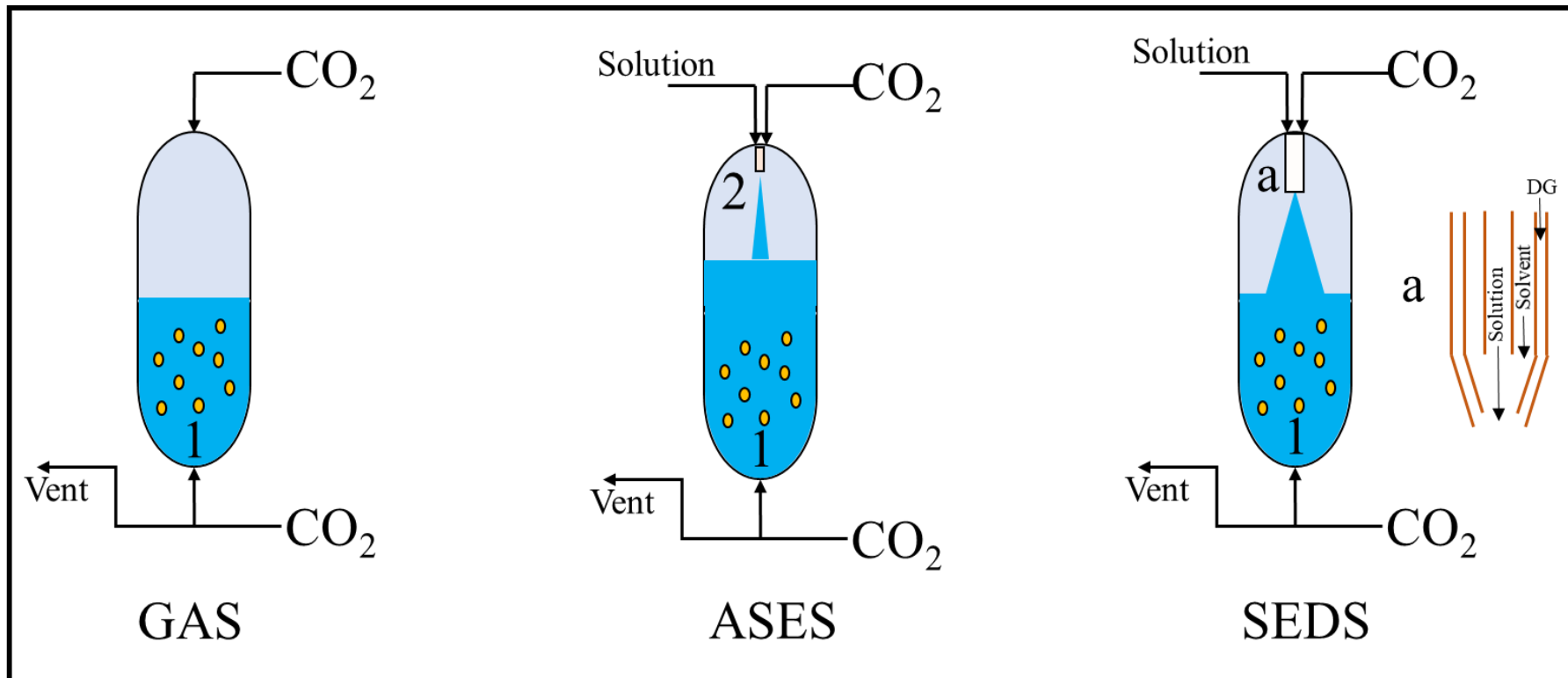


Figure 2.8 Schematic diagram of the DG antisolvent processes. 1: Gas expanded solvent with precipitates, 2: Nozzle for passing API solution and DG- CO_2 , a: Coaxial nozzle. (adapted from Foster et al[94]).

Table 2.5 List of anti-cancer drugs processed using DG antisolvent processes.

API	Excipient	Process	T (° C)	P (bar)	Particle Size (nm)	L* (%)	E* (%)	Ref
5-Fluorouracil (5FU)	Poly(L-lactide) (PLLA)	SEDS	33	120	980	3	17.80	[124]
Docetaxel	Polyethylene glycol (PEG)-liposome	SAS	34-46	100-220	269	--	79.20	[125]
Camptothecin	Soy lecithin, cholesterol	SAS	40	160	210	5.30	85.3	[126]
5FU	PLLA	SAS	50	180	220-670	36	--	[127]
5FU	Poly(lactide-co-glycolide) (PLGA)	GAS, SAS	GAS-40 SAS-40	GAS-120 SAS-110	--	GAS-9.8 SAS-45	--	[128]
Quercetin	OSA-starch, Lecithin	ScCO ₂ - spray dry- ing	40	120	1600-2900	--	OSA starch: 13.8 Leci- thin:97.4	[129]
Oridonin	Poly Vinylpyrrolidone (PVP)	GAS	55	140	--	--	--	[130]

API	Excipient	Process	T (° C)	P (bar)	Particle Size (nm)	L* (%)	E* (%)	Ref
Chelerythrine	--	SEDS	40	200	100-1000	--	--	[131]
Curcumin	--	SEDS	31-32.5	220-225	230-240	--	--	[132]
Methotrexate	--	SEDS	45	175	--	--	--	[133]
Rosemary extract	Polycaprolactone	GAS	40	300	254.5		82.8	[134]
Gemcitabine	mPEG-PLLA	ASES	--	--	--	--	--	[135]
Tamoxifen	PLLA	SAS	38	130	--	--	--	[136]
Quercetin	Pluronic F127	SAS	40	100	1000	56	--	[137]
Camptothecin	Bovine serum albumin-poly (methyl methacrylate)	SEDS	40	100	200-300	12.5	--	[138]
Curcumin	PVP	SAS	40	150	90	--	--	[139]
Curcumin	PLGA	Modified SAS	33-35	93-96	50	45	--	[140]
Paclitaxel	PLA	SAS-EM	35	90	435-930	--	83.5	[141]
Paclitaxel	Basilicum seeds mucilage	GAS	50	100,120,160	117-200	61.2,59,56.8	--	[142]

API	Excipient	Process	T (° C)	P (bar)	Particle Size (nm)	L* (%)	E* (%)	Ref
Etoposide	--	SEDS	40	180	586	--	--	[143]
9-Nitro-Camp- tothecin	--	SAS	30-45	80-125	436-910	--	--	[144]
Gefitinib	--	SAS	30-50	90-130	600-2510	--	--	[145]
5FU, Urea, Thio- urea	--	SAS	40	70-150	<u>5FU-Urea</u> Thickness: 500 Width: 2000-6000 Length: 10000- 60000 <u>5FU-Thiourea</u> Thickness: 10-20 Width: 2000-6000 Length: 10000- 60000	--	--	[146]
5FU	PLGA	SAS	55	207	--	0.05	--	[147]
5FU	Poly (D,L-lactide-co- glycolide)	ScCO ₂ foaming	40	180	58-364	5.4-17		[148]

API	Excipient	Process	T (° C)	P (bar)	Particle Size (nm)	L* (%)	E* (%)	Ref
Quercetin	Chitosan	GAS	30,40	100,200	--	0.1-2.6	--	[149]
Paclitaxel	Poly (D,L-lactic acid)	GAS	40	200	--	0.05-0.13	--	[150, 151]
Paclitaxel	Silk fibroin/PLLA-PEG-PLLA	SEDS	35	100	634	18	90.2	[152]
Gefitinib	PLLA	SAS	33-48	90-120	2480	15.8	95	[153]
Curcumin	PVP	SAS-FB	35,40	90	135-327,51-96	5.00-30.00	45.5-95	[154]

*L: Loading = mass of drug in the sample/total mass of sample, E: Encapsulation efficiency= mass of drug in the sample/ total mass of drug used.

The DG antisolvent processing involves several operating parameters: pressure, temperature, antisolvent/solvent flow rate, and solute concentration. These parameters have a combined influence over the process dynamics, supersaturation, and nucleation growth, making the analysis complex[155]. As a result, interpretations are focussed on specific materials and keeping certain process parameters unaltered.

Along these lines, the size and morphology of particles obtained from the ASES process depend mainly on the relative flow rate between API solution and DG-CO₂[103]. The high concurrent flow of API solution and DG produces small particles. The lowering of the DG-CO₂ flow rate causes an increase in API solution concentration and decreases supersaturation of the solvent rich phase, producing large particles. Moreover, the effect of operating temperature on the yield, particle morphology, and drug loading capacity is more dominant than pressure. Moderate operating temperature (ambient conditions) produce a better yield than high-temperature processing [156]. An example of such variation was reported by *Zhao et al.* in micronizing *Camptothecin* by the SAS process. The particle size of *Camptothecin* was reduced from 80 µm to about 0.25 µm. The study reported that the particle size increased by about 30%, with an increase in temperature up to 68° C. A similar trend was observed with an increase in solute concentration. The influence of pressure between 100-200 bar showed a decreasing trend in particle size, and pressure beyond 200 bar increased the particle size by 10% . *Naik et al.* [125] conducted a parameter optimization study using a Box Behneken Design (BBD) of response surface methodology (RSM) to understand the parametric influence of the DG antisolvent process on the formation of 5-Fluorouracil-Poly ethylene glycol (PEG) formulation. The results suggested that the reduction in particle size and increase in yield were facilitated by the rise in antisolvent flow rate and pressure. Operating temperature below 40° C favoured particle size reduction from 780 nm to 255 nm and high encapsulation efficiency of 79%, which was in agreement with findings from *Zhao et al* [157].

The GAS process can be carried out at a moderate pressure range (≈50-80 bar) [155]. Working in a high-pressure range is not suitable as it causes a change in nucleation dynamics due to the plasticizing effect on materials, specifically polymers. The plasticization alters the materials' glass transition temperature and binds the particle, forming aggregates [158].

In the report by *Hong et al.*[131], the influence of the solution flow rate in the ASES and SEDS processes on particle size was emphasized. The increase in flow rate from

2 to 3 ml/min produced small particles (0.2-0.8 μm) of *Chelerythrine* due to the increased momentum transfer between DG-CO₂ and solution, causing the disintegration of droplets. However, the pattern reversed with a further increase in flow rate from 3 to 5 ml/min. These varying trends in the physiochemical characteristics of the products confirm that the influence of the process parameters is co-ordinated, complex, and subjective to materials and process combinations.

Besides the mono drug-excipient combinations, *Zhao et al.* reported using the SEDS process in encapsulating *Paclitaxel* in polymer composite. The combination of natural polymer-Silk fibroin and synthetic polymers-PLLA and PEG demonstrated 18% of drug loading and 90% of encapsulation efficiency under the operating condition of 35 °C and 100 bar [152].

Deviating from the micronization and encapsulation of APIs in excipients, *Cuadra et al.* reported co-crystallization of 5-FU with Urea and Thiourea using the SAS and CSS processes. The co-crystallization of 5FU with a conformer Urea enhanced the bio-availability of the primary API (5FU) by forming supramolecular assembly through a non-covalent bond [146]. Long needles and plate-like co-crystals in a size range of 2-60 μm were produced under the process conditions of 40 °C and 70-150 bar.

2.3.2.1 ATOMIZED RAPID INJECTION FOR SOLVENT EXTRACTION (ARISE).

The Atomized rapid injection for solvent extraction process was initially developed and patented (Patent no: US,8,389,013B2) by *Foster et al.* in 2006 [94, 159]. The ARISE process is a single step-batch, a super gas process in which the energized solution is rapidly injected into the DG-CO₂ antisolvent to atomize solute particles [94]. In a way, the ARISE process derives the combined characteristics of the RESS and SAS processes. Looking closely into the process functioning, SAS, and ARISE processes utilize the anti-solvent ability of the DG-CO₂ and have spray atomization of the solution as the micronization mechanism. The schematic diagram of the ARISE process is shown in Figure 2.9 and the ARISE experimental set-up is detailed in Chapter 3, Section 3.2.2. The API/excipient solution is initially pressurized in the injection chamber with an inert gas. The solution is rapidly depressurized into the precipitation chamber filled with DG-CO₂ antisolvent maintained at a pressure lower than the injection chamber, using a rapid opening valve. The pressure-driven flow under the quasi-isothermal and isochronic condition atomizes the solution to form droplets[94].

The solvent phase from the droplet is extracted along the DG-CO₂, leaving behind the solid precipitate. The atomization and solvent extraction are achieved simultaneously, and the traces of residual solvents are further flushed with DG-CO₂ to recover dry powder formulation.

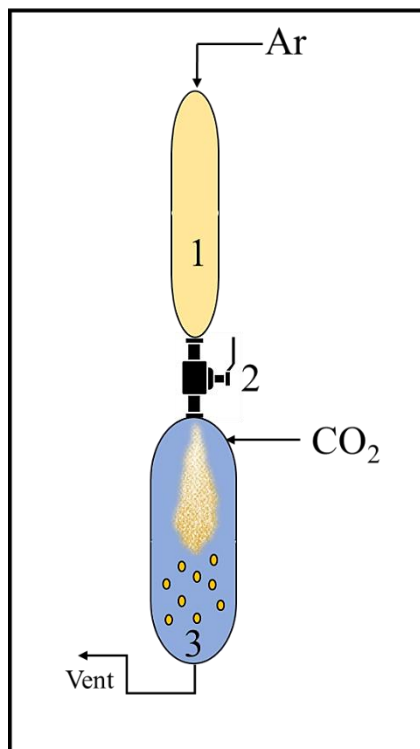


Figure 2.9 Schematic of the ARISE process. (1): Injection chamber, (2) Rapid opening valve, and (3): Precipitation chamber filled with atomized jet and particles formed.

The SAS/ASES process is semi-continuous, wherein the CO₂ and solutions are simultaneously fed into the precipitation chamber (Figure 2.8). Since the injection is continuous, the miscibility between CO₂ and solutions is ensured by operating at a pressure of 150 bar and higher. The pressure used is greater than the pressure in the GAS process[155]. Further, nozzles and capillaries are used in the RESS and SAS processes to inject the solution into the DG-CO₂ continuum [113, 160-162]. The change in nozzle position and geometry influence the mixing characteristics between solution and DG-CO₂, causing spatial variation in the degree of supersaturation within the precipitation chamber[163]. The flow rates are typical of the order of 0.1 to 4 ml/min, which causes delays in achieving the desired DG-CO₂ pressure in the precipitation chamber, thereby increasing the processing time. The low flow rate may develop a concentration gradient inside the precipitation chamber, causing non-homogenous crystallization, resulting in non-uniformity in particle size distribution[159].

In the ARISE process, the nozzle is replaced by an inbuilt narrow conduit, which simplifies the setup and reduces the chance of capillary wear in high-pressure applications. Further, the design complexity associated with nozzle geometry is eliminated, facilitating scale-up for industrial applications [159]. The classical difference between the ARISE and SAS processes is that the ARISE process operates on rapid injection ($\approx 1.5 \times 10^3$ ml/min- for the solution and ≈ 120 ml/min for pure solvent [163]) of solution into the CO₂ continuum, several orders of magnitude greater than flow rates used in the SAS process. The rapid injection ensures complete and homogenous atomization of the solution, assuring narrow particle size distribution. The atomization of drug solution occurs at the instance of injection within a space of approximately 500 ms (detailed in Chapter 5), reducing the processing time[159].

Further, the ARISE process can be operated in a low-pressure range of about 70-150 bar, lesser than the operating pressure of other DG processes. The process can be conducted at ambient temperature suitable for thermo-sensitive APIs. The moderate pressure and temperature range allow ease of operation and scalability while producing particles of quality similar to or better than the other supercritical fluid processes [94, 164]. The process is capable of producing particles within 5 μ m, acceptable for pulmonary and oral administration. Holistically, the process generates high throughput with low residual solvent compared to other DG antisolvent processes [94].

The kinetics of precipitation depend on the changes in solubility and concentration of the given system's solution. For instance, the dependency of precipitation on solution concentration in the DG-CO₂ system can be explained based on the nucleation theory described by *Ende et al* [165].

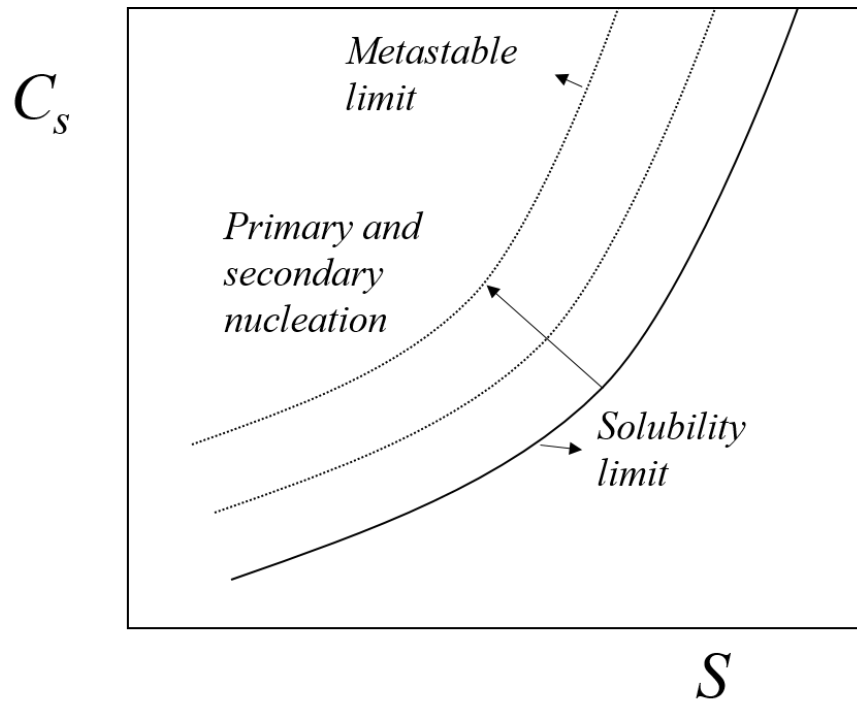


Figure 2.10 The dependency of precipitation on solute concentration- C_s . S : is the temperature [$^{\circ}\text{C}$] or Solvent composition for a given system. (adapted from *Ende et al.* [165]).

In Figure 2.10, the metastable limit defines the origin of nucleation due to the supersaturation of the solution. The closer the solute concentration (C_s) to the metastable limit, the greater the supersaturation [166-168]. For a fixed operating temperature and solvent composition, the increase in solute concentration (C_s) increases the advent of primary and secondary nucleation in the anti-solvent continuum, forming fine particles. Further, the nucleation growth is directly proportional to the degree of supersaturation, as represented by Eq 2.2.

$$p_g = K_{ss} \Delta C^n \quad (2.2)$$

where p_g is the nucleation growth rate, K_{ss} : nucleation rate constant, ΔC is the degree of supersaturation, and n is the order of nucleation [169]. In the ARISE process, the high degree of supersaturation due to the rapid injection of the solution in the anti-solvent CO_2 accelerates the nucleation growth rate, thereby producing fine solute particles. Further, the rapid expansion in ARISE reduces the extent of particle agglomeration. In the GAS process, antisolvent addition is slow, engendering slow mass transfer

between precipitate and DG-CO₂, slacking the supersaturation rate. With the low supersaturation, the particles are prone to agglomerate

The performance of the ARISE process depends on large sets of parameters as listed in Table 2.6 [95, 155, 170, 171].

Table 2.6 List of influential parameters in the Supercritical fluid/DG process.

Parameters		
Anti-solvent pressure	Process time	Anti-solvent volume
Temperature	Equilibration time	Back pressure
Anti-solvent/solvent feed rate	Nozzle/conduit diameter	Density of co-solvent
Concentration of solution	Injection/feed volume	Valve opening time
Depressurizing flow rate	Pressure vessel dimensions	

The parameters have a combined effect on the materials' particle size, morphology, and physiochemical properties [155]. The change in mass transfer rate, and fluid momentum, due to variation of parameters, affect the degree of supersaturation [163]. Unlike other DG processes, ARISE is characterized principally by the mass transfer due to the anti-solvent/solvent ratio and pressure differentials[172]. Investigating the individual effects of all the parameter is difficult and tedious, hence in the current work, the effect of concentration of solute and volume of injection on the physical and chemical properties of the micronized products are studied.

The ARISE process is recently developed, and research on formulations are sparsely investigated to date. The list of APIs and excipients processed through the ARISE technique are listed in Table 2.7.

Table 2.7 List of ARISE processed APIs and excipients.

API	Excipient	T (° C)	P (bar)	Ref
5FU	PLLA	25,30,35	90,100 ,110	[173]
Curcumin	--	25,40	95,100	[164]
Para-coumaric acid (PCA)	--	25	95	[172]
Insulin	--	40	90,120 ,150	[110]
--	Hydroxypropylated β - cyclodextrin (HP β - CD)	25,40	65,85, 120	[110]
--	Eudragit S100	37,40	80,120	[110]
Curcumin	HP β -CD, PVP	25,40	95	[174]
Budesonide	--	35	100	[163]
Amikacin	--	40	120	
Erythromycin	--	40	120	
Clarithromycin	--	40	120	
Sulfamethoxazole	--	35,40	120	
--	PLLA	35	80,100	
--	DSPC*	35	120	

*DSPC: Daistearoyl-sn-glycero-3-phosphatidylcholine.

The first ARISE process was demonstrated by micronizing *Bovine Insulin* for generating microparticles of high aerodynamic efficiency[175]. The work demonstrated the replacement of low-flow injection with rapid injection, processing 78% respirable fraction of re-processed insulin with a bulk density as low as 0.01g/ml.

Several drug/drug-excipient combinations can be processed through the ARISE technique. Antibacterial and anticancer drugs that are hydrophilic and hydrophobic, can be processed individually, and with polymeric excipients using the ARISE technique[163].

Lam [163] conducted preliminary trials on micronizing APIs using the ARISE process- Table 2.7. The process achieved particle size distributions ranging from 30 nm to 15 μm for varying solution concentrations. The drug recovery was within 60-85 % achievable. *Amikacin* nanoparticles within 30 nm were produced from a saturated solution. The *Budesonide* nanocrystals, 1 μm in size, were produced from a concentrated solution of 25 mg/ml, and *Erythromycin* particles of 10 μm were produced from a 152 mg/ml solution. The micronization of *Sulfamethoxazole* from 80 mg/ml solution produced agglomerated particles of size within 10 μm . The particle size did not vary between the 50 and 80 mg/ml concentrations and reduced to 5 μm when the concentration was reduced to 50 mg/ml near saturation limits.

The preliminary study on micronization of 5FU was performed at a saturation concentration of 8 mg/ml and a low concentration of 4 mg/ml. Particle size varied from 1 μm (for 8 mg/ml) to 800 nm (for 4 mg/ml) with MeOH as the primary solvent. However, the preliminary trials on micronization of polymers like PLGA and PDLLA were unsuccessful. Processing of PLLA and DSPC from MeOH and dichloromethane (DCM) solution produced fiber and flake-like formations within 10-30 μm size variations [163].

The study on the parametric variation of process temperature and pressure in co-processing *Curcumin*, hydroxypropyl- β -cyclodextrin (HP- β -CD), and polyvinylpyrrolidone (PVP) demonstrated production of microparticles of fine particle fraction (FPF) suitable for pulmonary delivery. The process produced 40% and 61% FPF in binary and ternary systems, demonstrating ARISE's versatility in processing drug/drug-excipient combinations [163, 174]. The overall product recovery was 92.5 % and 84.0 % for binary and ternary systems, respectively.

On comparing the effectiveness of the ARISE with other DG processes, the ARISE process yielded nanoparticles in size and morphology similar to other DG processes. Micronization of hypothyroidism drug, *Levothyroxine sodium* using GAS, and the ARISE process produced spherical nanoparticles of size, 360-1200 nm. The effect of temperature, pressure, and solvent on the particle size and morphology of the products showed almost similar variations between the GAS and ARISE processes. Processing of *Curcumin* from GAS and ARISE yielded polymorphic *Curcumin* particles with size variation from 30 μm to 160 μm . However, with the ARISE process, a 66.6% increase in recovery was noticed in comparison to the GAS process [164].

Further, the cytotoxicity study of the microparticles of co-processed *Curcumin* on the human carcinoma cells lines (MRC-5 and H1299) indicated that cytotoxicity activity (IC_{50}) was 2 folds higher to H1299 (cancer cells) than MRC-5 (Diploid human cells), proving that the ARISE-assisted formulations improved the FPF, and hence bioavailability of the drug for localized treatments [170].

Despite the similarity in the size, morphology, and physicochemical characteristics of the particles from various DG-processes, change in crystallinity, and high throughput of the ARISE technique confirms the relative ease of scalability of the process for industrial applications [164, 174, 176].

The scalability of the ARISE process was discerned from the three-scale operation batch process of *Para-coumaric acid* (PCA). The scale-up study was conducted in three stages by varying the volume of the precipitation chamber (0.15 L, 1L, and 2.2L), maintaining a constant length-to-diameter aspect ratio of 4.2. Particle size within the range of 0.8-3 μ m and product recovery up to 96% were achieved consistently at different scales of operations. The scale-up increased the quantity of production from 0.04 g/batch to 3-3.3 g/batch. The findings proved convincing in considering the ARISE process as a commercially viable technique for API formulations[172].

The above studies are prefatory trials on the implementation of the ARISE process. Detailed research and development on the materials and process optimization are still underway. This thesis focuses on exploring the ARISE processing of APIs and excipients towards realizing optimization of the process based on the material concentration for feasible scale-up operation in the near future.

Based on the initial findings from the above works, comprehensive advantages of the ARISE process can be enlisted as:

- A single-step batch process with high product recovery.
- Moderate operating pressure and temperature.
- One process-many formulations: Versatility for lipophilic API/API-excipient formulations.
- Rapid injection and atomization can be achieved.
- Homogenous particle size distribution.
- Fluffy, low bulk density, and high surface area particles.
- Integrated conduit-Compatible for scale-up.

2.3.3 DG AS CO-SOLVENT

The Depressurisation of an expanded liquid organic solvent (DELOS) process, developed by *Ventosa et al* [177], uses DG-CO₂ as a co-solvent with the organic solution. The DG-CO₂ completely solubilizes with the organic solution and produces a homogenous sub-cooling effect to form particles [178]. The working mechanism is schematically shown in Figure 2.11 and explained below.

1. The organic solution containing the API/excipients dissolved is pressurized inside the high-pressure chamber using DG-CO₂. The solution expands in volume due to the addition of CO₂ without precipitating the solute. This step's key feature is that the solution is maintained below the saturation concentration to avoid the GAS process.
2. The expanded volume is depressurized into the precipitation chamber maintained in ambient temperature and pressure through a one-way valve. Isobaric condition is maintained in the high-pressure chamber using inert gas throughout the injection process.
3. The depressurization results in nucleation of expanded solution and evaporation of CO₂, sub-cooling the precipitate, crystallizing homogenous particles.

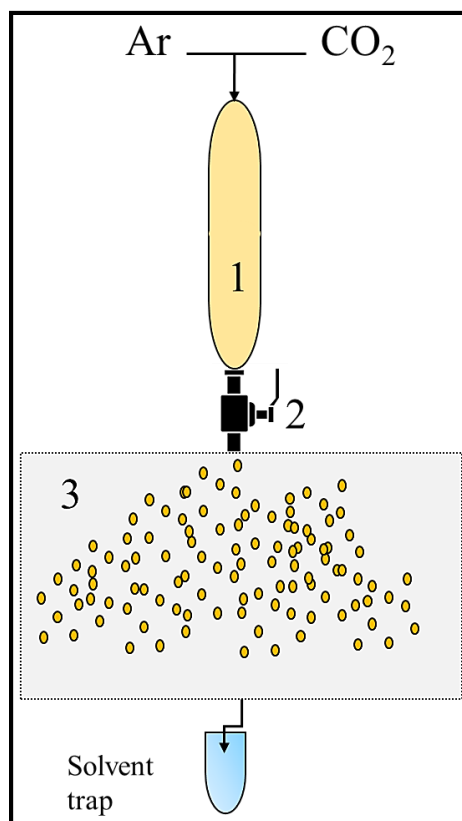


Figure 2.11 Schematic of the DELOS process. 1: High-pressure chamber, 2: one-way valve, and 3: precipitation chamber maintained at ambient condition. (Adapted from *Ventosa et al* [177], and *Foster et al* [94]).

Oil Blue 35, a blue anthraquinone dye was micronized using the DELOS process at a 20° C and 100 bar. The process produced 1.8 μm rod-shaped crystals with a large temperature reduction of -75° C after precipitation. The technique suffers the drawback of (i) Residual solvent content due to the incomplete evaporation of solvent while precipitation, due to the absence of CO₂ flushing steps, (ii) Partial crystallization of solute in gas expanded solution before depressurization (GAS phenomenon) causing non-homogenous precipitation[94, 177].

2.3.4 DG AS AN AID IN EMULSION

The Supercritical fluid assisted atomization (SAA), Carbon dioxide-assisted nebulization with a bubble dryer (CAN-BD), and Supercritical fluid extraction and emulsion process utilize DG-CO₂ as a nebulizing agent in API formulation. The schematic of the SAA and CAN-BD processes are shown in Figure 2.12. The API/excipient solution and DG-CO₂ are simultaneously flown into the mixing-tee, wherein the dynamic mixing of the solution and DG phase creates a homogenous emulsion, which is then passed

through a capillary restrictor into the precipitation chamber to depressurize and precipitate. The precipitates are dried by flowing dry nitrogen into the chamber and the particles are collected from the bottom of the chamber [179]. The significant difference between CAN-BD and SAA process is that the SAA process replaces mixing-tee with a thin wall injector, as shown in Figure 2.12. With the use of an injector, the process is driven by two-step nebulization. The initial particle formation commences during the pre-injection stage, and the particles are further broken down in the post-injection/depressurization stage[94]. Both CAN-BD and SAA processes can handle aqueous solutions favouring the encapsulation of hydrophobic drugs [178, 180]. The process is flow-driven and does not involve the rapid opening of valves. The disadvantage of these processes is the frequent blockage of mixing-tee and injectors due to partial precipitation during mixing. Also, the absence of rapid atomization produces heterogeneity in particle size distribution[94].

Capua et al. encapsulated hydrophobic plant flavonoid, *Luteolin* in PVP biopolymer using the SAA process and produced microspheres in size range of 0.22-0.33 μm with 99-100 % encapsulation efficiency. The drug loading was reported to increase from 11.0 % to 20.0 %, with a decrease in drug-polymer ratio from 1:8 to 1:4, respectively [181]. Similarly, *Curcumin* was loaded into PVP at 80° C and 1.5 bar precipitation pressure [182]. The encapsulation efficiency achieved was between 94-100 %. The long-elongated morphology of pristine *Curcumin* was converted to amorphous microsphere-particles with a size in the range of 0.24-0.38 μm . The loading was also observed to improve from 11.10 % to 32.50% with a decrease in PVP concentration similar to *Luteolin*.

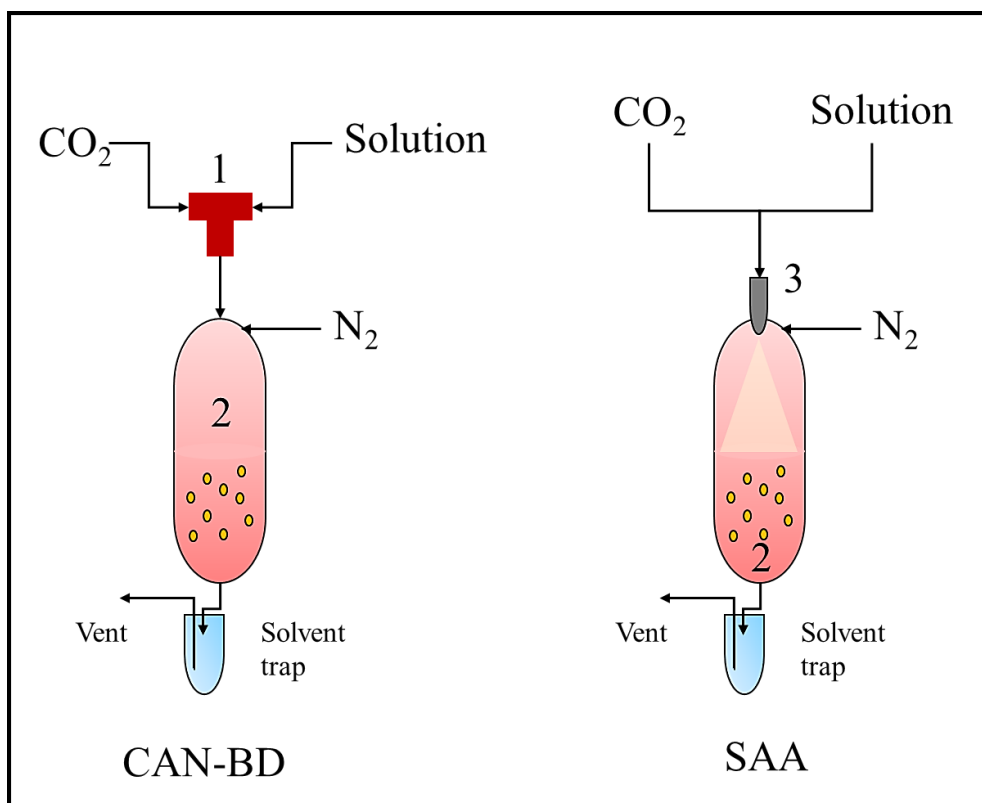


Figure 2.12 Schematic diagram of the CAN-BD and SAA process. (1): Mixing-tee, (2): Precipitation chamber with nitrogen flux, (3): Thin wall injector. (adapted from Foster et al [94]).

Peng et al. demonstrated 90 % encapsulation efficiency of *Doxorubicin hydrochloride* in Chitosan biopolymer using the SAA process. The average particle size of 120-250 nm was obtained at a mixing pressure of 120 bar and 70°C [183]. The successful encapsulation of these drugs from an aqueous media demonstrates the capabilities of DG-CO₂ as a nebulizing agent in forming micro/nano drug particles [178].

DG process is a neoteric technology used for formulating drug nanoparticles. Although several DG assisted formulations has been demonstrated and published, only some of them has been patented with a slight modification in the set-up and methodology with the perspective of commercialisation. Table 2.8 enlists some of the patented DG processes for formulation of drug nanoparticles.

Table 2.8 Patented DG assisted drug formulation.

Process	Year	Patent number	References
Supercritical fluid molecular spray thin film deposition and powder formation	1986	US4582731A	[184]
Supercritical fluid assisted electrostatic liquid spraying	1993	USOOSZI1342A	[185]
PLUSS (polymer liquefaction using supercritical solvation)	1998	US005766637A	[186]
Methods and apparatus for drug delivery using supercritical solution	1994	US005301664A	[187]
Supercritical fluid-assisted nebulization and bubble drying	2003	USOO663O121B1	[188]
SEDS	2002	USOO6440337B1	[189]
SAS-EM	2003	USOO6620351B2	[190]
Modified CAN-BD process	2004	USOO6830714B1	[191]
Modified GAS process	2007	US00725O152B2	[192]
Modified PGSS	2007	USOO7276190B2	[193]
PGSS	2011	US007862751B2	[194]
Modified PGSS	2012	USOO8142814B2	[195]
Supercritical fluid assisted sorption	2013	US 2013 O149430A1	[196]
Powder of cross-linked polymer formulation	2015	USOO9028806B2	[197]

2.4 EUDRAGIT AS AN EXCIPIENT FOR FORMULATION

Encapsulation of drugs provide effective ways of achieving targeted drug delivery by preserving drugs from degradation and premature release, as discussed in Section 2.2. Various nano-carriers/excipients are used for drug encapsulation such as liposomes, polymer micelles, dendrimers, hydrogel, polymeric nanoparticles, magnetic nanoparticles, and porous nanocarriers, to name a few [198, 199]. Amongst them, polymeric nanoparticles are exciting candidates for drug encapsulation due to their site-specific stimulus for localized delivery [200]. *Zang et al.* [201] categorized the use of polymer excipients based on colon metabolism and drug kinetics, as shown in Figure 2.13. Based on the classification, pH-triggered release favours improved efficacy in colon targeted therapy. Eudragit polymers are widely used for this purpose due to their sensitivity towards colonic pH conditions [202].

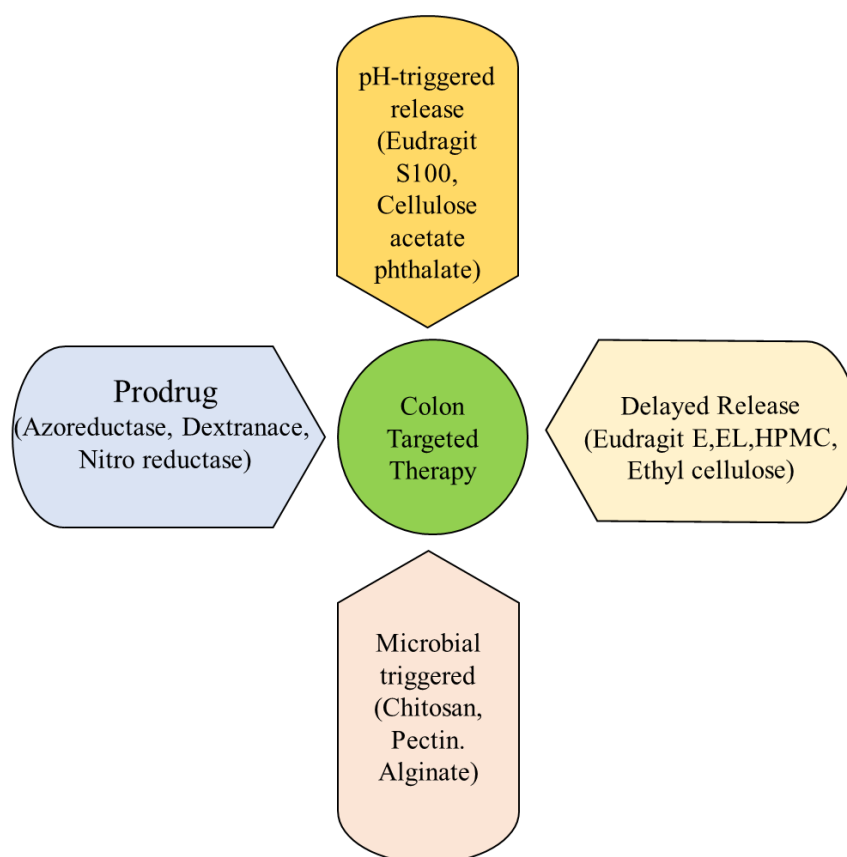


Figure 2.13 Categories of polymers/excipients used in colon targeted therapy. (Adapted from *Zang et al* [201]).

ES100 is an anionic copolymer of methacrylic acid and methacrylate (Figure 2.14). The long-chain enteric polymer has a molecular weight of 125,000 g/mol and is synthesized by reproducible free-radical polymerization [203, 204]. Based on the linkage

of functional and non-functional monomers, the solubility, physical and chemical properties can be modified. ES100 is hydrophobic, pH-dependent, and insoluble in gastric conditions and gradually soluble in intestinal conditions. Other types of Eudragit polymers like Eudragit SE, NE10, E100, and RL100 are used for sustained release and film coating applications. ES100 is an amorphous polymer with a glass transition temperature greater than 130° C, suitable for moderate-to-high temperature formulations [205]

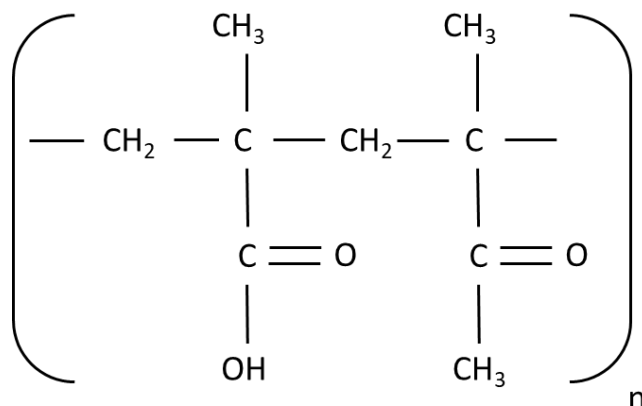


Figure 2.14 Chemical structure of ES100. (Adapted from *Yoo et al* [206]).

ES100 exhibits high solubility in organic solvents like Acetone, EtOH, MeOH, and Isopropanol and practically insoluble in ethyl acetate, petroleum ether, methylene chloride, and water [97, 204]. Due to their pH-dependent dissolution, they are used as drug carriers and coating materials in transdermal and colon targeted drug delivery systems [203]. Table 2.8 provides the list of anti-cancer drug formulations with ES100.

Table 2.9 List of anti-cancer drug formulation with ES100.

API	Excipient	Enteric Coating	Size (µm)	L (%)	E (%)	R_D * (%)	t * (h)	Ref
5FU+Leucovorin (LV)	Folate-Chitosan	ES100	15-35	--	5FU-17.5 LV-11.6	5FU-54 LV-49	8	[207]
5FU	Dextran	ES100	8.54-23.17	--	75.34-89.54	89.03-99.40	8	[208]
5FU	Hydroxypropyl methylcellulose (HPMC), Ethyl cellulose (EC)	ES100	--	--	--	70	8	[209]
5FU	HPMC E15	ES100	--	--	90	15-25	5	
5FU	PVP, EC	ES100	0.9-1.3	--	--	30-8	2	[210]
Prednisolone	PVA, EC, Triethyl citrate (TC)	ES100	35	--	86	80	24	[211]
5FU	Citrus pectin	ES100	0.218	20.84	35.15	70	24	[212]
Berberine hydrochloride	ES100	--	--	--	20	70	3.3	[213]
Camptothecin	ES100	--	0.120-8.8	--	--	--	--	[214]
Psoralidin	Chitosan	ES100	0.132		98.1	12	24	[215]

API	Excipient	Enteric Coating	Size (µm)	L (%)	E (%)	R_D *	t *	Ref
Genistein	Chitosan	ES100	0.035-0.079	20.67-62.69	52.25-80.26	100	24	[216]
Quercetin	ES100	--	48.25-100.40	--	73.48	98.76	24	[217]
5-Aminosalicylic acid (5ASA), Curcumin (CUR)	Chitosan	ES100	10-80	5AFA-6.4 CUR-5.6	5AFA-62.3 CUR-55.2	5AFA-76.5 CUR-73.9	12	[218]
Capecitabine	PLGA, Chitosan	ES100	386.13	--	63.81	91	150	[219]
Meloxicam	Chitosan	ES100	79.42-86.48	30-58- 43.09	69.2-84.10	6.01	5	[220]
Caspase 3	Chitosan	ES100	0.265	--	54.9	75	24	[221]
Curcumin	Chitosan	ES100	36.84-129.74	16.46-40.59	73.88-83.37	50	12	[222]
Paclitaxel	Polyurethane	EL100-55	0.59-0.71	--	--	100	7	[223]
Theophylline	Calcium pectinate	ES100	1750-2610	--	55.3-82.0	100	4	[224]
Paclitaxel	Chitosan	ES100	0.150-0.186	10.5	86	100	2.3	[225]
5ASA	Eudragit RSPO, RLPO, PVP K-30	ES100	--	--	99.30-99.74	94.91	24	[226]
5FU, Celecoxib	Chitosan	ES100	--	--	--	--	--	[227]

*R_D: Cumulative drug release, t: Drug release time

It can be inferred from Table 2.8 that ES100 has been used as a coating material to the polymer-drug microspheres. However, minimal works have been reported in exploring ES100 as a potential excipient. The *Caspase-3*, an apoptosis mediator, was encapsulated in chitosan and coated with ES100 using the oil-in-oil solvent evaporation method. The system showed an encapsulation efficiency of about 54.9 %. Mere encapsulation of drug in chitosan did not show a significant change in the release profile. In contrast, the enteric coating of ES100 prevented the premature release of the drug in the gastric environment. The release in the gastric medium was reduced by 90 % and 93 % from chitosan-caspase microsphere and pristine Caspase-3 respectively [221].

Similarly, the hydrophobic nutraceutical drug, *Curcumin*, was encapsulated in chitosan using an emulsion technique. Spherical microspheres in the size range of 37-130 μm were produced with varied chitosan concentrations. The highest drug loading of 38.2 % and encapsulation efficiency of 83.37 % were achieved for the drug-excipient ratio of 1:1 and 1:4, respectively. The inclusion of 10 w/v% of ES100 as enteric coating extended the release of curcumin in the colon by 12h [222].

Recently, *Sood et al.* [225] reported the improved efficacy of *Paclitaxel* by loading them into Chitosan-ES100 nanoparticle. The system showed 10.5 % drug loading and 86% encapsulation efficiency. The *in-vitro* drug release performed in the simulated gastrointestinal environment using the dialysis membrane showed only 5% drug release in the first 30 min and about 30 % cumulative release over 144h in pH 4.5. The *in-vitro* cell viability test performed using MTT assay of HCT116 colon cancer cells showed more than 85 % cell viability and a 15-24 % increase in drug efficacy in colon cancer cells with the drug-loaded chitosan-ES100 nanoparticle. Further, the biodistribution study on Balb/C mice revealed that the concentration of drug-loaded nanoparticles was high in the colon section within 6 h of oral administration. The drug concentration was further retained over 24 h in the colon, confirming that the encapsulation of drugs in the ES100 matrix not only reduced toxicity in the gastric region but also enhanced the therapeutic effect in the colon environment.

The core-shell formulation of citrus-pectin nanoparticles was reported by *Subudhi et al* [212], wherein the core consisted of 5FU loaded citrus pectin matrix. The ES100 (12 w/v %) was coated as a shell layer on the surface of the citrus pectin-5FU matrix. The ES100/citrus pectin-5FU formulation achieved a drug loading of 20.84 % and encapsulation efficiency of 35.15 %. 5FU is a hydrophilic drug with high solubility in

both gastric and intestinal pH. Enteric coating with ES100 reduced the release of 5FU by 95 % in gastric and by 22.5% in intestinal conditions within the first 8 h of dissolution. The reason was attributed to the high ionization of carboxyl groups of ES100 in pH >7, which disrupts the ES100 shell, solubilizing 5FU from the matrix at intestinal conditions. The efficacy was further established by conducting *in-vitro* drug release in the presence of rat caecal content. The cumulative release of 5FU in pH 7 after 24 h was reduced from 92% to 60% with the inclusion of the ES100 shell.

Deviating from the core-shell encapsulation, Berberine hydrochloride (HB) was directly encapsulated in ES100 using the solvent evaporation method by *Guo et al* [213]. The drug-excipient formed a solid matrix with HB molecules intercalated within ES100 molecules. The dissolution study was conducted using the dialysis method. The results showed a significant 57% decrease in HB release in the gastric medium and about 72% decrease in the intestinal medium within the first 2h of dissolution. The cumulative release showed inverse dependency with ES100 concentration, meaning that increasing the ES100 concentration increased the HB-ES100 matrix's viscosity, thereby restricting the dissolution of HB into the medium. It was also observed that the dissolution of HB molecules from the ES100 matrix was diffusion-driven due to the high viscosity of ES100 used. The cytotoxic effect of HB was also reported to reduce to about 40% after it was formulated with ES100, affirming the effectiveness of ES100 as an encapsulating material. A similar effect was observed by *Jat et al* [217] while releasing *Quercetin* from ES100 microspheres. The release rate was reduced with an increase in the concentration of ES100. Also, the encapsulation efficiency of the formulation increased with an increase in ES100 concentration. The Quercetin-ES100 produced the best results of 98.8% release in pH 7.4 and 73.5% efficiency for the drug-excipient ratio of 1:3.

Li et al [207] encapsulated 5FU and Leucovorin (LV) in folate-chitosan polymer composite using the solvent evaporation method. The microspheres formed were uniformly spherical within 35 µm size. The microspheres were further coated with ES100, a coat-core ratio of 5:1, and 10:1, respectively. The formulation with high ES100 concentration (10:1) produced high encapsulation efficiency of 21.8 % (5FU), and 12.8 % (LV) compared to 17.5% (5FU), and 11.6% (LV) at 5:1 coat-core ratio. The enteric coating decreased the release of 5FU and LV by 10% from 60% to 50% within the first 8h of dissolution.

The aforementioned studies indicate that drug formulations with ES100 either as a coating material or as direct excipient prevented gastric degradation of APIs, and pH triggered release at colonic conditions, proving advantageous for colon targeted therapy.

Alongside the discussions on encapsulation of 5FU and other APIs with ES100, formulation studies on ES100 with SLB (Table 2.9) were not extensively reported to date. Also, these formulations with DG techniques are not reported in detail. Encapsulation of SLB in polymers and liposomes produced particles in a wide size range of 10 nm to 360 nm-Table 2.9. However, direct encapsulation into ES100 has not been reported (Table 2.9). Consequently, the following chapters focus on exploring the feasibility of direct loading of 5FU and SLB in ES100 using the DG (ARISE) technique for colon targeted drug delivery systems.

Table 2.10 List of SLB formulations.

API	Excipient	Size (μm)	L (%)	E (%)	R _D (%)	t (h)	Ref
Cabazitaxel, SLB	Hyaluronic acid	0.100	10	90	--	--	[228]
SLB	Eudragit RL PO	0.106	--	98.3	40.8	24	[229]
SLB	Chitosan	0.263	--	82.9	82.4	8	[230]
SLB	HPMC, EC, Eudragit (S100, RL)	EC-0.220 ES100-0.251-0.282	--	EC-85.1-94.2 ES100-87.7	EC-70, ES100- 46.3	12	[231]
SLB	Oleoyl chloride, PEG	0.219	15.81	94.9	--	--	[232]
SLB	CM-CNT	--	35.1	--	96.6	16	[233]
Doxorubicin-SLB	Cholic acid-liposomes	0.097	--	93	20	12	[234]
SLB	Eudragit E, PVA	0.06-0.07	--	79	79.2	24	[235]
SLB	Pomegranate oil	0.157	--	--	31.3	9	[236]
SLB	PAMAM-Al ₂ O ₃ NT*	--	--	--	80	70	[237]
SLB	Trilaurin, Cholesterol	0.364		80	99	48	[238]
SLB	Soy-Zinc oxide	0.010-0.015	19.41	43.50	60	48	[239]

* CM-CNT: Carboxylated multiwalled carbon nanotube, PAMAM-Al₂O₃NT: PAMA conjugated alumina nanotubes.

2.5 HALLOYSITE NANOTUBES-A GREEN MATERIAL FOR NANOFORMULATION.

Halloysite nanotubes/nanoclays, otherwise called halloysites or HNT, are naturally occurring clay materials belonging to the class of kaolin clays having an empirical formula of $\text{Al}_2\text{Si}_2\text{O}_5(\text{OH})_4 \cdot n\text{H}_2\text{O}$ [240]. They were initially discovered and named after a Belgian geologist *Omalius d'Halloy* in 1826 [241]. HNTs are formed by natural alterations of igneous and non-igneous rocks [242]. They exist in various shapes such as spheroidal, tubular, platy, prismatic, and fibre, with the tubular shape very commonly available [240, 242]. The occurrence of various morphologies of HNTs can be found in New Zealand, Australia, Brazil, Japan, USA, and Cameroon, to name a few [242]. The tubular HNTs have inner octahedral alumina and outer tetrahedral silicate layers hydrated with interlayer water molecules rolled together as illustrated in Figure 2.15 [240]. The monoclinic crystalline alumino-silicates form a cylindrical shape with a hollow inner lumen. The inner lumen and the outer diameter of HNT span from 1-30nm and 30-50nm respectively(Figure 2.16) [243, 244]. Their length varies widely from 100nm up to $2\mu\text{m}$ and sometimes $>2\mu\text{m}$ [243]. The lumen of the HNT contributes to 10% of the total volume of the material [245].

Their biocompatibility, geographical abundance, and low cost make them an interesting candidate for various applications such as nano-composites, waste-water treatment, cosmetics, anticorrosive materials, and drug delivery systems [243, 246]. The addition of HNT to various polymers have been demonstrated to improve the thermal and mechanical properties of the polymer composites [247, 248].

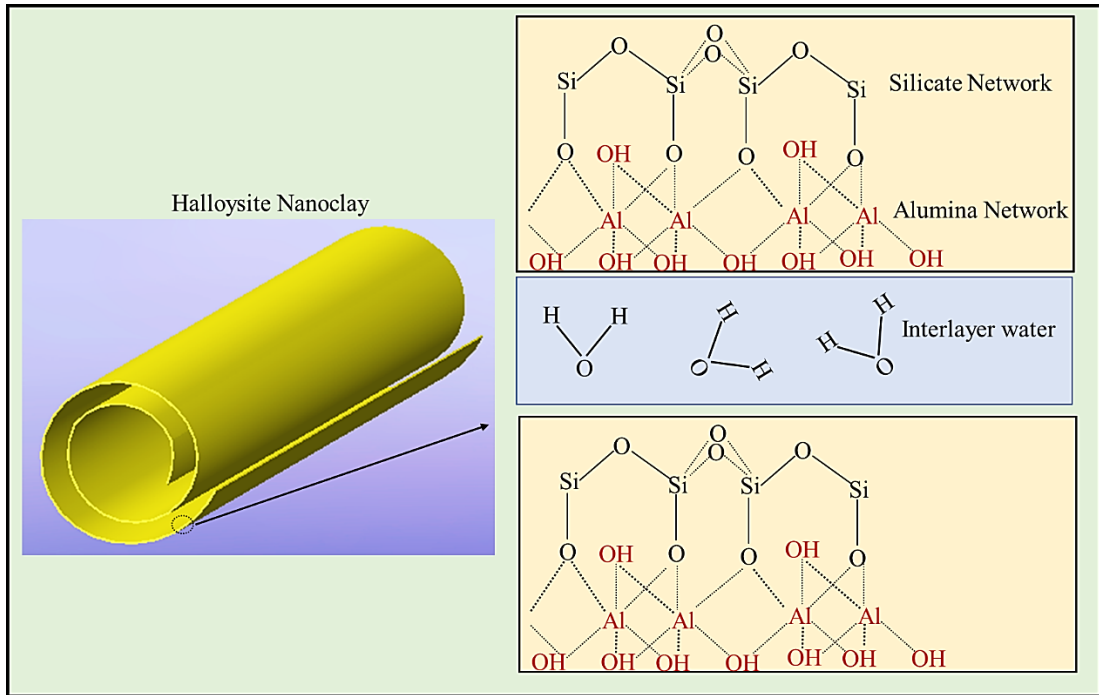


Figure 2.15 Schematic of Halloysite nanoclay and its chemical structure. (Adapted from *Leporatti* [243], and *Satish et al* [246]).

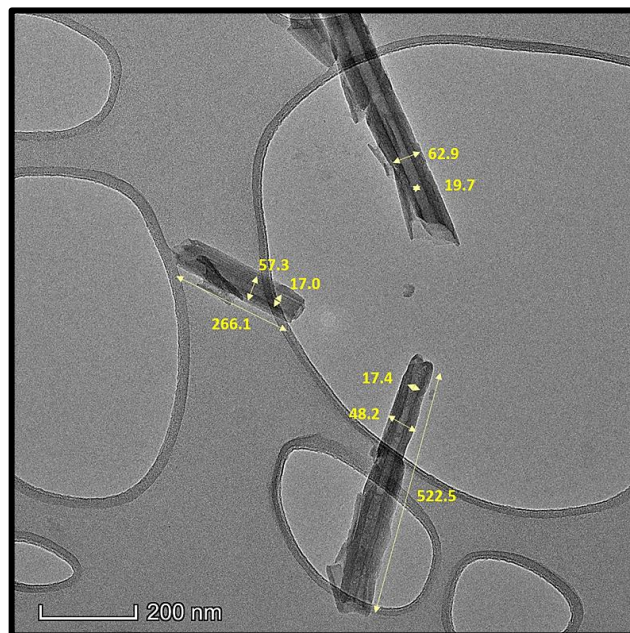


Figure 2.16 TEM image of Halloysite nanotubes.

2.5.1 HALLOYSITE NANOTUBES AS DRUG NANO-CARRIERS

HNTs have a high length-diameter ratio and different charge compositions between inner and outer surfaces, rendering them suitable for various biomedical applications such as gene delivery, tissue engineering, stem cell isolations, and drug encapsulation [243, 246]. The uniqueness of HNT is that drugs of opposite charges can be loaded in or on the outer surface of HNT through physical adsorption or ion exchanging [249]. The surface zeta potential of HNT, Silica, and Alumina particles are shown in Figure 2.17. The outer silicate layer's surface charge is negative over a wide range of pH (≈ -35 mV in pH 4-8), and inner alumina is positively charged ($\approx +30$ mV in pH 4-8). Due to the charge difference between inner and outer surfaces, they exhibit amphoteric behaviour when exposed to acidic or alkaline conditions, compatible for encapsulating both cationic and anionic drugs either inside, or on the outside surface [243, 250, 251]. *Price et al* [252] demonstrated the versatility of HNT as a low-cost, and green nanocarrier by loading hydrophilic oxytetracycline HCl, hydrophobic khellin, and nicotinamide adenine dinucleotide onto its surface and lumen. Further, HNTs form well dispersed, stable suspensions even for several months, increasing the shelf life of the formulations.

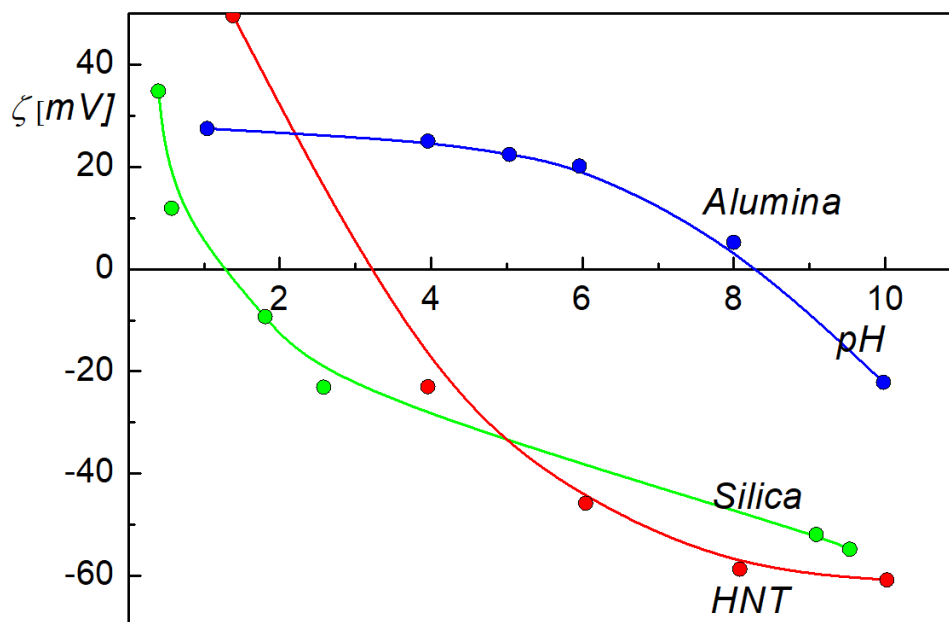


Figure 2.17 Zeta potential (ζ) of HNT, Alumina, and Silica. (Adapted from *Leporatti et al* [243]).

The low cytotoxicity and biocompatibility of HNTs render them suitable for encapsulating drugs for in-vitro and in-vivo administrations [253]. *Lai et al.* [254], conducted

an extensive study on the cytotoxicity of HNTs on the intestinal region by exposing Caco-2/HT29-MTX cell monolayers to HNT toxicity test. The results confirmed a finer degree of biocompatibility of HNTs even under high levels of the cytokine. Detailed work by *Yuri M. Lov and Fakhrullina et al.* [255] on the cytotoxicity of HNTs in-vivo with *Caenorhabditis elegans* nematode concluded that HNTs does not induce toxic effects on nematodes and are environmentally safe. The investigations exemplify that HNTs are excellent nano-carrier for colorectal cancer drug formulation and can be envisaged for scaling-up to industrial applications.

Conventionally, drug encapsulation in HNT is accomplished through the mechanical loading technique. The drug saturated solution is mixed with HNT powder by sonication and further placed in a vacuum desiccator for several cycles. The repeated vacuum cycles ensure that the drug molecules are loaded into the HNT lumen. The loaded HNTs are further washed to remove the excess drug from the product. However, elaboration of the washing steps has not been reported to date [256-260]. Table 2.10 lists the recently reported works on drugs encapsulated in HNT using conventional mechanical loading techniques. The detailed procedure on mechanical loading and washing can be found in Chapter 3, Section 3.4.2, and Section 3.1.3, respectively.

Table 2.11 List of drugs encapsulated in HNT.

API	Treatment	Solvent used	Surface Activation	Washing Solvent	L (%)	Ref
Brilliant green	Antiseptic agent	Acetone	Benzotriazole-copper	D.I.water	--	[261]
Silver Nitrite	Antibacterial	Ethanol	Curcumin	--	1.31	[262]
Acid orange II dye	Model drug	--	Γ-Aminopropyltriethoxysilane	--	5.91,7.83	[263]
Paclitaxel	Multiple Cancer	Ethanol	Poly (methacrylic acid-co-methyl methacrylate)	Ethanol	7.5 ± 0.5	[260]
Dexamethasone	Allergy medication	--	--	--	5-10	[264]
Amoxicillin	Anti-bacterial	--	--	--	--	[261]
Ibuprofen	Anti-inflammatory	Ethanol	--	--	11.8	[265]
Ibuprofen	Anti-inflammatory	Ethanol	3-aminopropyltriethoxysilane	--	12.7,14.8	[265]
Peppermint oil	Anti-bacterial	--	Pectin, Cucurbit [6]uril	--	--	[266]
Tetracycline hydrochloride	Anti-bacterial	D.I.water	PLGA	--	26.77, 28.62, 42.65	[267]
Aspirin	Anti-inflammatory	Ethanol	--	D.I.water	2.1	[268]
Aspirin	Anti-inflammatory	Ethanol	Chitosan	D.I.water	42.4	[268]

API	Treatment	Solvent used	Surface Activation	Washing Solvent	L (%)	Ref
Ofloxacin	Anti-bacterial	Acetic acid	Sodium hydroxide	D.I.water	44.70 ±0.57 62.77 0.49	[269]
Diphenhydramine hydrochloride (DPH), Diclofenac sodium salt (DS)	Allergy medication	D.I.water	--	--	DPH-59.19, DS-20.97	[257]
Diphenhydramine hydrochloride (DPH), Diclofenac sodium salt (DS)	Allergy medication	D.I.water	(3-aminopropyl) triethoxysilane, α -bromoisobutyryl bromide, and poly(N,N-dimethylaminoethyl methacrylate)	--	DPH-44.7, DS-35.35	[257]
Silibinin (SLB), Quercetin (QU)	Thyroid cancer	--	Cyclodextrin	--	SLB-6.1, QU-2.2	[270]
Cardanol	Liver cancer	Methanol	--	D.I.water	5	[271]
Cardanol	Liver cancer	Methanol	Triazolium salt	D.I.water	10	[271]

API	Treatment	Solvent used	Surface Activation	Washing Solvent	L (%)	Ref
Dexamethasone	Allergy medication	Aqueous Ethanol	--	D.I.water	2-5.5	[272]
Losartan	High blood pressure	Ethanol	--	--	4	[273]
Losartan	High blood pressure	Ethanol	Aqueous H ₂ SO ₄	--	8	[273]
Losartan	High blood pressure	Ethanol	Calcination at 400 °C	--	2	[273]
Irinotecan	Colon cancer	D.I.water	Eudragit S100	D.I.water	4.22	[258]
5FU in Kaolinite	Various cancer	Methanol	--	--	103 mg/g	[274]
Norfloxacin	Urinary tract Infection	Acetic acid	Ferric chloride hexahydrate (Fe ³⁺)	--	72.10 mg/g	[275]
Norfloxacin	Urinary tract Infection	Acetic acid	Acrylamide, Methacrylic acid,	--	--	[275]
Curcumin	Multi-functional	Ethanol	Cellulose	--	4.1	[276]
Curcumin	Multi-functional	Ethanol	Cellulose and Epichlorhydrine	--	--	[276]

The spectrum of drugs encapsulated in HNT is very large, covering anti-inflammatory, anti-bacterial, enzymatic, and anti-cancer drugs (Table 2.10). *Ibuprofen* (IBU), an anti-inflammatory drug was successfully loaded into HNT. The results showed the presence of IBU in both amorphous and crystalline states with a maximum loading of 14.8% [265]. The report also indicated that the loading of lipophilic drugs like IBU in HNT was achieved through hydrogen bonding of drug molecules to the hydroxyl group of the outer silicate layer [277]. *Price et al* [252] demonstrated the versatility of HNT as a low-cost, and green nanocarrier by loading hydrophilic oxytetracycline HCl, hydrophobic khellin, and nicotinamide adenine dinucleotide onto its surface and lumen. The amount of material loaded can be enhanced through selective modification of the inner and outer layers of HNT. Silver (Au) nanoparticles with antimicrobial properties were encapsulated in HNT by *Sudhakar et al* [262]. The HNT surface was functionalized using N-(β -aminoethyl)- γ -aminopropyl trimethoxysilane (AEAPTES) before loading. Spherical Au nanoparticles (20-40nm) were later immobilized on the surface of HNT using the chelation method using tea polyphenol as a reductant.

Deviating from the mechanical loading method, *Liu et al* [278] demonstrated the loading of colon cancer drugs, *Atorvastatin*, and *Celecoxib* into the HNT matrix using a microfluidic platform. The drug-loaded HNTs were further coated with hydroxypropyl methylcellulose acetate succinate (HPMCAS) polymer using oil-in-water emulsion in a flow-focusing device. The resultant polymer-HNT-drug encapsulates were spherical with 70 ± 8 μm average size. The loading of *Atorvastatin* and *Celecoxib* improved from 8 % and 0.35 % in polymer to 14 % and 6% in HNT, respectively. The high porosity of HNT enabled drug molecules to firmly get adsorbed into and on the HNT surface. Further, the *in-vitro* cytotoxicity study reported that the toxicity level of drugs was low and the drug concentration of the encapsulates was lower in the gastric environment compared to free drugs, propounding that HNT encapsulation favours colon targeted delivery.

In another instance of colon targeted delivery, *Paclitaxel* was loaded onto HNT and the release kinetics were studied under the simulated intestinal environment. Methacrylate polymer, similar to Eudragit, was used as a coating material. Additionally, the ends of HNTs were capped with dextrin to enhance intracellular release and the formulation achieved 7.5% drug loading. The surface potential of the drug loaded HNT indicated that the zeta potential value did not alter before (-24.2 mV) and after (-27.1 mV) encapsulation, indicating that the majority of the drug molecules were loaded into

the HNT lumen. Also, the *in-vitro* anti-cancer effect was evaluated on human cancer cells showing a high therapeutic effect within low drug concentration ($10 \mu\text{g}/10^4$ cells)[260].

The drug of interest, 5FU, was loaded in HNT-Sodium hyaluronate/poly (hydroxyethyl methacrylate) nanocomposite hydrogel by free radical redox polymerization by *Rao et al* [279]. The encapsulation efficiency varied from 44-60%. The study revealed that efficiency decreased by 25% with a 7.5% increase in the HNT concentration in the hydrogel. The reason was ascribed to forming a rigid polymer-HNT network, preventing drug molecules from easily diffusing into the composite interlayers. The release study suggested that the release mechanism of 5FU from HNT was non-Fickian diffusion controlled with a 65% release within 70h in colonic conditions.

Tan et al [280], and *Abukhadra et al* [274], demonstrated selective loading of 5FU in Kaolinite nanotubes (which are a similar class of HNT). The kaolinite nanotubes were surface modified using Dimethyl sulfoxide (DMSO) and drug loading variations were analyzed. The study suggested that 5FU (35.5nm) nanoparticles were adsorbed on the surface of kaolinite through hydrogen bonding. A maximum loading of 22.4 % was achieved with pristine kaolinite, and the loading increased to 55.4% with methoxy-modification. The surface modification improved the surface area of kaolinite from $10 \text{ m}^2/\text{g}$ to $105 \text{ m}^2/\text{g}$, promoting both surface and interlayer adsorption of drug molecules. However, significant release (74%) of 5FU was observed within the first 0.4h of dissolution in the gastric medium due to the burst release of predominantly surface attached drug molecules. The studies reveal that surface modification enhanced the loading capacity of kaolinite nanotubes.

2.5.2. SURFACE MODIFICATION OF HALLOYSITE NANOTUBES

Increasing the surface area and hence the surface-to-volume ratio of HNT begets enhancement in physical and chemical property, facilitating improved loading capacity[281]. The high porosity of the HNT helps in diffusion of functional groups into the lumen. The surface modification of HNTs can be achieved primarily by thermal, and chemical treatments. The thermal treatment involves heating of HNTs at high temperatures (above 400°C). The crystallinity and chemical composition are altered, changing the surface area and adsorptive catalytic activity of HNTs. The thermal treatments are uncommon in industries due to the dehydroxylation and structural loss of HNT at elevated temperatures. The effect of thermal treatment on clay materials such as Bentonite

was performed by *Sarikaya et al* [282], and *Hussin et al* [283]. The studies conclude that while working at temperature above 400° C, may increase the surface area up to 90 m²/g, but would cause irreversible dehydration and dehydroxylation, thereby decomposing the clay materials.

On the other hand, modification of the HNT surface can be accomplished by either linking functional groups on the surface or removing functional groups from its outer/inner surface. Polymers are attached to the porous surface of the HNT through polymerization [284]. A vivid narrative of various surface modification techniques was reported by *Tharmavaram et al* [284]. The use of polymers enhances the thermal and mechanical stability of the HNT. Depending upon the functional groups of polymers attached, the properties such as impact resistance, mechanical stiffness, and strength of the HNT composites can be improved. Several examples of polymer modifications were discussed in Section 2.5.1, Table 2.10. The emphasis of polymer modification was made based on their stabilizing effects during drug immobilization on the surface of HNT[243, 285]. *Li et al* [268], modified the HNT surface with Chitosan using the microemulsion method. The resultant porous microsphere was loaded with aspirin as a model drug. The presence of the chitosan functional group on the surface of HNT improved the loading from 2.1 % to 42.4%.

Apart from polymer modification, HNT surfaces are hydrophobized using Organosilanes such as 3-aminopropyltriethoxysilane (APTES), and 3-Mercaptonpropyltrimethoxysilane (MPTS), 3-chloropropyltrimethoxysilane (3-CPTS), and many more [286-288]. During organosilation, the silanol group of the alkoxy silane, forms hydrogen bonds with the surface hydroxyl group of the HNT in the presence of non-polar solvents, as illustrated in Figure 2.18 [284]. Through this method, both the outer surface and inner lumen of the HNT can be modified. The organosilation improves the adsorptive capacity and hence the loading ability of the nanotubes. For instance, modification of HNT using APTES improved the loading capacity by 32 % while loading Acid orange II dye [263].

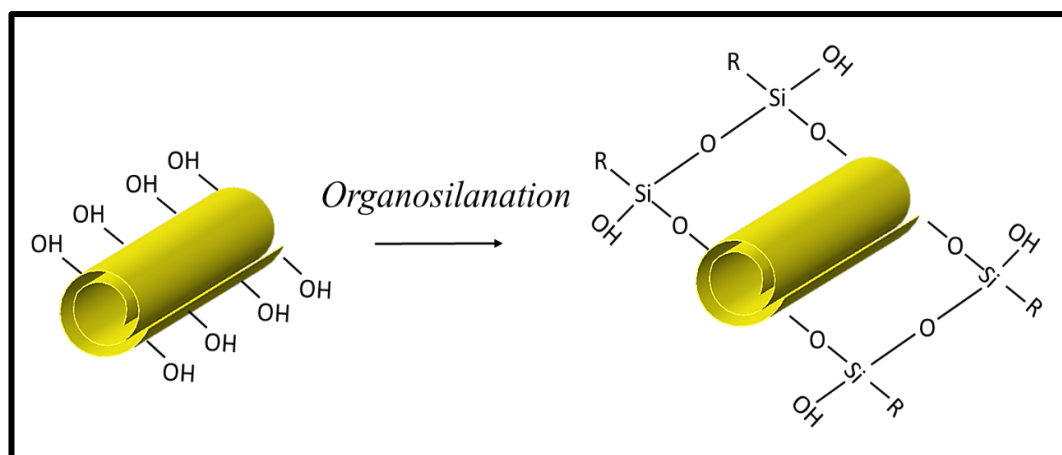


Figure 2.18 Illustration of organosilanation of HNT surface. (adapted from Tharmavaram *et al* [284]).

These techniques do not alter the structural integrity. Research has shown that organosilanation and polymerization of the surface prevent aggregation of HNT significantly [284].

2.5.2.1 ACID AND ALKALINE ETCHING

The enlargement of HNT through acid and alkaline etching is a commonly used technique to selectively etch the alumina and silicate layer by utilizing the difference in their surface chemistry. The process involves the suspension of HNT in an acidic or alkaline solution at elevated temperature for several hours. The treated samples are washed several times with water and dried. Table 2.11 enlists recently reported works using different etchants.

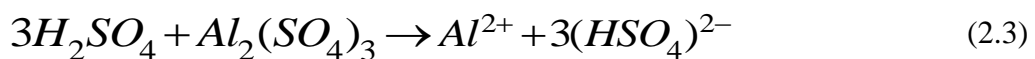
Table 2.12 Surface modification of HNT using acid/alkaline etching.

Etchant	T* (°C)	t* (h)	Surface Area (m ² g ⁻¹)	Ref
Sulphuric acid	40-90	0-60	250.00	[245]
Sodium carbonate and sodium nitrate	350	2	51.07	[289, 290]
Sulphuric acid	90	1-13	267.10	[291]
Sulphuric acid	--	1-21	306.43	[292]
(3-Aminopropyl) tri-ethoxysilane	110	22	23.90	[290]

Sulphuric acid	50	72	132.40	[281]
Acetic acid	50	72	60.10	[281]
Acrylic acid	50	72	52.90	[281]
Sodium hydroxide	50	1	39.21	[269]
Sulphuric acid	90	6	42.20	[273]
Calcination	400	2	27.52	[273]
Piranha solution	120	2	--	[293]
Sulphuric acid	50-70	24-48	253.40	[294]
Sulphuric acid	105-110	16	--	[295]
Aqueous Hydrochloric acid	80	4-18	--	[296]

*T: Etch temperature, t: Etch time.

The outer surface primarily composes of silanol group which readily react with an alkaline solution. Exposure to alkaline solution generates the formation of more hydroxyl groups on the surface [297]. Sodium hydroxide (NaOH) is the commonly used alkali to etch the outer silicate cage structure. The NaOH dissociates to form Na⁺ and OH⁻ ions. The Na⁺ associates with the Si-OH and deprotonates the silanol group, weakening and breaking the Si-O bond [298, 299]. Increasing the concentration of NaOH causes more deprotonation of silica and thinning of the outer wall of HNT [284, 297]. Treatment of HNT using 6 mol/L NaOH solution for 1h increased the surface area by 20%, whereas with 1 mol/L NaOH for 28 and 84 days increased the surface area by 85% and 93% respectively [269, 300]. A high concentration of NaOH ($\geq 1 \text{ mol dm}^{-3}$) produces a distorted structure of HNT from the outer layers and forms aggregates on the surface [300]. On the other hand, the inner lumen of the HNT is etched using acids like sulphuric, acrylic, hydrochloric, and acetic acids. Acid etching is initiated by the diffusion of hydrogen ion into the lumen and reaction with the alumina layer as illustrated in Figure 2.19. The reaction inside the lumen can be expressed by Eq. (2.3) [249]. In sulphuric acid, the HNT forms aluminum sulfate and further dissociates aluminum ion to etch off the alumina layer. The silicate cage structure is unaltered in the acid etching.



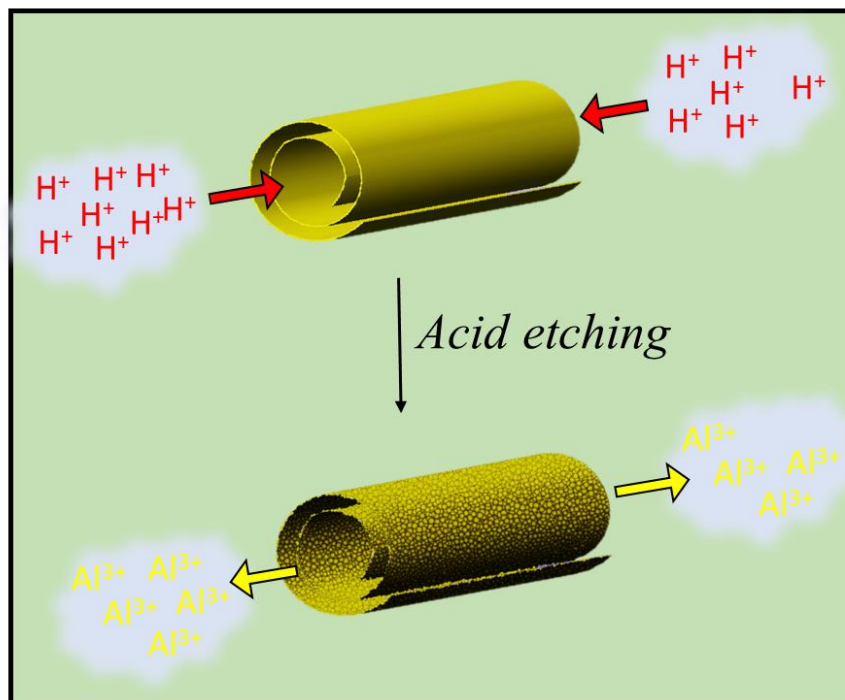


Figure 2.19 Illustration of acid etching of inner alumina layers. (adapted from Abdul-layev et al [245]).

It is observed that etching of HNT with sulphuric acid enhances the loading by 30-40% [264]. The effectiveness of etching depends on factors such as acid concentration and temperature. Weak acids, such as acetic and acrylic acids, induce homogenous and controlled widening of the lumen. In contrast, sulphuric acid produces a higher percentile (18%) increase in lumen diameter, as reported by *Garcia-Garcia et al*[281]. Albeit the mammoth improvement in lumen size and specific surface area, the effect of sulphuric acid on HNT is aggressive and decomposes the material due to vigorous etching[281]. Due to the high acidic strength, both inner lumen and outer layers are removed and produce a roughened surface with the destruction of the tubular morphology[291].

Further, acidic etching at a temperature above $70^{\circ}C$ produces a non-uniform widening of the lumen[284]. These limitations render the process unsuitable for applications requiring low toxicity and material purity, specifically in nano-drug delivery systems. Additional particulars of the etching are explained in the following Chapter 8.

The development of green alternative processes would alleviate the limitations of the existing chemical modification methods. The use of SCW can pave the way towards a non-toxic modification of HNT. The SCW acts as a green etchant in modifying HNT without harming the structural integrity. This work, to the author's knowledge, is the

first of its kind in demonstrating the use of SCW as an alternative to chemical etchant in modifying HNT (Chapter 8).

2.6 SUBCRITICAL WATER AS A GREEN ETCHANT

Water is considered as the universal solvent for largely polar compounds, and specifically for few non-polar compounds. Water at elevated temperature and pressure displays change in its physical properties like dielectric constant, polarity, and ionic strength. SCW is the state of water in a temperature range of 100°C to 374°C and pressure of 1-220 bar[301]. The pressure-temperature diagram of the SCW system is shown in Figure 2.20. The tunable property of water in subcritical conditions makes it an effective solvent for polar and non-polar compounds. At elevated temperature, the dielectric constant decreases, matching the polarities of the organic solvents (more details in-Chapter 8, Section 8.1). This enables the water to dissolve non-polar and organic compounds effectively[302, 303]. This property is exploited to use for extracting several organic and non-polar compounds from plants and other materials.

Water molecules in ambient conditions have strong hydrogen bonding, which engenders a high dielectric constant. An increase in temperature and pressure causes thermal agitation and weakening of hydrogen bonds in the water molecule. This, in turn, leads to an exponential decrease in dielectric strength and polarity, as shown in Chapter 8, Figure 8.2 (a) [304]. The weakening of hydrogen bonds increases the hydrogen ion concentration, and the solution becomes highly protonated. The polarity of water decreases; thus, water at SCW condition behaves like acid leading to the dissolution of suspended material[303].

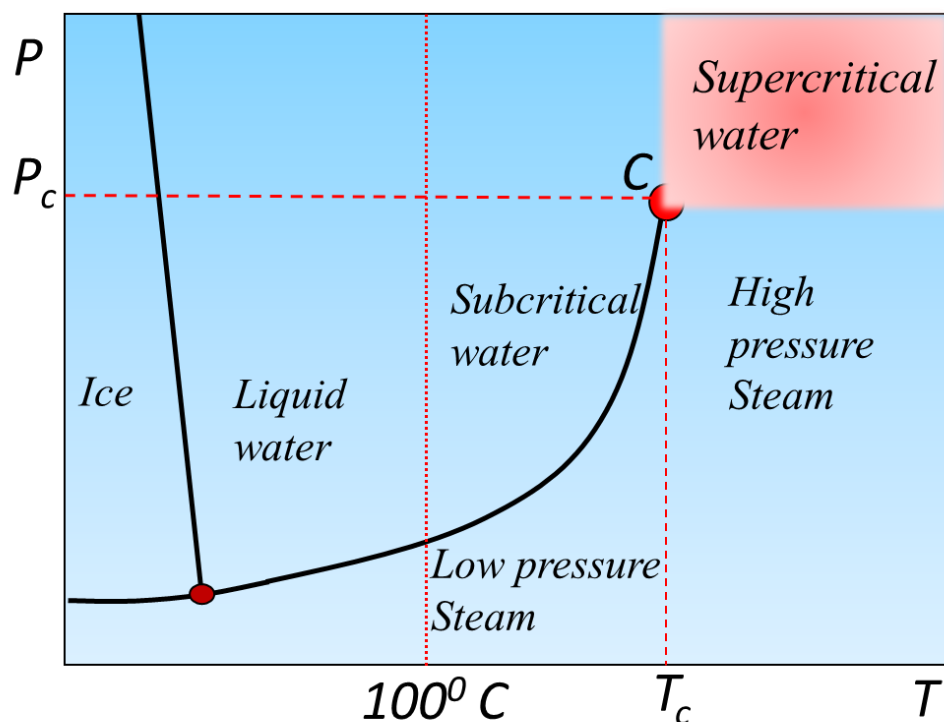


Figure 2.20 Pressure (P)-Temperature (T) equilibrium curve. T_c : Critical temperature-3740C, P_c : Critical pressure-220 bar, (C): Critical point. (adapted from Okajima et al [305]).

The impact of temperature on the physical property of SCW is more dominant than pressure. A change in pressure produces a negligible effect on the solubility of compounds in SCW[306]. Albeit the difference, a minimum pressure within the range of 20 bar to 100 bar is generally used to maintain the liquid phase of the system at elevated temperature[307]. In the current work, a pressure of 20 bar is maintained throughout the process.

The change in polarity and hence the solvation power of SCW has been put to use in extraction and particle formulation processes of several compounds such as aromatic hydrocarbons, metal complex, pharmaceutical and nutraceuticals [302, 308, 309]. Extraction of bioactive compounds such as oxygenates, lignans, antioxidants, proteins, anti-inflammatory, anti-carcinogens using SCW at a moderate pressure range of 50-100 bar produced 95 % yield on an average [310-312].

The etching capabilities of SCW has not been explored widely. *Yoshida et al* [313] demonstrated the etching of Indium from LCD panel displays. The effect of temperature and etching time was studied elaborately, and the results suggested that working in the subcritical region at 360°C for 5 min showed 85% recovery of Indium. The

etching of Indium from the LCD panel comprising of thin-film-transistor liquid crystal display and colour filter glass was driven by hydrolysis and exfoliation of Indium into the aqueous phase with prolonged exposure to SCW condition.

The etching of Cobalt and Lithium from the Lithium-ion batteries were performed using SCW. The process yielded 95% and 98% recovery of Cobalt and lithium, respectively using SCW-Polyvinyl chloride (PVC) solution at 350°C, 30 min process time. The addition of PVC was to enhance the acidic environment during the leaching of Cobalt and lithium. Although PVC was used as an additional catalyst, the toxic effect of the chlorine content was eliminated by the dechlorination in the SCW condition[314].

The etching of silicon using SCW was demonstrated by *Morita et al.* [315], and *Gonzalez-Pereyra et al.* [316]. The hydrolysis of silicon dioxide film in the SCW condition generates a large concentration of anions that readily react with silicon dioxide, leaching out silicon. The temperatures between 200-300 °C and 100 bar produced a maximum etching rate of 2 nm/min. Further increase in temperature beyond 300° C decreased the etching rate of silicon due to the low density of water-vapour at the supercritical condition. Etching of silicon from silicon nitride films was performed between 150 to 300° C and 100 bar pressure. A comparison was drawn between etching with SCW and phosphoric acid. The results showed that hydrous silica had high solubility in SCW compared to the acid. Moreover, working in SCW produced an etching rate of 7.5 nm/min comparable to 10 nm/min in phosphoric acid. The works confirmed that SCW produces fine etching compared to conventional acid etching methods with additional green benefits of being non-toxic and environment friendly[315].

Gonzalez-Pereyra et al [316], used dilute solutions of KOH (0.03-0.7wt%) and NH₄OH (1wt%) in conjunction with SCW at 103 bar and 200-300° C, to etch monocrystalline silicon wafer. The etch rate was high (450 μm/h) in SCW conditions with a KOH concentration of 0.005wt% compared to atmospheric conditions. Similarly, an increase in etch rate (10⁻³ nm/s to 30 nm/s) was observed by *Bagratashvili et al* [317] while etching germanium silicate from silica fiber in supercritical water at 400 °C and 250 bar.

The harmful effects of handling hydrogen fluoride in etching glass microchips were avoided by employing the SCW method. The effect of pressure, temperature, and etching time were studied. The results ascertain that silicon wafers' etching in the subcritical condition of 300 °C and 400 bar for 30 minutes produced well-defined corners.

Working in the supercritical state above 400 °C and 500 bar produced a high aspect ratio (width/diameter=1.16) structures. Both subcritical and supercritical water etching proved to be less harsh and faster compared to Hydrogen fluoride etching[318].

The SCW treatment of porous materials such as kaolinites and carbon nanotubes has not been explored and provides a wide scope for investigation.

The advantages of being nontoxic, cost-effective, faster, and viability towards scale-up processing, establish the SCW treatment, as not only a tuneable solvent in formulating drug delivery systems, but also as an etching media in surface modification of HNTs.

2.7 CONCLUSION

The efficacy of the Colorectal Cancer treatment can be improved by employing micro/nanoformulation of APIs. The drug micro/nanoformulation reduces the side effects of overdosage and improves the bioavailability at the targeted locations. Amongst the various formulation methods, green processing, such as DG processing and SCW technology, provides innumerable advantages over conventional methods. The toxic impact associated with the extensive use of chemicals and solvents in the conventional process can be minimized through DG processing. The unique feature of the tunability of density, diffusivity, and solvation power of dense carbon dioxide enables in handling a wide range of APIs and excipients. The DG processes such as GAS and ARISE provides efficient routes of formulating hydrophilic and hydrophobic drugs with uniform morphology and particle size distribution within the acceptable range for oral administration (5-10 µm). The processes use moderate operating conditions, which is favourable for thermo-sensitive APIs and excipients. The high sensitivity of the processes to change in parameters facilitates ease of tuning to obtain required formulations. The colon targeted drug delivery can be achieved by employing naturally occurring excipients such as HNT and synthetic polymers such as ES100 for encapsulating APIs such as 5FU and SLB. Apart from the DG formulation, the environmental toxicity associated with the use of strong acids and chemicals in surface modification of crystalline compounds can be decreased by employing SCW treatment. The low polarity and dielectric constant of water at elevated temperature and pressure make it an excellent solvent for processing various compounds. The SCW process is chemical-free, faster, and effective compared to conventional etching methods. Both DG and

SCW technologies provide lab-to-industry transition opportunities, realizing the commercial viability in the pharmaceutical industry.

CHAPTER 3

MATERIALS AND METHODS

3.1 ENCAPSULATION OF 5-FLUOROURACIL ONTO HALLOYSITE NANOTUBE USING GAS ANTISOLVENT PROCESS.

3.1.1 SAMPLE PREPARATION

The halloysite nanoclay (CAS Number 1332-58-7), 5-fluorouracil 99%, HPLC (CAS Number 51-21-8), MeOH for HPLC $\geq 99.9\%$ (CAS Number 67-56-1), Phosphate buffered saline (pH 7.4) P4417, and Sodium Hydroxide $\geq 98\%$ (CAS Number 1310-73-2) were purchased and used as received from Sigma-Aldrich. Dialysis Cassettes, 2k MWCO, 12ml (Catalog Number 66212) was purchased from Thermofisher scientific. Preliminarily, the solubility of 5FU in MeOH was determined by dissolving an excess amount of 5FU in 10 ml of MeOH. The solution was mixed well inside the incubator shaker (SORC.60.100, Thermoline Scientific) at 25 °C and 175 rpm, to ensure solubilization of 5FU to saturation. The solution was centrifuged at 4700 rpm for 10 min in a centrifuge (Heraeus D-37520, Thermo electron co-operation, Germany) to separate the excess drug and supernatant. Excess 5FU was dried and measured to estimate the solubility. The solubility of 5FU in ethanol, water, and acetone was performed similarly. A nearly saturated solution of 5FU in MeOH was prepared by dissolving 70 mg of 5FU in 10 ml of MeOH. HNT was added to the 5FU solution and stirred at 25°C, 1000 rpm for 2h. The suspension was sonicated in an ultrasonic bath, Unisonics, FXP-10 M, to ensure uniform dispersion. This suspension was used as the input medium in the process. The amount of 5FU and volume of solvent used in the present study was fixed to 70 mg and 10 ml, respectively. The ratio of HNT and 5FU was varied by varying the amount of HNT as listed in Table 3.1.

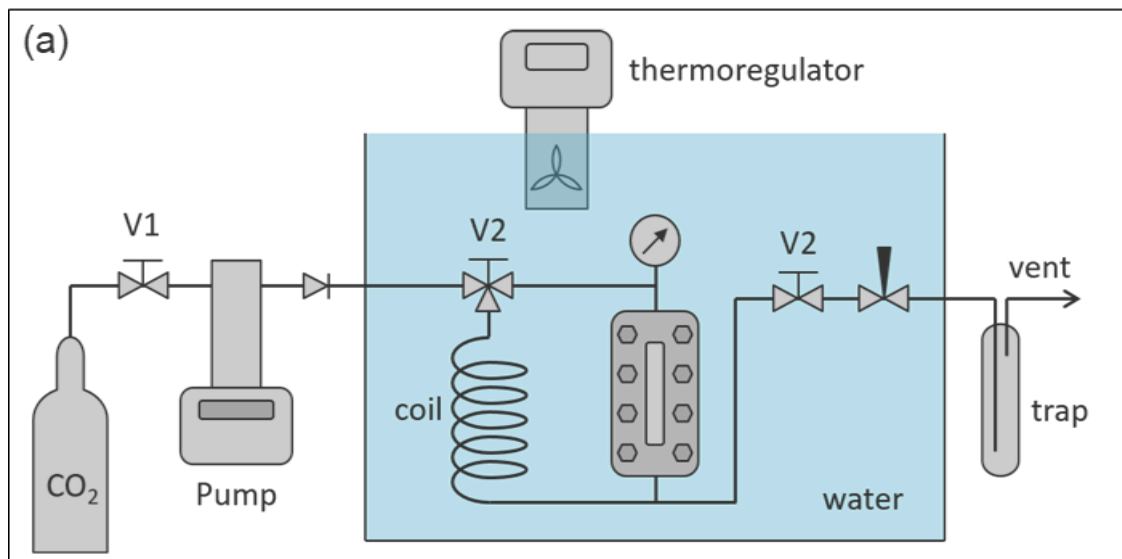
Table 3.1 Amounts of drug, m_{tot} , and HNT, m_{HNT} , used and their mass ratio, $R =$

$$m_{HNT}/m_{tot}.$$

m_{tot} [mg]	m_{HNT} [mg]	R
70	70	1.0
70	105	1.5
70	210	3.0
70	420	6.0

3.1.2 GAS PROCESS

The schematic of the GAS process used for encapsulation of 5FU in HNT is shown in Figure. 3.1a. The image of the set-up used is shown in Figure. 3.1b.



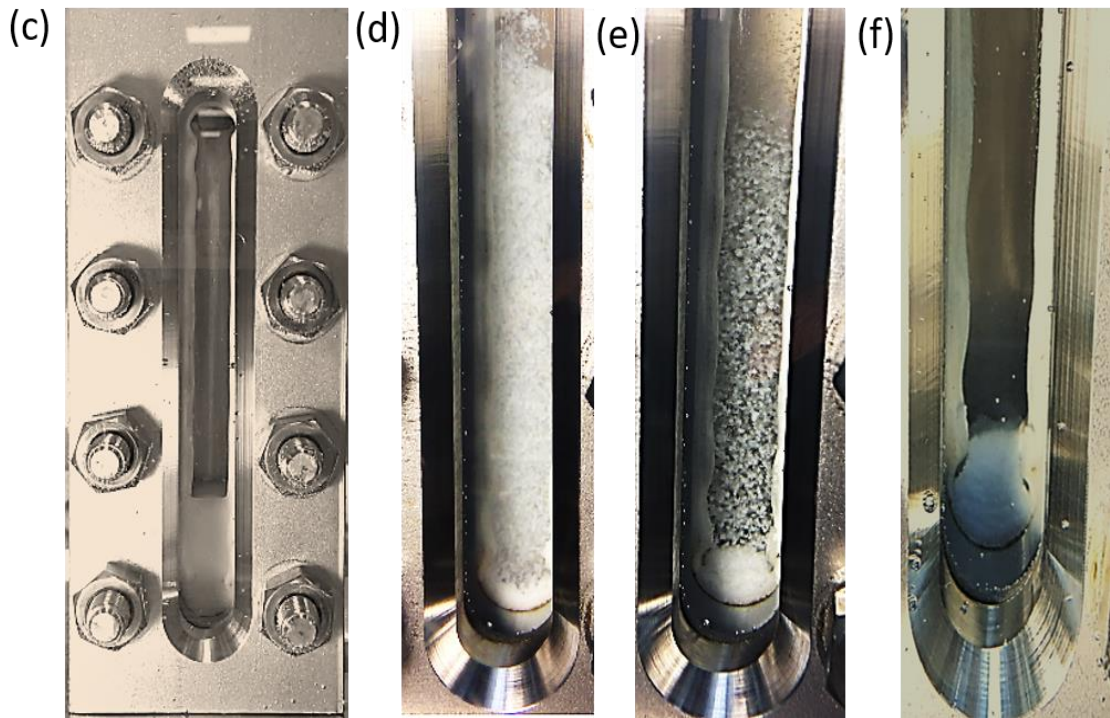
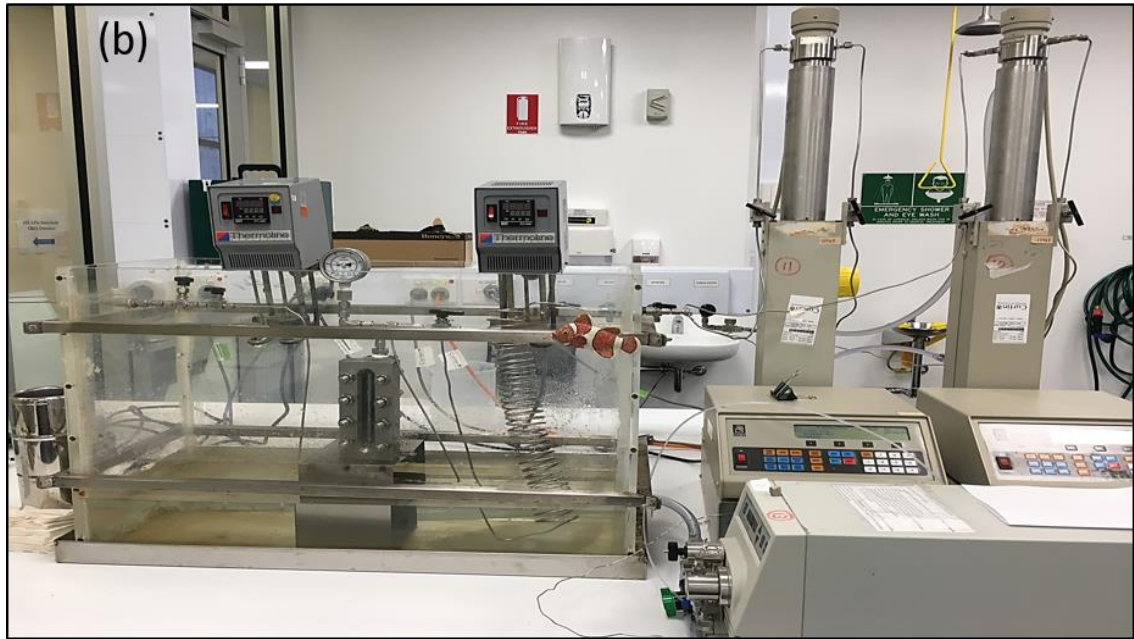


Figure 3.1 (a) Schematic of the rig used to perform the GAS process, (b) Experimental set-up. Precipitation of HNT clay loaded with 5FU: (c) Suspension loaded in the Jerguson cell at atmospheric pressure; (d) Early expansion stage; (e) Late expansion state; (f) Final precipitated product.

The prepared 10 ml of 5FU-HNT suspension was loaded into a 60 ml high-pressure Jerguson cell with a viewing window (Jerguson Gauge R-32 Size 13). The experiments were conducted at a constant temperature of 25 °C. The CO₂ was pumped gradually

form the bottom of the cell using a syringe pump (Teledyne ISCO 260D). The process was performed in two stages: (i) Gas expansion stage, wherein the drug-nanoclay suspension is expanded rapidly from 60 bar to 120 bar at a 20 ml/min flow rate. The high flow rate ensures rapid expansion and a high supersaturation state. During the expansion phase, the suspension volume expands more than five times its initial volume at a pressure of 76 bar. With an increase in pressure, the drug-loaded nanoclay precipitates and settles at the bottom of the cell, as shown in Figure. 3.1(c-f).

After reaching maximum pressure of 120 bar, the system was maintained isobaric for a further 30 min to equilibrate and achieve complete precipitation. (ii) In the flushing stage, the CO₂ was fed at a 10 ml/min flow rate for 12 min from the top of the cell and released through the vent (Figure. 3.1a). This stage ensures that the residual solvent in the precipitate is removed along with the CO₂ and solvent-free product is obtained. During the flushing, the pressure was maintained at 120 bar so that re-solubilization and precipitation are avoided. The mass of CO₂ used in flushing is sufficiently high (≥ 12.8 times) than the mass of the solvent used. This ensures that the solvent content in the product is well below the pharmacopeia limit of 5-8 ppm[319]. The flushing was followed by depressurizing the cell isothermally and the samples were collected manually for further analysis.

3.1.3 REMOVAL OF CO-PRECIPIRATE

The precipitate from the GAS process contains both 5FU loaded HNT and co-precipitated 5FU. Some of the drug particles are loosely attached to the outer surface of the HNT. The loosely attached drug and the co-precipitates were removed before the estimation of loading. The precipitate was gently washed with 10 ml MeOH for 1 min in an orbital shaker (Ratek OM1) and centrifuged at 4500 rpm for 10 min. The residual 5FU content in the supernatant was measured using UV-vis spectrometry (Shimadzu, UV-1800) at a characteristic wavelength of 266 nm. This concentration corresponds to the amount of free drug washed from the precipitate. The washed product is further dried in an oven at 60 °C overnight before further analysis.

3.1.4 PARTICLE CHARACTERIZATION

Scanning electron microscopy was performed using (Zeiss, Neon 40 EsB CrossBeam) to determine particle morphology and average size. A small amount of the sample was suspended in MeOH and placed on an aluminium stub (Ted Pella, 12.7 mm x 8 mm), and left to evaporate. The samples were coated with a 5 nm layer of platinum using Sputterer coater, Cressington 208HR. The sample stubs were loaded onto the SEM, and images were acquired at 5kV excitation voltage using combined InLens and Secondary electron detectors.

In order to confirm the presence of loaded 5FU in the sample, Energy Dispersion X-ray spectroscopy (EDS) was performed using Backscatter detection. The interlayers of nanoclay and the lumen were analyzed using Transmission Electron Spectroscopy (TEM) in FEI Talos FS200X. The sample suspension was placed on a holey carbon grid (Ted Pella) and dried overnight to remove the moisture content. The imaging was performed at 10kV input voltage.

The samples' surface Zeta potential in different pH was measured using the Dynamic light scattering method in Zetasizer Nano ZS (Malvern). Folded capillary zeta cell (DTS10170) was used to obtain the zeta potential of the HNT suspension. Particles were dispersed in water with pH adjusted by adding 0.1M HCl or 0.1M NaOH. The dispersion was sonicated for 30 min before measurement.

3.1.5 FTIR CHARACTERIZATION

Fourier-Transform Infrared Spectroscopy was performed with (Perkin Elmer, Spectrum 400 FTIR) on the pristine HNT, 5FU, and the drug-loaded samples. Dry samples were placed on the crystal and compressed with the diamond-tipped probe until a specific force is achieved (40 units). The scan resolution was set to 2 cm^{-1} . Four scans between 500 cm^{-1} and 4000 cm^{-1} were performed to acquire the spectra. The background spectra were measured in every scan and were subtracted to ensure reproducibility. Attenuated total reflection (ATR) correction was performed on the acquired spectra to ensure low noise level by compensating the shift in the absorption peak due to anomalous dispersion [320].

3.1.6 THERMOGRAVIMETRIC ANALYSIS

The drug loading of the washed product was determined by Thermogravimetric analysis (TGA, Mettler Toledo, V1.03). Dry samples weighing about 20 mg was placed in a platinum crucible and subjected to thermal treatment in an argon atmosphere (flow rate of 20ml/min). Before the loading estimation, the decomposition temperature of pristine HNT and 5FU was determined by subjecting to a temperature sweep from 100 °C to 800 °C. Table. 3.2 details the process parameter. The time derivate of the mass indicates the maximum mass loss, and the corresponding temperature indicates the decomposition temperature of the material. The peak decomposition temperature of HNT and 5FU was found to be 510 °C and 340 °C, respectively. These values are in agreement with published results [321-324].

The drug loading was determined by estimating the mass loss due to the decomposition of 5FU in the sample. The furnace temperature was maintained at 340 °C for 30 min to ensure complete decomposition of 5FU (Table 3.3).

Table 3.2 TGA parameter for determining decomposition temperature of pristine HNT and 5-FU.

Temperature (°c)	Heating rate (°c/min)	Time (min)	Comment
35 to 100	25	--	
100	--	15	Removal of Moisture
100 to 800	10	--	
800	--	5	
800 to 35	25	--	
35	--	10	Cooling

Table 3.3 TGA parameter for determining drug loading.

Temperature (°C)	Heating rate (°C/min)	Time (min)	Comment
35 to 100	25	--	
100	--	15	Removal of Moisture
100 to 340	25	--	
340	--	30	Decomposition of 5FU
340 to 600	25	--	
600	--	30	Decomposition of HNT
600 to 35	50	--	
35	--	10	Cooling

The drug loading, L , was determined using the initial mass of the sample, m_0 , and mass after 5-fluorouracil decomposition, m_1 :

$$L = \frac{m_0 - m_1}{m_0} \quad (3.1)$$

The encapsulation efficiency, E , was calculated as the mass of drug loaded, m_A ($= m_0 - m_1$) to the mass of drug used, m_{tot} :

$$E = \frac{m_A}{m_{tot}} \quad (3.2)$$

3.1.7 IN VITRO DRUG RELEASE

In vitro drug release was performed using the dialysis method, which is a modified Franz diffusion cell [325, 326]. The drug release was studied in pH 1.2 and pH 7.4,

representing gastric and intestinal conditions [327, 328]. A Slide-A-Lyzer dialysis cassette (ThermoFisher, 2000 MWCO) was used as the donor compartment containing the drug-nanoclay suspension. The membrane was made of biodegradable regenerated cellulose with a pore size of 1 nm and less. The average pore size of the intestine is about 10 Å and above [329]. Further, the pore size of the membrane is small enough to allow the drug and confine the nanoclay from releasing into the acceptor compartment.

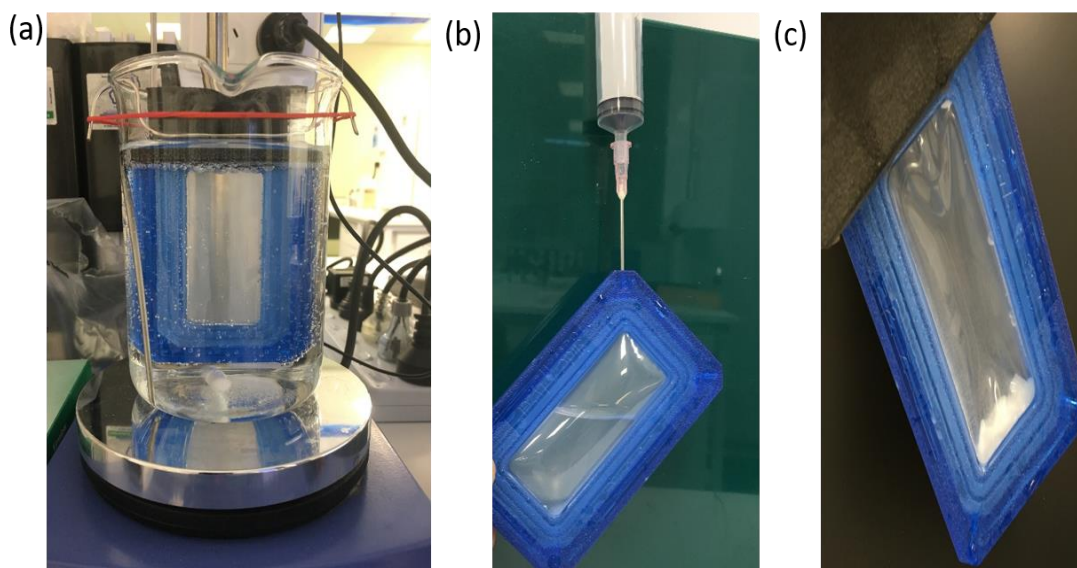


Figure 3.2 (a) Dialysis set-up with donor and acceptor compartment, (b) Cassette filled with 5FU-nanoclay suspension before dialysis, (c) Nanoclay suspension after dialysis.

About 25 mg of dried product was dispersed in 12 ml of PBS buffer and filled inside the cassette. The loaded cassettes were placed in a 500 ml beaker containing PBS buffer (acceptor compartment). The set-up was stirred at 100 rpm to maintain a uniform concentration of the buffer, as shown in Figure 3.2. The dialysis was conducted at a temperature of 37.5 °C, and the release of 5FU was monitored over several hours. Aliquot of 4 ml were retrieved at regular time intervals and replaced with fresh medium to maintain the concentration gradient. Data points were collected every 20 min for the first 2 h and again after 24 h to assess the complete (maximum) release.

3.2 MICRONIZATION AND SPRAY CHARACTERIZATION IN ATOMIZED RAPID INJECTION FOR SOLVENT EXTRACTION (ARISE) PROCESS

3.2.1 SAMPLE PREPARATION

Biopolymer Eudragit S-100 was supplied by Evonik Australia, MeOH for HPLC \geq 99.9% (CAS Number 67-56-1) was purchased and used as received from Sigma-Aldrich. Argon \geq 99.997% (Product code 260150) and Carbon dioxide \geq 99.5% (Product code 376142) were purchased from Coregas Australia.

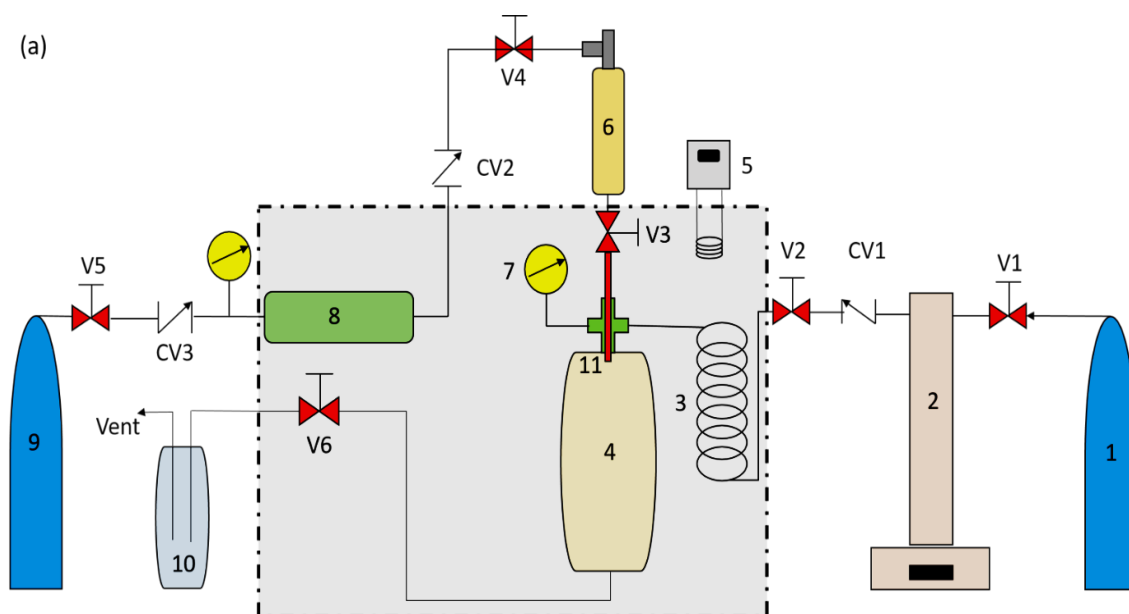
The input polymer solution was prepared by solubilizing Eudragit S-100 in Ethanol in an incubator shaker (SORC.60.100, Thermoline Scientific) at 25 °C and 175 rpm for 2 h. The concentration of the solution was varied by increasing the amount of Eudragit S-100 in a fixed 10 ml solvent. The solution was filtered using a 0.45 μ m PVDF syringe filter (Fisher Scientific) and used in the ARISE process.

3.2.2 ARISE SET-UP

The ARISE rig was assembled, as shown in the schematic in Figure 3.3(a). The ARISE rig consists of a 10 ml high-pressure injection chamber (Sandvik 3R60 ASTM A213-AW /A269), connected to a 150 ml precipitation chamber (Swagelok 316L-50DF4-150 Stainless steel double end DOT-Compliant cylinder), through a ball valve-V3 (Swagelok 316-SS42GS4) regulated narrow conduit (SS-316L, 1/8 in. OD, 0.028 in, Swagelok, USA). The feed circuit consists of injection chamber-6, back pressure chamber-8, and Argon gas supply-9, connected through valves V4-5 and CV2-3. The precipitation circuit consists of precipitation chamber-4, heating coil-3, narrow conduit-11, CO₂ pump-2 and CO₂ supply-1 joined through valves-V1-3 and CV1. The injection chamber was maintained at a pressure higher than the precipitation chamber in order to generate a constant pressure differential. The ball valve-V3 was in close position, and the feed solution (input polymer solution) was injected into the injection chamber and pressurized to 130 bar by adjusting the valve-V4. Argon gas was used as a medium in the injection chamber to maintain an inert atmosphere and avoid contamination of the feed solution.

The back-pressure chamber-8 ensured the volume surplus of argon during the experiment. The CO₂ was metered into the precipitation chamber at a rate of 10 ml/min using

a syringe pump (Teledyne ISCO 260D) up to 80 bar pressure. The system was allowed to equilibrate isothermally in a water bath maintained at 25 °C. Upon reaching the thermal equilibria, valve V3 was opened rapidly for 5 seconds and closed. The rapid opening generates instantaneous pressure-driven flow into the precipitation chamber, allowing the feed solution to precipitate due to rapid expansion in the antisolvent environment. The precipitation chamber was isolated to equilibrate for 10 min. The CO₂ was flown through valve-V2 at 10 ml/min for 60 min to flush the residual solvent. The Valve-V6 was adjusted such that the flow rate is maintained constant during flushing. After flushing, the system was depressurized, and the samples were retrieved manually from the precipitation chamber for further analysis.



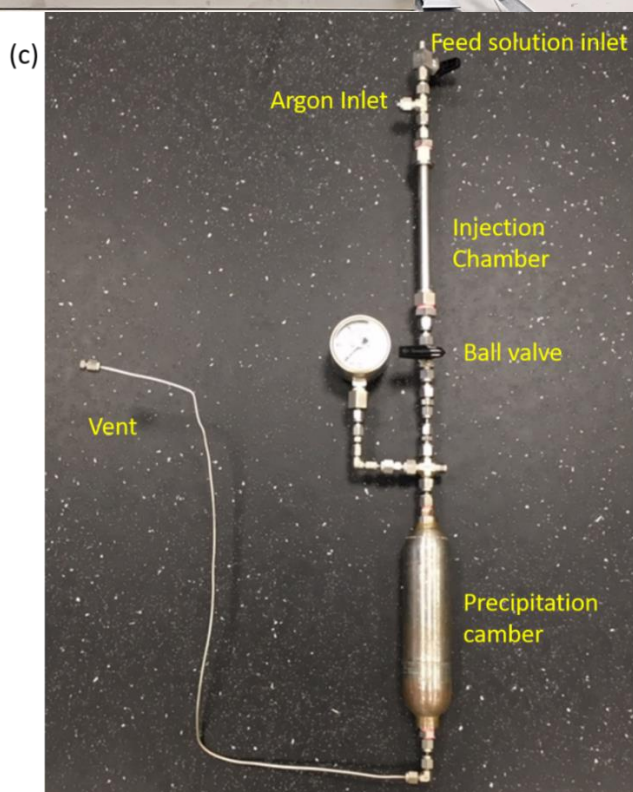


Figure 3.3 (a) Schematic of the ARISE rig used. 1: CO₂ supply, 2: Syringe Pump, 3: Heating coil, 4: Precipitation Chamber, 5: Re-circulating heater, 6: Injection chamber, 7: Pressure indicator, 8: Back-pressure chamber, 9: Argon supply, 10: Solvent trap, 11: Injection conduit, Vn: Ball valve, CVn: Check Valve; (b) ARISE assembly; (c) parts of ARISE setup.

The process parameter and concentration of feed solutions used are listed in Table 3.4.

Table 3.4 Parameters used in the ARISE process for micronizing ES-100.

Parameters	Values
ES100 concentration (%)	3,5,10 &15
Injection volume (ml)	2,5 & 10
Pressure differential (Δp)(bar)	50
Equilibration time (min)	10
CO ₂ flow rate (ml/min)	10
Operating pressure (bar)	110
CO ₂ Volume (ml)	600

3.2.3 SPRAY ATOMIZATION SETUP

The spray experiment, resembling the ARISE process, was conducted to visualize the spray pattern during the ARISE operation. The investigation gives insight into the way in which micronization happens inside the precipitation chamber. The experiment was conducted at a driving pressure of 50 bar, which is the pressure differential of the ARISE in the current work. The injection chamber with the narrow conduit (SS-316L, 1/8 in. OD, 0.028 in, Swagelok, USA) was filled with the feed solution and pressurized to 50 bar using Argon as mentioned in Section 3.2.1. The schematic and image of the set-up are shown in Figure 3.4 (a,b). The setup was placed in the water bath maintained at 25 °C. The valve V2 was opened rapidly, and the spray through the conduit was recorded with 2160p resolution and 30 fps camera. The images were processed and analyzed using ImageJ software. The spray simulation was carried both in air and water medium, covering extremes of the ambient conditions.

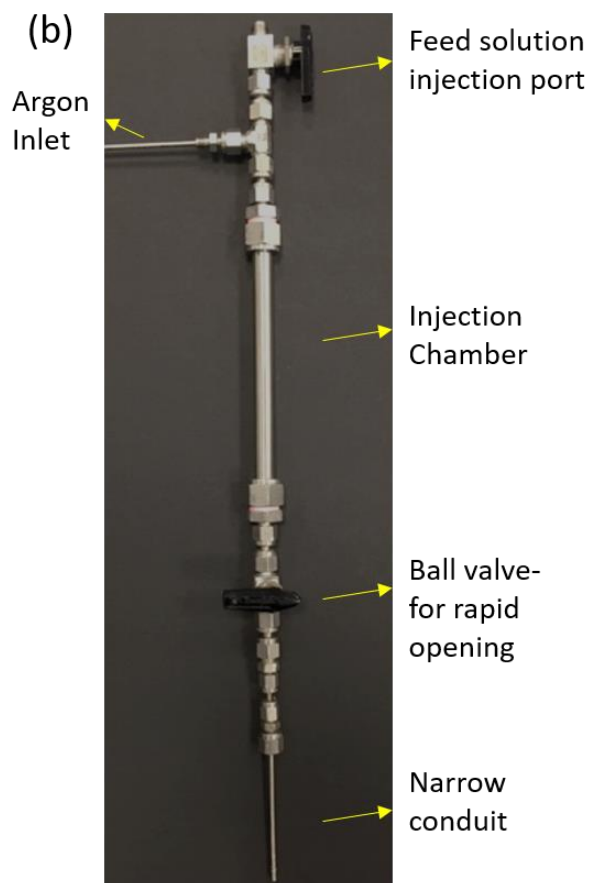
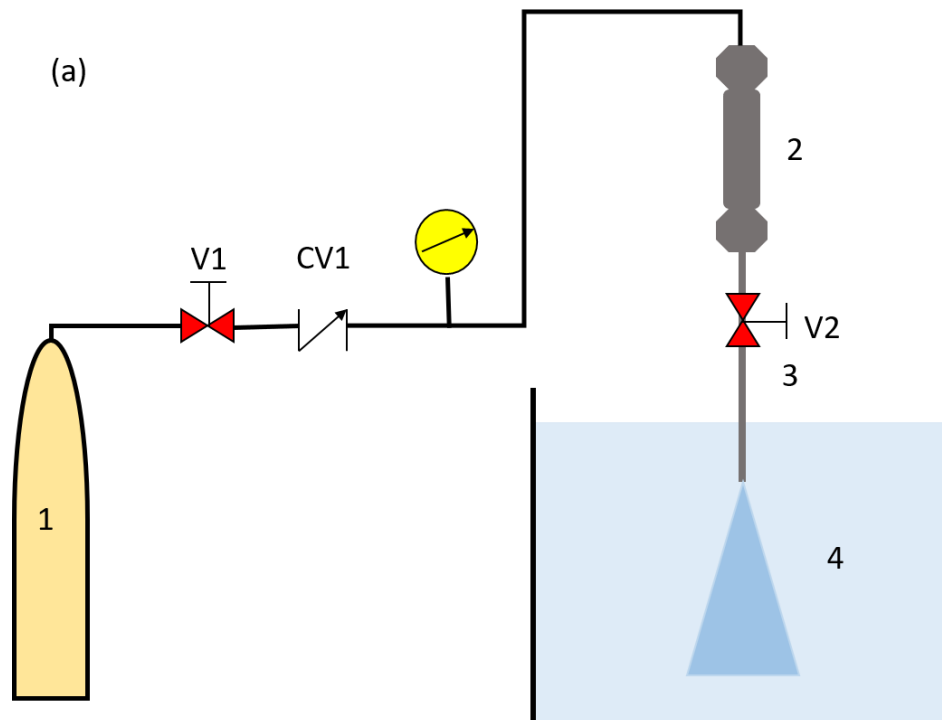


Figure 3.4 (a) Schematic of the Spray setup. 1: Argon supply, 2: Injection chamber, 3: Injection conduit, 4: Water bath, V_n : Ball valve, CV_n : Check valve; (b) Image of the Injection chamber, ball valve, and the injection conduit used in the experiment; (b) Assembled spray setup.

3.2.4 VISCOSITY MEASUREMENT

The viscosity of various concentrations (3, 5, 10, 15 & 20 w/w) of ES100 solution in ethanol was measured in Rheometer (Haake Mars, Catalog number: 379-0340). Cup and Cone configuration (Z20DIN-8.2 ml) was used to measure the viscosity. 8 ml of prepared solution was placed inside the sample holder and sheared at the rate of 0.01-50 s⁻¹. The shearing time was adjusted to 5 min at an ambient temperature of 25 °C.

3.2.5 BULK DENSITY MEASUREMENT

The bulk density of the ARISE processed ES100 was measured based on the guidelines of United States Pharmacopeia (2003), Monograph-616, Method 1. The measurement procedure was adapted from *Roderick et al.*[110]. The dry sample from the ARISE was filled in a graduated cylinder without compacting [330]. The mass and volume of the samples were measured, and the bulk density (ρ_{bulk}) was determined as the ratio of the mass of the sample retrieved (M_r) and uncompact volume occupied (V_r).

$$\rho_{bulk} = \frac{M_r}{V_r} \quad (3.3)$$

3.2.6 PARTICLE CHARACTERIZATION

The morphology of the ARISE processed ES100 was analyzed by Scanning electron microscopy using (Zeiss, Neon 40 EsB CrossBeam). The dry samples obtained from the ARISE were mounted on the carbon tapped aluminum pin stub (Product number: 16202, Tedpella), and 3 nm thick platinum was coated using (Sputterer coater, Cressington 208HR). The imaging was done under vacuum condition with combined InLens and Secondary electron detector at 5 kV excitation voltage. The Energy Dispersion X-ray spectroscopy (EDS) was performed using Backscatter detection.

The average particle size distribution was measured in Zetasizer Nano ZS (Malvern). 2 mg of sample was suspended in 10 ml deionized water and 0.5 v/v% Tween 20 surfactant. The surfactant was added to avoid the agglomeration effect due to electrostatic adhesion. The suspension was sonicated for 10 min before the measurement to ensure homogeneity throughout the volume.

3.2.7 FTIR CHARACTERIZATION

The infrared spectrum and the corresponding chemical characteristics of the samples were performed in (Perkin Elmer, Spectrum 400 FT-IR) spectrometer. The procedures are described in Section 3.1.5.

3.3 ARISE ASSISTED ENCAPSULATION OF HYDROPHOBIC AND HYDROPHILIC DRUG IN EUDRAGIT S-100

3.3.1 SAMPLE PREPARATION

5-fluorouracil 99%, HPLC (CAS Number 51-21-8), MeOH for HPLC \geq 99.9% (CAS Number 67-56-1), Phosphate buffered saline (pH 7.4) P4417, Hydrochloric acid 31-33% (CAS Number 7647-01-0), and Sodium Hydroxide \geq 98% (CAS Number 1310-73-2) were purchased and used as received from Sigma-Aldrich. Dialysis Cassettes, 2k MWCO, 3ml (Catalog Number 66203) was purchased from Thermofisher Scientific. Eudragit S-100 was supplied by Evonik Australia, Argon \geq 99.997% (Product code 260150), and Carbon dioxide \geq 99.5% (Product code 376142) were purchased from Coregas Australia.

The encapsulation of 5FU in ES100 and SLB in ES100 were performed separately with similar sample preparation procedures.

The feed solution was prepared in three different concentrations (3, 5, & 10 w/w %) of Eudragit S-100(ES100) and 7 mg/ml of 5FU in 10 ml of Absolute MeOH as solvent. The concentration of 5FU and volume of feed solution were unaltered throughout the process. Similarly, 7 mg/ml of SLB was used with ES100 in 10 ml Ethanol as a solvent for encapsulation.

The initial concentration of 5FU and SLB was measured in a UV-vis spectrometer (Shimadzu, UV-1800) at a characteristic wavelength of 266 nm and 288 nm, respectively.

3.3.2 ENCAPSULATION USING ARISE PROCESS

The encapsulation of 5FU and SLB in ES100 was carried out separately using the method described in Section 3.2.2. The parameters are listed in Table 3.5.

Table 3.5 Parameters used in ARISE for encapsulation of 5FU and SLB in ES100.

ES100 (w/w %)	SLB (mg/ml)	5FU (mg/ml)	R_{ES100-drug}	ΔP (bar)	CO₂ vol (ml)
3	7	7	3.4	50	600
5	7	7	6	50	600
10	7	7	11.4	50	600

3.3.3 BULK DENSITY MEASUREMENT

The measurement of bulk density of the ARISE processed products was performed as described in Section 3.2.4.

3.3.4 REMOVAL OF CO-PRECIPIRATE

The processed samples from ARISE contains (a) drug loaded ES100 and, (b) co-precipitated drug nanoparticles. Further, some of the drugs may be loosely attached to the surface of the particles. The removal of co-precipitates and loosely attached drugs were performed before the estimation of drug loading. The removal was performed in two conditions, harsh and moderate conditions, respectively. This step provides information to draw a comparison between suitable removal conditions. The harsh condition includes washing of the produce in distilled water for 5 min in an orbital shaker (Ratek OM1) and centrifuging at 4500 rpm for 5 min. Whereas in moderate condition, the products are washed for 1 min, and vacuum filtered gently using a vacuum pump [Sparmax TC-63V]. The residual drug content in the supernatant was measured using UV-vis spectrometry (Shimadzu, UV-1800) at a characteristic wavelength of 266 nm for 5FU and 288 nm for SLB, respectively. The washed product is further dried in an oven at 40 °C overnight before further analysis.

3.3.5 PARTICLE CHARACTERIZATION

The particle morphology and average size estimation were performed, as mentioned in Section 3.2.6. The zeta potential of the samples was measured using Zetasizer Nano ZS (Malvern). About 2 mg of samples were suspended in distilled water and sonicated

for 30 min prior to measurement. Folded capillary zeta cell (DTS10170) was used to obtain the zeta potential of the suspension. The particles produced from ARISE were fluffy; hence 0.5 % v/v Tween 20 was added to the produce homogenous suspension.

3.3.6 XRD CHARACTERIZATION

The X-ray diffraction analysis of the ARISE processed sample was performed using D8 Advance (Bruker AXS, Germany) analyzer with a copper K α radiation source operated at 40 Kv and 40 mA with a LynxEYE detector. Dry powdered samples were mounted on a Si low background holder (Bruker AXS, Germany). The samples were scanned over the range of 7.5 ° to 90 ° 2 θ with a step size of 0.015° at 2.5 x 10⁻⁵ °/s. The background diffraction was subtracted to obtain the diffraction pattern of the loaded sample.

3.3.7 DRUG LOADING ESTIMATION

The loading of 5FU and SLB in ES100 was determined using UV-vis spectrometry (Shimadzu, UV-1800). About 8 mg of samples were taken and solubilized in 10 ml MeOH (for 5FU) and in Ethanol (for SLB) for one hour in an incubator shaker (Thermoline Scientific) at 25 °C and 175 rpm. The solution was filtered, and the UV absorbance was measured at the characteristic wavelength of 266 nm (5FU) and 288 nm (SLB). The loading, L , was estimated using the mass of drug-loaded, m_{drug} , and, total mass of the sample, m_s .

$$L = \frac{m_{drug}}{m_s} \quad (3.4)$$

The encapsulation efficiency was estimated as the ratio of the mass of drug-loaded to the mass of drug used as in Eq (3.2).

3.3.8 IN VITRO DRUG RELEASE

The drug release profile was studied by mimicking the gastric and colon environment using the dialysis method, as described in Section 3.1.7. About 6 mg of sample was

dispersed in 3 ml PBS buffer and filled inside the dialysis cassettes (donor compartment). The cassettes were placed in a 150 ml external buffer and stirred at 100 rpm for maintaining uniformity in concentration in an external buffer. 4 ml of samples were retrieved every 30 min for 6 h and again after 24 h to access the maximum release and replaced with an equal volume of buffer to maintain constant concentration gradient. The experiment was conducted at 37.5 °C, in pH 1.2 and pH 7.4 to study the release pattern in both gastric and intestinal environment.

3.4 COMPARISON STUDY ON ENCAPSULATION OF 5-FLUOROURACIL ONTO HALLOYSITE THROUGH THE GAS, ARISE, AND MECHANICAL PROCESS

3.4.1 SAMPLE PREPARATION

The materials and sample preparations were based on the technique described in Section 3.1.1.

3.4.2 MECHANICAL LOADING

The GAS assisted loading of 5FU onto HNT was described in Section 3.1.2. The ARISE process was used in encapsulating 5FU onto HNT using the procedure described in Section 3.2.2. The feed solution consists of HNT-5FU suspension of different concentrations mentioned in Table 3.1. The mechanical loading was performed based on the procedures described in the published work [259, 260, 265, 280, 331]. The HNT in 5FU solution was mixed using a mixer at 25 °C and 1000 rpm for 2h (Figure 3.5) to obtain a homogenous solution. The clumps and aggregates were removed by sonication for 30 min. The suspension was then placed in a vacuum for 3 cycles to ensure that the drug penetrates the interlayers of the HNT. The samples were centrifuged at 4500 rpm for 10 min to remove the supernatant and dried at 50 °C overnight before further analysis.



Figure 3.5 Setup for mechanical mixing of HNT and 5FU.

3.4.3 REMOVAL OF CO-PRECIPTATE

The co-precipitate from the ARISE processed HNT-5FU samples were washed as described in Section 3.1.3.

3.4.4 PARTICLE CHARACTERIZATION

The SEM and EDS analyses were performed on the dry sample, as described in Section 3.1.4.

3.4.5 FTIR CHARACTERIZATION

The infrared spectrum of the samples was obtained by the procedure as described in Section 3.1.5.

3.4.6 DRUG LOADING ESTIMATION

The percentage of 5FU loaded in HNT was estimated using Thermogravimetric analysis. The procedures for determining drug loading are described in Section 3.1.6.

3.5 SUBCRITICAL WATER TREATMENT OF HALLOYSITE NANOTUBE-GREEN ALTERNATIVE TO CHEMICAL ETCHING

3.5.1 SAMPLE PREPARATION

The halloysite nanoclay (CAS Number 1332-58-7) was purchased from Sigma-Aldrich, Australia. Nitrogen $\geq 99.999\%$ (Product code: 221152) was purchased from Coregas, Australia.

3.5.2 SUBCRITICAL WATER TREATMENT

The schematic of the SCW treatment rig is shown in Figure 3.6 (a). The setup consists of an 8 ml pressure vessel (Swagelok MF6779001 filter) mounted inside a heating chamber maintained at an elevated temperature of 170 °C. One end of the pressure vessel was connected to a T-junction connector. One end of the connector was connected to a syringe pump (Teledyne ISCO 260D). Nitrogen was delivered through the other port of the T-junction, as seen from Figure 3.6 (a-c). The pump and nitrogen supply are regulated by the check-valve to regulate pressure and flow rate. The other end of the vessel was connected to the sample collection vial. 500 mg of HNT was placed inside the vessel and pumped with distilled water until the entire circuit was filled using a syringe pump. Metal filters were fitted at both the ends of the vessel in order to confine the HNT within the vessel. A magnetic stirrer was used for creating homogenous suspension and avoid sedimentation of HNT during the process (Figure 3.6 (c)). The rig was pressurized to 20 bar by supplying nitrogen purge through valve 8 as shown in Figure 3.6(a-b). Individual experiments were carried out for different treatment time- 1 h, 4 h, 5 h, 7 h, 8.5 h, 10 h, and 12 h respectively. The treated samples were retrieved and dried in an oven before further analysis.

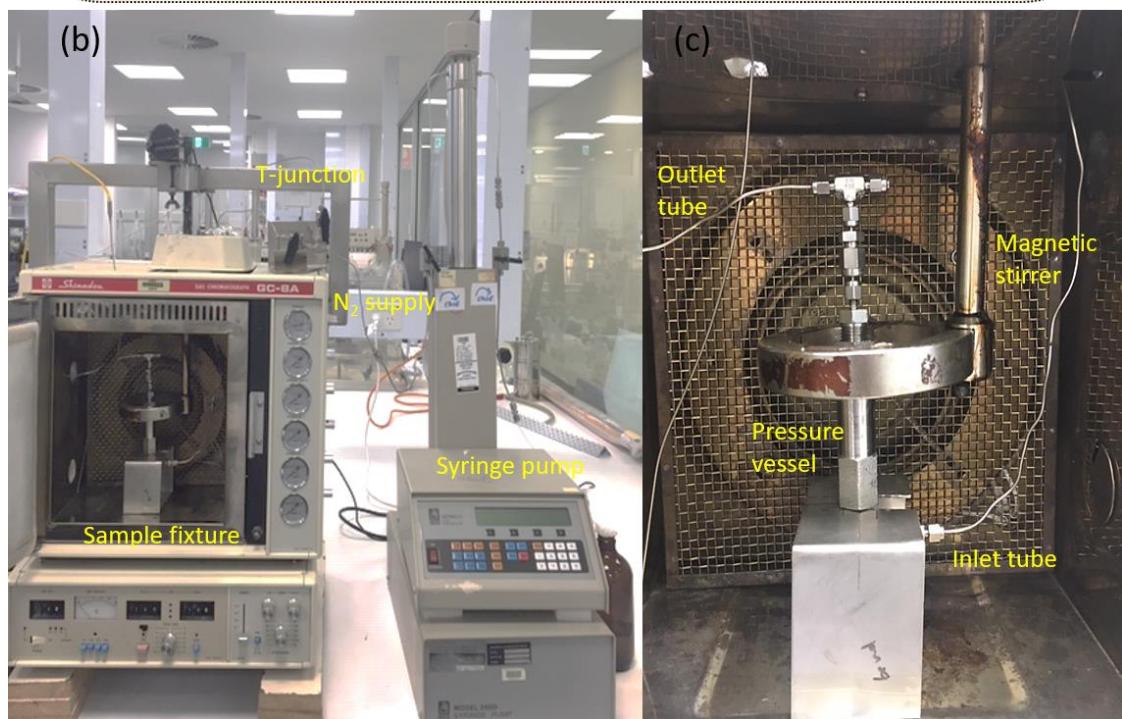
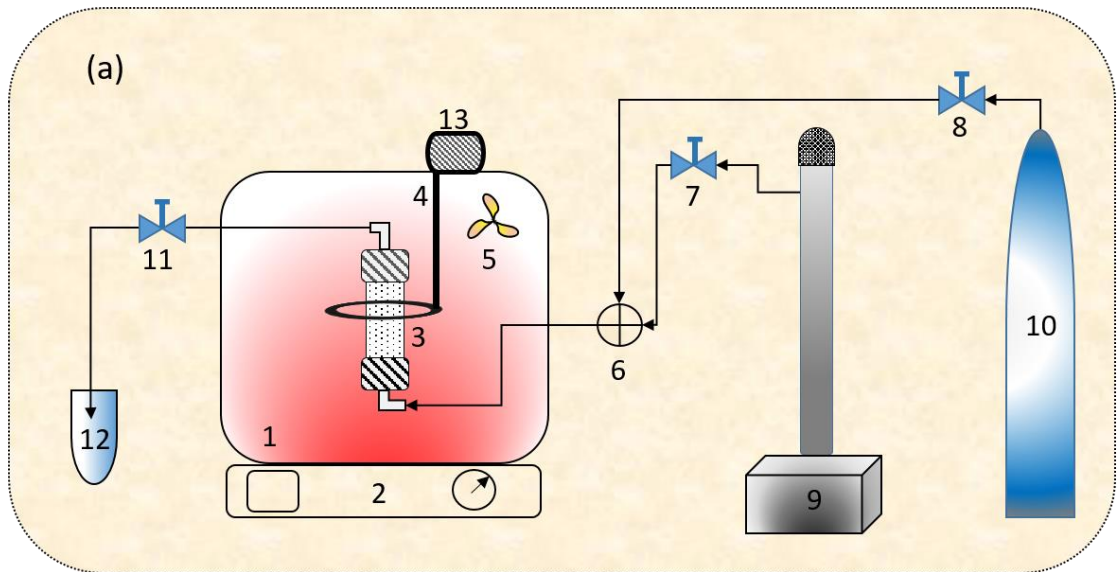


Figure 3.6 Schematic diagram of the Subcritical Water-HNT Treatment set-up. (1) Furnace, (2) Temperature and pressure controller, (3) Pressure vessel, (4) magnetic stirrer, (5) Heating fan, (6) T-junction connector, (7, 8, 11) check valve, (9) ISCO high-pressure pump, (10) Nitrogen supply, (12) Exhaust sample collection, and (13) Drive motor; (b) Assembled setup; (c) Assembly of parts inside the furnace.

3.5.3 THERMAL TREATMENT OF HALLOYSITE

In order to ascertain the effect of SCW treatment, the HNT's were thermally treated in a Soxhlet apparatus separately. The physicochemical characteristics were compared

with the SCW treated counterpart. The Soxhlet apparatus used for the treatment is shown in Figure 3.7. An equal amount of HNT was suspended in deionized water and heated at 170 °C for 7 h in ambient pressure. The Soxhlet setup ensures the re-circulating of water, maintaining suspension volume throughout the process.

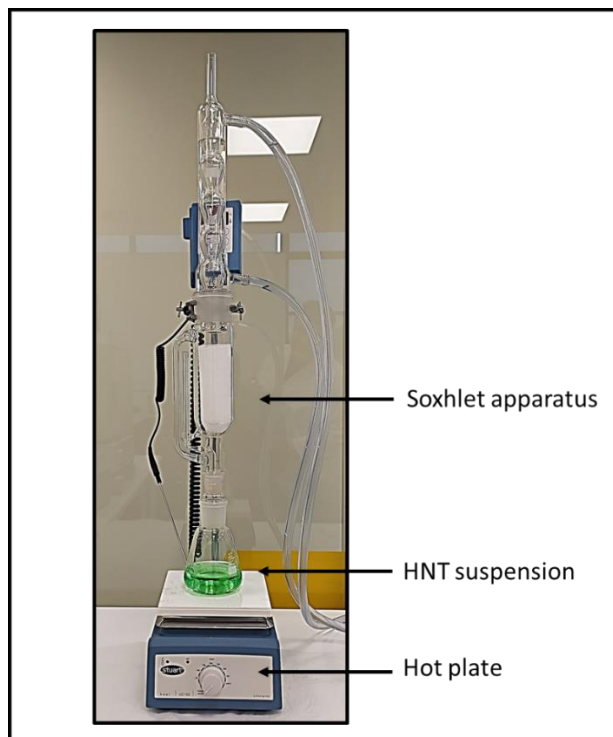


Figure 3.7 Thermal treatment of HNT using Soxhlet apparatus.

3.5.3 SURFACE AREA MEASUREMENT

The surface area and porosity of HNTs were measured using nitrogen adsorption-desorption isotherm at 77 K. The samples were degassed at 50 °C before measurement in Micrometrics VacPrep 061. The degassing ensures complete removal of air trapped inside the HNTs. The samples were then loaded to Tristar II (Micrometrics) with an isothermal jacket to ensure uniform temperature distribution across sample volume. The specific surface area was measured using the Brunauer-Emmett-Teller (BET) method. Single point desorption pore volume was determined from nitrogen desorption volume at a relative pressure of $(P/P_0=0.95)$ [332, 333].

3.5.4 FTIR CHARACTERIZATION

The infrared spectra were measured by procedures as described in Section 3.1.5.

3.5.5 XRD CHARACTERIZATION

The crystallinity and crystal growth were estimated using X-ray diffraction analysis in D8 advance (Bruker AXS, Germany). The diffraction pattern was measured by the procedure described in Section 3.3.6. The sample mass, loading pattern, and instrument parameters were kept fixed for all the samples to ensure that the difference in diffraction patterns are due to the effect of SCW treatment. The peak intensity and crystallite size from the acquired patterns were analyzed using Topas (Bruker-Diffrac.suite) software. The phase identification was performed using DIFFRAC.EVA 3.2 (Bruker-AXS, Germany), using the ICDD PDF4+ database.

3.5.6 PARTICLE CHARACTERIZATION

The transmission electron microscopy (TEM) and selected area diffraction (SAD) were performed on samples in FEI Talos FS200X at 10 kV input voltage. The samples were dispersed in distilled water, and a drop was placed on holey carbon grids (Ted Pella) and dried before measurement.

The surface charge on HNT was measured in Zetasizer Nano ZS, Malvern Panalytical. A small amount of the sample was dispersed in deionized water and measured using folded capillary cell (DTS1070, Malvern panalytical) at 25 °C ambiances.

CHAPTER 4

**Gas antisolvent process (GAS) as-
sisted loading of 5-Fluorouracil onto
Halloysite nanoclay**

RESULTS AND DISCUSSION

The Gas Antisolvent (GAS) process is a DG process in which active pharmaceutical ingredients are precipitated by using carbon dioxide as antisolvent [91, 334, 335]. A detailed description of the process and experimental setup can be found in Chapter 2, Section (2.3.2), and Chapter 3, Section (3.1). The API is dissolved in a suitable solvent and then the API-solvent system is rapidly pressurized with carbon dioxide. Carbon dioxide is miscible with most organic solvents but a poor solvent for many drugs (solubility of 5FU in DG-CO₂ is of the order of 5×10^{-6}) [336]. As the solvent mixes with carbon dioxide, its volume expands and its solvent power reduces [337]. At a certain point, the drug solution becomes supersaturated and precipitation occurs [338]. The precipitate is then washed with carbon dioxide and retrieved as a dry powder. Thus, using the GAS process, micronization and/or encapsulation are achieved in a single step. The amount of organic solvent used is reduced and the levels of residual solvent are extremely low [339-341].

The prodrug 5-fluorouracil (5-fluoro-2,4(1H,3H)-pyrimidinedione or 5FU) is an anti-metabolite used clinically for the treatment of colorectal, breast, and head and neck cancers [342]. It is administered intravenously or orally [343, 344]. Conventional intravenous injection increases its bioavailability but treatment is often ineffective due to the drug not reaching the target site in sufficient amounts [345]. There are also side effects due to the cytotoxicity of 5FU to normal cells [346]. Oral administration is considered most effective in treating colon cancer as it is simple and allows targeted delivery in the colon-(Chapter 2, Section 2.1).

HNT have recently emerged as a cheap, natural, and biocompatible nanocarrier for drug delivery [347, 348]. The aluminosilicate sheets are rolled into tubes, in a carpet-like manner, exposing silica on the outer surface and alumina on the inner one (Chapter 2, Section 2.5). Because of this geometry, the interior volume is rather small and inaccessible. Successful drug loading necessitates acidic etching to increase the inner diameter [347]. Acid activation is a common procedure in the clay industry [349] and the conditions are harsh. We propose that acid treatment can be avoided by using the GAS process because DG processes, in general, provide better molecular access to the adsorption sites on the solid surface.

The micronization of 5FU using a GAS process at 40 °C and 100 bar or 150 bar has been reported by *Kalantarian et al.* [350]. The product precipitated from a 50:50

MeOH -dichloromethane mixture, showed uniform spherical morphology with an average particle size of 248 nm. *Esfandiari et al* [351] also micronized 5FU using a GAS process after dissolving the API in dimethyl sulfoxide (DMSO). Finer particles were produced when increasing the pressure (500 nm at 90 bar, 260 nm at 150 bar) or the flow rate of CO₂ (480 nm at 1.6 ml/min, 360 nm at 2.4 ml/min). Larger particles were obtained when increasing the temperature (400 nm at 34 °C, 600 nm at 46 °C) or the initial 5FU concentration (310 nm at 20 mg/ml, 520 nm at 100 mg/ml). Cabezas et al. [352] employed a GAS process to micronize 5FU and also to impregnate polymer scaffolds with it. Poly (D, L-lactide) (PLA) and poly (D, L-lactide-co-glycolide) (PLGA) were used as encapsulating agents with a polymer: drug ratio of 4. A relatively high drug loading (17%) was achieved with PLGA at 40 °C and 180 bar. To the best of our knowledge, loading of HNT with an API using the GAS process has not been reported.

In this work, a version of the GAS technique using subcritical carbon dioxide is used to load 5FU onto HNT. The work examines the role of the drug/nanocarrier mass ratio. Drug loadings for chemically unmodified clay nanotubes are higher than those achieved by conventional methods. A quantitative distinction is made between tightly bound and loosely attached drug molecules. Drug release in aqueous media is pH-dependent and can be used in developing pH-triggered delivery systems.

4.1 REMOVAL OF CO-PRECIPTATES

During the GAS process, the 5FU was loaded onto the nanoclay by adsorption. Previous studies, using kaolinite as a carrier, have shown that drug molecules adsorb mostly through hydrogen bonding and van der Waals interactions [353]. HNT has the same composition as kaolinite but has a tubular, rather than platy, morphology [354]. Therefore, the same type of forces should be responsible for 5FU adsorption.

The product of the GAS process contains clay nanoparticles with adsorbed drug molecules but also an excess of the co-precipitated drug. In order to discriminate between the loosely attached drug and the adsorbed API, the product was gently washed with MeOH. The detail of the procedure is explained in Chapter 3, Section 3.1.3. The outcome is presented in Figure. 4.1. The mass fraction of the loosely attached drug, α_F ($=m_{free}/m_{tot}$, where m_{free} is the mass of the free drug and m_{tot} is the total mass of drug used), rapidly decreased as the mass ratio R ($=m_{HNT}/m_{tot}$, where m_{HNT} is the mass of

the HNT) increased. It is worth mentioning here that 5FU has low solubility in acetone compared to other organic solvents. Washing with acetone did not show variation in α_F and L compared to MeOH (Appendix A, Section A2), confirming that washing conditions did not affect the encapsulates and favoured only removal of loosely attached and co-precipitate drugs.

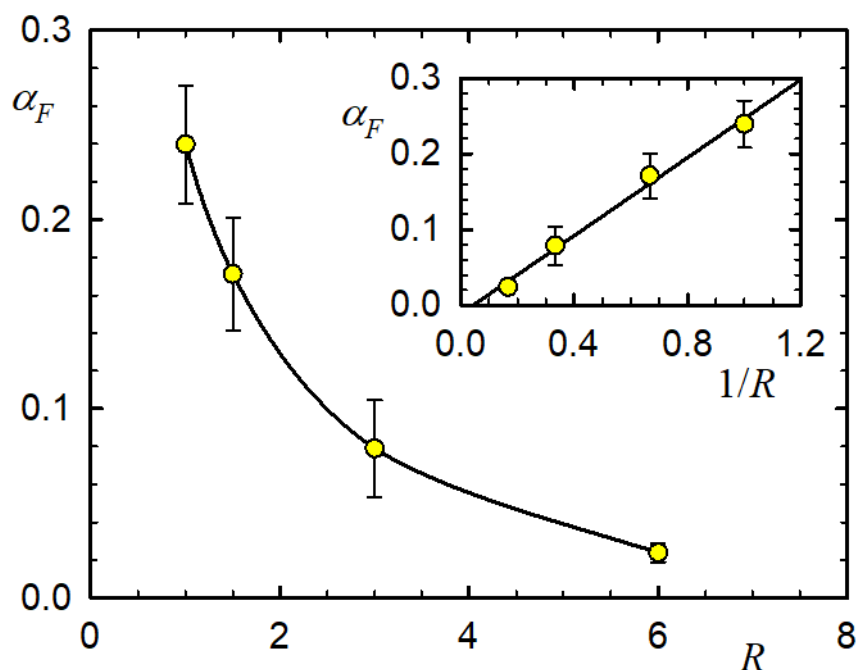


Figure 4.1 Mass fraction of free drug α_F ($=m_{\text{free}}/m_{\text{tot}}$, where m_{free} is the mass of the free drug and m_{tot} is the total mass of drug used), washed with MeOH as a function of the mass ratio R ($=m_{\text{HNT}}/m_{\text{tot}}$, where m_{HNT} is the mass of the HNT). Inset: Mass fraction of free drug as a function of the inverse mass ratio.

Since the total amount of 5FU, m_{tot} , used in each test was kept constant, the amount of drug firmly adsorbed on the nanoclay carrier should increase with the number of adsorption sites on the HNT surface and, therefore, with the mass ratio R . At the same time the excess amount of 5FU removable by MeOH washing, m_{free} , should decrease as clearly seen in Figure. 4.1. Drug molecules can either adsorb or co-precipitate as free drug, and the total amount is constant. The amount of free drug decreases with R because of the increasing amount of adsorbing nanoclay. The inverse of R can be interpreted as an increasing amount of drug at a fixed amount of nanoclay. In that case, the mass fraction of free drug, α_F , would be expected to increase proportionally to $1/R$ – as illustrated in the inset in Figure. 4.1.

The fact that the loosely attached drug was washed away for all levels of R studied is consistent with the fact that an excessive amount of drug was used.

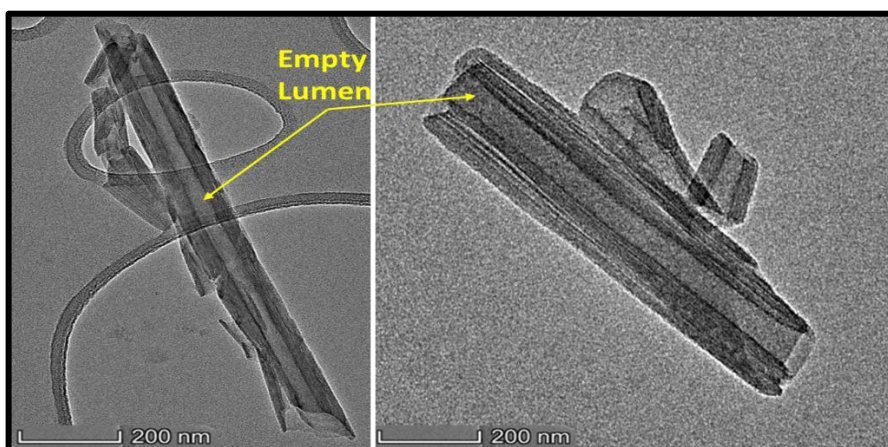
The molecular volume of 5FU, V_m , can be reliably estimated by using its molecular mass, M , and density, ρ , as $V_m = M / (N_A \cdot \rho)$. The area per molecule is then estimated as $V_m^{2/3} = 28 \text{ \AA}^2$. Given that the specific surface area of HNT is $64 \text{ m}^2/\text{g}$ (BET method), we estimate that sub-monolayer adsorption of fluorouracil could only happen at mass ratios larger than $R=20$.

We emphasize the washing step as it discriminates between loosely and tightly attached drug molecules. It is sometimes ignored (Table (2.9), Chapter 2, Section (2.5.1)) in the literature, and reported drug loadings can be misleading. In general, the loosely attached drug does not have to be removed from the product as it may be useful in providing a burst release ahead of a slower release of the adsorbed drug.

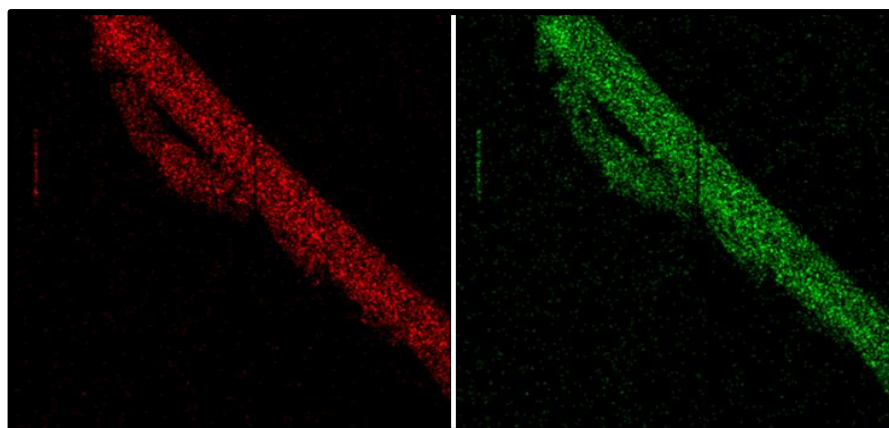
4.2 PARTICLE CHARACTERIZATION

4.2.1 ELECTRON MICROSCOPY

The tubular morphology of the nanoclay was confirmed by SEM/TEM imaging (Figure 4.2 a, b) performed based on the procedure in Chapter 3, Section 3.1.4. The inner space (lumen) is clearly seen in the TEM image (Figure 4.2 a). The external diameter ranges from 50 nm to 80 nm and the lumen width is 10 nm to 15 nm. The length of the nanotubes varies between about 500 nm and 2 μm . These numbers are consistent with published reports [346, 355]. Because nanoclays have alternating silica and alumina sheets rolled together, the elemental mapping in Figure 4.2 b showed an even distribution of silica and alumina through the entire volume.

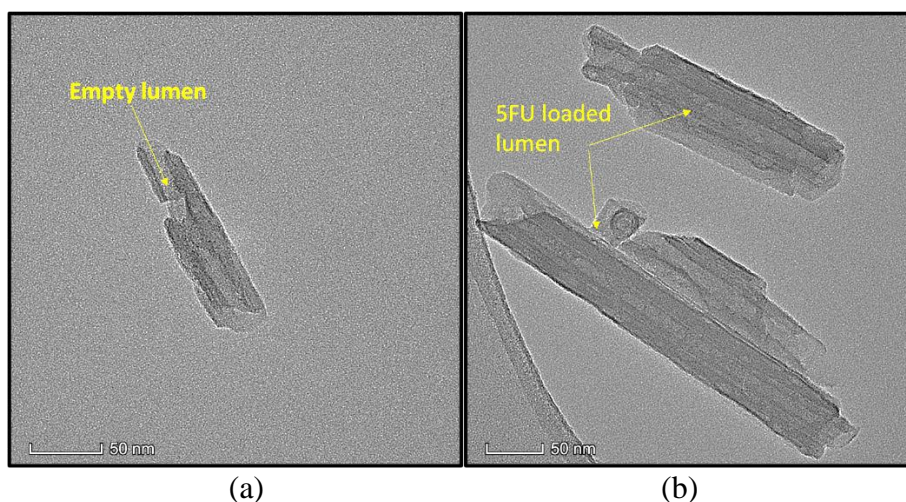


(a)



(b)

Figure 4.2 TEM images of HNT. (a) Pristine, and (b) Elemental mapping of Alumina (red) and Silica (green) from TEM-EDS analysis.



(a)

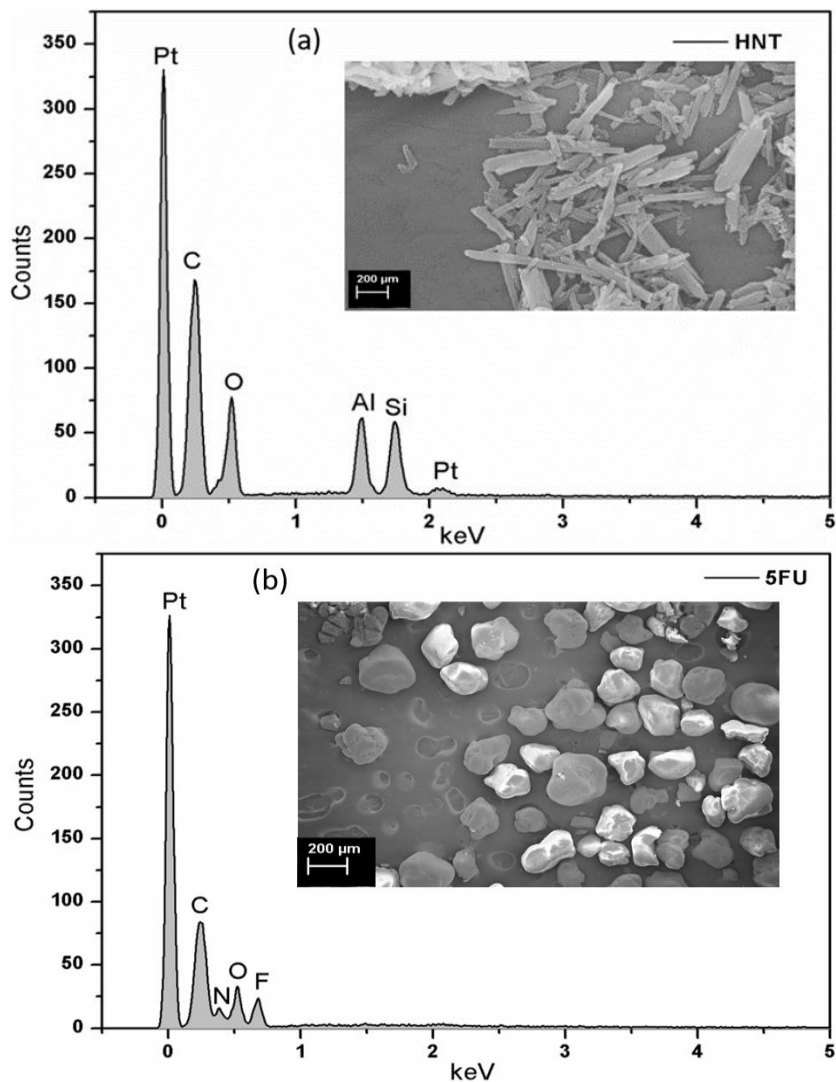
(b)

Figure 4.3 TEM images of HNT (a) Pristine, (b) after loading 5FU.

It should be noted that images of individual clay nanotubes can be misleading as the quality and behaviour of the total clay sample is determined by the average characteristics.

The adsorption of 5FU was confirmed from Figure 4.3 (a,b) and using Energy Dispersive X-Ray Spectroscopy (EDS) – Figure 4.4 (a-c) . The peaks of aluminum (1.5 keV), silicon (1.7 keV), and oxygen (0.5 keV) are the signature of the nanoclay (Figure. 4.4a), reflecting its chemical composition. Similarly, the peaks of nitrogen (0.4 keV) and fluorine (0.7 keV) reveal the elements present in the 5FU molecule (Figure 4.4b). The carbon and platinum peaks are due to the carbon mounting tape and the thin platinum coating needed for correct SEM imaging.

All peaks specific to the clay material and the drug were reliably detected in the precipitation product of the GAS process – Figure 4.4c. Thus, EDS imaging of the washed product confirmed that a certain amount of 5FU was adsorbed (firmly attached) onto the nanoclay carrier.



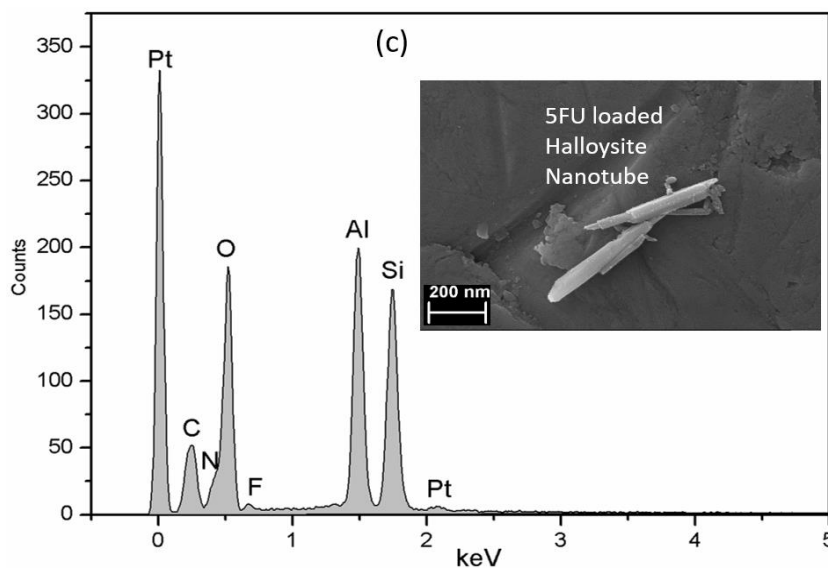


Figure 4.4 EDS spectra and SEM images of (a) pristine HNT, (b) 5FU, and (c) HNT loaded with 5FU.

4.2.2 FTIR SPECTROSCOPY

The IR spectra of the individual materials as well as the washed product of the GAS process are presented in Figure 4.5. The procedure can be found in Chapter 3, Section 3.1.5. The characteristic wavenumbers of the chemical bonds encountered in HNT are 910 cm^{-1} (Al–OH bending [356]), 1007 cm^{-1} (Si–O–Si symmetric stretching [356]), 1634 cm^{-1} (water deformation), 1724 cm^{-1} (stretching vibration of water interlayer), 3623 cm^{-1} and 3698 cm^{-1} (O–H stretching of inner hydroxyls [357]). For 5FU we have 795 cm^{-1} (surface hydroxyl translation [356]), 1242 cm^{-1} (C–F stretching), 1630 cm^{-1} (C=O stretching) and 3000 cm^{-1} (N–H stretching).

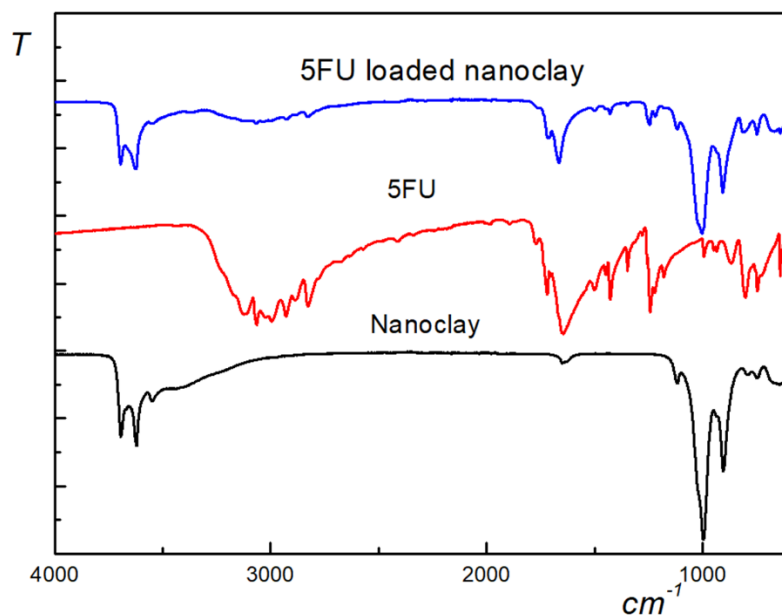


Figure 4.5 FTIR spectra of pristine HNT, 5FU, and 5FU loaded HNT.

The presence of NH, carbonyl, and C–F stretching bands at 3000, 1630, and 1242 cm^{-1} in the GAS-treated nanoclay confirms the presence of 5FU in the product. The absorbance peaks of HNT at 910 cm^{-1} and 1007 cm^{-1} , corresponding to Al–OH and in-plane Si–O–Si stretching, retained their position after the GAS process. Similarly, the inner OH stretching vibration corresponding to peaks at 3623 cm^{-1} and 3698 cm^{-1} is also retained, indicating that the chemical signature of nanoclay is not altered during the GAS process. It has been previously shown that the structure of 5-fluorouracil is unaffected by the temperature and pressure conditions used during the GAS process [351]. Thus, FTIR results confirm the loading of the HNT with 5FU and the physical nature of the adsorption.

4.2.3 BET SURFACE AREA

The HNT is exposed to a subcritical CO_2 environment during the GAS loading process. The effect of CO_2 on the physiochemical characteristics are still unknown. In order to examine the impact of CO_2 on the HNT, the BET surface area was measured using the procedure described in Chapter 3, Section 3.5.3, and the adsorption isotherm is presented in Figure 4.6. As mentioned previously, the specific surface area of HNT is 64 m^2/g . Treating with subcritical CO_2 did not significantly change the surface area (60.05 m^2/g).

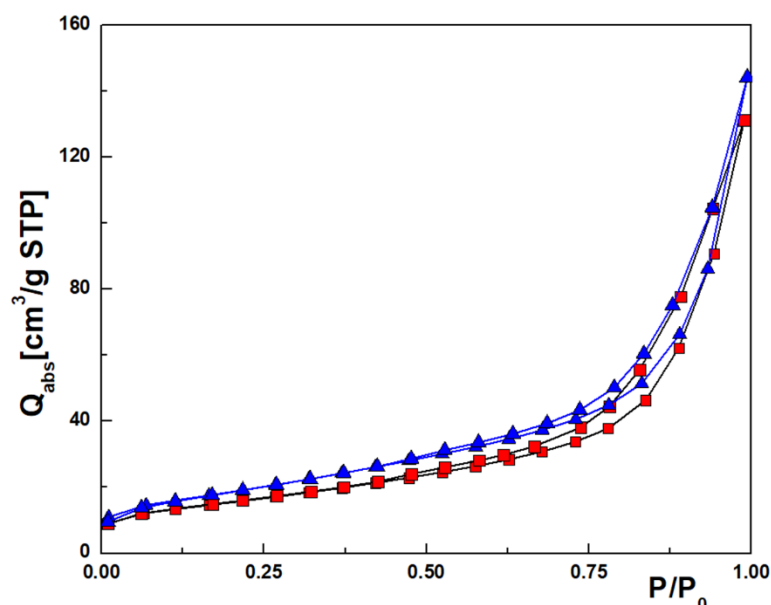
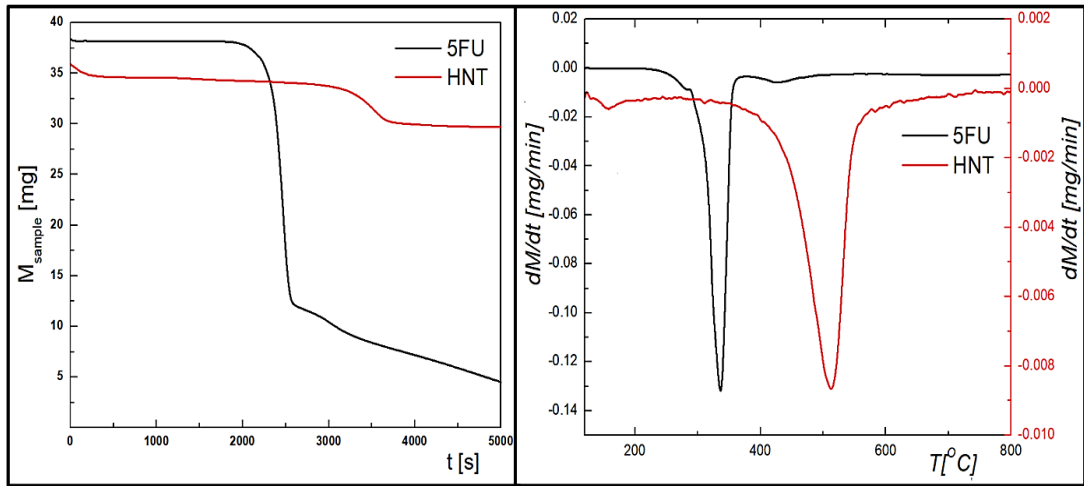


Figure 4.6 Nitrogen adsorption-desorption isotherm of pristine HNT (blue) and GAS processed HNT (red).

HNT belongs to the kaolinite group which has an affinity towards polar molecules such as MeOH, N-methyl formamide, and urea [358]. It is often found in hydrate forms $\text{Al}_2\text{Si}_2\text{O}_5(\text{OH})_4 \cdot 2\text{H}_2\text{O}$ and requires chemical hydrophobization to improve the adsorption of hydrophobic molecules (APIs). CO_2 being non-polar has little affinity for the hydrated HNT surfaces and thereby does not react as water has low solubility for CO_2 [23]. These characteristics are beneficial in pharmaceutical applications as the structural integrity and purity of HNT is preserved after the DG process.

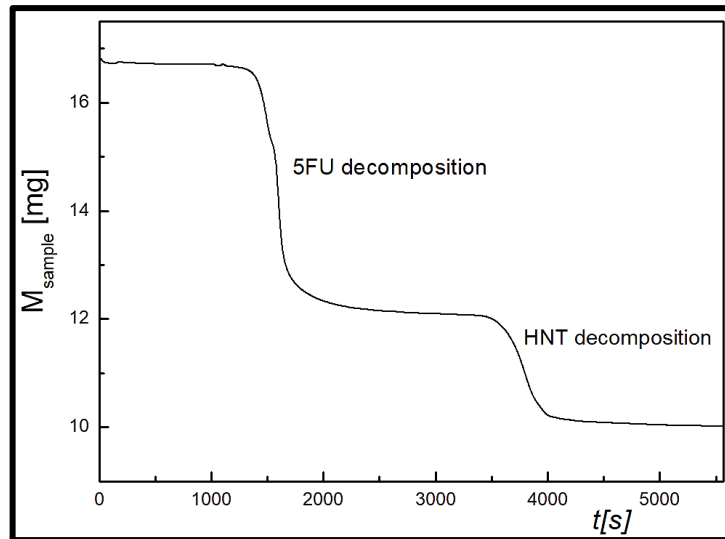
4.2.4 DRUG LOADING

The drug loading was estimated using Thermogravimetric analysis detailed in Chapter 3, Section 3.1.6. Before estimating the drug loading, the individual decomposition temperature of 5FU and HNT was measured, and TGA curves are presented in Figure 4.7 (a,b). The individual decomposition temperature of 5FU and HNT was found to be at 340°C and 510°C , respectively (Figure 4.7b) and further used in the loading estimation. A representative image of the mass loss curve is shown in Figure 4.7c.



(a)

(b)



(c)

Figure 4.7 (a) TGA mass loss curve of sample (M_{sample}) of pristine HNT and 5FU, (b) first derivative of M_{sample} of pristine HNT and 5FU, and (c) Mass loss curve of 5FU encapsulated HNT.

The drug loading achieved with the GAS process is shown in Figure 4.8a as a function of the mass ratio R . The loading, L , gradually decreases with the mass ratio of HNT to 5FU. Since this precipitation product was washed with MeOH, the loading represents the adsorbed (tightly attached) drug molecules. Treatment of the HNT (on its own) with the GAS process did not change its properties and, in particular, its specific surface area (64 m²/g BET method). If adsorption is the loading mechanism and it is in turn decided by the inherent properties of the drug-carrier combination, then one may expect the loading to be independent of the mass ratio R . However, the fraction of the adsorbed drug is significant, and this causes a depletion of the solution to which the

HNT is exposed. The adsorption, Γ (in g 5FU per g HNT), is a linear function of the concentration of the free drug in the solution, C_F – inset in Figure 4.8a. This trend is similar to the Henry adsorption isotherm which applies under equilibrium conditions and explains the decrease in loading with the mass ratio R .

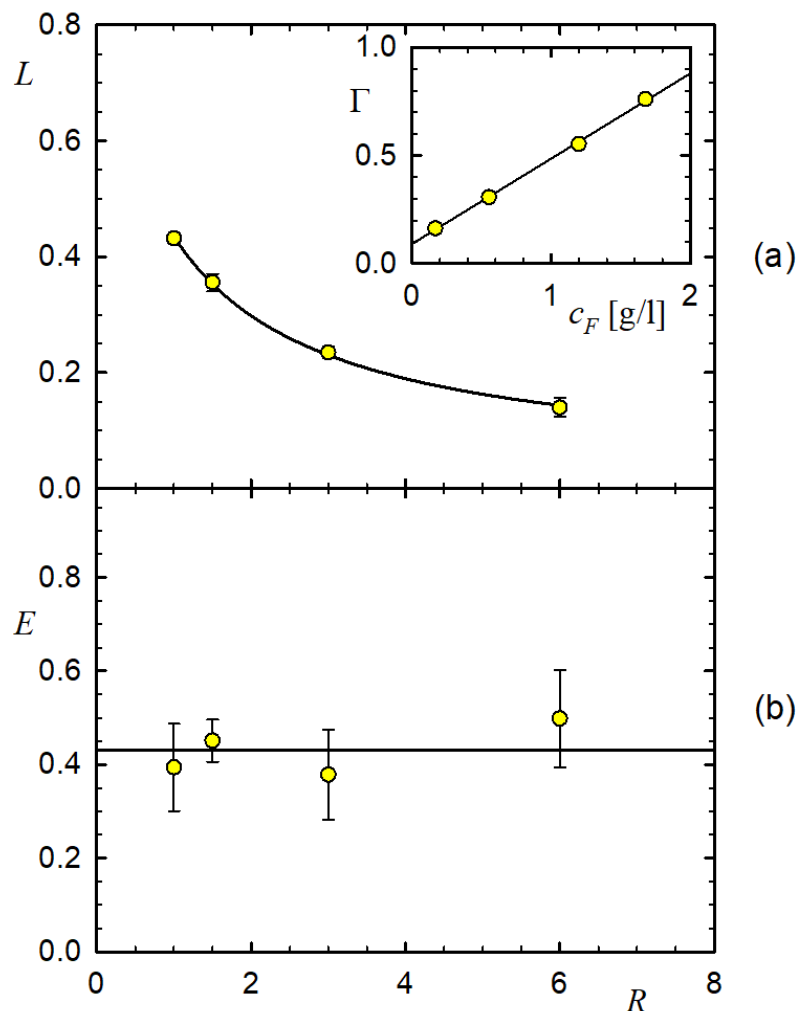
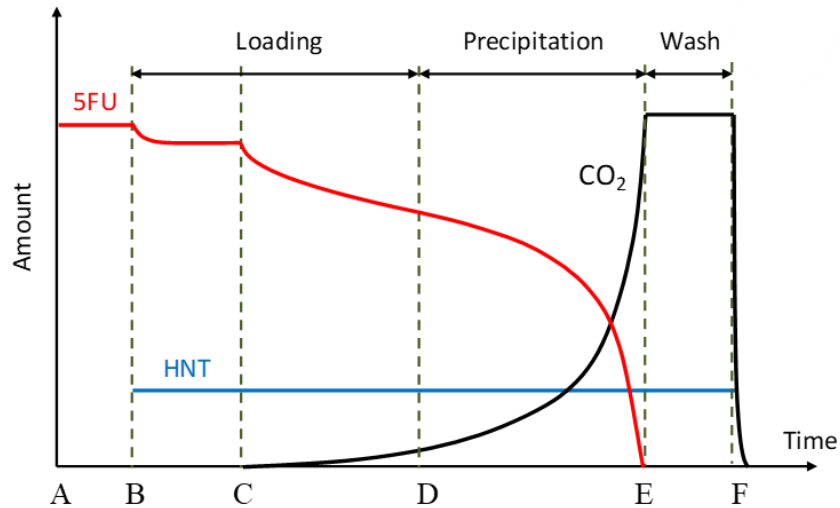
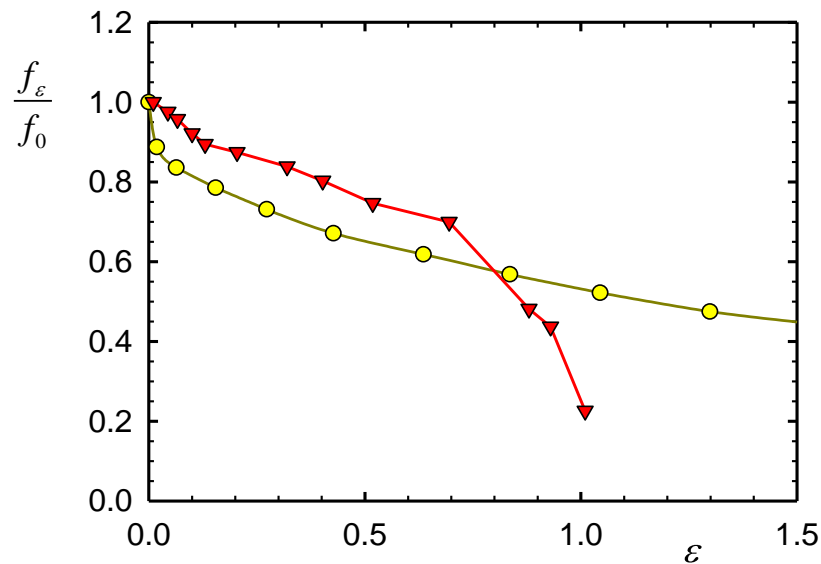


Figure 4.8 (a) Drug loading, L (mass of loaded drug relative to total mass of the precipitation product), of the washed product as a function of the mass ratio R ($=m_{\text{HNT}}/m_{\text{tot}}$, where m_{HNT} is the mass of the HNT and m_{tot} is the total mass of drug used). Inset: Adsorption, Γ (mass of drug adsorbed per mass HNT), as a function of the solution concentration of free drug, c_F [g/L]. (b) Encapsulating efficiency, E (mass of loaded drug relative to the total mass of drug used), as a function of the mass ratio R .

The encapsulation efficiency, E , as a function of the ratio R , is shown in Figure 4.8b. It is practically constant and averages at about 40%. This value could be improved given that an excess amount of drug was used in these experiments – see Equation (3.2) in Chapter 3, Section 3.1.6. *Rao et al.* [346] achieved a better efficiency ($E = 52\%$) of encapsulating 5FU, but their system was chemically different – the HNT were embedded in a hydrogel.



(a)



(b)

Figure 4.9 (a) Qualitative sketch of the stages of the GAS process: amount of dissolved drug (5FU) – red line, amount of HNT – blue line, and amount of carbon dioxide – black line. See text for description. (b) ○ – Decrease of the relative viscosity, μ_ε/μ_0 (μ_ε is viscosity at expansion ε and μ_0 is viscosity at expansion $\varepsilon=0$), and ▽ – Decrease of the relative polarity parameter, $\pi_\varepsilon^*/\pi_0^*$, (π_ε^* is the polarity parameter at expansion ε

and π_0^* is the polarity parameter at expansion $\varepsilon=0$), as functions of the volumetric expansion.

The observations made in this work lead to the schematic representation of the GAS process shown in Figure 4.9a. In stage AB a drug solution of fixed concentration is prepared (red line in Figure 4.9a). When the nanoclay is added at point B, some of the drug molecules adsorb on the clay surface. This creates a small depletion in the amount of 5FU in the dispersion. Stage BC is a spontaneous “mechanical” loading as practiced by many authors (e.g. [347]). The GAS process starts in earnest at point C when carbon dioxide is pumped into the system at a constant mass rate (the amount of CO₂ is shown with a black line in Figure 4.9a). In the stage CD, solvent expansion is small, but the increase in diffusivity is significant, and that increases the overall loading as drug molecules reach previously unavailable adsorption sites. As expansion proceeds beyond point D, there is a further decrease in viscosity, but the dominant effect is a decline in the solvent power and the ensuing precipitation of the drug. At point E, the precipitation is complete, and the precipitate is then back washed with carbon dioxide (EF). At point F, the system is depressurized, and the product is retrieved as a dry powder.

At all times, the amount of HNT is constant (blue line in Figure 4.9a) and the nanotubes are uniformly dispersed throughout the liquid by the incoming CO₂ flux. This scheme shows that the diminished viscosity of the gas-expanded solvent (stage CD) is the main source of improvement to the mobility of the drug molecules and therefore the final drug loading.

In support of the above scheme, we compare the viscosity (representing molecular mobility) and the polarity (representing solvent power) of the CO₂-expanded MeOH in Figure 4.9b. The data from *Sih et al.* [359] show a sharp decrease in viscosity, μ , at very low volumetric expansion, ε (the viscosity dependence was normalized by the viscosity value at $\varepsilon=0$). Since diffusivity is inversely proportional to viscosity (Stokes-Einstein equation) a significant improvement in diffusive transport is achieved in the CD stage of the GAS process. The polarity of the gas-expanded liquid determines the solubility of the 5FU, and we discuss the Kamlet-Taft parameters (α , β , and π^*) reported by *Wyatt et al.* [360] for MeOH -CO₂ mixtures. The hydrogen bond donor parameter ($\alpha = 0.98 \pm 0.03$) and the hydrogen bond acceptor parameter ($\beta = 0.74 \pm 0.05$) are practically constant over the whole range of CO₂ mole fractions [360]. Most of the decrease in polarity of the gas-expanded solvent with increasing CO₂ concentration is

due to decreasing polarity parameter, π^* . Its value (normalized by the value of the pure MeOH) is graphed in Figure 4.9b. Initially, π^* decreases slower than the viscosity and this corresponds to stage CD in Figure 4.9a. With further expansion (beyond $\varepsilon=0.7$), the polarity parameter decreases at a faster rate than viscosity, and precipitation becomes dominant. This corresponds to stage DE in Figure 4.9a.

The maximum drug loading achieved in the present work using the GAS process is about 45% (Figure 4.8a). Such a high loading has not been matched by other methods used to load 5FU onto various carriers. For instance: 8% on montmorillonite [361], 7% on porous clay heterostructures [362] and 22% on kaolinite [363], when using the soaking method, and 12% to 28% on chitosan via solvent evaporation emulsification [345]. Higher loading of 5FU (55%) has been reported [363] but the kaolinite carrier was methoxylated prior to drug loading. Thus, we conclude that the GAS process provides the highest drug loading onto natural (chemically unaltered) HNT.

4.3 IN-VITRO DRUG RELEASE

The benefit of a drug carrier is largely determined by the type of drug release that it enables. The gastrointestinal tract has a varying pH from about 1.2 in the stomach to 7.4 in the intestine. It is therefore of key interest to examine drug release at these two pH values. The time-release profiles of 5FU from the washed product, in simulated gastric and intestinal pH, are presented in Figure 4.10.

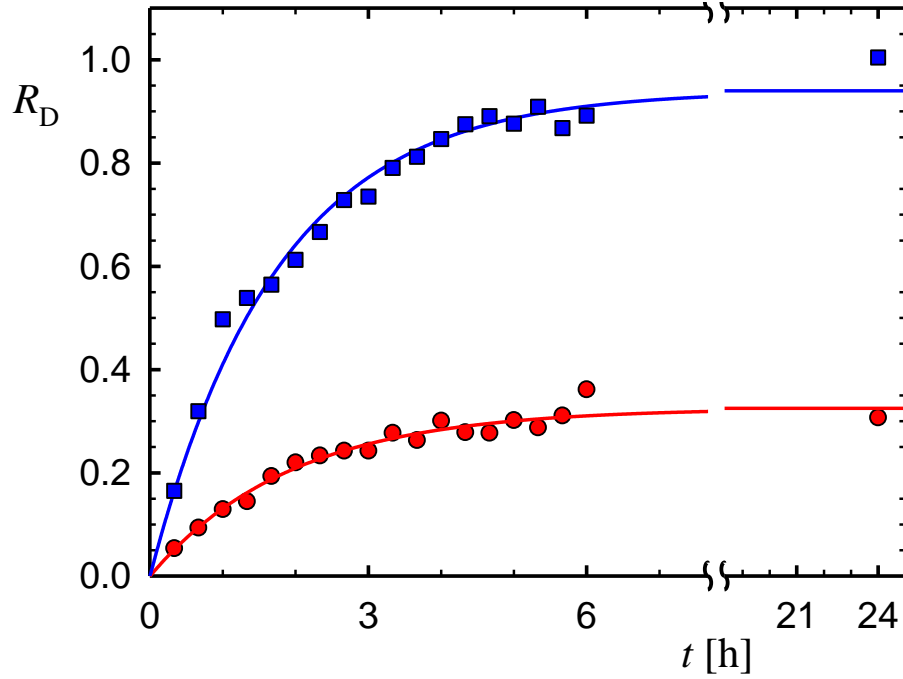
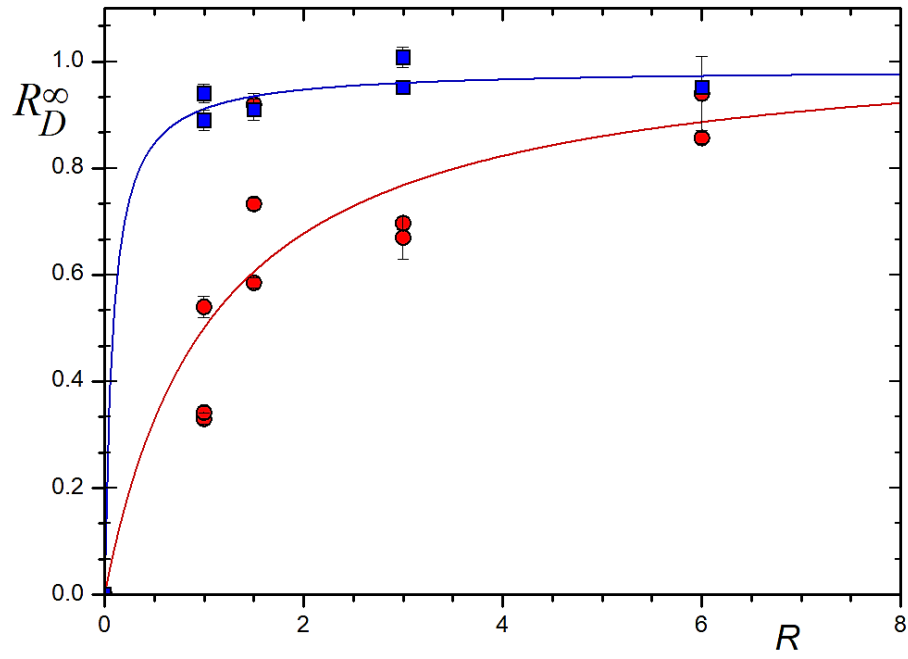


Figure 4.10 Cumulative drug release, R_D (ratio of amount of drug released and total amount of loaded drug), from the 5FU-loaded HNT in aqueous environment as a function of time at pH = 7.4 (\square) and pH = 1.2 (\circ).

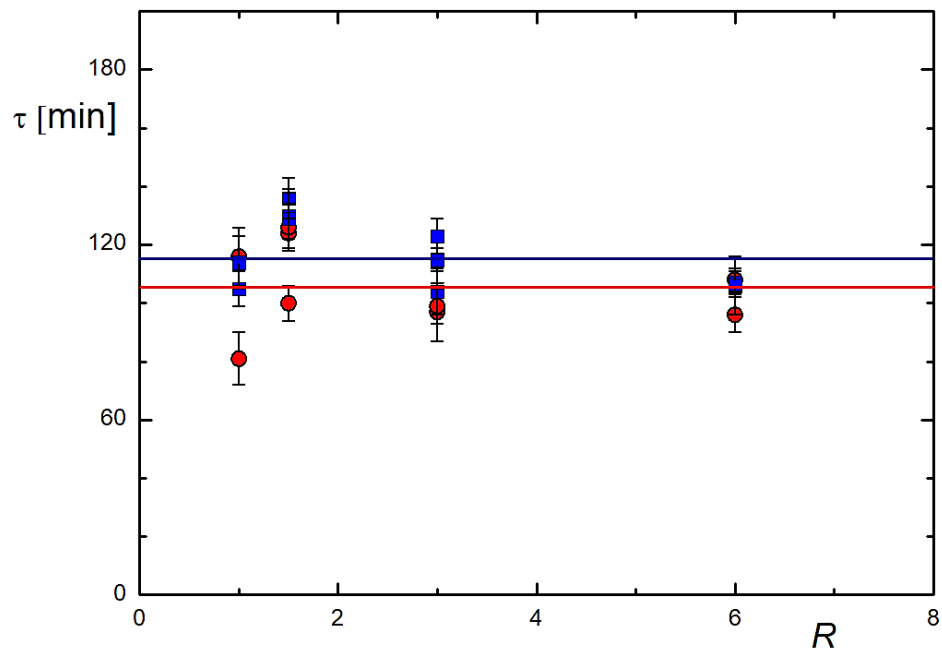
The release at intestinal pH is faster (about 80% after the first 3 h) and practically complete ($R_D = 1$) after 24 h. At gastric pH the release is slower (25% after the first 3 h) and even after 24 h remains just under 30%. The release profiles shown in Figure 4.10 are well described with an exponential increase of R_D in time using only two parameters R_D^∞ and τ (R_D^∞ is R_D at $t=\infty$, i.e. maximum release, and τ is characteristic time and more precisely the point of $R_D = 1 - e^{-1} \approx 0.63$):

$$R_D = R_D^\infty \left(1 - e^{-t/\tau} \right) \quad (4.1)$$

Equation (4.1) describes the first-order kinetics of formation which is encountered in many practical situations including the release of a drug-loaded onto a carrier [364]. The variations in the maximum release, R_D^∞ , and characteristic time, τ , with the mass ratio, R , are graphed in Figure. 4.11.



(a)



(b)

Figure 4.11 Dependence of (a) the final cumulative release, R_D^∞ at pH =7.4 (\square) and pH = 1.2 (\circ), and (b) characteristic time, τ [min], at pH = 7.4 (\square) and pH = 1.2 (\circ), on the mass ratio R ($=m_{\text{HNT}}/m_{\text{tot}}$, where m_{HNT} is the mass of the HNT and m_{tot} is the total mass of drug used).

At the higher pH, the maximum release is consistently high (above 90%). At the lower pH, it steadily increases with R (Figure 4.11a). The characteristic time does not depend on pH (Figure 4.11b) and, within the scatter, remains approximately constant at a value of about 2 h. The characteristic time of 5FU release is in the range between gastric half emptying (1.2 ± 0.3) h and time to reach the colon (2.8 ± 1.5) h [365]. Therefore, the 5FU-HNT drug-carrier combination is relevant to the development of oral delivery systems.

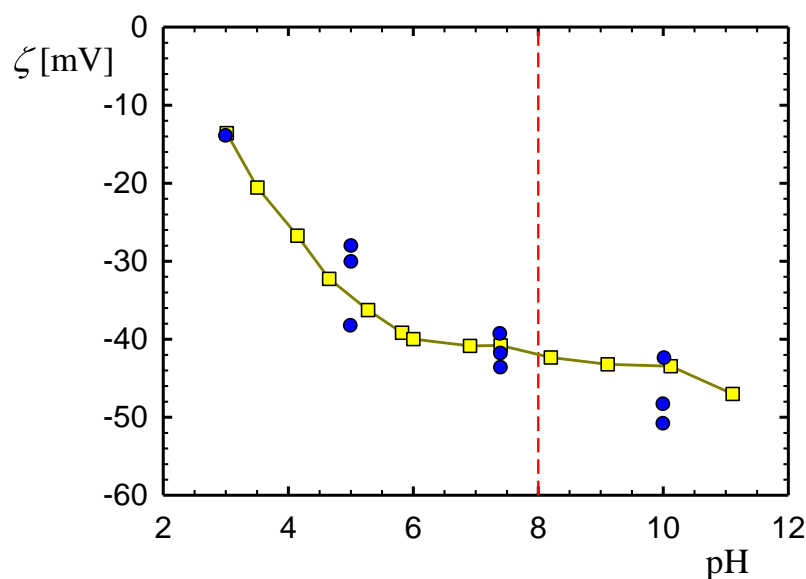


Figure 4.12 Electrokinetic potential, ζ [mV], of HNT dispersed in water (\square – Ref.[366]; \bullet – this work) as a function of pH of the aqueous solution. The pK of 5FU is shown with a vertical dashed line.

The clear similarity between the two release profiles shown in Figure 4.10 together with the fact that the characteristic time did not change with pH or mass ratio (Figure 4.11b) suggest that the mechanism of desorption and dissolution is the same. Given that 5FU is a water-soluble drug (11.1 g/L [367]) we attribute the complete release at $\text{pH} = 7.4$ (Figure. 4.12) to electrostatic interactions between the 5FU molecules and the HNT. At $\text{pH} = 2$ the zeta potential of HNT particles is practically zero [366] – Figure 4.12. Therefore, the HNT surface carries a very small surface charge, i.e. it is practically neutral. A similar situation is observed with both silica [368] (the outer surface of the HNT is mostly composed of silica) and with kaolinite [369] (a clay very similar to HNT). At the higher $\text{pH} = 7.4$, the zeta potential is -40 mV (Figure 4.12) and therefore the HNT surface is charged negatively.

The 5FU behaves like a weak acid [370], i.e. at low pH the molecule is neutral and at high pH it deprotonates to become an anion. The pK of 5FU is 8.0 [371] and therefore at pH=7.4 a significant portion of the molecules (exactly 50% at pK) should be in their anionic form. A recent NMR study concluded that 5FU is completely ionized at physiological conditions [370]. At such pH, the electrostatic repulsion between the negatively charged HNT surface and the 5FU anions ensures complete drug release. At acidic pH, electrostatic interactions are insignificant and drug release is only partial. The dissolution profiles of pure 5-fluorouracil at gastric and colonic pH are very similar. The release, R_D , after 6 h is 98% at pH=7.4 and 88% at pH=1.2. This difference reflects the increased ionization of the 5FU molecule under alkaline conditions [372]. Both profiles match well the dissolution profile of HNT-5FU at pH=7.4 (Figure 4.10). This confirms the dominant role of electrostatic interactions in the formation of the 5FU-HNT complex.

4.4 CONCLUSION

The Gas Antisolvent Process (GAS) can be used to load HNT with 5FU. For chemically untreated nanotubes, the drug loading (43%) is better than what was achieved by other methods. The fraction of tightly attached drug (via physical adsorption) is compared quantitatively to the fraction of loosely attached (co-precipitated) drug. The later can be used to deliver a burst release. The mass ratio between clay nanotubes and 5FU affects both the drug loading due to adsorption and the ratio of loose to tightly attached drug molecules. The GAS process proceeds in two key stages and during the first one improved mass transport creates an increased drug loading. Overall, it is a one-pot green process with a low consumption of solvent and high-purity of the precipitated product. The strongly attached drug is released completely at physiological pH but only up to 30% in acidic pH. In both cases the release follows first-order kinetics with a characteristic time of about 2 hours. The differences are attributed to variations in electrostatic interactions with pH. We have described an efficient method to load HNT with 5FU in a single step. The mass ratio R can be used to tailor the amounts of readily available and sustainably released drugs.

CHAPTER 5

**Atomized rapid injection for solvent
extraction (ARISE)- micronization
and spray characterization of ES100
polymer**

RESULTS AND DISCUSSIONS

The ARISE process set-up and the experimental procedures are described in Chapter 3, Sections (3.2.1, and 3.2.2). Eudragit S100 (ES100) exhibits high solubility in ethanol and hence ethanol was used as the solvent in the current work. The products obtained from different concentrations and volumes of injection were further analyzed for their physicochemical properties as detailed in the following sections.

5.1 POLYMER SOLUTION VISCOSITY

ES100 is a long chain copolymer with a molecular weight of 135,000 g/mol [373]. The details of its properties can be found in Chapter 2, Section (2.4). Before using the ARISE process, the workable range of ES100 concentration was determined by measuring the viscosities (η) at various solution concentrations as described in Chapter 3, Section 3.2.4. The change in viscosity is shown in Figure 5.1. The viscosity of the polymer solutions depended on polymer structure, molecular weight, and solvent properties. The concentration dependency of viscosity in polymer solution is generally expressed by Huggin's and Martin's equation. The specific viscosity (η_{sp}), and measured viscosity (η) are related by the K_H -Huggins parameter, and ES100 concentration (C_{ES100}) as described by Equation 5.1 and 5.2 for low and high concentration solution respectively [374, 375].

$$\frac{\eta_{sp}}{C_{ES100}} = \eta[1 + K_H \eta C_{ES100}] \quad (5.1)$$

$$\frac{\eta_{sp}}{C_{ES100}} = \eta[1 + K_H \eta C_{ES100} + (K_H \eta C_{ES100})^2 / 2!] \quad (5.2)$$

From Eq 5.1, it can be noticed that the increase in viscosity is linearly proportional to the C_{ES100} at low concentrations. In accordance with this, the measured viscosity changed almost linearly within a 3-10 wt% concentration (Figure 5.1). When the polymer concentration was increased, the long-chain interactions and entanglements between polymer matrix increased, increasing the viscosity. Hence the Huggin's equation was modified as shown in Eq 5.2 [376]. Following this, the viscosity (η) doubled, deviating from linearity, from 98 mPa.s to 200 mPa.s at 20 wt% concentration (Figure 5.1). Based on these observations, handling of solutions greater than 15 wt% restricted

the flowability of the solution and, hence, 15 wt% was set as the concentration limit in the current work.

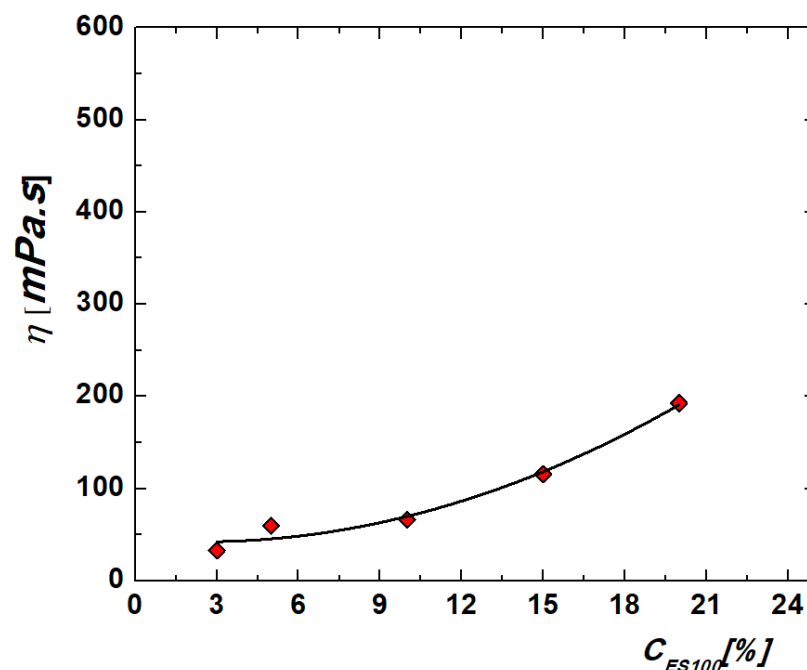


Figure 5.1 Graph of change in viscosity (η) with the concentration of ES100. Shear rate (μ_s at 0.02 s^{-1} , 25° C , solution in Ethanol).

5.2 PRODUCT RECOVERY

The experimental conditions and the product recovery of micronized ES100 are shown in Table 5.1. The recovery was calculated as the ratio of the mass of the sample retrieved from the ARISE process to the input mass of the sample used. Recovery of about 85 % was achieved with a 10 ml injection volume for all the concentrations. The average recovery decreased with decreasing injection volume. The reason is attributed to the fluffy and low-density particles produced which were difficult to manually recover due to electrostatic adhesion to the inner walls of the precipitation chamber. At a low volume of injection, the ratio between the anti-solvent (dense CO_2) and injection volume is high, causing a high degree of supersaturation (explained in Section 5.3)[377]. The supersaturation effects atomization of fine particles. Principally, the objective of nano-formulation using the ARISE process is to produce fine and fluffy particles, hence the concomitant drawback of the recovery due to electrostatic adhesion can be overcome by neutralizing the precipitation chamber through designing fixtures with a grounding (earthing) system in further scale-up processing.

In a similar instance, about 90 % of product recovery was reported by *Sih et al.* [110] while micronizing ES100 from acetone using the ARISE technique. These identical results confirm the reproducibility of the ARISE process. The ARISE is a batch process involving the semi-continuous injection of feed solution to precipitate fine particles. The product recovery (above 50 %) and process reproducibility qualify the ARISE as an economically viable process for industrial applications.

Table 5.1 Experimental conditions for the micronization of ES100 using ARISE process.

Expt. No.	Material		Solvent		Operating Conditions		Product Recovery (%)
	C _{ES100} (%)	Mass (g)	Name	Volume (ml)	Operating pressure (bar)	Temperature (°C)	
1	3	0.25	EtOH	10	110	25	89.04
2		0.123		5	110	25	89.27
3		0.05		2	110	25	62.05
4	5	0.40		10	110	25	98.53
5		0.23		5	110	25	76.35
6		0.08		2	110	25	67.91
7	10	0.80		10	110	25	87.18
8		0.40		5	110	25	66.01
9		0.16		2	110	25	62.03
10	15	1.2		10	110	25	65.32
11		0.63		5	110	25	76.98
12		0.24		2	110	25	32.23
B01	3	0.250	EtOH	10	110	40	--
B02	5	0.440		10	110	40	--

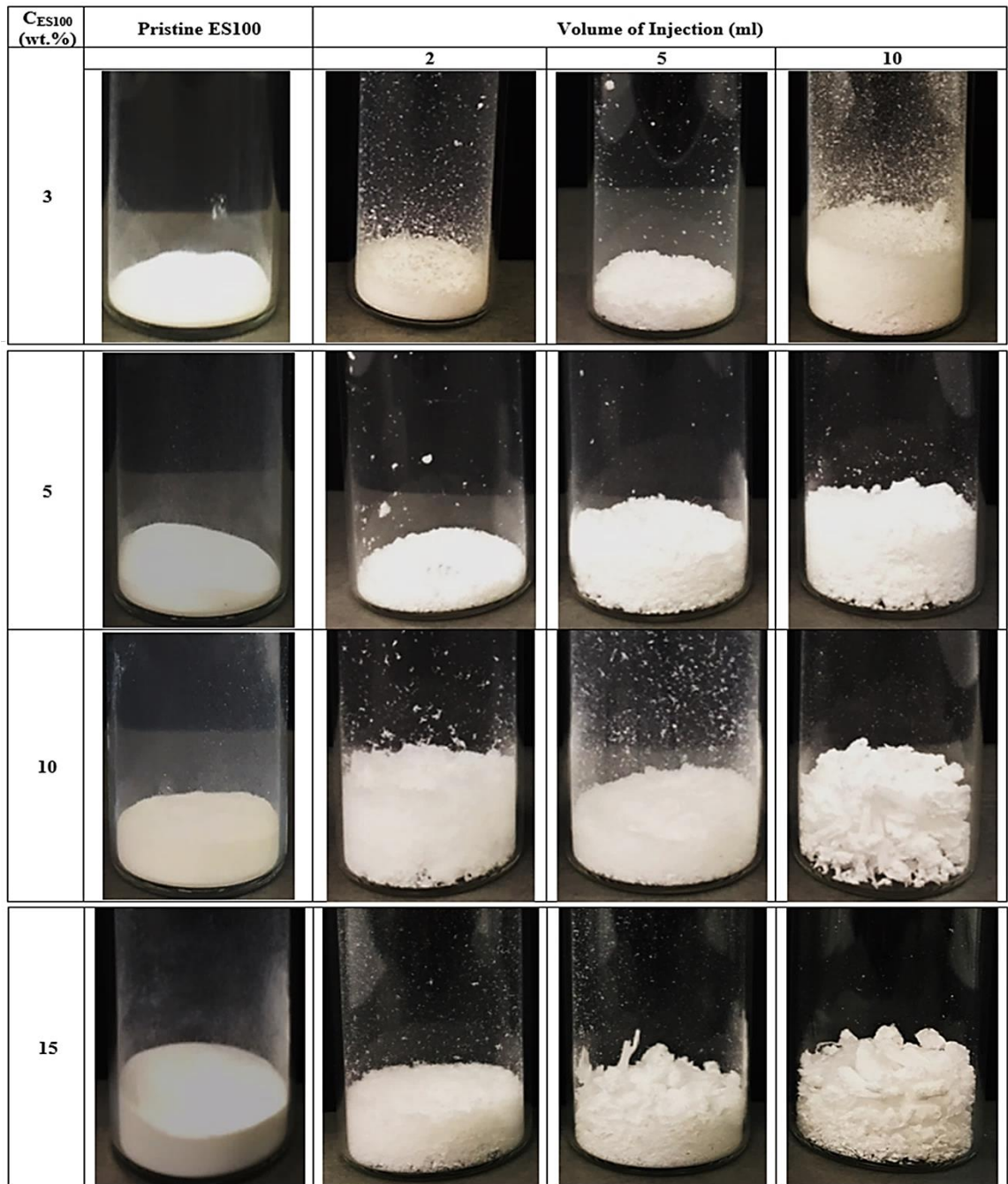


Figure 5.2 Samples of pristine ES100 and the ARISE processed ES100 from different injection volumes for different ES100 concentration.

5.3 BULK DENSITY

The samples retrieved from the ARISE process are shown in Figure 5.2. The bulk density is measured based on the procedures described in Chapter 3, Section 3.2.5. The density of unprocessed ES100 is 0.831-0.852 g/ml (Chapter 2, Section 2.4). Figure 5.3 shows the variation in bulk density of ES100 after ARISE processing. The process produced highly micronized and fluffy powders with a bulk density much lower than

the raw material. The bulk density varied linearly with the concentration of the feed solution. Injection volumes of 5ml and 10 ml produced a similarly dense product at a low ES100 concentration. A minimum density of 0.02 g/ml was measured with a 5ml feed solution of 3% ES100. The bulk density was 50% more with a 10ml feed solution for the same concentration. With an increase in concentration from 3% to 15%, the density of the product increased over 6-fold. However, the bulk density was not measurable for 2ml feed volume due to issues in handling (electrostatic adhesion), especially at low ES100 concentration. It is to be noted that the ARISE process produced particles with a bulk density as low as 0.02g/ml, which is 97.5% lower than the density of pristine ES100. The reduction in density favours aerodynamic size and suitability for oral and nasal drug delivery systems.

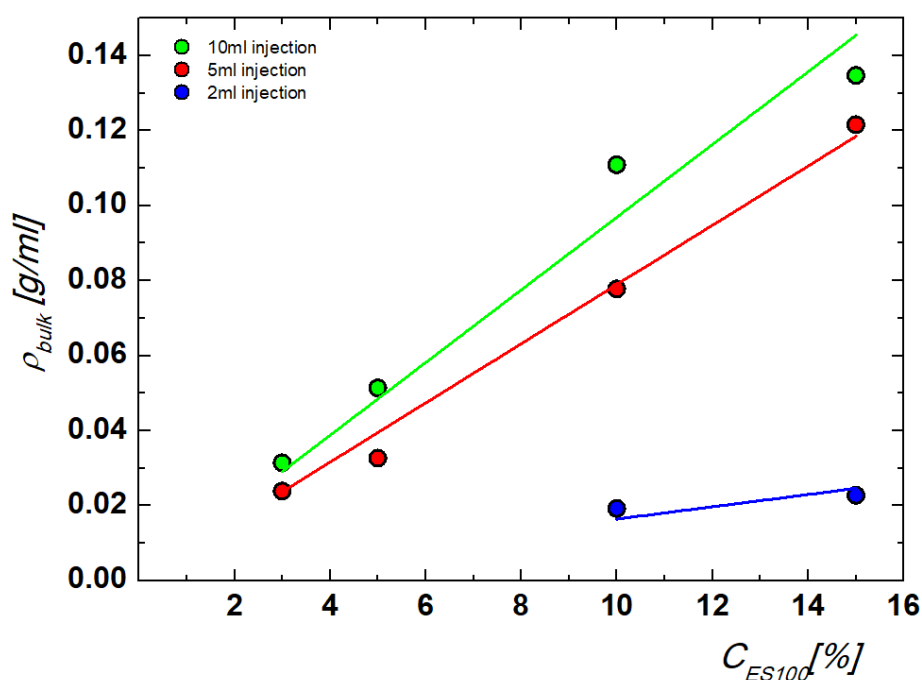


Figure 5.3 Bulk density (ρ_{bulk}) of product from the ARISE process measured at various ES100 concentration.

The reduction in bulk density through ARISE processing is a distinct feature of the process, making it a preferred method for drug formulation. For a given mass of ES100, the volume occupied by the produce from ARISE is nearly 10 times greater (Figure 5.4). The volume occupied by the uncompacted free particles provides large inter-particle space (or) voids occupying larger volumes for the equal mass of the polymer used. The low bulk density of the particle produced improves the dispersivity

and flowability, which serves as a qualitative indication for application in oral and nasal drug delivery systems [110].

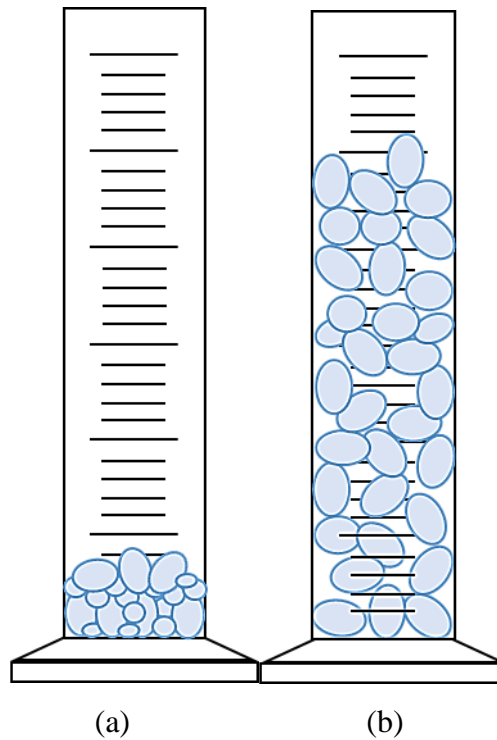


Figure 5.4 Illustration of volumetric particle distribution in (a) solid particles in ES100, (b) freely settled particles from ARISE processed ES100.

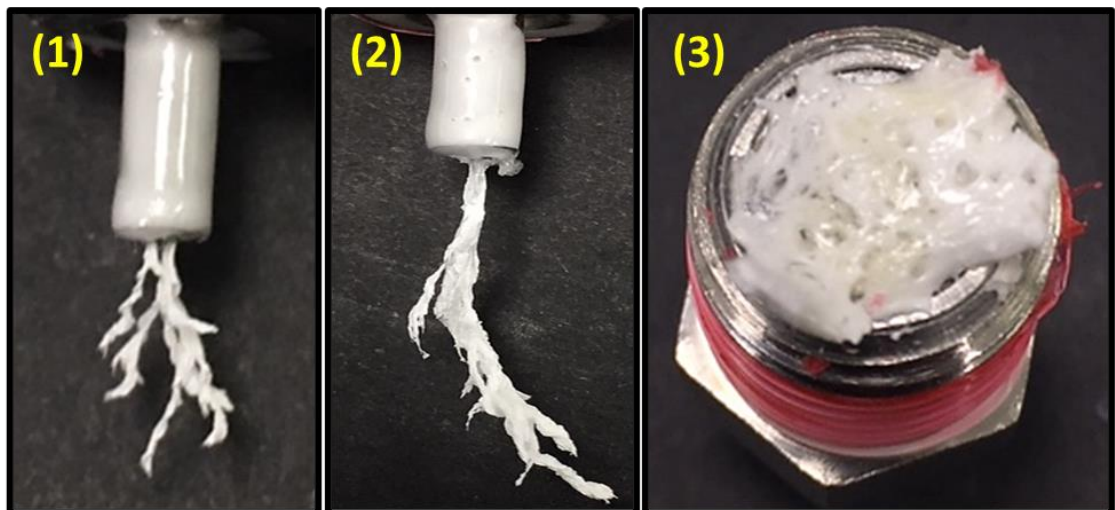


Figure 5.5 Samples of ES100 from the ARISE process performed at 40 °C. (1) Conduit surface in C_{ES100} : 3 %, (2) Conduit surface in C_{ES100} : 5 %, and (3) Bottom filter of the precipitation vessel.

The volume of feed solution affects the bulk density as illustrated in Figure 5.4. The trend in the graph can be explained in terms of the ratio of the concentration of solute in solution to the concentration of anti-solvent. At a low volume of the feed solution,

the anti-solvent concentration is high. As a result, the dissolution rate of the anti-solvent in the primary feed solution increases, causing a rapid reduction in the solubility limit of the solute during expansion. On the contrary, with an increase in the volume of the feed solution, the concentration of feed solution is increased, the ratio of the concentration of solute to the anti-solvent decreases, and the dissolution rate of anti-solvent drops. As a result the bulk density increases as illustrated in Figures 5.4 [378]. The formation of large particle chunks at high volume as seen in Figure 5.2 is consistent with the trend seen in Figure 5.3. However, batch trials (B01, B02) at 40 °C operating temperature did not produce microparticles and ES100 strands were formed near the conduit and filters, as seen in Figure 5.5. The noncompliance of particle formation at elevated temperature compliments the argument on the effect of temperature discussed in Chapter 2, section 2.3.2. Therefore, the operating temperature of 25 °C was fixed for the entire process.

5.4 PARTICLE CHARACTERIZATION

5.4.1 PARTICLE SIZE DISTRIBUTION

The procedural details for measuring the particle morphology and size distribution are described in Chapter 3, Section 3.2.6. The average size of pristine ES100 is 25µm (Figure 5.6. a, b). The particles micronized with the ARISE process have reduced size, less than 5µm, with uniformly spherical morphology. The individual particle with size as low as 124 nm was achieved with the ARISE process, as illustrated in Figures 5.6 to 5.10. The spherically micronized particles cluster together and form aggregates (Figure 5.7(a), 5.8 (a), and 5.9 (a)). Initially, the particle size was measured in different suspension volume, and the results in Figure 5.12(a) showed identical size distribution between all the suspension volume. The observation implies that the concentration used for measurement is ideal for further reliable measurements.

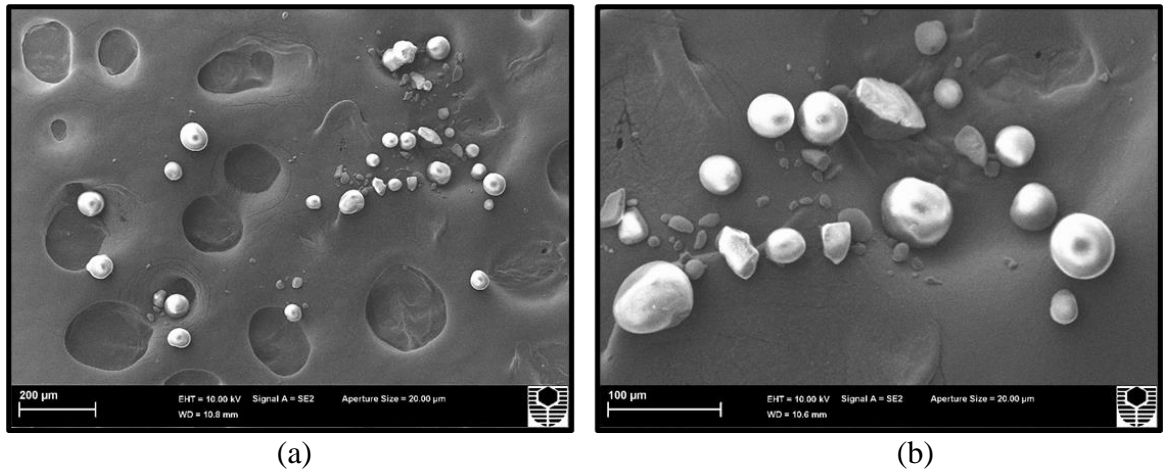


Figure 5.6 SEM micrograph of (a) pristine ES100, (b) magnified view of ES100.

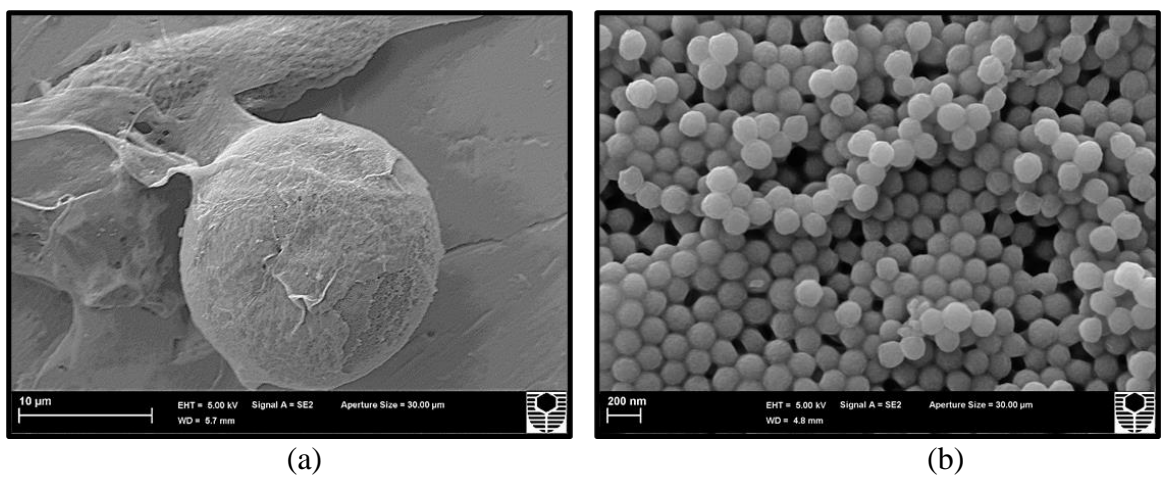


Figure 5.7 SEM micrograph of $C_{ES100}: 3\%$ (a) at low magnification, (b) magnified view.

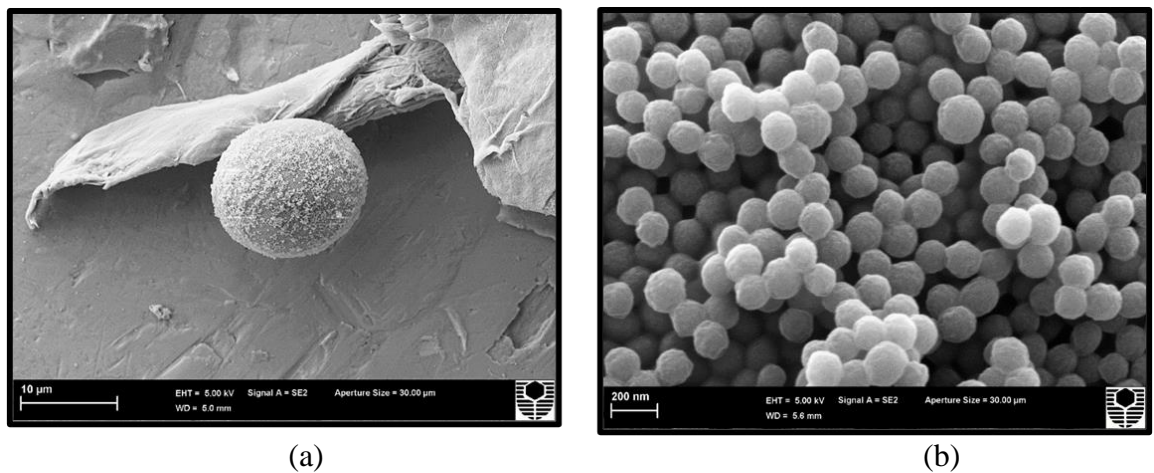
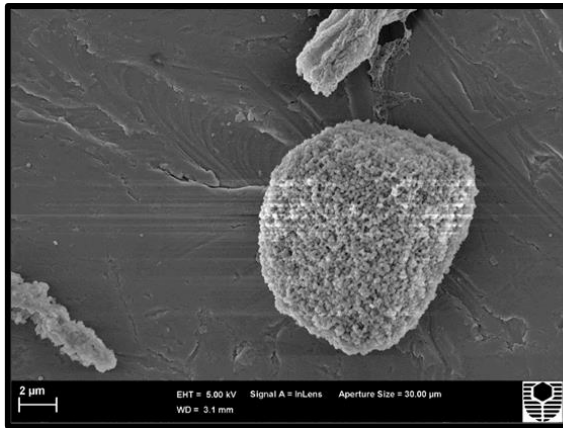
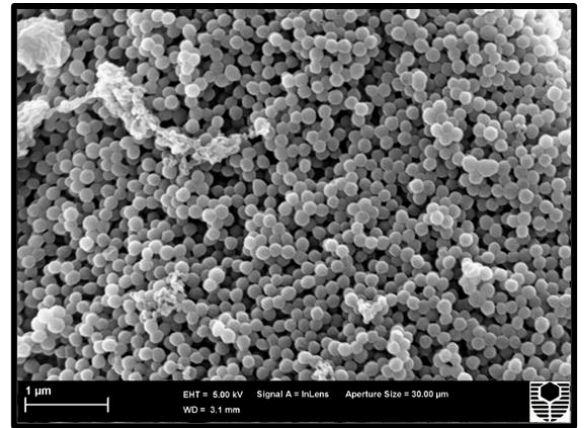


Figure 5.8 SEM micrograph of $C_{ES100}: 5\%$ (a) at low magnification, (b) magnified view.

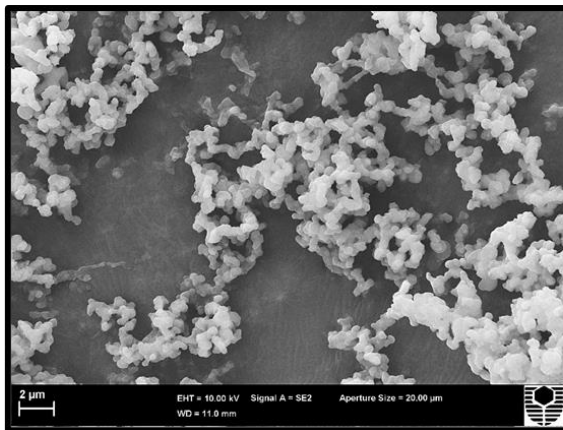


(a)

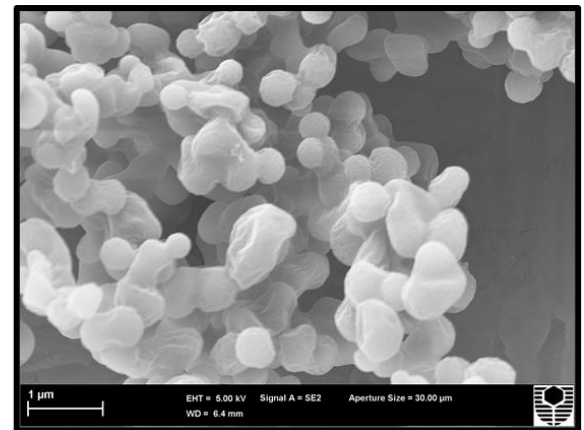


(b)

Figure 5.9 SEM micrograph of C_{ES100} : 10 % (a) at low magnification, (b) magnified view.



(a)



(b)

Figure 5.10 SEM micrograph of C_{ES100} : 15 % (a) at low magnification, (b) magnified view.

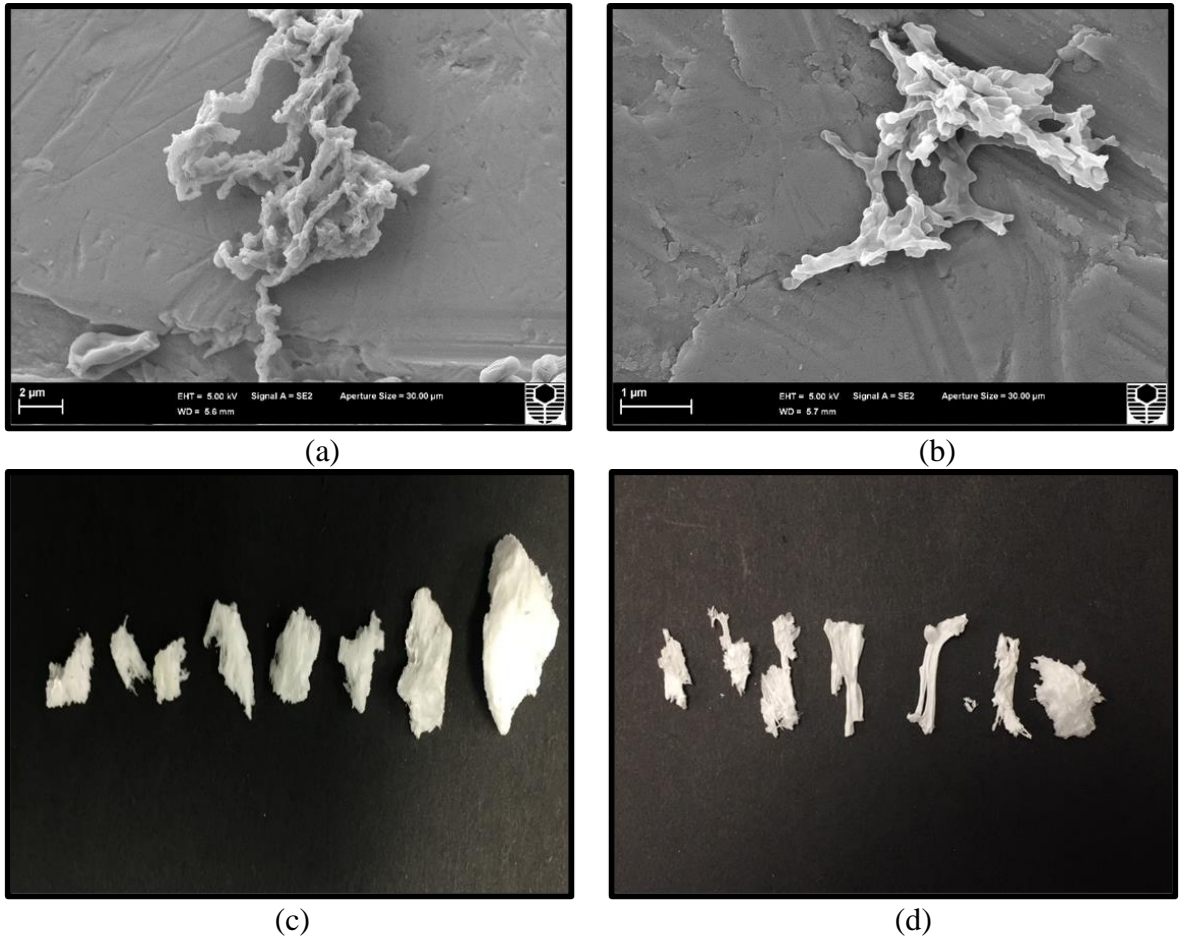
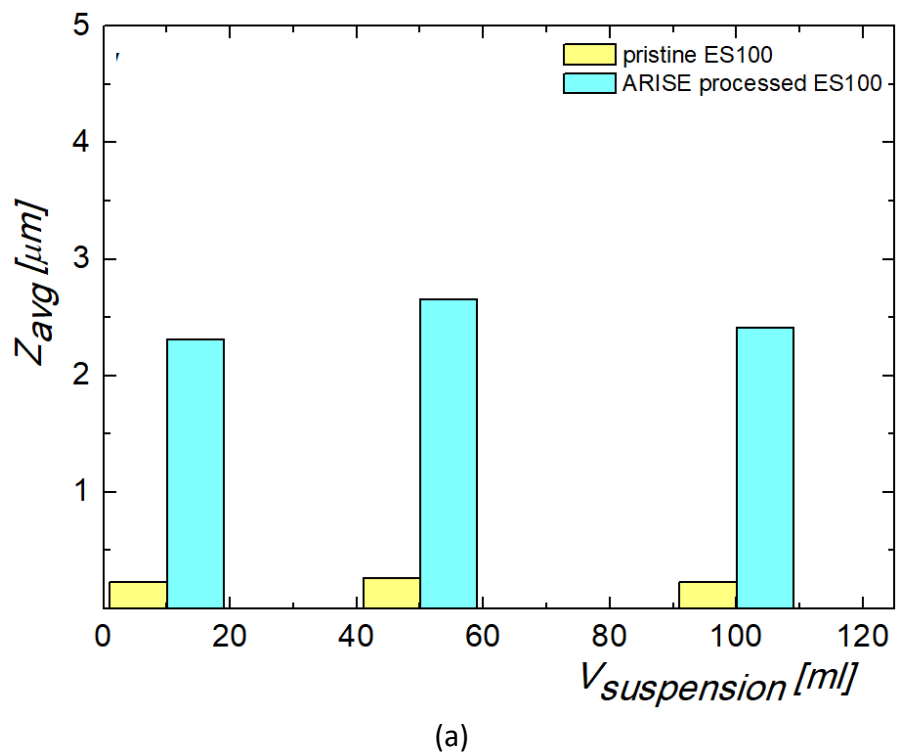
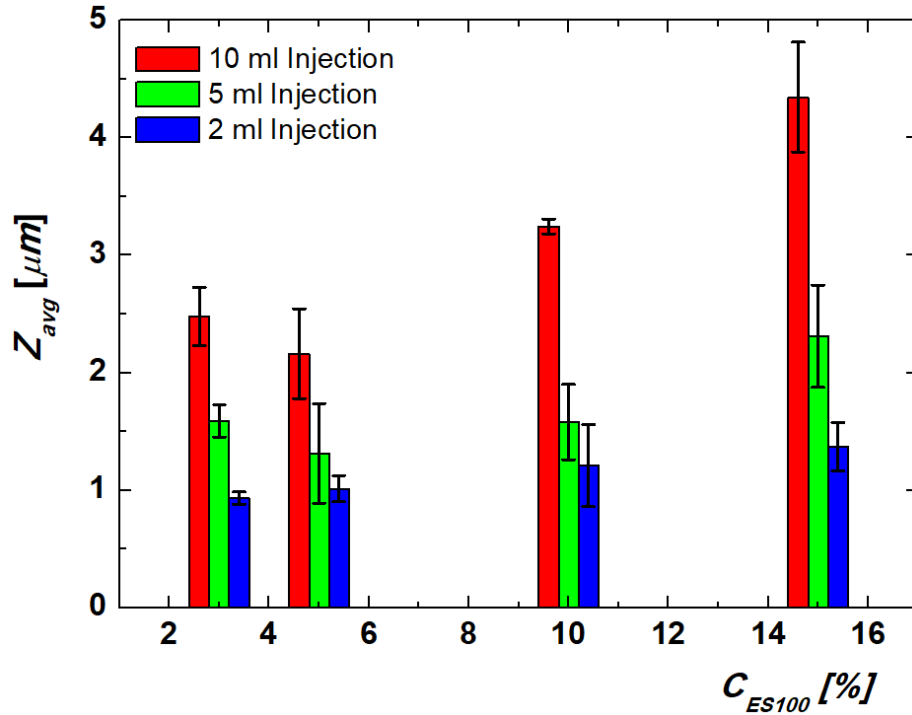


Figure 5.11 (a, b) SEM micrograph of high concentration (10 %, 15 % C_{ES100}), 10 ml injection, (c, d) irregular precipitates from the ARISE at high concentration.





(b)

Figure 5.12 (a) Graph displaying the effect of suspension volume Z_{avg} of ARISE products, (b) Z_{avg} measured for C_{ES100} produced from ARIS. (Error is SD of 3 trials).

In the GXL condition, the precipitation of particulates depends on the supersaturation of the solution which is measured as the ratio between the solute concentration and the saturation concentration[155].

$$S = \frac{y_{mix}}{y_{eq}} \quad (5.3)$$

where y_{mix} is the solute concentration in the solution, and, y_{eq} is the saturation concentration of the solution. The higher the saturation concentration, the greater the micronization rate and the smaller the particle size as explained in Chapter 2, Section (2.3.2.1).

Also, the high viscosity and surface tension in the feed solution does not support atomization. The viscous media inhibits the onset of micronization near the nozzle, shifting the micronization downstream of the jet propagation [379]. In the ARISE process, the presence of CO_2 decreases the viscosity and surface tension of the feed solution, facilitating the rapid mass transfer and micronization [380]. While expanding the feed

solution with anti-solvent at a temperature below the critical point, the mass-transfer rate of CO₂ into the solution is faster than the transfer rate of solvent out of the solution, resulting in the nucleation of the solvent within the solute-rich phase, micronizing porous particles [97, 381, 382].

The flow velocity (U) and Reynolds number (Re) for the pressure-driven flow in the ARISE process can be estimated from the Poiseuille's equation:

$$Q = U.A_c = \frac{\pi.r^4.\Delta P}{8.\mu.L_c} \quad (5.4)$$

where: Q : flow rate of the solution, ΔP : pressure differential at the conduit opening, r : conduit radius, μ : Viscosity of the feed solution, L_c : characteristic length of the conduit, and A_c : cross-sectional area of the conduit.

The Reynold number (Re) and Weber number (We) are defined as:

$$Re = \frac{\rho.U.L_c}{\mu} \quad \text{and} \quad We = \frac{\rho.U^2.L_c}{\sigma} \quad (5.5)$$

where ρ : density of the solution, L_c : characteristic length, and σ : surface tension.

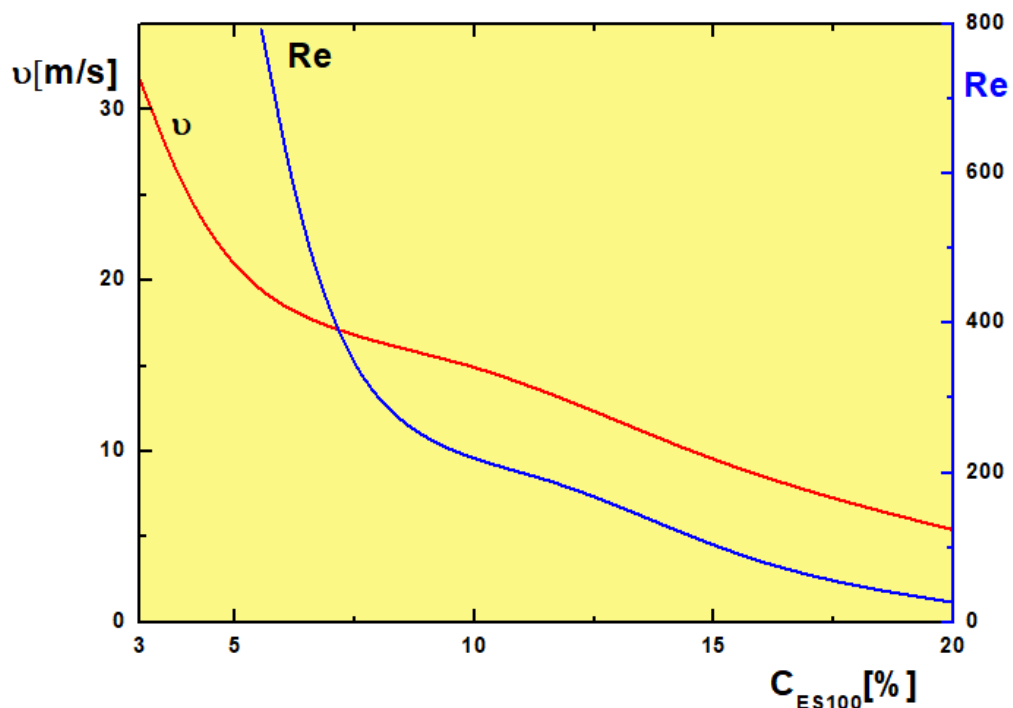


Figure 5.13 An estimate of flow velocity (v) and Reynolds number (Re) of the feed solution inside the conduit at the onset of valve opening.

The estimate from Figure 5.13 shows that Re for all the concentrations remains below 1000, indicating that the flow regime inside the conduit at the operating pressure differential is laminar. The value is 100 folds higher than the SAS process ($Re=16$), indicating complete and rapid mixing of the solution and DG-CO₂ [163]. Theories on atomization predict that complete atomization and hence smaller particles are achievable with an increase in We . The We balances the surface tension force against the inertial force. During the valve opening and consecutively at equilibration time, the surface tension between the solvent phase of the feed solution and the antisolvent (CO₂) reduces. The reduced surface tension results in an increase in We and hence a high degree of atomization [383, 384].

The increase in average particle size with an increase in concentration is due to the increase in viscosity of the solution as illustrated in Figure 5.12 b and Figure 5.1. As the concentration of ES100 increases, the viscosity increases. The increase in viscosity exerts resistance to disintegration along the spray length. The resultant larger surface to volume ratio slows down the particle nucleation rate causing precipitation of chunks of ES100 particles as can be interpreted from Figure 5.11 [383, 385]. Apart from the influence of viscosity, the increase in average particle size can be explained based on solute-solute interaction [386]. When the solute concentration inside the precipitation chamber is high, the chances of interposing of newly formed droplets with the preceding droplets formed during atomization are high, enabling the formation of large particles and aggregates [143, 387]. A similar effect was observed by *Chhouk et al* while micronizing Curcumin-PVP using the SAS process [139].

Despite this variation, the average particle size from all the samples remained below 5 μ m, which is still an 80% decrease from its pristine form, the material thereby deemed potentially suitable for in-vivo drug delivery as mentioned in Chapter 2, Section 2.2. With the decrease in particle size, the surface area to volume ratio increases, facilitating easy absorption of the micronized particle on the cells, thereby improving drug efficacy [388].

Further, looking at the effect of injection volume, the microscopic examinations of the size distributions from Figure 5.7 to 5.10 indicates that the individual particle size varies within the range of 124-450 nm. The average hydrodynamic diameter (Z_{avg}) measured were in the range of 0.5 μ m-1.5 μ m in size with 2ml injection volume and 1.5 μ m-2.25 μ m for 5ml injection volume as illustrated in Figure 5.12 (b). The 10 ml injection volume produced particles of size greater than 2.5 μ m which is due to the change in the

mole fraction of CO₂ with respect to the volume of solution. The concentration of CO₂ is higher at low solution concentration, decreasing the dielectric constant of the solution, promoting the formation of smaller particles. The effect diminishes with an increase in the concentration of feed solution. The increase in Z_{avg} and heterogeneity in 15 % ES100 substantiates the above observation [97].

A comparative study on micronization of ES100 using the GAS and ASES process was performed by *Tandya* [97]. According to the study, homogeneity in precipitation depends on the threshold pressure of the system. Threshold pressure is the pressure at which the API solution supersaturates, and particle precipitation commences. Different API solutions have different pressure limits. ES100 solution in ethanol has a threshold pressure of 55 bar. Unlike in other DG processes, the point of miscibility of the anti-solvent and solvent cannot be determined in the ARISE process since the precipitation chamber is pressurized to the desired pressure before the injection. The pressure chosen in the current process is well above the threshold pressure, ensuring complete precipitation of the solute from the solution.

Further, in the work, *Tandya* mentioned that the particles were irregular in size with increased concentration of the solution. Particle size as high as 300 μm was produced with ethanol as a solvent in the GAS process. Whereas the ASES process produced particles within the range of 100-200nm. Although the experimental parameters were different from the current work, it is worth mentioning that both the GAS and ASES processes failed to produce particles from ethanol solution, at a temperature of 25°C. The ARISE process generated particles smaller than 5 μm for all concentrations of feed solution in near ambient temperature. The reason can be attributed to the rapid mass transfer and a high degree of supersaturation as explained in Chapter 2, Section 2.3.2. The rapid micronization qualifies the ARISE process, as a completely adaptable technique for processing thermosensitive API's and excipients.

5.4.2 FTIR CHARACTERIZATION

The FTIR spectra of the pristine and the ARISE processed ES100 was acquired based on the procedure described in Chapter 3, Section 3.1.5. The spectra are shown in Figure 5.14. The characteristic peak positions of the ES100 are tabulated in Table 5.2.

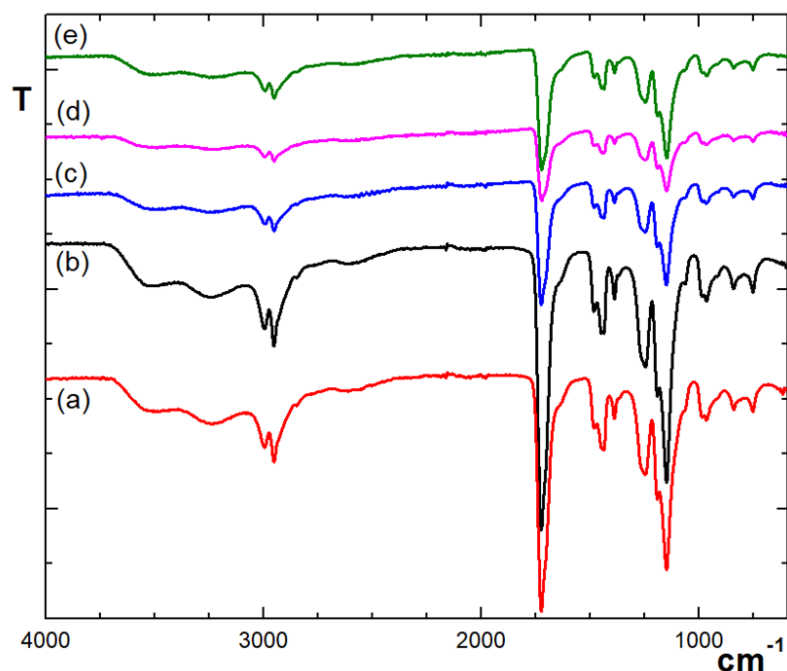


Figure 5.14 FTIR spectrum of (a) pristine ES100, (b) C_{ES100} : 3%, (c) C_{ES100} : 5%, (d) C_{ES100} : 10%, and (e) C_{ES100} : 15%, processed from ARISE.

Table 5.2 FTIR spectrum peak identification [389, 390].

Wavelength (cm^{-1})	Chemical bond and assignment
3000	O-H carboxylic acid
2998	O-CH ₃ stretching
1200-1500	CH ₃ - bending
1720	C=O carboxylic acid
3100-3500	C-H stretching alkene
1520	C=O ester

The characteristic peaks of ES100 at 3000 cm^{-1} , 1750 cm^{-1} and, 1200 cm^{-1} remained intact before and after the ARISE processing, confirming that the process did not induce any chemical modification on the polymer. The chemical characteristics of the polymer are preserved, validating that the ARISE process does not provide a harsh environment and maintains the purity and chemical integrity of the samples produced.

5.5 SPRAY ATOMIZATION

5.5.1 SPRAY PROFILE ANALYSIS

ARISE process takes place inside a stainless-steel pressure vessel under the conditions described in Chapter 3, Section 3.2.2. As mentioned before, rapid atomization occurs at the instance of valve opening, and the micronized product is obtained. In order to visualize the spray pattern and estimate the time taken for micronization, a simulated set-up was made, as described in Chapter 3, Section 3.2.3. Since it was not practically feasible to create a GXL environment in this case, the experiments were conducted in conditions with air and water as media. Air and water have densities of 1.2 kg/m^3 and 997 kg/m^3 respectively at 25°C . Carbon dioxide has a density of 777 kg/m^3 and 833 kg/m^3 at 80 bar and 110 bar respectively. These are the operating pressures before and after rapid valve opening in the ARISE process. Conducting spray simulations in both air and water media covers the GXL region within the spectrum. Moreover, *Uchida et al.* [391] observed that the particle micronization behaviour described in gas and liquid phases coincides with the behaviour in a supercritical phase, meaning that the current study on micronization in air and water phase holds valid for partially understanding particle formation in the supercritical and GXL regimes. The spray patterns were analyzed at a region 20 mm below the conduit opening as shown in Figure 5.15. The region was chosen based on the actual placement of the conduit inside the pressure vessel in the ARISE. The spray simulation was conducted for an injection volume of 2ml and C_{ES100} : 3,5,10 and 15%, respectively.

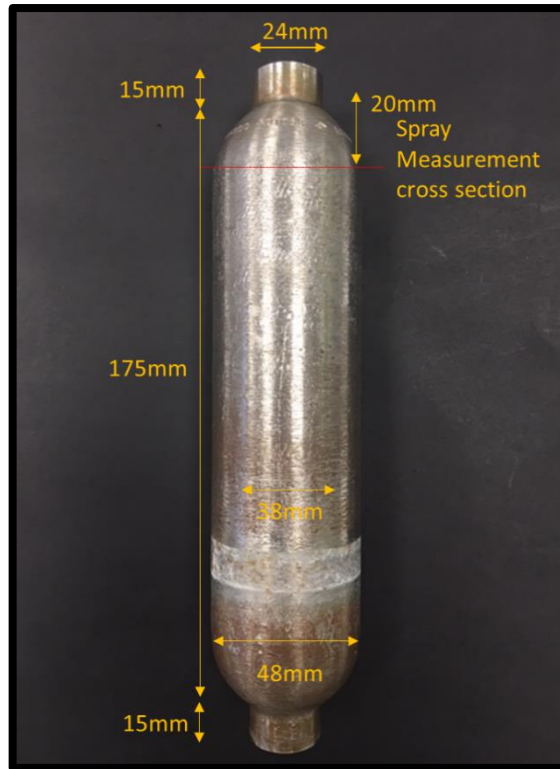
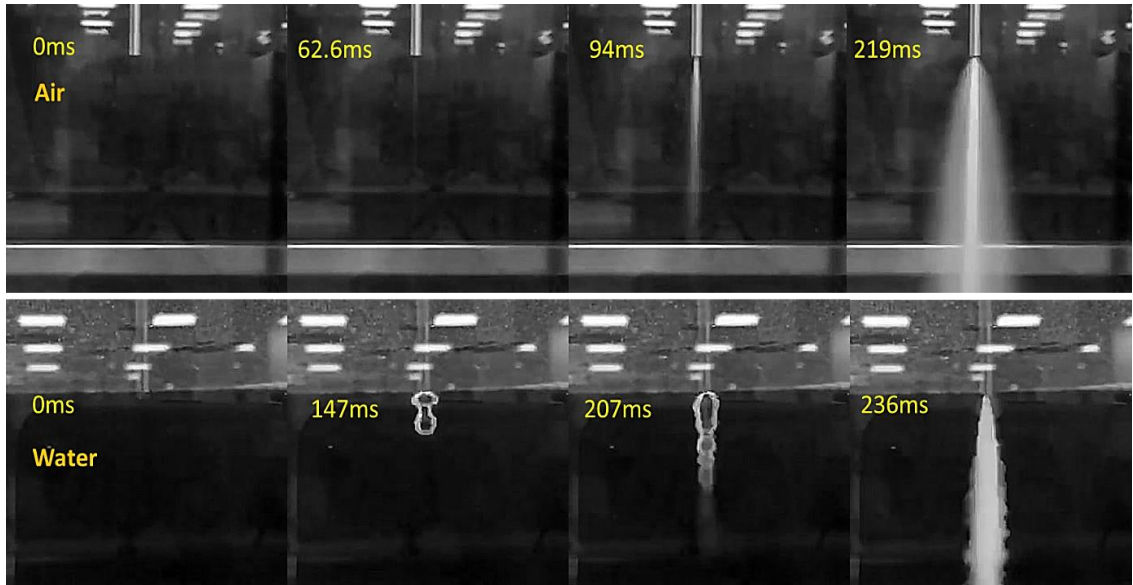


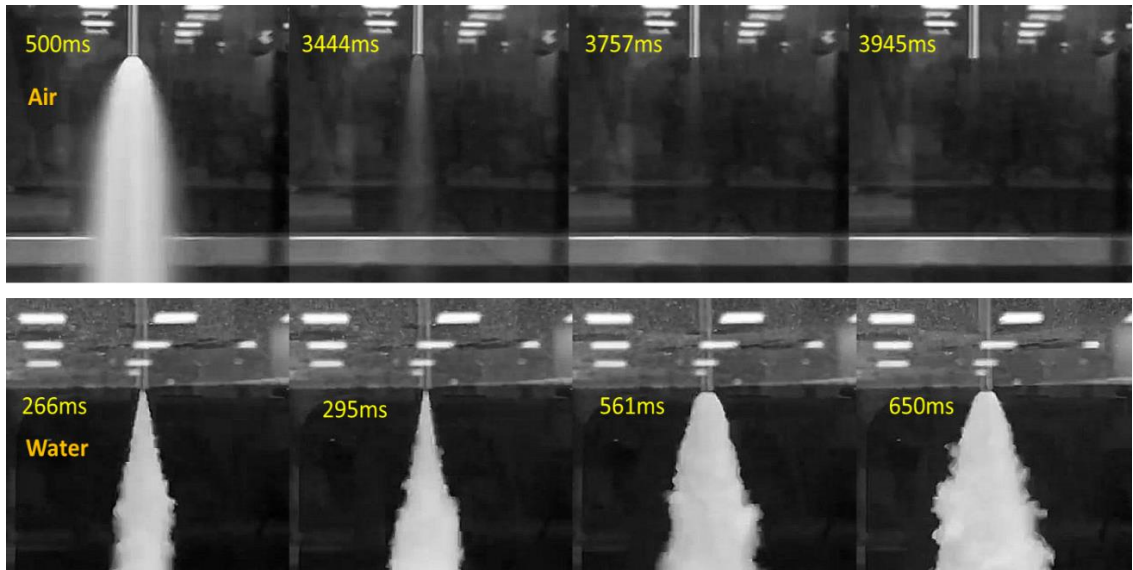
Figure 5.15 Dimensions of pressure vessel used in the ARISE process.

The intensity distribution across the spray jet is analyzed using ImageJ software, and the variation in intensity with respect to valve opening was plotted. The spray timing was further estimated from the images acquired. Representative images of the spray pattern in air and water are shown in Figure 5.16 (a, b). The jet propagation in air and water has different spray profiles. The jet profile in air initiates with a thin strip of feed solution exiting from the conduit at approximately 63 ms after the valve opens. In contrast, the jet initiation occurs at 147 ms in water. The difference in the initial release of the feed solution is due to the variation in the density of the medium.

The spray profile in air and water has two phases, namely, the initial phase where the jet initiates from the feed solution and the fully developed phase where the major volume fraction of the feed solution is sprayed. The initial phase of the spray profile in the air at 219 ms reveals two regions (Figure 5.17). The core, which forms the inner region of the spray has high-intensity profile producing maximum jet velocity, and the shell, which forms the periphery of the spray.



(a)



(b)

Figure 5.16 Spray propagation of ES100 in (top) air, and (bottom) water medium. (a) The initial phase of jet propagation, (b) Fully developed phase of jet propagation.

In the fully developed phase, the maximum intensity in the spray profile was observed at 500 ms in the air with a parabolic spray pattern whereas the profile observed in the water at 650 ms showed a full cone pattern. The formation of mist in water is due to the loss of coherence of the spray in the denser medium.

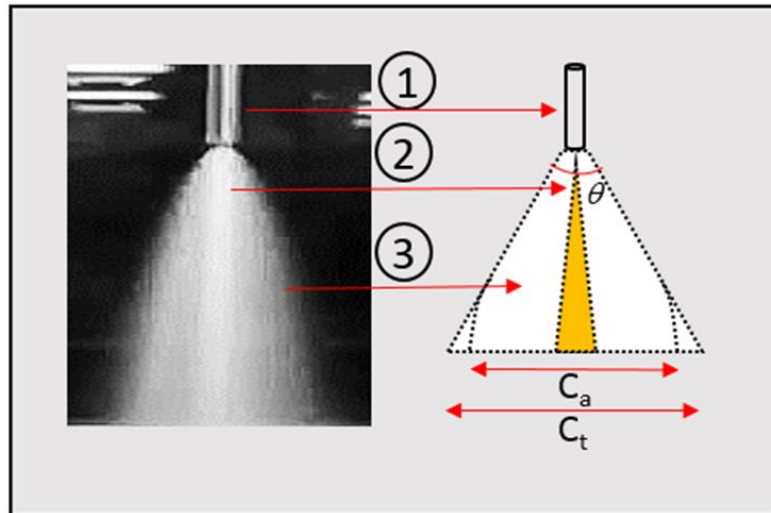


Figure 5.17 Illustration of the spray pattern in ARISE process. (1): Pre expansion region-injection chamber, (2): Conduit, and (3): Expansion region (precipitation chamber).

The rapid opening of the valve originates rapid injection of the feed solution through the narrow conduit resulting in spray atomization. The spray pattern can be explained in terms of spray width (W_d), which in the current case is defined as the width of the spray 20 mm below the tip of the conduit. Both the intensity of the spray profile and the corresponding width was measured for different concentration of ES100.

The intensity profile of the spray with two distinct peaks corresponding to the initial phase and fully developed phase for all ES100 concentrations are shown in Figures 5.18, and 5.19. The initial peak corresponds to the initiation of the jet from the conduit within the first 500 ms of valve opening. The low intensity of the initial peak corresponds to the minimal volume of the feed solution released. Similarly, the high-intensity peak correlates to the fully developed phase in spray simulation.

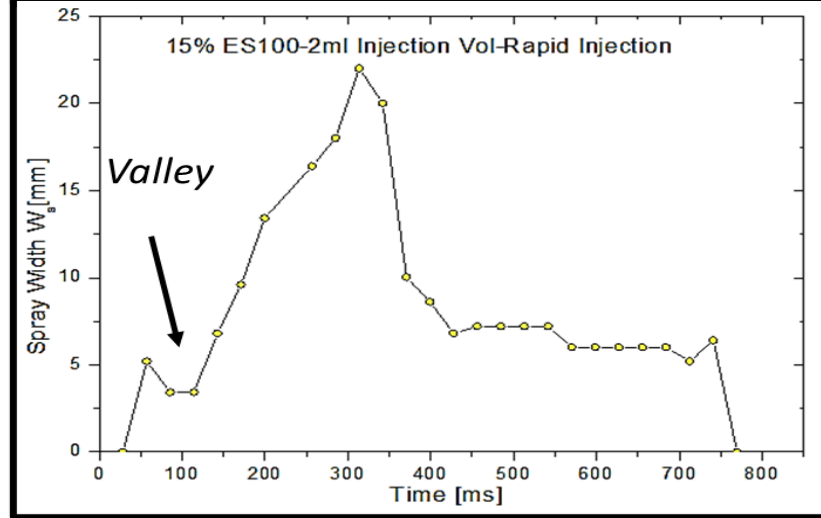
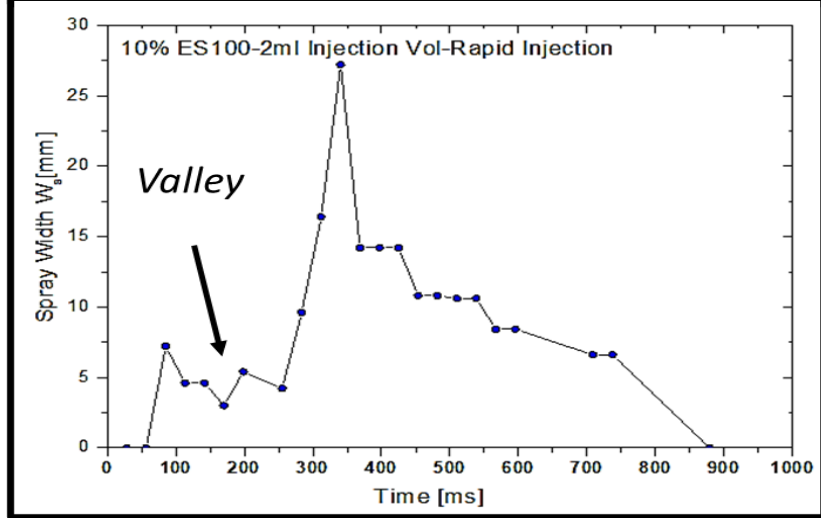
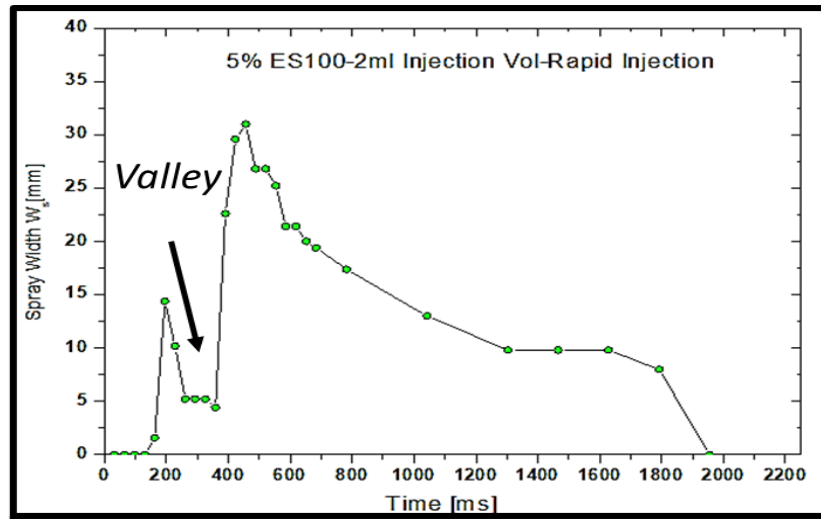
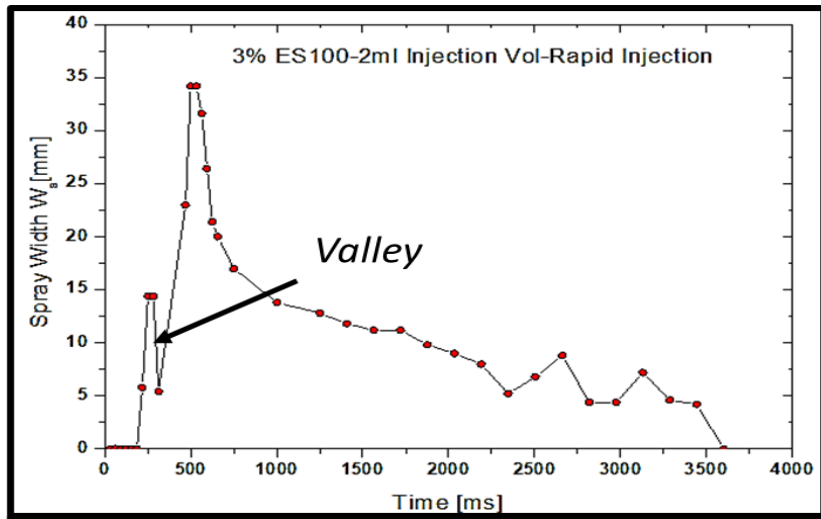


Figure 5.18 Spray width as a function of spray time for different concentrations of ES100 in air.

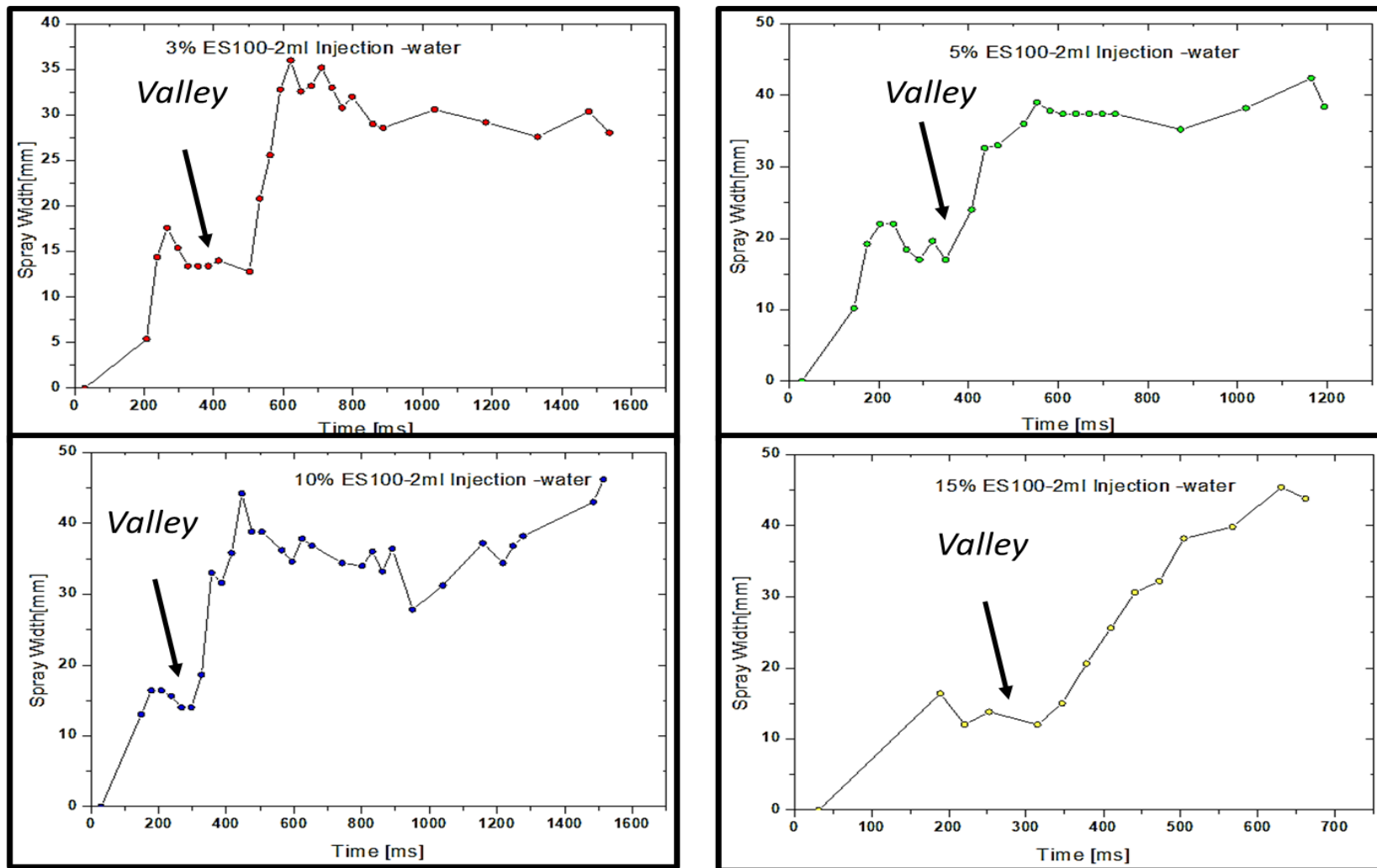


Figure 5.19 Spray width as a function of spray time for different concentrations of ES100 in water.

The spray profile in the air was plotted for the entire valve opening time. On the other hand, the spray profile plot was restricted to a fully developed phase in water due to the formation of fogs and bubbles at a later stage of valve opening, making image analysis difficult. Since the region of interest was on analyzing the spray pattern until the fully developed phase, the change in intensity profile following the fully developed phase was not considered in the current study.

As the name suggests, atomization involves breaking of a liquid jet into droplets by applying pressure or mechanical vibration [379]. The applied pressure is transformed into kinetic energy of the liquid which in-turn atomizes the liquid while exiting the conduit. The atomization process produces a broad spectrum of spray characteristics due to the influence of various operational parameters [392].

In the ARISE process, the injection chamber is maintained at a higher pressure than the precipitation chamber. The pressure differential between the injection and precipitation chamber sources the atomization. In Chapter 2, section (2.3.1), it is explained that, in the RESS process, the API solution-CO₂ mixture is sprayed into the chamber having ambient air as medium. Contrasting to the RESS process, the ARISE process uses dense CO₂ at elevated pressure as the medium. In this case, the resistance provided by the medium influences the spray width, angle, and hence the particle size. When the valve is opened rapidly, the pressure difference across the injection and precipitation chamber is transient until an equilibrium pressure is reached. During this stage, the feed solution experiences an increase in resistance from the dense CO₂ due to the difference in densities between the feed solution and medium. The variation in the densities between solution and medium affects the spray pattern and explains the difference in spray profile between air and water (Fig 5.16).

The effect of surrounding pressure in the precipitation chamber on atomization has been discussed for several years. *Klüsener et al.* proposed an equilibrium condition for droplet formation in a liquid spray system[393]. The *Klüsener et al.*'s model can also be adapted to the given GXL system by replacing the ambience with the GXL condition. The formation of particles in the dense CO₂ medium in line with the equilibrium condition was described by *Lewis et al* [394].

At any given instance, the internal pressure at any point on the surface of the atomized particle P_p is balanced by GXL pressure P_{gxl} and the surface tension pressure P_s on the particle.

$$P_p = P_{gxl} + P_s = k, \text{ where } k \text{ is equilibration constant.} \quad (5.6)$$

Assuming that the particle formed are spherical,

$$P_s = \frac{4\sigma}{d} \quad (5.7)$$

Where σ is the surface tension of the feed solution (N/m) and d (nm) is the diameter of the atomized particle.

From Eq 5.6 it is inferred that at any given instance, the atomized particle is stable as long as the effect of change in GXL pressure on any point on its surface is balanced by the surface tension pressure. During the expansion of the feed solution inside the precipitation chamber, P_{gxl} increases large enough that the change in P_s is insignificant and the droplet is deformed, resulting in a reduction in the size of the particle formed. The P_s of the particles thus formed increase due to a decrease in d , as indicated in Eq 5.7. The increase in P_s equilibrates the variation in P_{gxl} . These dynamics continue and the atomization stops when the equilibrium is reached at all points of the particles formed. For this reason, a 10 min equilibration time is allowed after the rapid opening of the valve to provide sufficient time to completely atomize the feed solution and stabilize the conditions inside the precipitation chamber. However, experimental verification of the above process is beyond the scope of the present work.

The change in P_{gxl} between air and water contributes to the difference in spray pattern as seen in Figures 5.18, and 5.19. In a dense medium like water/scCO₂, the feed solution supersaturates as the spray exits the conduit and undergoes rapid pressure drop [394]. The pressure drop exerts P_{gxl} (greater than in air medium) on the droplet emerging from the conduit, resulting in a coherent spray pattern near the conduit. The effect diminishes as the jet travels downstream creating plume/fog patterns as seen in Figure 5.16 (b).

Further, the variation in the miscibility of organic solvent-CO₂ with pressure explained by *Martin et al* [155], suggests that a pressure range of 90-150 bar is optimal for the complete mixing of CO₂ into the solvent phase without interface limitations. In congruence with the above observation, the operating pressure of 110 bar in the current study creates completely miscible conditions inside the precipitation chamber. During the spray atomization, the miscibility of solvent-CO₂ reduces the surface tension of the

solution at a distance shorter than the characteristic jet breakup length, causing the spreading of the mixture forming fog/gaseous plume[155, 383].

Based on the study by *Helgen et al* [395], which primarily focuses on modelling rapid expansion in the RESS process, the micronization in dense CO₂ can be divided into three different regiments as illustrated in Figure 5.17. The regiments consist of the pre-expansion region (injection chamber), the conduit, and the expansion region (precipitation chamber) respectively. At the event of a rapid opening, the pressure differential creates high velocity (about 3.1×10^1 m/s) near the opening. The high-velocity jet generates a pressure drop near the conduit region which is lower than the bulk pressure of the precipitation chamber. The combined decrease in pressure and temperature near the opening causes the condensation of CO₂. In the RESS process, the expansion occurs in the precipitation chamber maintained at ambient (air) conditions. Hence, the chance of CO₂ condensing and forming droplets is high. However, in the ARISE process, the precipitation chamber is maintained with CO₂ at constant pressure and temperature. This means that the condensation of CO₂ near the opening is balanced by the chamber pressure avoiding the formation of CO₂ droplets. As the jet advances towards the center of the chamber, the pressure and temperature increase and equilibrates. This rapid increase in pressure and temperature causes supersaturation in the feed solution and institutes precipitation. The pressure-temperature profile is illustrated in Figure 5.20.

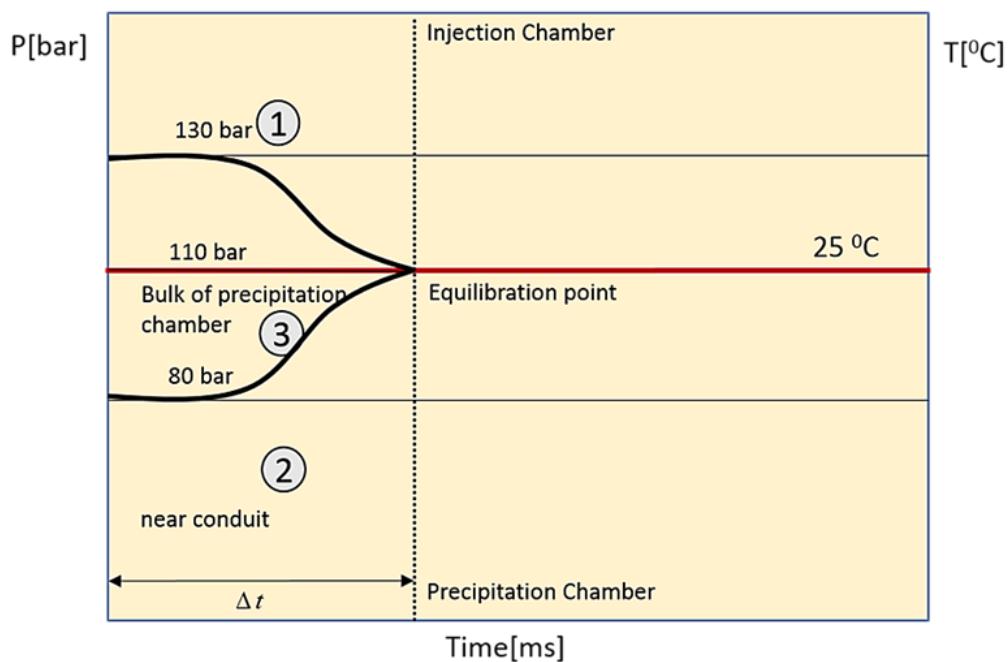


Figure 5.20 Illustration of the pressure-temperature dynamics in the ARISE process.

5.5.2 EFFECT OF ES100 CONCENTRATION ON SPRAY ANGLE

The spray angle (θ) is the angle of spread of the spray from the tip of the conduit as illustrated in Figure 5.17. The spray angle was measured from the acquired spray image, and the effect of feed concentration was plotted, as shown in Figure 5.21. The spray angle determines the particle size of the droplet formed. In this study, the spray angle decreases with an increase in the concentration of the feed solution. The variation in spray angle with respect to the ES100 concentration is about 13.30 % and 5.30 % in the initial jet phase in both air and water, respectively. However, in the fully developed phase, there is a sharp decrease of 49.00 % and 32.60 % in spray angle in air and water, respectively. The variation is due to the difference in density and hence the surface tension of the medium. The decrease was gradual in water whereas a sharp decrease was observed in air.

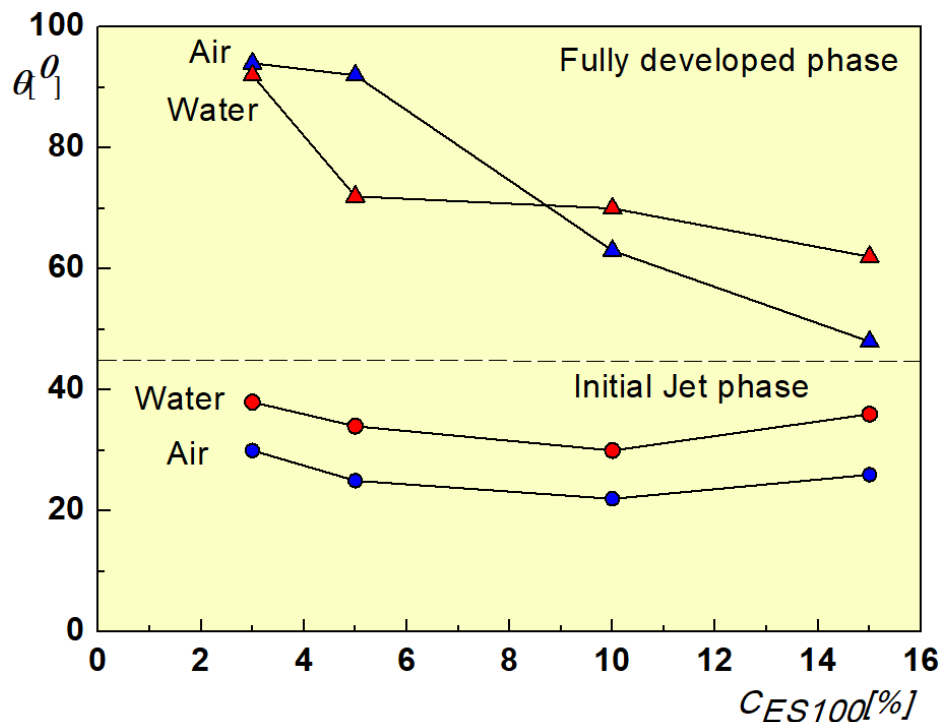


Figure 5.21 Spray angle variation with change in ES100 concentration in air and water medium.

As mentioned in the previous section, at the instance of valve opening, the pressure near the conduit decreases rapidly and creates a supersonic jet velocity generating a core spray profile, as seen in Figure 5.16(a) at 219 ms and in Figure 5.16(b) at 236 ms respectively. The spray distribution equilibrates and forms a uniform fully developed

cone profile, as seen in Figure 5.16(a) at 500 ms and Figure 5.16 (b) at 561 ms, respectively. Since air is less dense than water, the formation of the core regime near the conduit is distinctly visible. The relation between the spray medium and the spray solution influences the spray pattern. The effect can be explained based on the specific gravity and interfacial surface tension between the medium and spray solution.

The flow rate (Q) of the solution, as mentioned in Eq (5.4), can be related to the specific gravity of the medium as:

$$Q = \frac{\pi.r^4.\Delta P}{8.\mu.L} = q * \sqrt{\frac{G_{medium}}{G_{sol}}} \quad (5.8)$$

wherein, G_{medium} : the specific gravity of the medium and G_{sol} : specific gravity of feed solution and, q : flow rate constant of the medium. The specific gravity is proportional to the viscosity of the medium. In the current work, the viscosity (η) of the feed solution is within the Newtonian boundaries (refer to Figure 5.1). Hence the above Eq (5.8) can be explained in terms of viscosity (η).

During the initial jet phase, the specific gravity and viscosity follow the gradient:, and $G_{air} < G_{water} < G_{sol}$, and $\eta_{air} < \eta_{water} < \eta_{sol}$. The high solution viscosity relative to the spray medium produces low spray volume and hence lower spray angle (θ). The interfacial surface tension between the atomized particle and medium is large in the air compared to water, causing the homogenous spread of spray in water. Hence, a 27 % increase in spray angle (θ) was observed in water (Figure 5.21). It was observed that the variation in concentration of feed solution has a less significant effect on spray angle (θ) during the initial jet phase owing to the low spray volume.

During the fully developed phase, the pressure inside the precipitation chamber equilibrates over time. The flow rate (Q) increases and reaches a stable value during the transient time between valve opening and equilibration. The equilibration pressure is higher than the pressure during the initial jet phase (which is closely nearer to 80 bar precipitation chamber pressure). Consequently, this increase in pressure (ΔP) in turn increases the spray volume (Eq 5.8), thereby increasing the spray angle (θ), as seen from Figure 5.21.

The influence of the concentration of the feed solution dominates during the fully developed phase due to the high volume of feed solution sprayed. A sharp decrease in

spray angle (θ) was observed in the air than water due to the denser medium generating homogenous distribution across the spray width resulting in stable spray over time.

5.5.3 EFFECT OF ES100 CONCENTRATION ON SPRAY WIDTH

The spray width (C) of the initial and fully developed phase decreases with an increase in ES100 concentration, as illustrated in Figure 5.22. About 64.40 % decrease in C was observed in the air and about 44.80 % decrease in water.

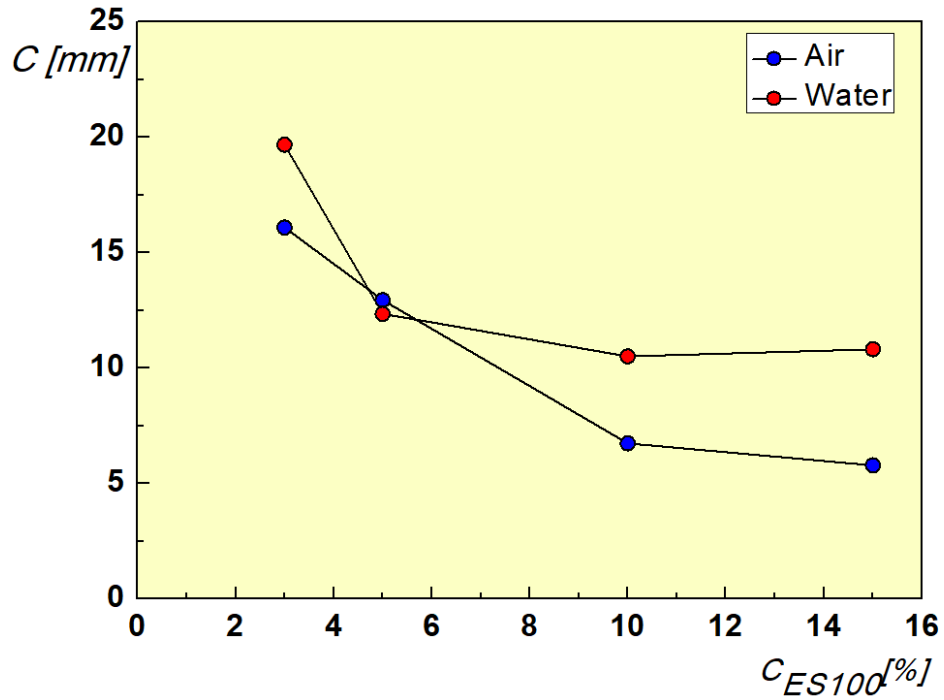


Figure 5.22 Variation of theoretical spray width “C” with ES100 concentration in air and water medium.

Considering the spray profile to be axisymmetric and the initial jet velocity to be uniform, the spray width “ C_t ” can be related to the momentum flux (φ) of the jet as [383]:

$$\varphi = 2\pi\rho \int_0^{\infty} v_i^2 y dy = \rho\pi \frac{d^2}{4} v^2 \quad (5.9)$$

where v_i is the instantaneous velocity of the jet. Considering the spray as an equilateral triangle as shown in Fig 5.17, spray width C_t can be expressed as:

$$C_t = 2D \tan\left(\frac{\theta}{2}\right) \quad (5.10)$$

where D : spray length and θ : spray angle. The momentum flux generated by the jet can be related to the spray width by:

$$C_t = 2D \tan\left(\frac{\theta}{2}\right) = \frac{49.1\mu D}{\sqrt{\phi\rho}} \quad (5.11)$$

The formation of idealized spray geometry depends on many factors such as conduit size, pressure, and flow rate. Fluids with high viscosity have a low spray angle as revealed from Figure 5.21. Theoretically, the spray width C_t is directly proportional to the spray length (D) as in Eq 5.11. However, the effect of gravity influences the spray pattern resulting in the curvature of the spray width indicated as C_a in Figure 5.17. From Eq [5.10], the decrease in spray velocity decreases the momentum flux (ϕ) of the jet. The low flux generated is balanced by the viscosity of the feed solution as seen from Eq [5.11]. With the increase in the concentration of the feed solution, the viscosity increases. The viscous force surpasses the flux-viscosity balance, resulting in a decrease in spray width. Additionally, the size of the pressure vessel restricts the spread of the spray. A narrow vessel causes atomized particles to recombine and coagulate causing the formation of lumps[155]. The formation of such lumps is predominant at a high concentration of feed solution as seen in Figure 5.2.

5.5.4 VARIATION IN SPRAY TIME WITH THE CHANGE IN ES100 CONCENTRATION

The time difference (Δt) between the two peaks of the initial and fully developed phase is plotted as a function of ES100 concentration in Figure 5.23. The Δt is associated with the time lag in the opening of the valve. Albeit the rapid opening of the valve, the use of a manually operated valve causes an imperceptible delay in opening. The delay also sources the valley in the intensity plot (Figures 5.18 and 5.19). The delay is the process limitation and can be overcome by replacing the manual valve with an automated solenoid valve. (The pictures of spray propagation and time delay sequence for the gradual opening of the valve is shown in Appendix B, Figure 11.1-11.2).

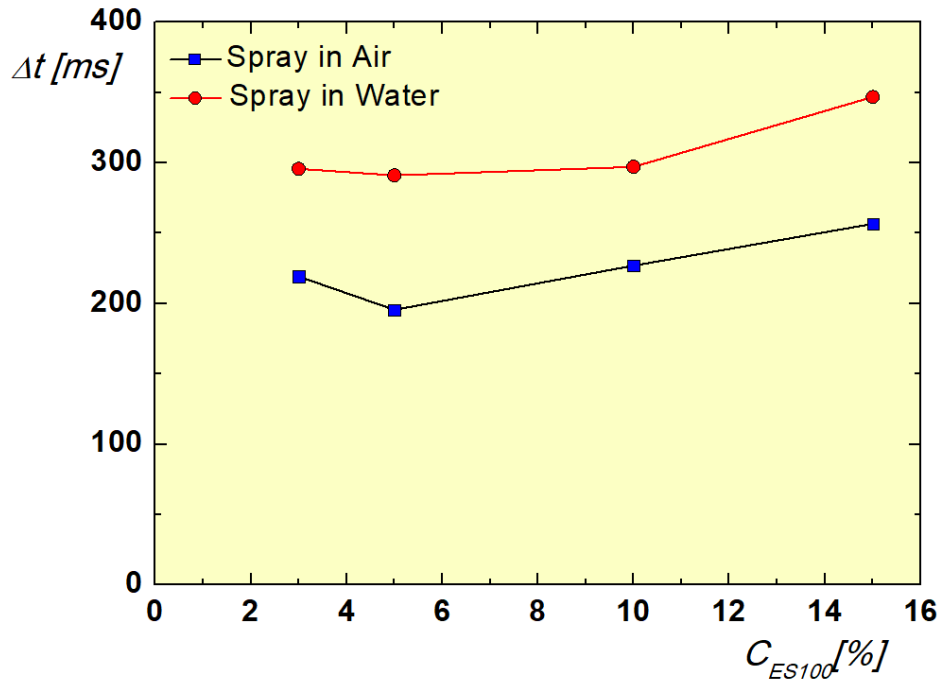


Figure 5.23 Time lag (Δt) as a function of ES100 concentration in both air and water as a medium.

Increasing the concentration of ES100 increases Δt . The increase in Δt is as low as 0.45% with an increase in ES100 concentration from 3 % to 10 % in the air whereas, the Δt variation in water was observed to be 3.52 % greater. The variation in Δt with concentration was significant, with a 17.00 % increase in both air and water at 15 % ES100 concentration. These variations show that the time lag in the ARISE process is proportional to both valve opening and concentration of ES100. Hence a range between 3 to 10 % ES100 would be an optimal working concentration for the ARISE process. The shift in Δt in the graph in Figure 5.23 also informs that the time taken for spraying increases by an average of 37.50% between air and water for all concentrations of ES100. The reason is also due to the change in the density of the medium. The operating region of the GXL in the ARISE is in proximity to water, implying that the spray behaviour (atomized droplet formation) in water resembles the behaviour in the actual ARISE process, excepting the supersaturation and precipitation effect in the GXL system.

5.6 CONCLUSION

The ARISE technique produces particles of high fine particle fraction suitable for oral, nasal, and parenteral drug delivery. pH-sensitive ES100 polymer was successfully micronized with a minimum particle size of 150 nm achievable. The process produced fluffy particles of low bulk density (0.02 g/ml) and improved surface-to-volume ratio. The effect of feed solution concentration and volume on the particle morphology and size indicate that high volume and concentration of feed solution generates particles bigger in size and increased bulk density. The volume of feed solution depends on the volume capacity of the ARISE system. Three and five percent (wt) concentration produced particles of uniform spherical morphology with an average size of less than 2.5 μ m-3 μ m. The moderate operating pressure and temperature of the process proves advantageous in formulating thermos sensitive API's. The mechanism of micronization in ARISE was demonstrated by analyzing the spray intensity profile. The analysis revealed that the pressure differential across the injection and precipitation chamber and the solution's viscosity significantly affect the spray pattern and hence the micronization. The current work results help in the further formulation of an API-excipient combination for improved targeted delivery in both lab and commercial scale-ups.

CHAPTER 6

Formulation of hydrophobic and hydrophilic drugs in ES100 using Atomized rapid injection for solvent extraction (ARISE) process

RESULTS AND DISCUSSION

The ARISE technique is a DG process involving rapid atomization driven by the pressure differential across the injection and precipitation chamber. The ability of the process to produce fine particles of aerodynamic diameter and their credibility towards processing fluffy and low bulk density biopolymer were discussed in Chapter 5. Their effectiveness of the ARISE process in encapsulating API is discussed in detail in this chapter. The compatibility of nano-carriers in carrying both hydrophilic and hydrophobic drugs are investigated. Mainline drugs for treating colorectal cancer such as Leucovorin, 5FU, Irinotecan, Oxaliplatin, to name a few, are hydrophilic [396-398], meaning that the dissolution in aqueous solution is more significant and hence readily absorbed in the human body. However, these hydrophilic drugs' bioavailabilities decrease the efficacy as a substantial portion of them get absorbed at non-targeted locations [399]. On the other hand, most of the anticancer drugs are water-insoluble such as SLB, Methotrexate, Curcumin, and, Paclitaxel (PTX), making the intestinal absorption and circulation difficult, hence, reducing the efficacy of the API's [400]. Introducing solubilizing agents such as dimethyl sulfoxide or other surfactants to the drugs may enhance the solubility but comes with the cost of neurotoxicity[401, 402]. The formulation of a drug-nanocarrier system can partly overcome the problem associated with the use of the hydrophilic and hydrophobic free drug. Micronizing and encapsulating the drugs into the nanocarriers in the form of nano-spheres, nano-capsules, inorganic porous material carriers enhances the bioavailability of the APIs by (1) increasing the concentration of drug into the circulation system, (2) promoting effective absorption at localized sites, and (3) preventing the drugs from releasing at undesired locations.

The use of conventional encapsulation techniques and the advantages of using DG techniques have been described in Chapter 2, Section (2.2 and 2.3). The ARISE technique overcomes the issues faced by the conventional DG precipitation processes by incorporating a rapid injection of organic solution into a homogeneous anti-solvent phase. The quasi-instantaneous spraying of the feed solution into the anti-solvent phase favours the nucleation kinetics of the droplets. It alleviates the drawback of gradual elution and non-homogeneity encountered in other processes. As discussed in Chapter 2, and Chapter 5, ES100 polymer is a suitable candidate for targeted drug delivery [403]. The APIs encapsulated in ES100 are protected from the exposure to

the acidic pH environment of the gastric region (pH 1.2) are simulated for a time-extended release in the intestinal environment (pH 7.4). In the current work, the evaluation of encapsulation 5FU, a hydrophilic drug, and SLB, a hydrophobic drug, in ES100 was analysed. The encapsulation studies of 5FU and SLB were performed under a similar process condition to compare their loading behaviours. Amongst the series of organic solvents suitable, the degree of solubility of ES100 follows the order: DMSO > Acetone > Ethanol (EtOH) > Methanol (MeOH). DMSO and Acetone showed the highest solubility in both ES100 and scCO₂. Using these solvents in the scCO₂ continuum improves the supersaturation and mass transfer rate. However, 5FU showed low solubility with acetone and EtOH. The solubility of 5FU was highest in DMSO > 10mg/ml, followed by MeOH \approx 7-8 mg/ml. DMSO was avoided due to the chemical hazard and side effects associated with handling. Hence MeOH was chosen as a solvent for both ES100 and 5FU. Similarly, EtOH was used as the solvent for encapsulating SLB. The solubility of SLB in EtOH was better than in MeOH. The sample preparation and the ARISE procedures are explained in Chapter 3 (Section 3.3.1 and 3.3.2).


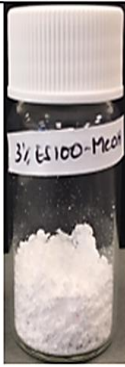
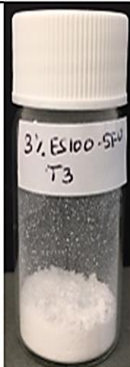


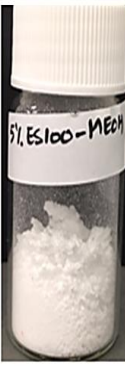
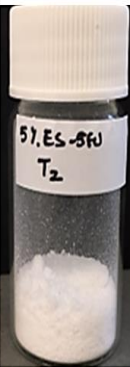
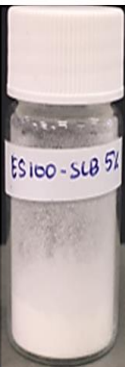

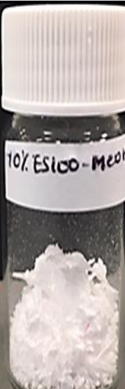
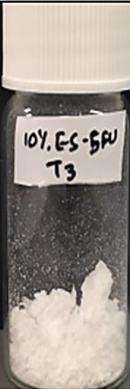
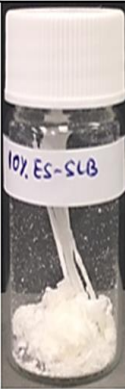
(a) Pristine ES100 3%	ARISE processed		
	ES100 3%	ES100-5FU 3%	ES100-SLB 3%
			
(b) Pristine ES100 5%	ES100 5%	ES100-5FU 5%	ES100-SLB 5%
			
(c) Pristine ES100 10%	ES100 10%	ES100-5FU 10%	ES100-SLB 10%
			

Figure 6.1 Samples of pristine ES100 and ARISE processed ES100, ES100-5FU, and ES100-SLB for different ES100 concentrations.

Table 6.1 Experimental conditions for the encapsulation studies of 5FU and SLB in ES100 by the ARISE process.

Expt. No.	Material		Solvent		Operating Conditions		Product Recovery (%)
	Name	Mass (g)	Name	Volume (ml)	Operating pressure (bar)	Temperature (°C)	
1	ES100	0.25	MeOH	10	110	25	81.2
2	ES100	0.45	MeOH	10	110	25	82.5
3	ES100	0.85	MeOH	10	110	25	92.0
4	ES100	0.25	EtOH	10	110	25	89.0
5	ES100	0.45	EtOH	10	110	25	98.5
6	ES100	0.85	EtOH	10	110	25	87.2
7	ES100-5FU	0.32	MeOH	10	110	25	87.0
8	ES100-5FU	0.52	MeOH	10	110	25	84.0
9	ES100-5FU	0.92	MeOH	10	110	25	82.0
10	ES100-SLB	0.32	EtOH	10	110	25	83.2
11	ES100-SLB	0.52	EtOH	10	110	25	85.0
12	ES100-SLB	0.92	EtOH	10	110	25	76.0

6.1 PRODUCT RECOVERY

The experimental conditions for the ARISE process are tabulated in Table 6.1. The details on the concentration of drug and experimental parameters are mentioned in Chapter 3, Table 3.4, and 3.5. The operating pressure is the equilibration pressure in the precipitation chamber after the rapid injection of the organic solution. The recovery of the products from ARISE averages 80-90 % (Table 6.1), implying that the ARISE processing is efficient in batch production, as mentioned in Chapter 5, Section 5.2. The variation in recovery between batches is due to mechanical handling and electrostatic stiction along the chamber's inner walls. The particles are fine and light, and they tend to stick on the inner walls of the chamber, filters, and on the circumference of the conduit. Access to such areas while retrieving was quite a challenge. These contribute towards loss of ES100 and hence, a slight decrease in recovery. With an increase in ES100 concentration (10 % and more), twigs of ES100 were formed on the tip of the conduit during micronization as shown in Figure 6.2.

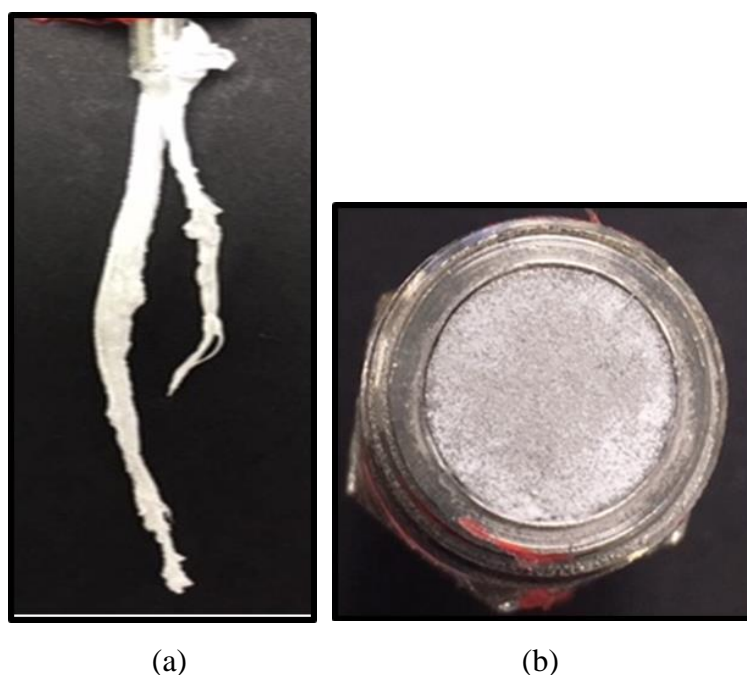


Figure 6.2 Images of the parts of ARISE after the micronization process. (a) Tip of the conduit, (b) Bottom filter of the precipitation chamber while using 10 % ES100 solution.

However, in any DG process, the concentration of the solute plays a vital role in deciding the operability and efficiency of the process [95]. This study was conducted to realize the maximum concentration of the solute and determine the optimum concentration of the solute for the ARISE processing system. It has been demonstrated that

the higher concentrations of the solute may produce fine particles while using scale-up systems, wherein the effect of concentration is countered by the increased volume of the precipitation chamber, in the study of micronization of Curcumin using ARISE set-up by *Foster et al.* [172].

6.2 BULK DENSITY

The bulk density (ρ_{bulk}) of ARISE processed ES100-5FU was measured based on the procedure described in Chapter 3 (Section 3.2.4). The input/feed solutions were micronized under similar pressure and temperature conditions to compare the variation in bulk density of drug encapsulated ES100 particles from its pristine form. The ARISE processed ES100 was too fluffy and light. The images of the product obtained from the ARISE is shown in Figure 6.1.

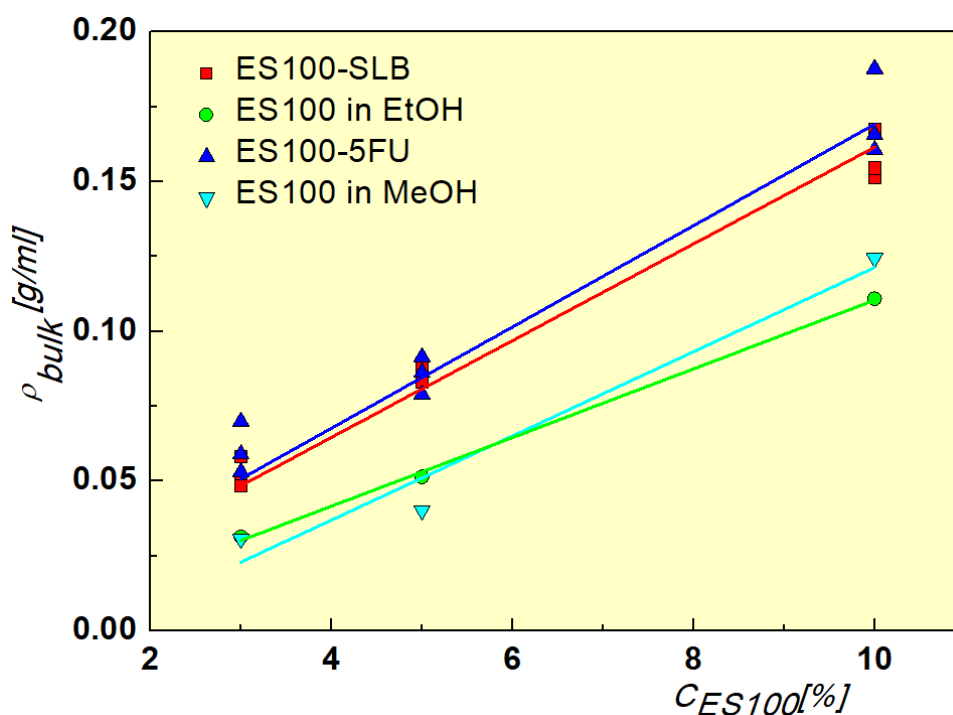


Figure 6.3 Bulk density of ES100, ES100-5FU, and ES100-5FU processed by the ARISE at 50 bar (ΔP) and 25°C, as a function of the concentration of ES100.

The bulk density of both pristine and drug encapsulated ES100 showed significant reduction after the ARISE process (density of ES100 is 0.85 g/ml). The formulation of low bulk density particles facilitates dispersion and flowability in any given medium. The increase in trend of the graph in Figure 6.3 can be correlated to the particles' fluffiness retrieved from the ARISE process, as shown in Figure 6.1. The bulk density in-

creases with an increase in the concentration of ES100 in the feed solution. With pristine ES100, the increase in bulk density is over six folds from 3 % to 10 % concentration. A high ES100 concentration produces particles in chunks, as seen from Figure 6.1(c). The irregular particles increase the void space and reduce the point of contact between them, helping to improve the effective dispersion [404, 405]. Further, the formation of fine and fluffy particles depends on the concentration of the solution and the volatility of the solvent used. *Roderick et al* produced a finer fraction of ES100 from the ARISE process using Acetone as solvent [110]. The experiments were performed at 37 °C and 40 °C in scCO₂ conditions. In the current work, the experiments were carried out in GXL phase at 25 °C. The solubility of MeOH in scCO₂ is lesser compared to acetone [23]. Thus, the mass transfer between the solution phase and the GXL is moderate in MeOH than acetone. Further, with a higher concentration of ES100, the bulk of volume exposed to the GXL environment inside the precipitation chamber is increased, creating particle chunks and twigs, as mentioned in Section 6.1.

Interestingly, the bulk density of drug encapsulated ES100 is higher than pristine ES100 (Figure 6.3). The reason can be attributed to the drug which was co-precipitated and encapsulated in ES100. The molecular weights of 5FU is 130.077 g/mol (Sigma Aldrich), and SLB is 482.44 g/mol (Sigma Aldrich) respectively, which are negligible compared to ES100 (135,000 g/mol) [210, 373, 406]. Despite this difference, the inclusion of drugs in ES100 produces a significant change in the particles' characteristics.

The bulk density did not show significant variation between 5FU and SLB loaded samples and between pristine ES100 extracted from MeOH and EtOH in all the experimental trails, indicates that the solvent extraction and supersaturation effects are similar between the two solvents used.

6.3 REMOVAL OF CO-PRECIPIRATE

ES100 has been used extensively as a coating material for maintaining sustained and site-specific targeted release of cancer drugs-Chapter 2, Section 2.4 [407, 408]. The drugs are carried by the core excipient and ES100 is coated on the surface of the microsphere/tablets to protect chemical degradation under acidic and non-targeted sites [409]. The formulation of several colon targeted drug delivery systems using ES100 has been reported previously. *Mehta et al.* used a combination of Eudragit RLPO and

S100 polymer to encapsulate naproxen for treating colon cancer [407]. Similarly, Mesalazine (5-amino salicylic acid) was encapsulated in Eudragit L100 and S100 to produce tablets for colon targeted drug delivery. Several binding agents and stabilizers are used to bind the drugs onto the excipient before further coating with ES100. Chitosan, Polyvinyl alcohol (PVA), polyvinyl pyrrolidone, Citrus Pectin, egg phosphatidylcholine (EPC) liposomes, and Tween 80 are some of the commonly used additives [212, 408, 410, 411]. Supercritical antisolvent process (SAS) was employed to prepare ES100 nanospheres by *Ansari et al.* The process demonstrated that ES100 coating on the calcium alginate-chitosan improved the efficacy. All the formulations use ES100 as coating materials and not as the excipient. Direct loading of drugs onto ES100 is less explored, and hence the current work focuses on direct loading of API's onto ES100 using the ARISE technique.

6.3.1 EFFECT OF THE WASHING PROCEDURE

During the ARISE process, the substance in the solution re-crystallize into fine particles based on the mass transfer rate from solute to the solvent phase of the aqueous solution [95]. The difference in the degree of supersaturation and re-crystallization may cause the drugs to load into the polymer matrix, re-crystallize as a separate entity (co-precipitate), and loosely attach on the surface of the polymer excipient as illustrated in Figure 6.4. Estimating the loading of an as-retrieved sample from the ARISE process may mislead us from the actual load content. Hence, it is necessary to wash the samples before further analysis. Washing removes the co-precipitate and surface-attached drugs from the sample. The solvent used, operating condition, wash time, and wash method have an integrated effect on the loading. Although published works have mentioned the washing step, detailed analysis of the wash parameters and its impact on loading have not been reported.

McCarron et al. conducted work on encapsulation of 5FU onto biopolymers such as poly(isobutyl-cyanoacrylate), poly(lactide-co-glycolide), poly(caprolactone), and Eudragit L100, suggested that washing of particles using centrifugation and ultrasonication caused dislodging of drugs and resulted in misestimation of drug loading [412]. In the present work, a detailed analysis of washing methods and the effect of washing time was performed on 5FU encapsulated ES100. The washing procedure was performed in two conditions, namely as harsh and moderate condition. The drug content

from the supernatant after washing was examined using UV spectroscopy. The analysis emphasized washing steps and optimal washing procedure to be adopted for drug loading estimation. The resultant optimized conditions were used in further studies. The washing conditions and methods are detailed in Chapter 3 (Section 3.3.4). The percentage of the washed drug (α_d) is estimated as the ratio of the mass of drug washed (W_{drug}) to the mass of the sample (M_{sample}).

$$\alpha_d = \frac{W_{drug}}{M_{sample}} \times 100 \quad (6.1)$$

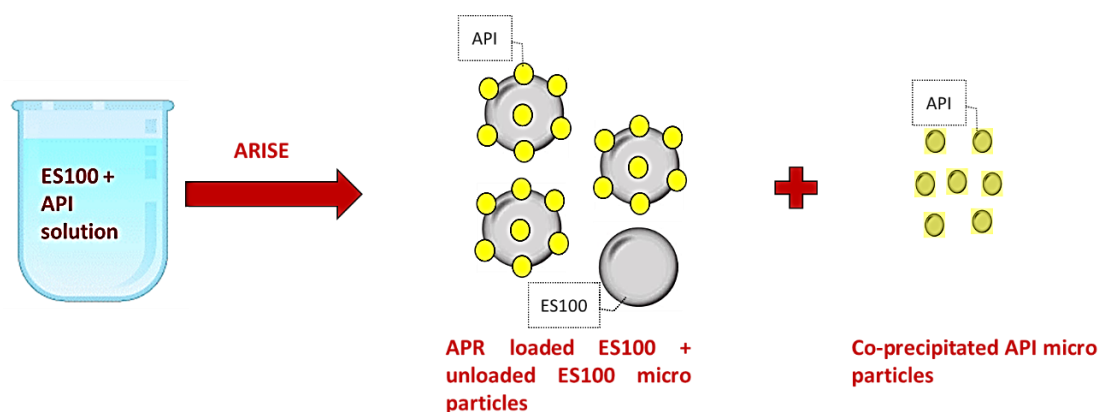


Figure 6.4 Illustration of various forms of formulations within the ARISE process. (The images are for illustration purpose and not to the scale).

Deionized water was chosen as eluent since ES100 is hydrophobic and 5FU is hydrophilic, which means that any loosely attached or co-precipitates of 5FU may dissolve in water and can be separated. The illustration of the washing mechanism is shown in Figure 6.5 for visualization.

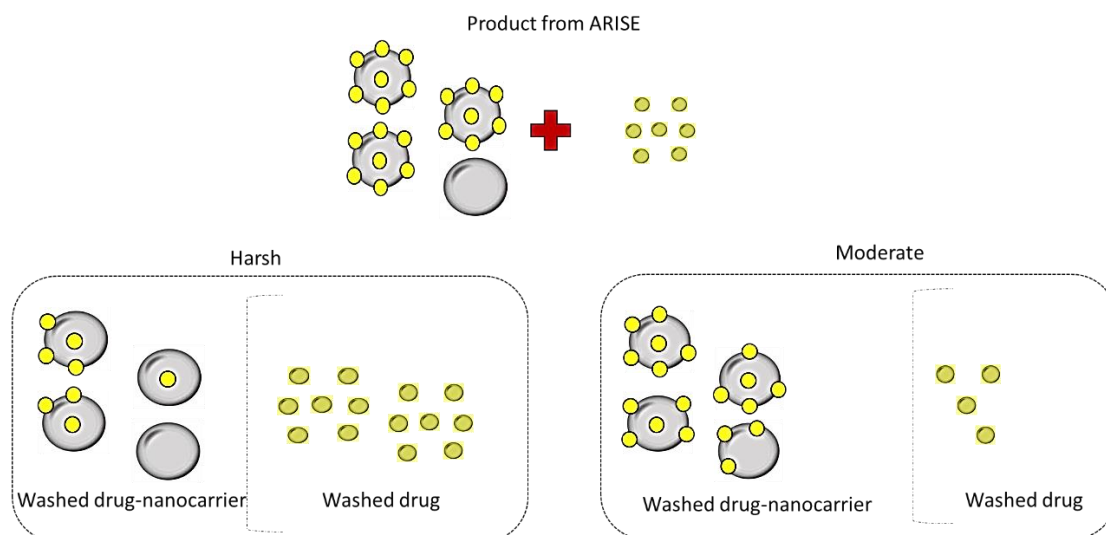


Figure 6.5 Illustration of the washing mechanism of the ARISE produce. Harsh washing results in the extraction of free and encapsulated drugs and moderate conditions retain a major portion of encapsulated drugs. (The images are for illustration purpose and not to the scale).

The fraction of drug washed (α_d) as a function of the excipient concentration is shown in Figure 6.6. It is clear from Figure 6.6 that moderate conditions produced $3.8\% \pm 1.6\%$ variation in α_d , whilst harsh condition produced $15\% \pm 4.2\%$ variation in α_d at low ES100 concentration. The dependency of α_d on the concentration of ES100 shows a similar trend in both the cases, barring a minor variation between 3% and 5% concentration. The excess amount of drug in the suspension decreases with an increase in the concentration of ES100, Meaning that more absorption sites of the polymer are available for the given amount of drug [413].

Harsh washing condition generates severe agitation through prolonged mixing in the orbital shaker and high-speed centrifugation. The encapsulated and strongly adsorbed drugs on the ES100 surface may be extracted with the loosely attached drugs. Further, the structural integrity of the samples can get affected in the harsh environment [412]. Contrarily, a moderate washing condition exposes the drug-loaded samples for a short duration of time to have adequate contact with the eluent and filtered without disturbing the bulk of the sample. In this way, most of the drug attached to the ES100 is retained. The illustration in Figure 6.5 and the trend observed in Figure 6.6 can be correlated.

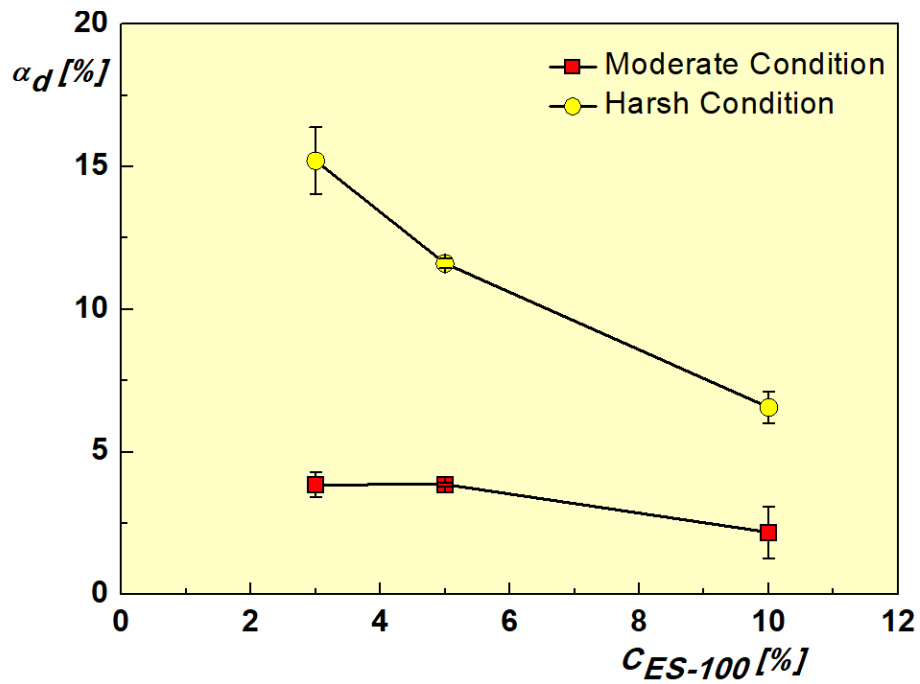


Figure 6.6 Graph showing the trend of harsh and moderately washed product from the ARISE process as a function of Eudragit S100 concentration. (Errors are SD of 3 trials).

6.3.2 EFFECT OF WASHING TIME

Withal to the consideration of moderate washing, the effect of wash time was investigated in this study. If a moderate washing condition is considered desirable, then one must know the optimal wash time to conclude on the wash parameters. In the present study, the effect of wash time on α_d was determined by measuring α_d at a regular interval of time for the first 8 min. Figure 6.7 presents the influence of wash time on the fraction of drug washed (α_d).

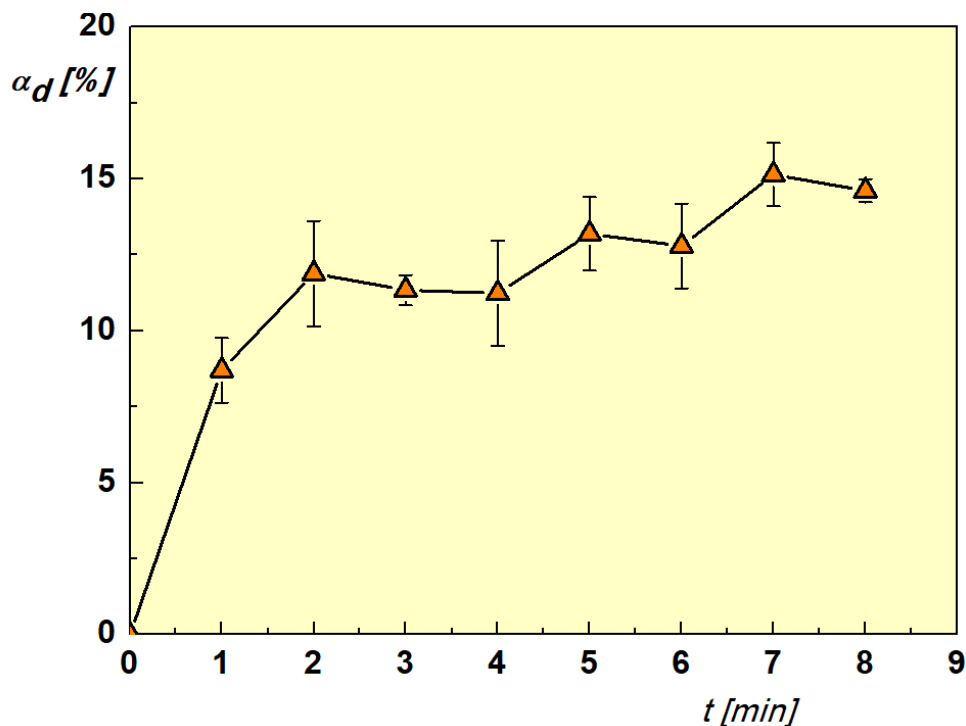


Figure 6.7 Graph showing the variation of the fraction of drug washed (α_d) as a function of wash time (t) of the ARISE processed samples. (Errors are SD of 3 trials).

An increase in washing time increases α_d proportionally. The first 1 min of wash produced 8.7 % of the drug to release and consecutively increased up to 15 % within 8 min. At the onset, the eluent may wet the surface of the microparticles, thereby solubilizing the loosely attached ones on the surface and the co-precipitates into the solution. Further exposure increases the contact time of eluent with the microparticles, causing more drug to dissolve into the solution. This situation is similar to the harsh condition varying that the excess removal of encapsulated drug is driven by the harsh process conditions. The value of α_d might increase further if the exposure time was extended beyond 8 min. In this event, the structural integrity could be lost, and the drug would completely be washed off from the sample (SEM imaging in Figure 6.9 substantiates observed scenario). Thus, moderate washing for 1 min was chosen as the optimal condition in the current study, and the drug loading was estimated after wash procedures.

SLB, on the other hand, did not show any variation in α_d . The washed and unwashed product did not show any difference in loading capacity (explained in Section 6.5).

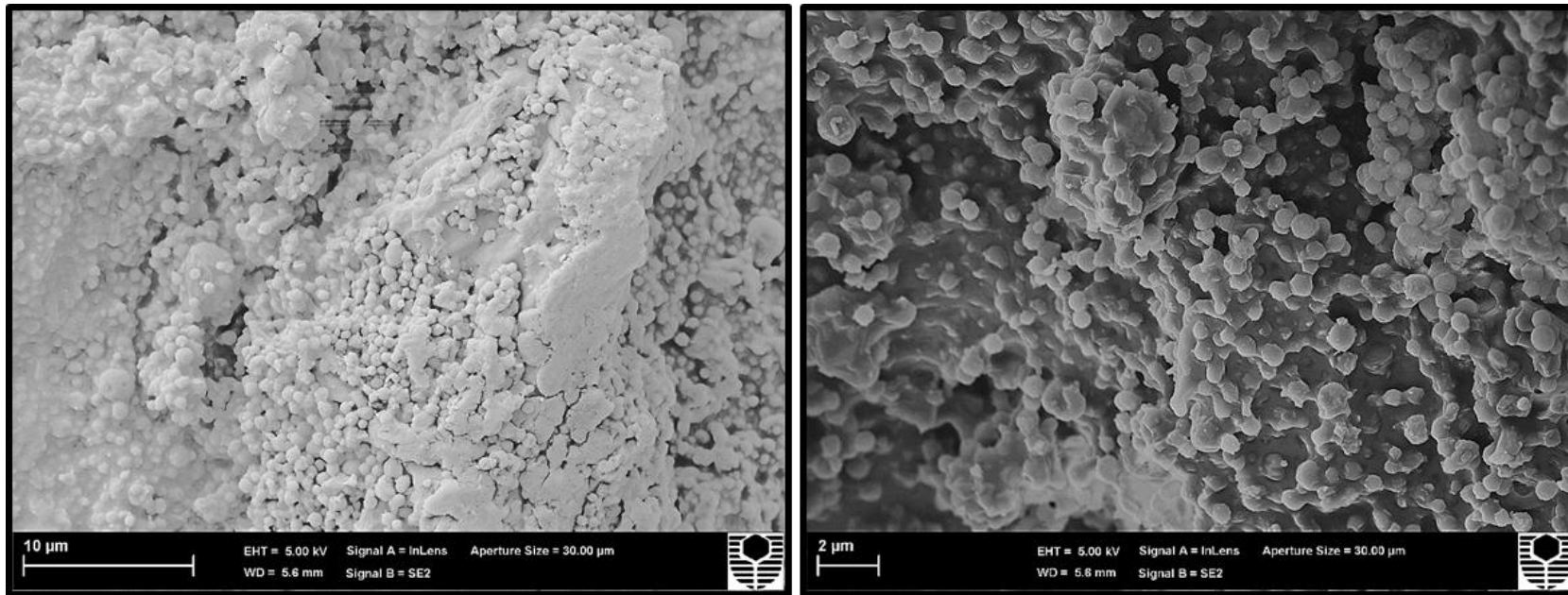
6.4 PARTICLE CHARACTERIZATION

The morphology and average size of particles were measured based on the method described in Chapter 3, Section 3.2.6. The imaging was conducted using the dry powders as retrieved from the ARISE process.

6.4.1 SCANNING ELECTRON MICROSCOPY (SEM)

6.4.1.1 IMAGE ANALYSIS ON MICRONIZED ES100 FROM MEOH SOLUTION

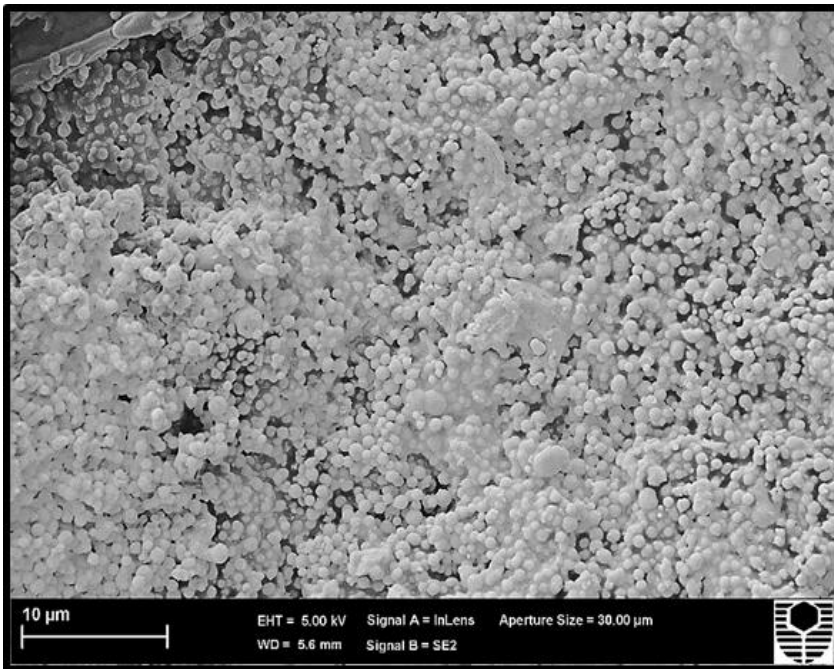
The SEM images in Figures 6.8- 6.11 show spherical particles of about 600-700 nm size from the ARISE processed ES100 using MeOH as solvent. The morphology of all the particles remained mostly spherical within the size range of 700 nm. Individual spherical particles are seen to be fused with the adjacent particles forming agglomerates. When the concentration of ES100 was increased to 10 %, particles with the appearance of large chunks and microspheres were produced, as mentioned in Section 6.1 and Figure 6.11 b.



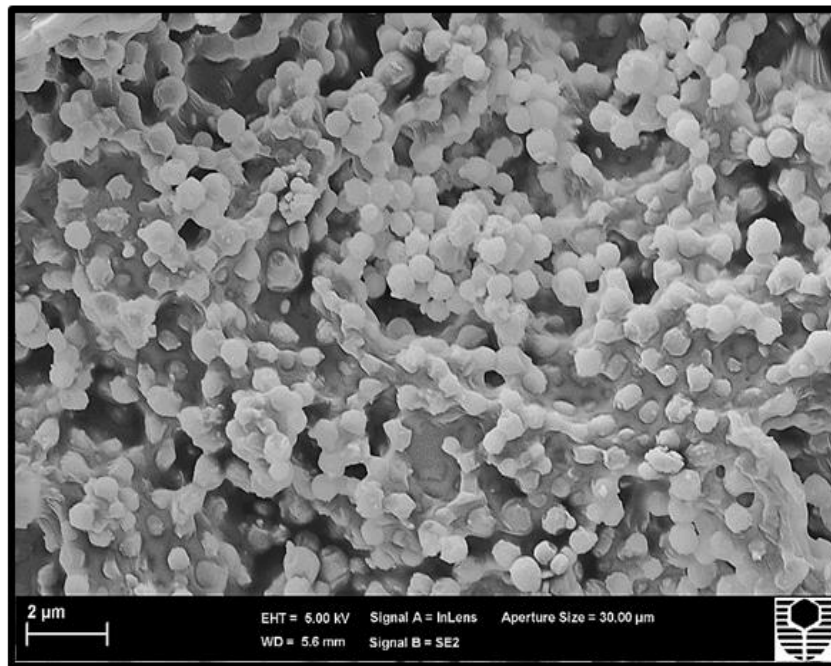
(a)

(b)

Figure 6.8 SEM images of ARISE processed ES100 from MeOH, (a) 3% conc, (b) 3% conc –magnified view.

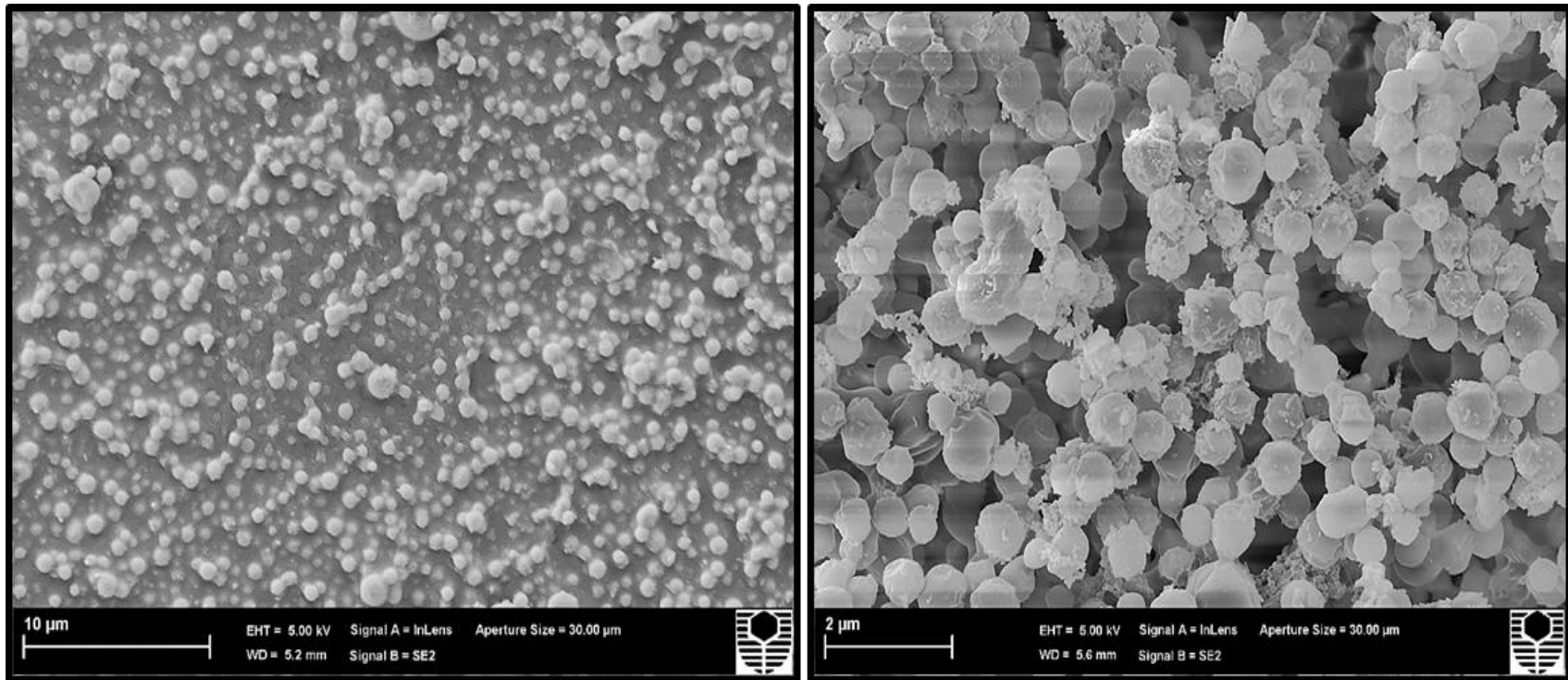


(a)



(b)

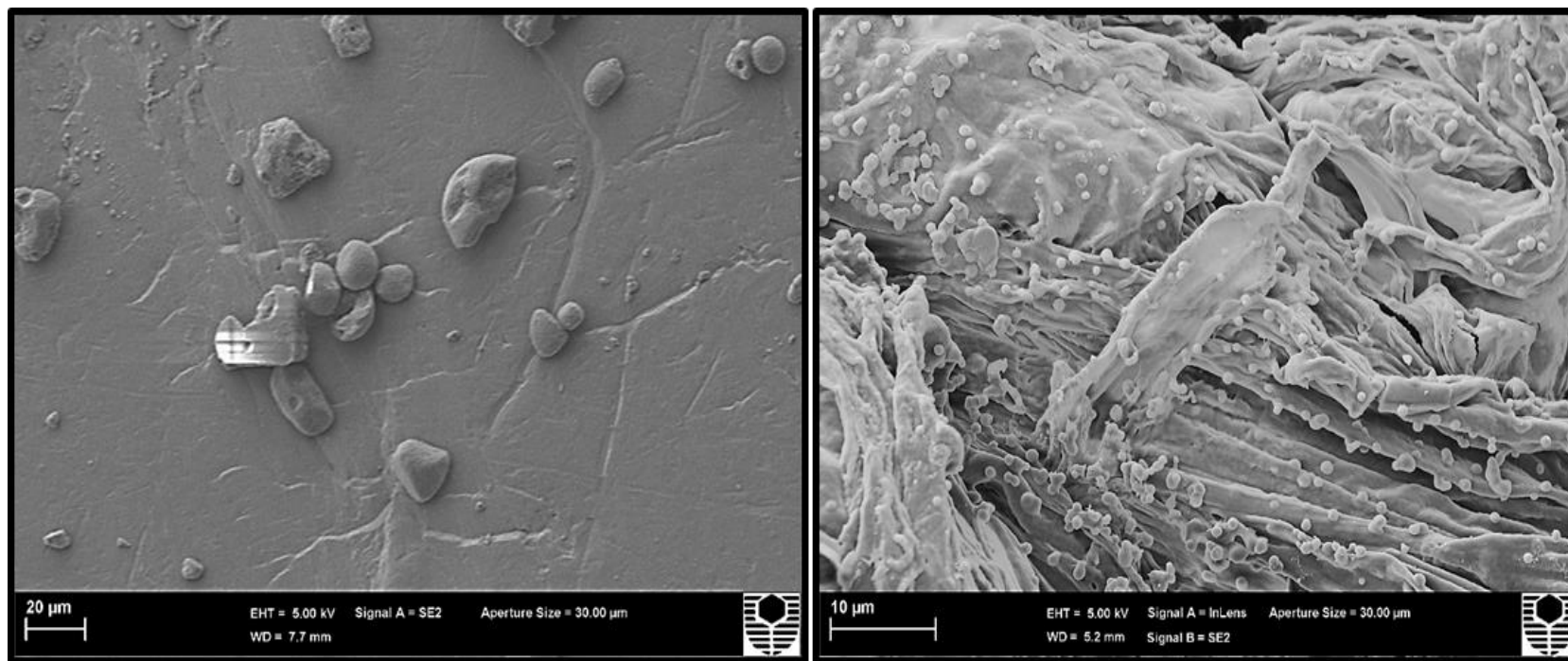
Figure 6.9 SEM images of ARISE processed ES100 from MeOH, (a) 5% conc, (b) 5% conc –magnified view.



(a)

(b)

Figure 6.10 SEM images of ARISE processed ES100 from MeOH (a) 10% conc, (b) 10% conc –magnified view.



(a)

(b)

Figure 6.11 SEM images of ARISE processed ES100 from MeOH, (a) unprocessed ES100, (b) 10 % conc-formation of chunks and microspheres.

The agglomerates and clusters on the samples are the results of the change in process parameters such as anti-solvent (CO₂) pressure, transient pressure during valve opening, and, operating temperature [110]. Controlling parameters to obtain discrete spherical particles is complex and challenging due to the operational constraints. Pristine ES100 has an average size of 25 μm (Figure 6.11 a). Micronization through the ARISE process reduced the particle size by approximately 96 %. Detailed analysis of the micronization of ES100 is explained in Chapter 5, Section 5.4.1. A similar agglomeration effect and spherical morphology were observed by *Tandya* while processing ES100 using the ASES process, which is partially identical to the ARISE process. The particles produced by the ASES process used EtOH as a solvent showed similar morphology as the particles produced by the ARISE process in the current work [97].

6.4.1.2 IMAGE ANALYSIS ON MICRONIZED ES100-5FU FROM MEOH SOLUTION

The SEM-EDS imaging was performed on the 5FU encapsulated Eudragit particles micronized in the ARISE process. The images were taken before and after washing steps to observe the change in morphology due to washing. Figures 6.12- 6.14 shows the SEM imaging of unwashed samples from ARISE. The 5FU-ES100 solution is atomized in the precipitation chamber, and the residual organic solvent is extracted from the solute by the DG CO₂ environment. From the SEM images, it is inferred that 5FU has not been completely encapsulated within the polymer, rather, 5FU re-crystallized separately on the surface of ES100. This phenomenon was observed in all concentrations used in the process. ES100 formed bridged structures, and individual crystals were seemed to adhere to their surface. The effect can be prominently seen at 10 % concentration (Figure 6.14 a, b). The morphology of individual crystals of 5FU resembles a hexagonal (0, 0, 1) shape similar to one obtained by *Esfandiari et al* [414].

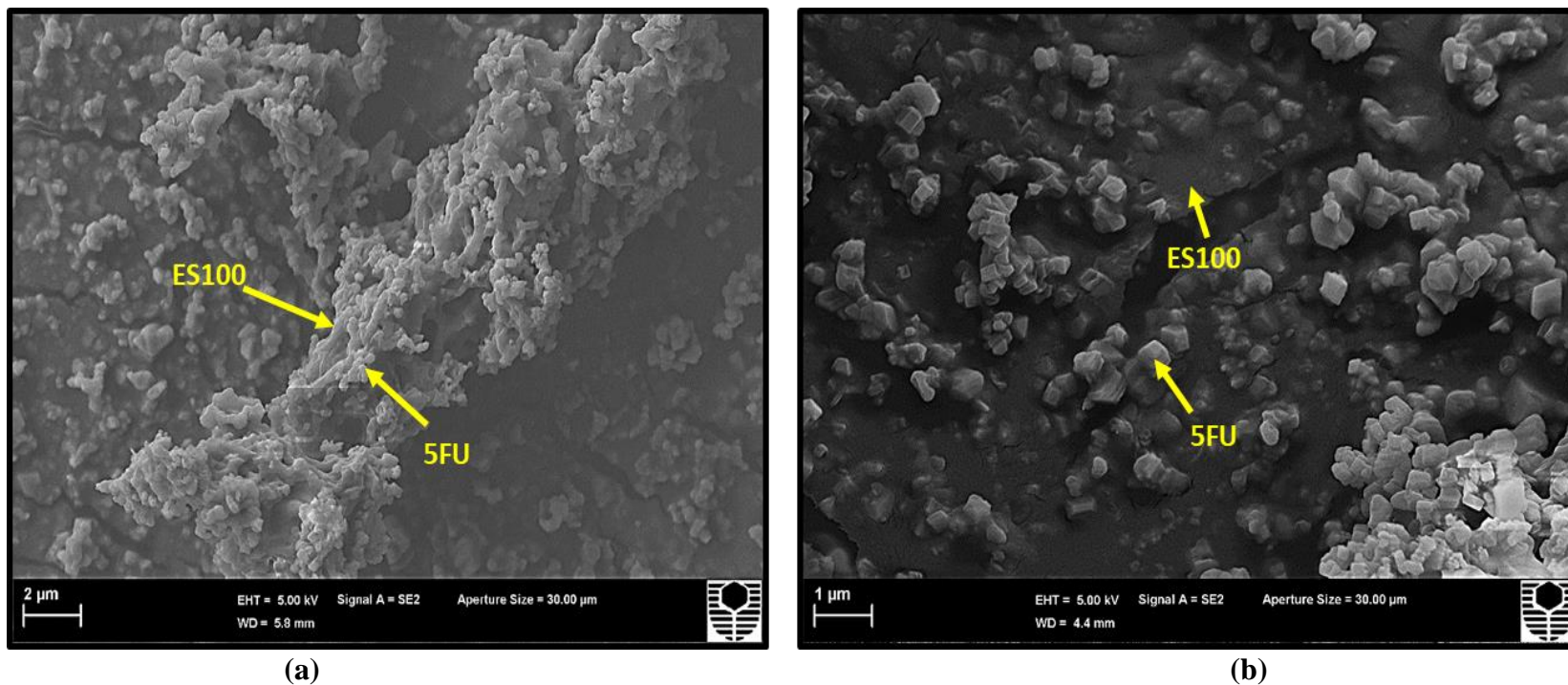
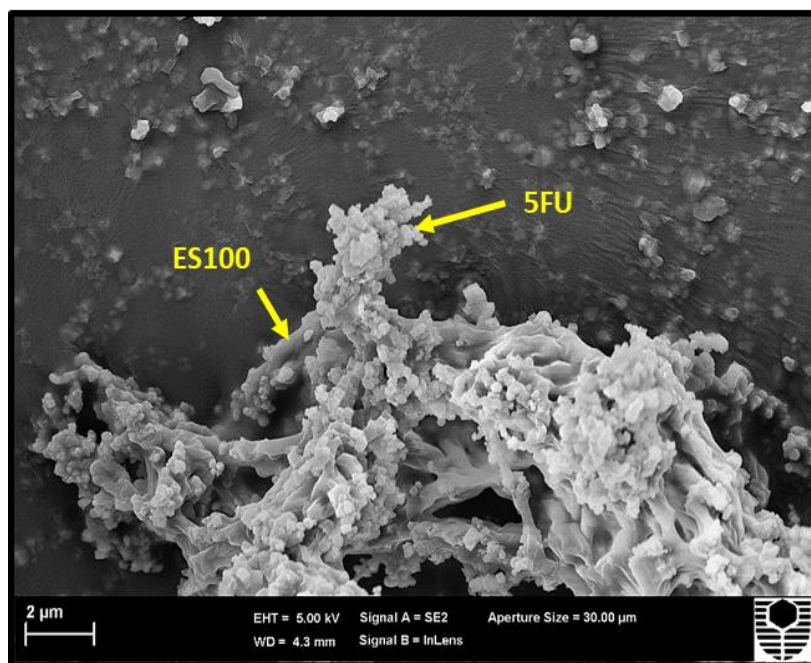
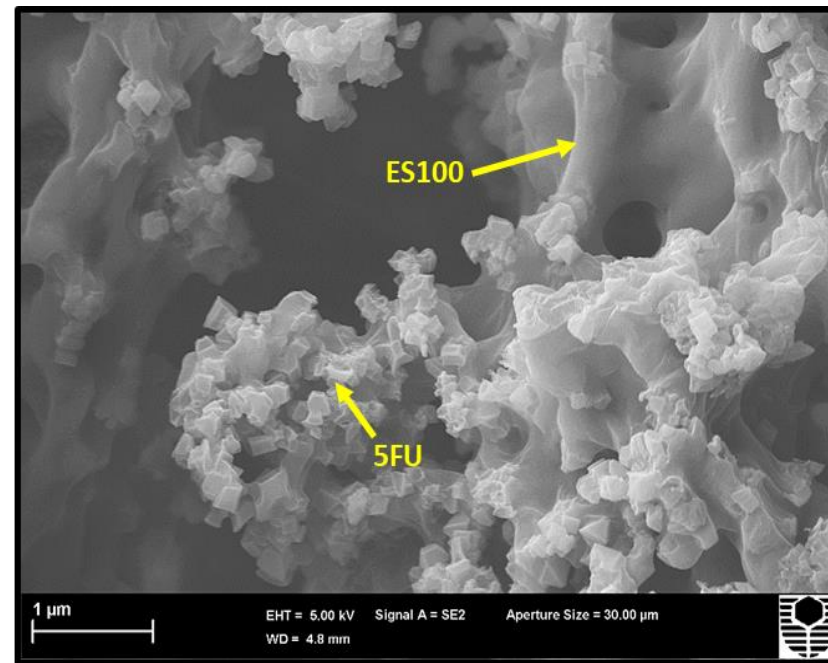


Figure 6.12 SEM images of unwashed-5FU encapsulated ES100 by the ARISE process. (a) 3 % conc (ES100), (b) magnified image showing individually crystallized 5FU on top of the surface of ES100.

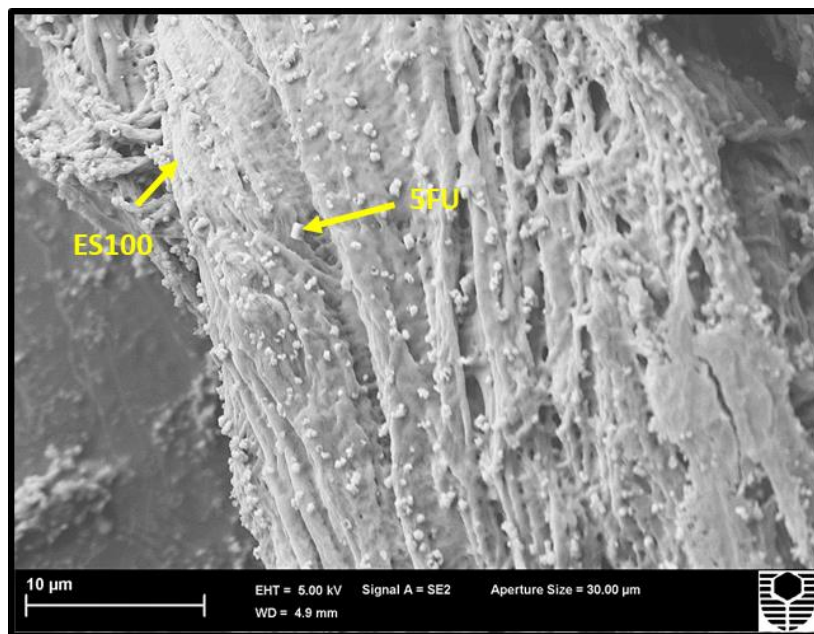


(a)

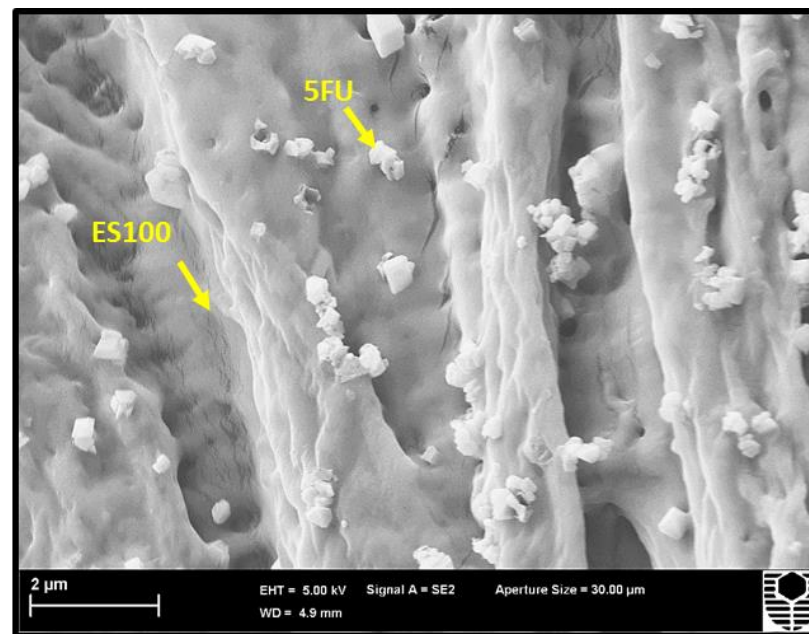


(b)

Figure 6.13 SEM images of unwashed-5FU encapsulated ES100 by the ARISE process. (a) 5 % conc (ES100), (b) magnified image showing individually crystallized 5FU on top of the surface of ES100.



(a)



(b)

Figure 6.14 SEM images of unwashed-5FU encapsulated ES100 by the ARISE process. (a) 10 % conc (ES100), (b) magnified image showing individually crystallized 5FU on top of the surface of ES100.

Pristine 5FU has an average size of around 20 μm (Figure 6.15 a). The re-crystallized 5FU generated by the ARISE process has an average size of about 500 nm, as seen from Figure 6.15 b. About 97.5 % decrease in the particle size achieved by ARISE micronization. The independent re-crystallization of ES100 and 5FU is due to the materials' varying solubility with the solvent. At 25 $^{\circ}\text{C}$, a multi-phase system exists during the droplet formation. The difference in the degree of supersaturation in the solvent-rich phase of the solution and the CO_2 phase influences heterogeneous particle formation. The presence of interfacial tension between the miscible solvent phase and the immiscible solute slows down the rapidity of the solvent extraction inducing bridge formation between micronized particles [163].

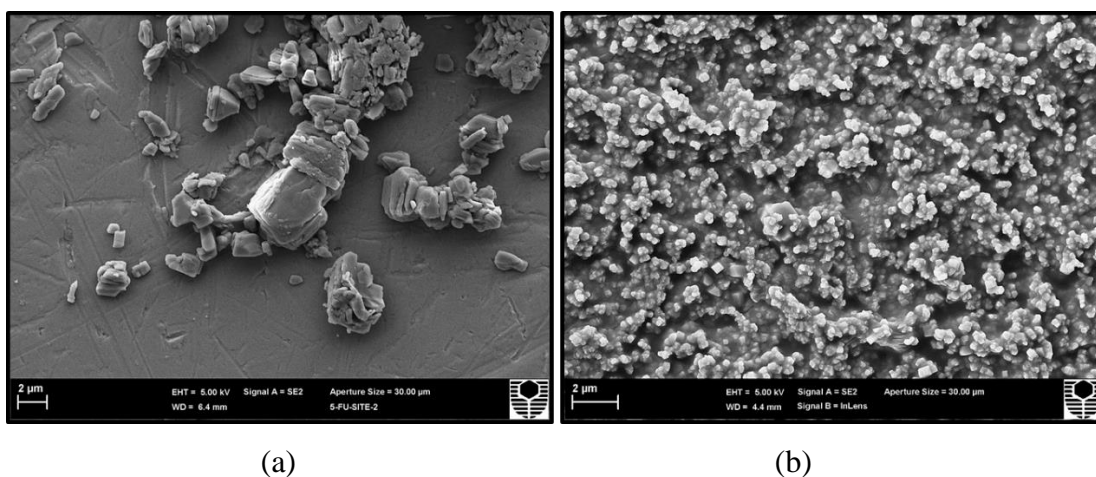


Figure 6.15 SEM image of (a) pristine 5FU, and (b) re-crystallized 5FU by the ARISE process.

The SEM images after moderate washing are shown in Figure 6.18-6.20. Washing of the sample creates craters on the locations where 5FU crystals were attached, indicating that the 5FU molecules were not strongly adsorbed onto ES100 microspheres. A similar effect was observed by *Lamprecht et al* [415] while encapsulating 5FU onto Eudragit RS100, where crater-like imprints were formed on the surface of Eudragit after exposure to the aqueous phase at pH 6.8. The adhesive Van der Waals force between 5FU and ES100 was weak, and the number of craters thus formed increased with an increase in washing time, as seen from Figures 6.18-6.20. The illustration of the formation of craters is shown in Figure 6.16 for visualizing purposes.

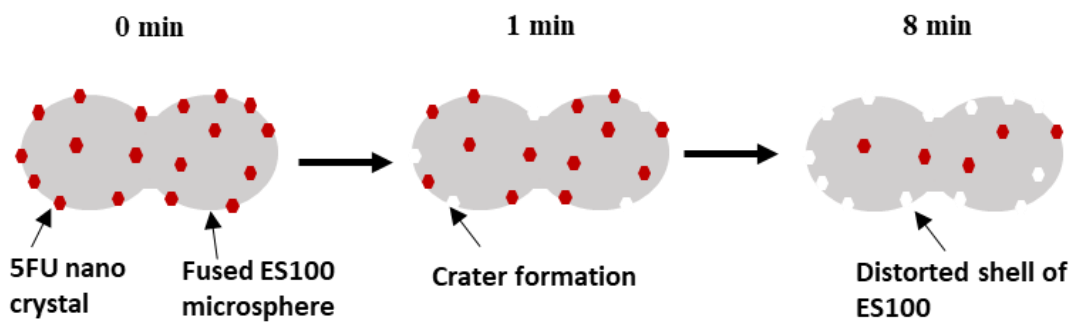


Figure 6.16 Illustration of formation of craters on ES100 microspheres because of washing. (Drawings are for illustration purpose and not to the scale).

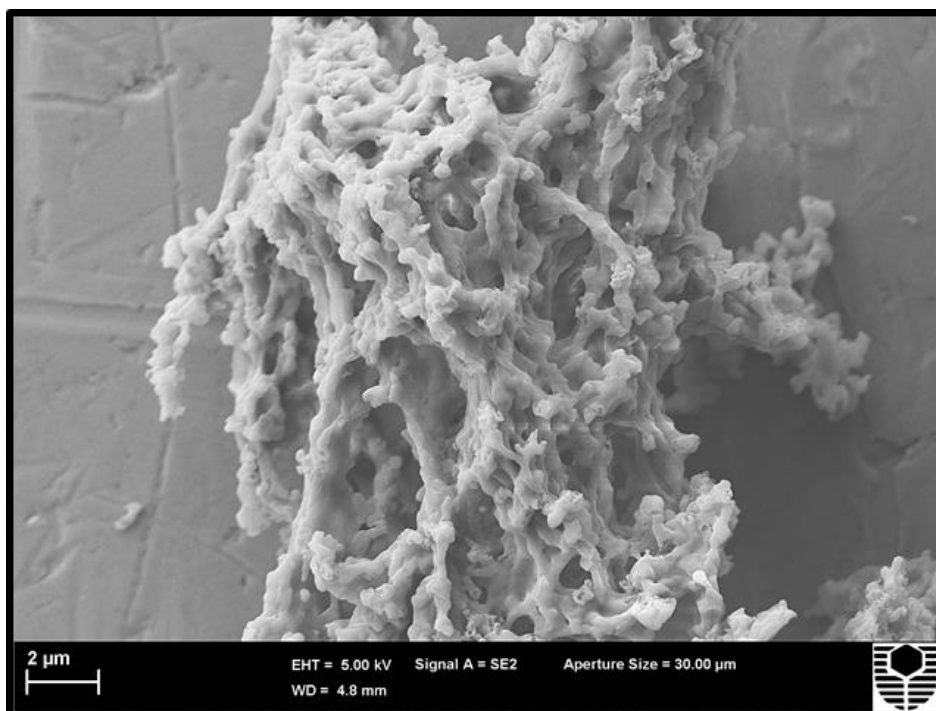
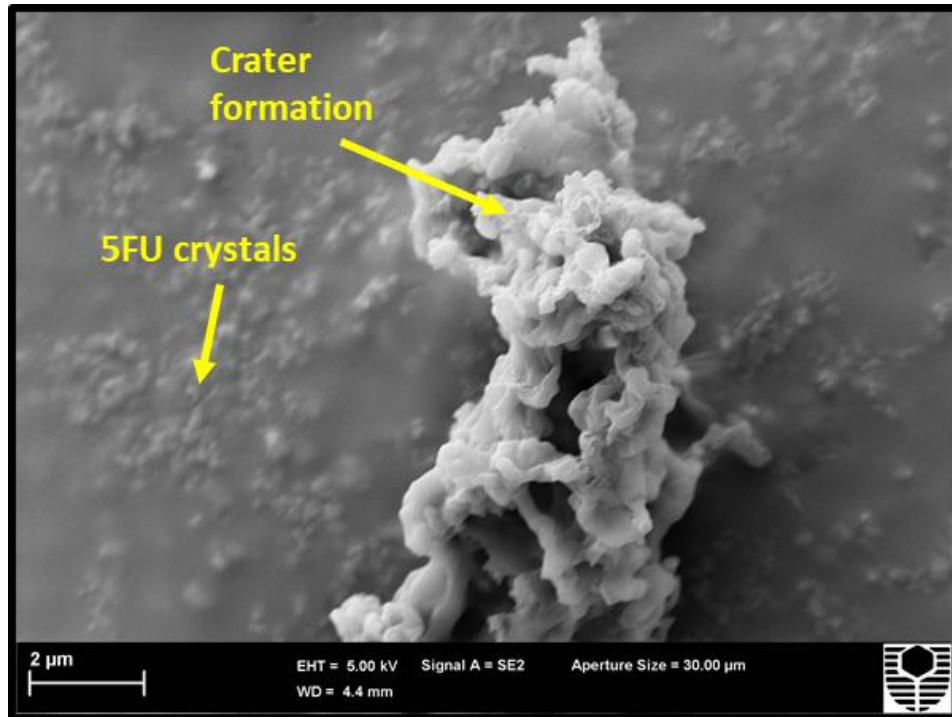
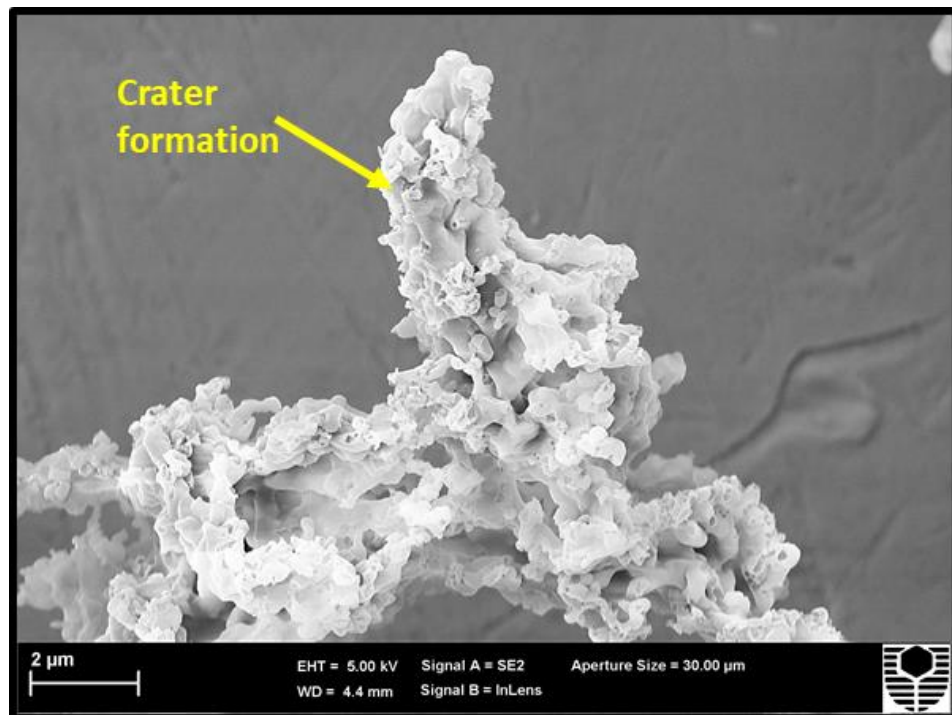


Figure 6.17 SEM images of washed 5FU encapsulated ES100 from ARISE. 3 % conc (ES100) before wash.

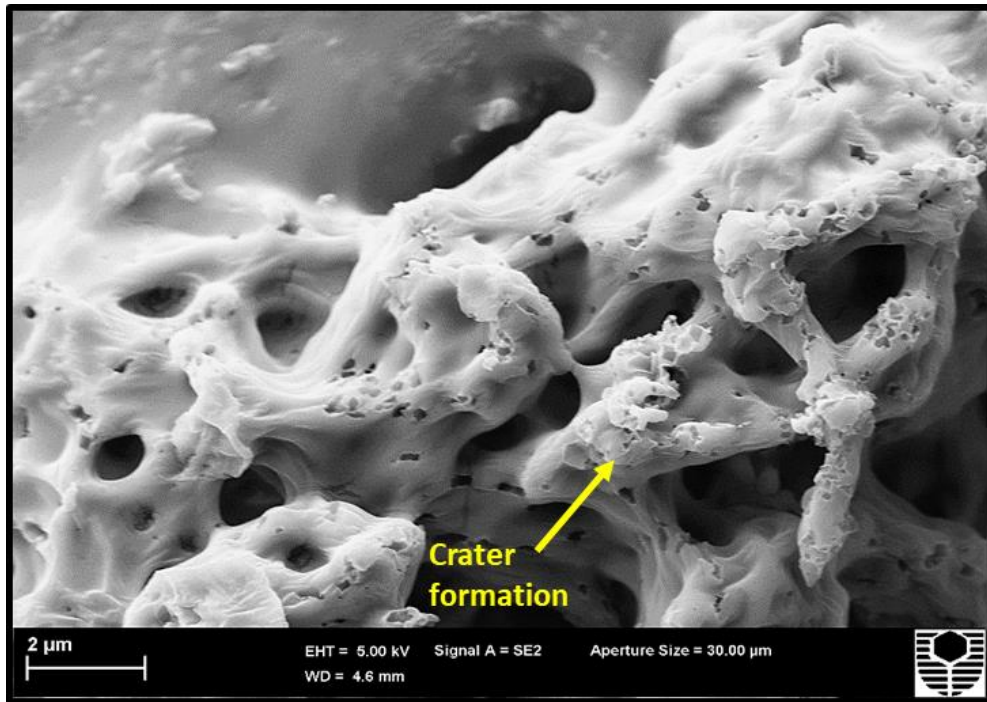


(a)

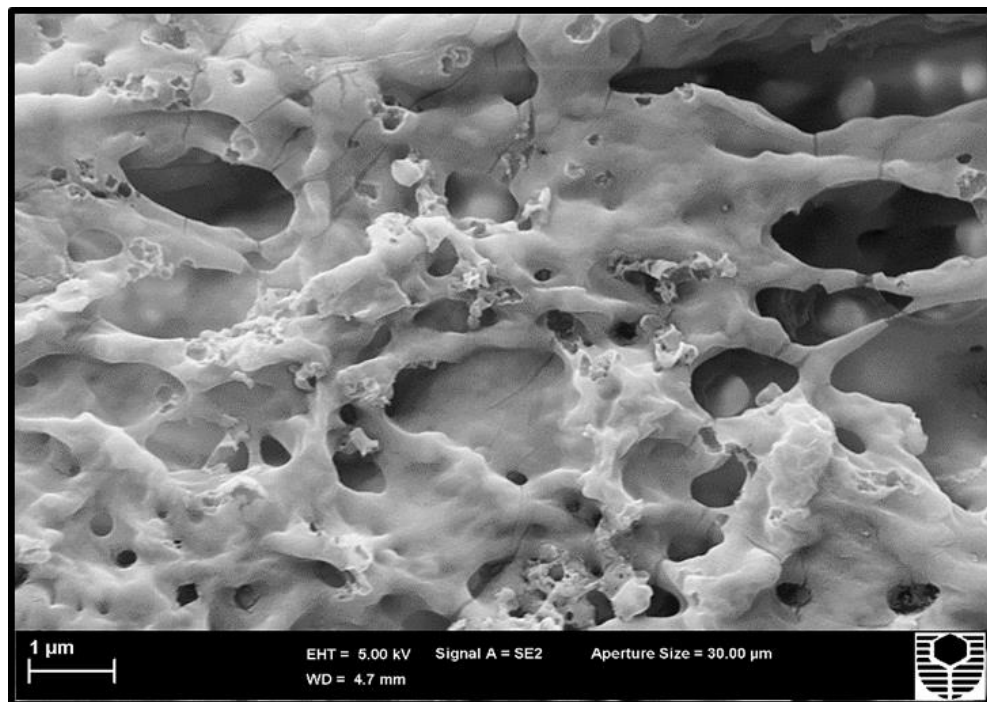


(b)

Figure 6.18 SEM images of washed 5FU encapsulated ES100 from ARISE. (a) 3 % conc (ES100) after 1 min, (b) 3 % conc after 8 min.

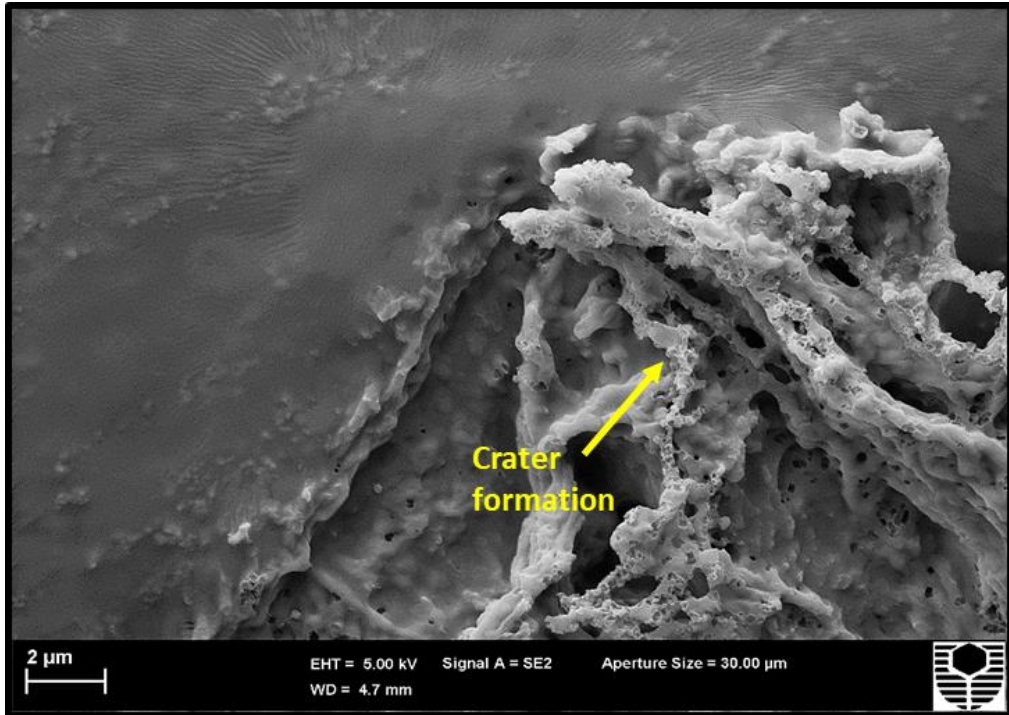


(a)

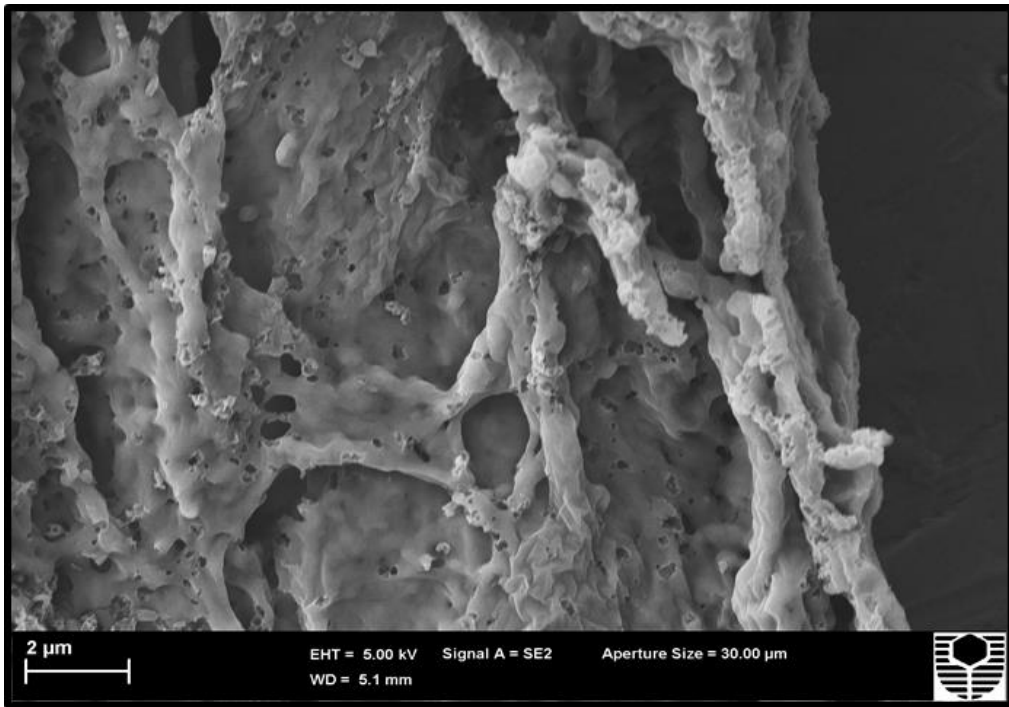


(b)

Figure 6.19 SEM images of washed 5FU encapsulated ES100 from ARISE. (a) 5 % conc (ES100) after 1 min, (b) 5 % conc after 8 min.



(a)

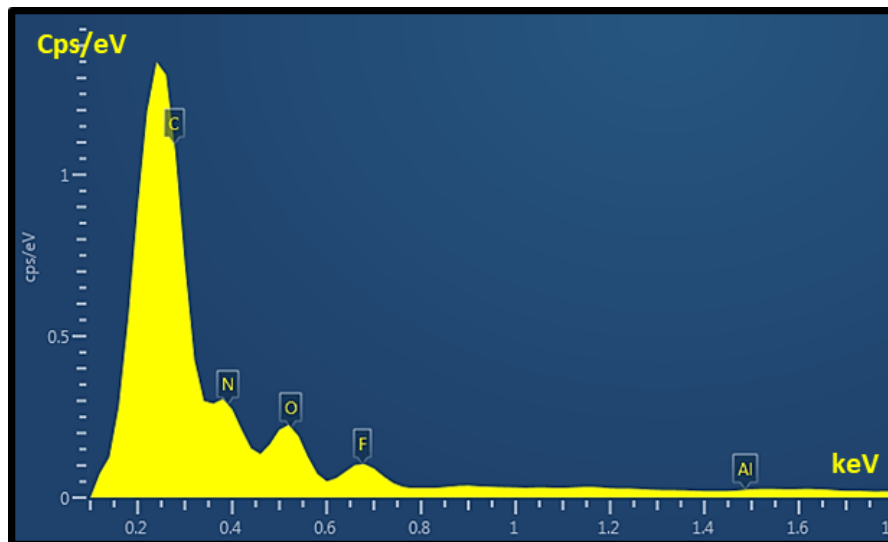


(b)

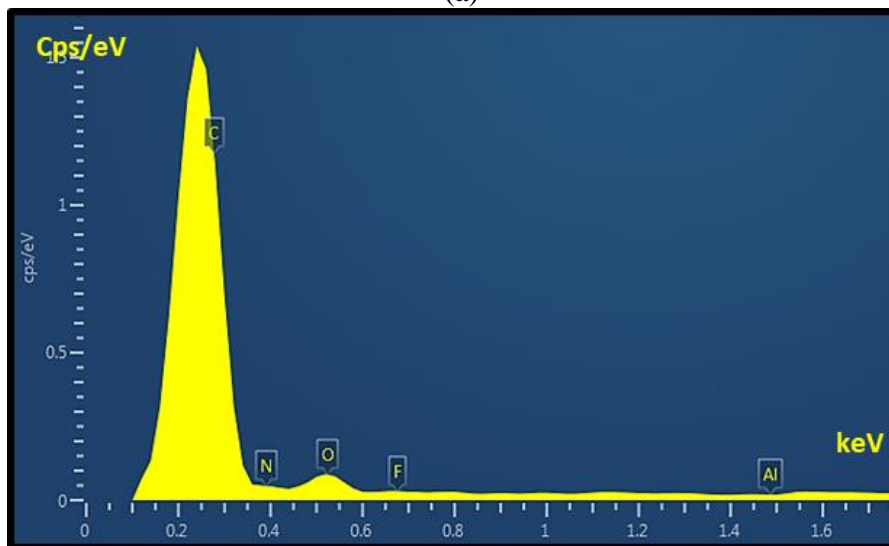
Figure 6.20 SEM images of washed 5FU encapsulated ES100 from ARISE, (a) 10 % conc (ES100) after 1 min, and (b) 10 % conc after 10 min washing in deionized water.

It can be observed that the formation of the microsphere is affected by the inclusion of a foreign compound (drug) to the polymer ES100. Micronized ES100 from MeOH (Figures 6.8-6.11) and EtOH (Chapter 5-Figure 5.7-5.11) show uniform microspheres. Chunks and bridges were formed along with microspheres at high polymer concentrations. Contrarily, the inclusion of 5FU into the polymer matrix did not favour microsphere formation and produced long strands of ES100 with crystals of 5FU adhered to the surface. A similar situation was observed by *Matos et al.* while encapsulating curcumin in Poly Vinylpyrrolidone (PVP) using the SAS process. The Curcumin was not encapsulated onto the PVP matrix, and strands of PVP were formed at 40° C-90 bar and 120 bar conditions. The reason was the difference in the solubility of Curcumin and PVP in the solvent (Ethanol), which caused a change in the supersaturation ratio between the two, restricting simultaneous precipitation[154]. In a similar trend, in the current system, the non-compatibility between 5FU and ES100 and the difference in their solubility in MeOH could be the reason for unsuccessful encapsulation. However, *Lam et al.* employed the ARISE to encapsulate 5FU into Poly-L-lactic acid (PLLA) and noticed spherical morphology with 5FU particles adhering to the surface of the polymer. The formation of strands and chunks were not reported, indicating that PLLA was compatible with 5FU for encapsulation [163]. Similarly, Insulin was encapsulated in ES100 by *Tandya et al* [97] using DG techniques. The process produced a significant population of uniform microsphere of 20 µm with surface-attached Insulin nanoparticle. The variations observed in the above examples indicate that the API-excipient system's behaviour varies not only on the process parameters but also on the compatibility between them and the solvent used.

The elemental analysis from Energy-dispersive X-ray spectroscopy (EDS) performed on the samples is shown in Figure 6.21 (a, b). The peak corresponding to nitrogen and fluorine indicates the presence of 5-Fluorouracil in the sample (Figure 6.21 a). Other peaks of carbon, oxygen, and aluminum are from the mounting stub and tape. The characteristic peak of nitrogen and fluorine disappeared after washing (Figure 6.21 b), indicating that 5FU was washed from the ES100 surface. These results complement the observations mentioned above, suggesting that the inclusion of 5FU with ES100 does not favour the formulation of uniform microspheres as desired under the given experimental conditions.



(a)



(b)

Figure 6.21 Energy-dispersive X-ray Spectroscopy (EDS) of 5FU encapsulated ES100 from ARISE. (a) Unwashed sample, (b) After washing.

6.4.1.3 IMAGE ANALYSIS ON MICRONIZED ES100-SLB FROM ETOH SOLUTION

SLB is a significant constituent of silymarin extracted from milk thistle. It is hydrophobic similar to ES100. The compatibility of SLB with Eudragit with respect to particle formation and morphology was analyzed in similar conditions as that of the 5FU-ES100 system.

Pristine SLB showed an irregular crystalline flaky shape of different sizes ranging from 1 μm to 40 μm - Figure 6.22 [416]. SEM images of SLB encapsulated ES100 is shown in Figures 6.23-6.25. There was no significant variation in morphology observed between washed and unwashed samples. Low concentration of Eudragit produced fused microspheres with individual particles resembling a golf ball of the size of 1-2 μm . The 10 % conc (ES100) solution produced a mix of small microspheres adhered to the surface of larger ones. Evidence of discrete crystal formation of SLB was not seen unlike in 5FU. Pristine SLB, when re-crystallized using CO_2 with EtOH and acetone as solvents, produced flaky and lamellar morphology similar to its pristine form. It was observed that the effect of organic solvent played a significant role compared to CO_2 in deciding the morphology of the SLB produced [417]. In the present study, ethanol was used as the solvent, meaning that a similar flaky morphology as that of pristine SLB could be expected. However, the mixture of SLB and ES100 produced uniform spherical morphology (Figure 6.25), indicating that the combination is effective in terms of polymer-drug compatibility.

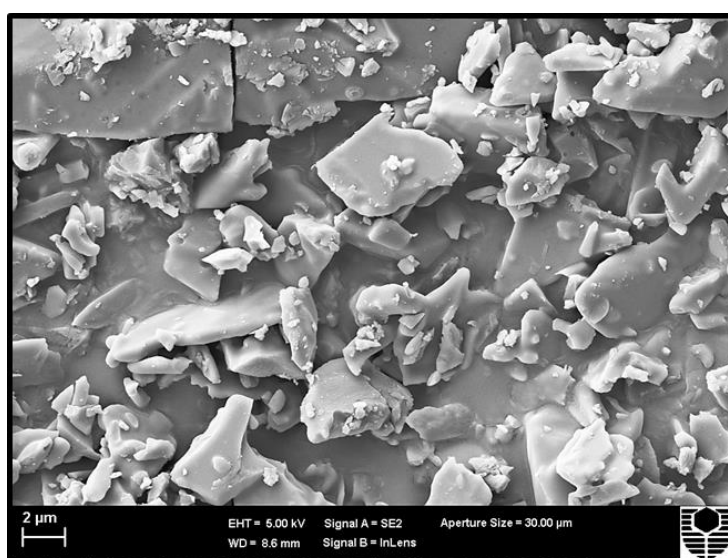
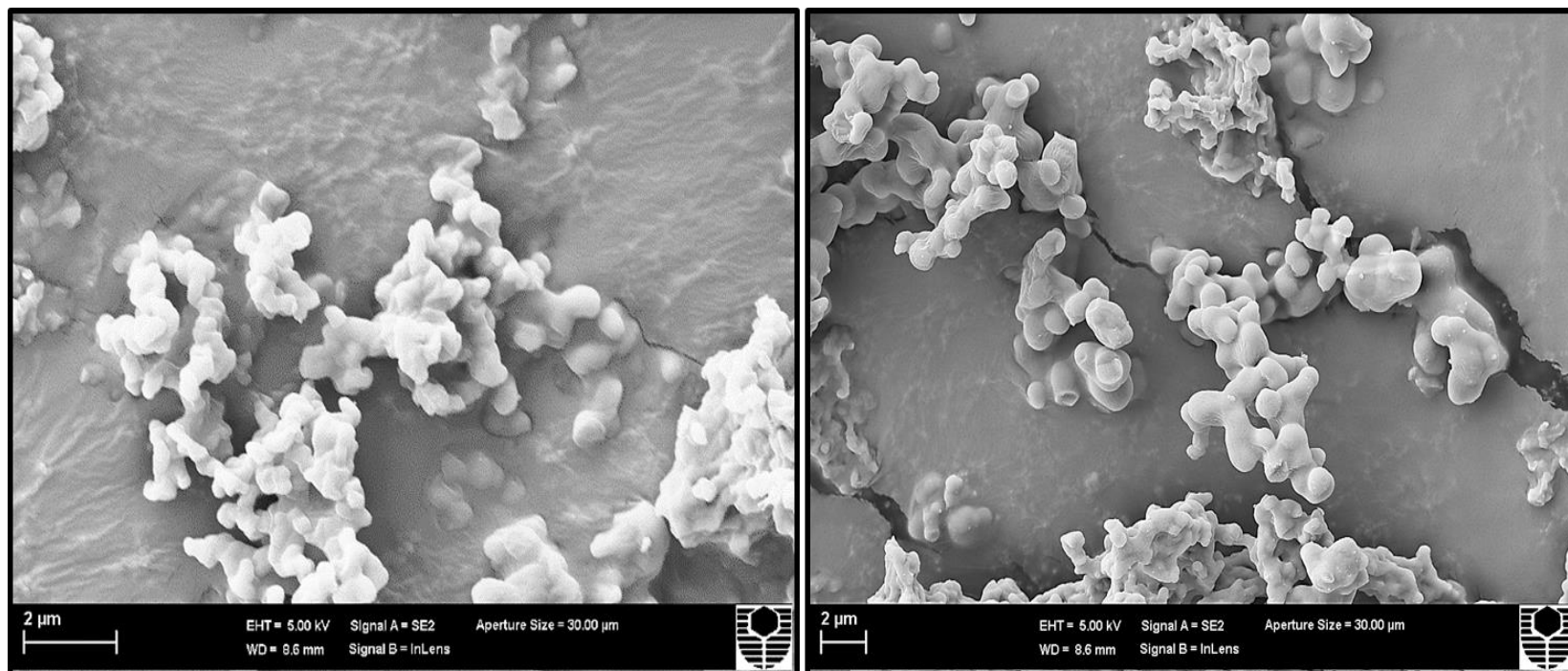


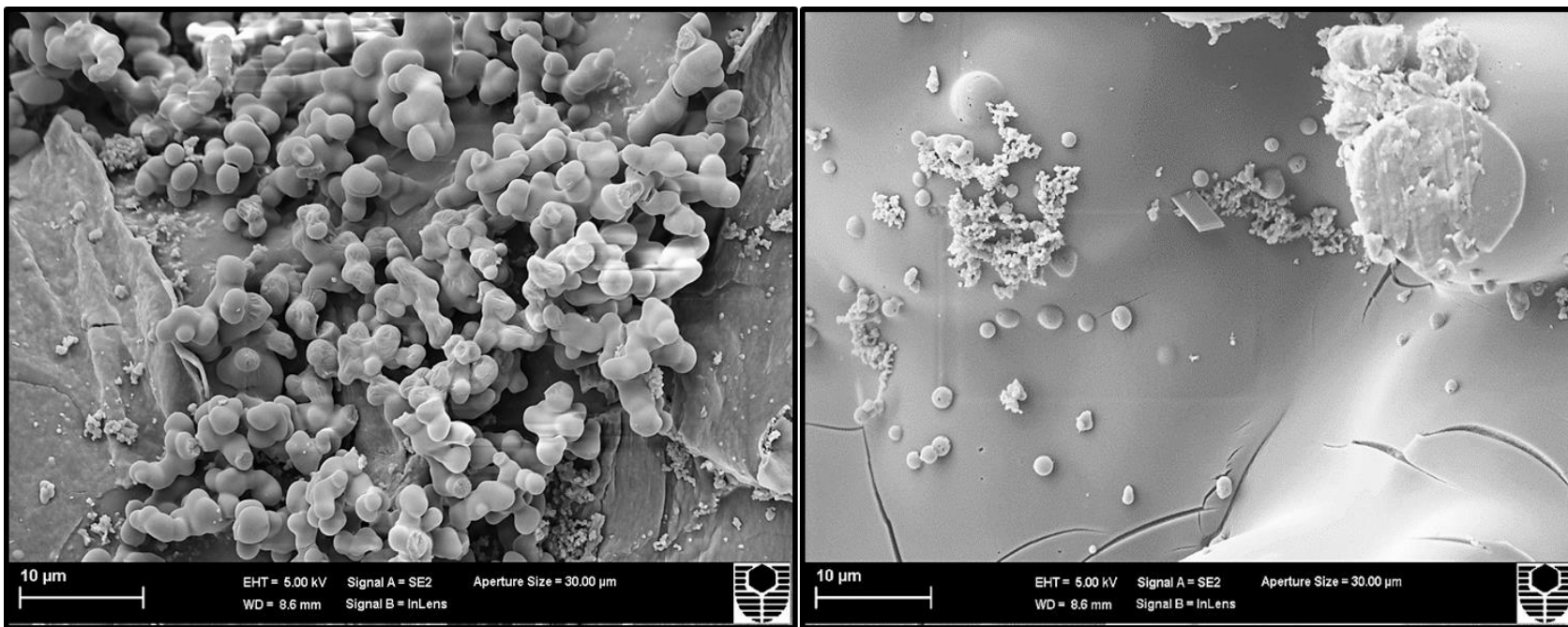
Figure 6.22 SEM image of pristine SLB.



(a)

(b)

Figure 6.23 SEM image of washed samples of SLB encapsulated ES100 from ARISE. (a) 3 % conc (ES100), (b) 5 % conc.



(a)

(b)

Figure 6.24 SEM image of washed samples of SLB encapsulated ES100 from ARISE. (a, b) 10 % conc (ES100).

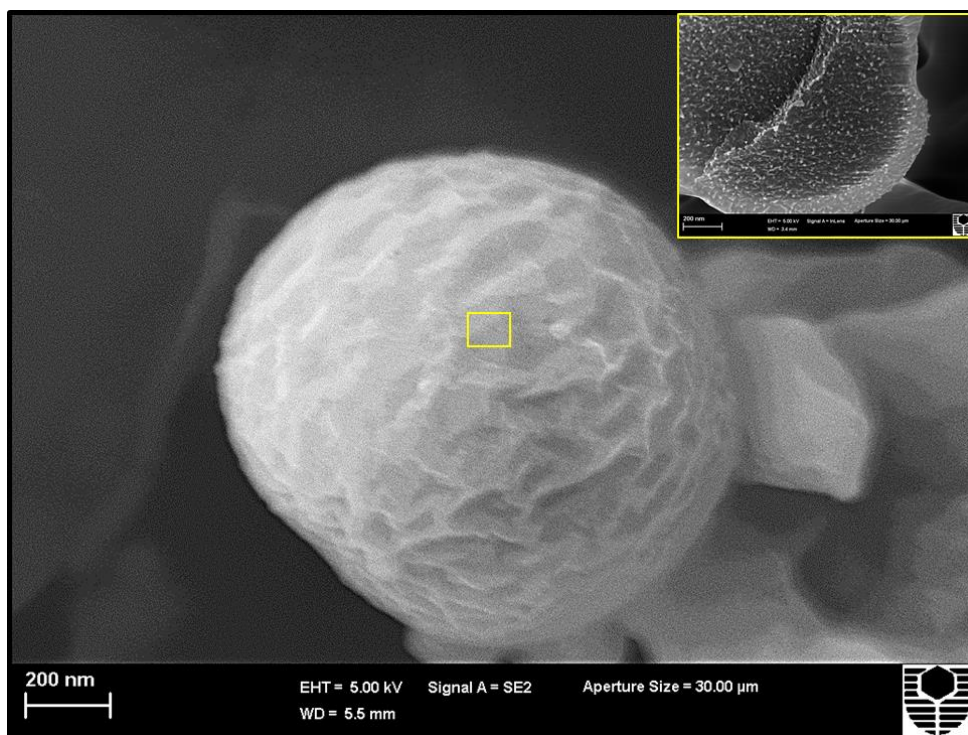


Figure 6.25 SEM image of the individual microsphere of SLB encapsulated ES100 from ARISE. The inset includes the magnified image of the microsphere surface.

6.4.2 DYNAMIC LIGHT SCATTERING MEASUREMENT

The average hydrodynamic diameter of the formulated microspheres is shown in Figure 6.26. The average size (Z_{avg}) of the particles from all the samples were within the range of 2-4 μm , except the samples from 10 % conc of ES100-5FU combination. The average size was identical to the acceptable range for aerodynamic particle size criteria as reported by *Tandya* [97]. The aerodynamic particle size indicates the fine particle fraction in the powder formulation. Ideally, the average hydrodynamic diameter should coincide with the individual particle size measured. However, due to particle size reduction, the electrostatic interaction between the particle surface increases, forming agglomerates [418]. The agglomeration effect can be reduced by the addition of surfactant moderately but cannot be eliminated [419]. Hence the average size reported corresponds to the volume average of the sample suspension used. The ARISE sample showed a variation of $\pm 1.5 \mu\text{m}$ due to the large chunks produced, as mentioned in Section 6.4.1.2. The particle size achieved from the processed ES100 and ES100-SLB combination was in size range of 2 μm to 2.5 μm and showed little variation

between all concentrations and trials. The SLB-ES100 sample exhibited homogenous particles.

The operating temperature of 25 °C is favourable for the production of small particles. With an increase in temperature, the solubility of the solute in the organic solvent increases, making the solute molecules to stay within the solvent domain, retarding the nucleation rate. The particles thus formed tend to agglomerate due to solute-solute interaction [131, 417]. Comprehensively, the ARISE processing of ES100 has proven to produce uniformly spherical microparticles with an individual particle size of 600-700 nm and an average size of 2-4 μm , which is over 75 % reduction in size.

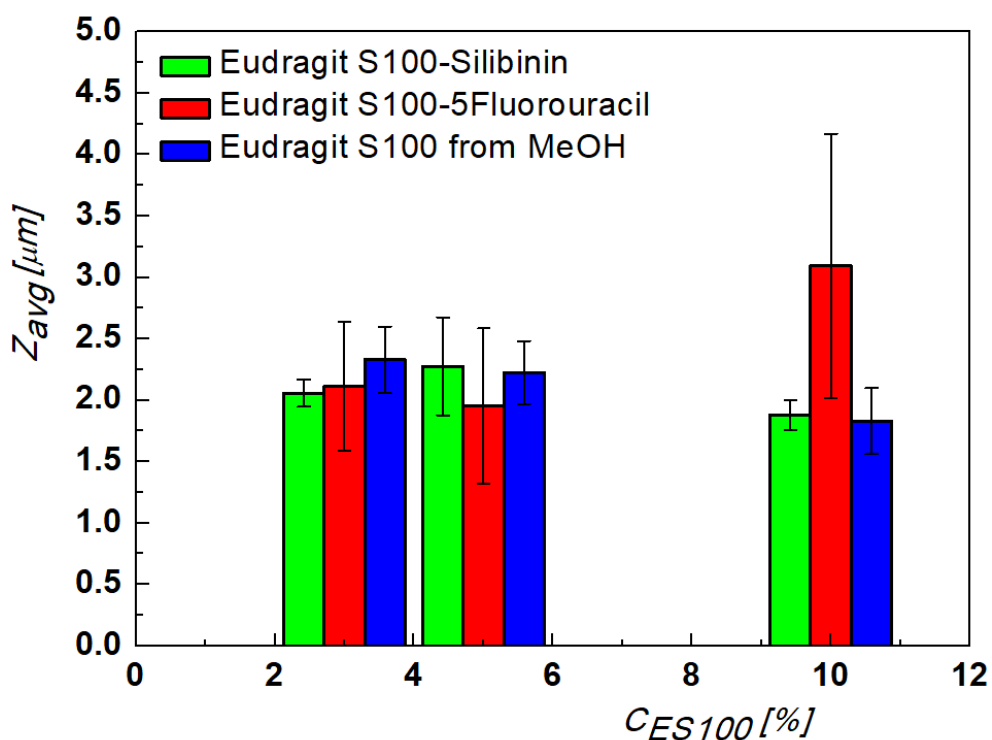


Figure 6.26 Average hydrodynamic diameter (Z_{avg}) of ARISE processed samples of ES100, ES100-5FU, and ES100-SLB microparticles. (Error is SD of 3 experimental trials).

6.5 DRUG LOADING

The loading of 5FU and SLB onto ES100 was estimated following the procedure mentioned in Chapter-3, Section 3.3.7. The drug loading is presented in Figure 6.27.

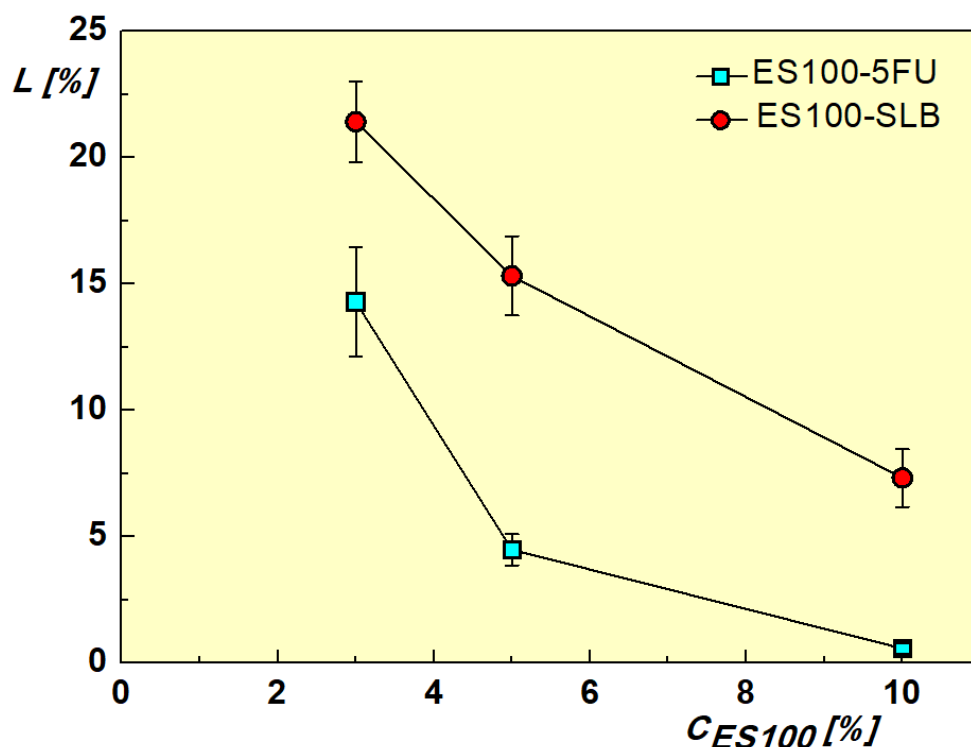


Figure 6.27 Drug loading, L , as a function of Concentration of ES100 (C_{ES100}).

The drug loading, L , was found to be high with SLB-ES100 combination than that of 5FU-ES100 in all concentrations. Maximum loading of 21.4 % was observed with SLB at 3 % ES100 conc, while a minimum of 0.6 % loading was achieved with 5FU at 10 % ES100 conc. The trend in L was observed to decrease with an increase in the concentration of excipient (ES100) in both cases. This means that the fraction of polymer molecules exposed to the available free drug molecules is higher at any given time.

The chemical structure of Eudragit consists of a repeated arrangement of carbonyl groups- Chapter 2, Section 2.4. Molecules of CO_2 have an affinity towards interacting with basic sites in polymers [102]. The presence of such basic sites like carbonyl group favours CO_2 to interact with ES100 molecules, enhancing its segmental and chain mobility creating a swelling effect on the polymer [420, 421]. This enhanced mobility can significantly ease the diffusion path for solute (drug) molecules to impregnate within ES100. Thus CO_2 acts as a molecular lubricant facilitating encapsulation [422]. Fur-

ther, the high-pressure (110 bar equilibration pressure) range used in the process improves the solubility of CO₂ with the polymers [179], which is favourable for the above-mentioned reasons. The encapsulation process is illustrated in Figure 6.28.

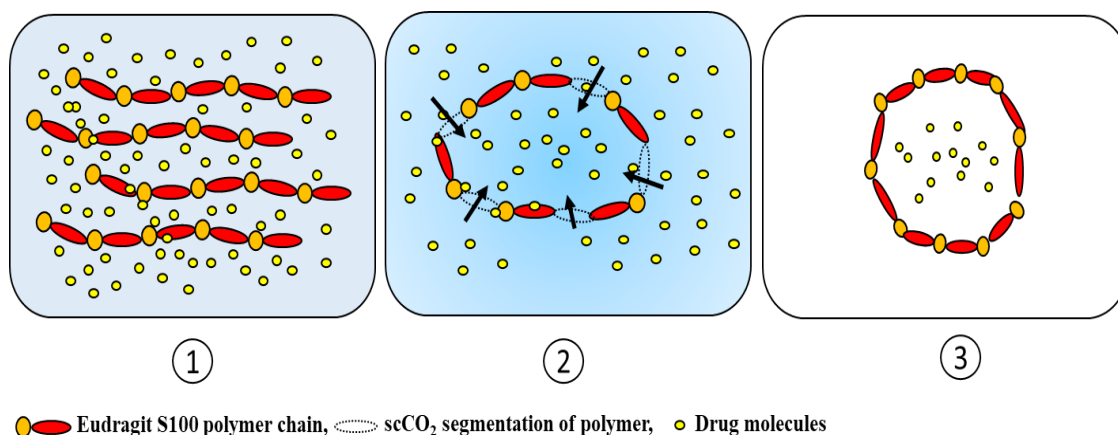


Figure 6.28 Illustration of encapsulation of drug in the polymer in a DG environment. (1) Homogeneous drug-polymer solution, (2) Expansion of solvent under DG environment and segmentation of polymer chain for the diffusion of drug molecules into the polymer matrix, (3) Solvent extracted drug encapsulated microsphere. (Drawings are for illustration and not to the scale).

According to *Kazarian et al* [423], the encapsulation of drug into polymers takes place through (i) infusion of scCO₂ soluble drug into the polymer matrix and depressurization for precipitating the solutes, or (ii) partitioning process wherein scCO₂ insoluble drugs are encapsulated in polymer matrix due to the high affinity of the drug towards polymer than scCO₂. The high solubility of 5FU and SLB in the polymer mixture enables the drug loading through the partitioning process [422].

The effectiveness of loading depends on the number of parameters, particularly on the drug and excipient concentration and the compatibility between them [122]. The polymer-drug compatibility or miscibility is decided upon the total solubility parameter (δ_t) of the materials [424]. The solubility parameters affects various types of interaction between drug and polymer molecules such as Van der Waals dispersion forces, dipole-dipole interactions, and hydrogen bonding [378, 425, 426]. *Liu et al* [427] proposed that drugs and polymer with similar total solubility parameters (δ_t) have mutual solubility. The total solubility parameter of a hydrophobic drug, Ellipticine, was compared with water-insoluble polymers, and the degree of compatibility was analyzed. In the present work, SLB and Eudragit are both hydrophobic and have a high affinity towards

each other[424]. This facilitates effective encapsulation of SLB into ES100, hence high loading.

On the other hand, hydrophilic 5FU has a low affinity towards ES100, causing segregated precipitation during the process and a decrease in loading [179, 428]. Unlike 5FU, the SLB-ES100 system forms a microsphere wherein SLB is homogeneously dissolved in the polymer matrix without forming separate crystals. The high lipophilicity of both ES100 and SLB enables successful entrapment, whereas hydrophilicity of 5FU induces separation of ES100. SEM images (Figures 6.17-6.20, and Figures 6.23-6.25) conform to these observations [429]. Hence, the combined advantage of SLB-ES100 compatibility and improved solubility of ES100 in CO₂ promotes the high encapsulation efficiency of the drug and the formation of microspheres.

6.5.2 EFFECT OF WASHING ON DRUG LOADING

In Section 6.3.2, the effect of washing time on α_d was detailed for the 5FU-ES100 system. The study suggested that prolonged washing of the drug-loaded sample removes the encapsulated drugs and deludes the drug loading estimation. Complementing the α_d obtained in Section 6.3.2-Figure 6.7, the corresponding drug loading, L , was estimated after every wash, and the graph was plotted, as shown in Figure 6.29.

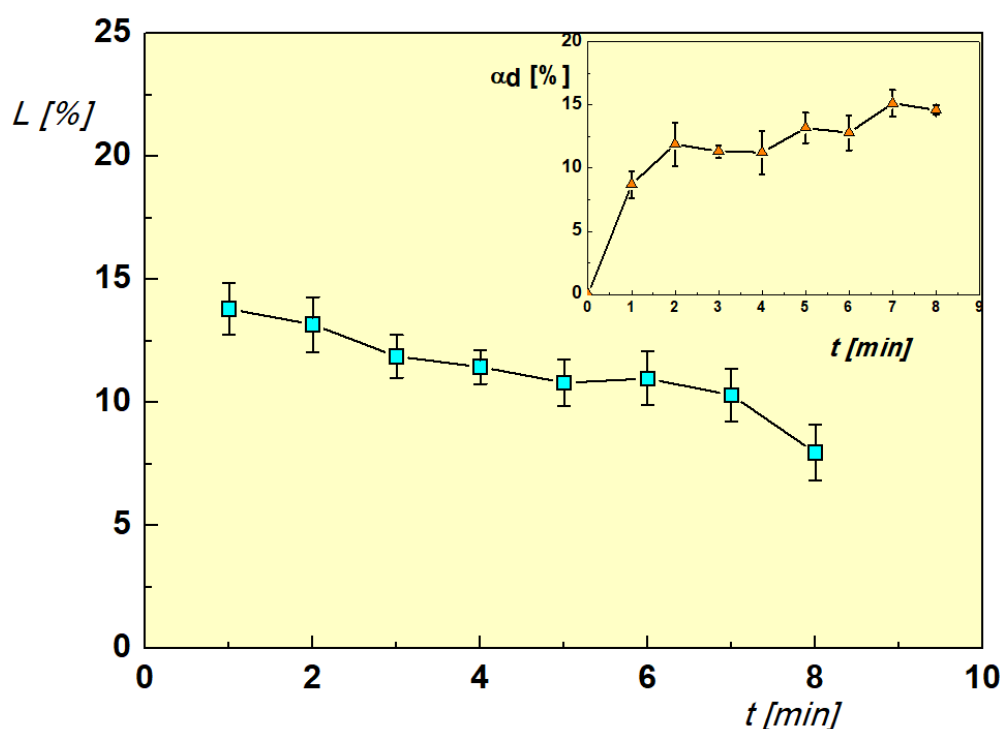


Figure 6.29 Variation of loading, L with washing time, t for 3 % conc ES100-5FU system. (Error is SD of 3 trials). Inset graph from Figure 6.7 in Section 6.3.2.

The loading decreases proportionally to the increase in α_d (graph in inset). As mentioned earlier, increasing the wash time increases the contact time between the solvent and bulk of the sample, successively removing drug particles that leads to the decrease of the loading. Hence, 1 min mild washing of samples was chosen as the optimal wash time.

6.6 ENCAPSULATION EFFICIENCY

The encapsulation efficiency (E) of the process was calculated using the formula mentioned in Chapter 3, Section 3.3.7. The E of SLB-ES100 formulation was observed to be over 90 % consistently for all the ES100 concentrations as evident from Figure 6.30. High E value with variation of ± 2 % concerning SLB-ES100 indicates that most of the input drug was encapsulated through the ARISE process. The compatibility between SLB and ES100 and the formation of a homogenous amorphous phase enhance the overall E . From Chapter 2, Table 2.8, Section 2.4, we can infer that SLB produced E above 90 % with similar hydrophobic polymers such as Eudragit RL, PO, and Cholic acid [229, 234].

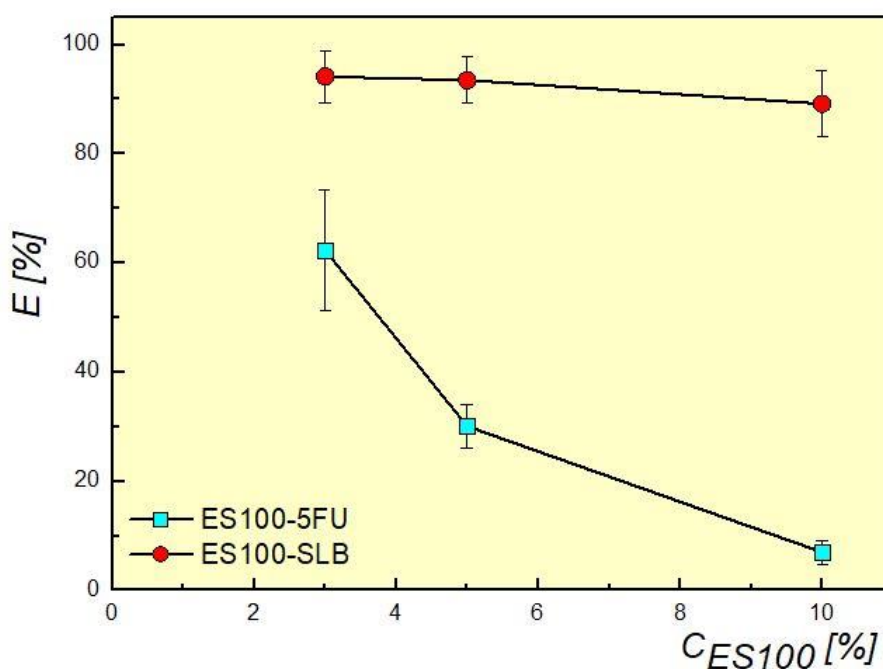


Figure 6.30 Encapsulation efficiency (E) as a function of ES100 concentration.

The SLB-HPMC-EC (Hydroxypropyl methylcellulose-Ethyl cellulose) microsphere formulated by *Garg et al* [231] demonstrated a high E of 94.2 %. However, the direct loading of SLB onto the ES100 polymer matrix resulted in a maximum E of 87.7% E . In a similar scenario to the current work, encapsulation of hydrophobic Curcumin and Palmitoylethanolamide (PEA) in polyvinylpyrrolidone (PVP) using the SAA process produced ≈ 100 % encapsulation efficiency for all the drug-polymer ratios [182, 430]. Contrary to the high E effect in the SLB-ES100 formulation, the E decreased exponentially with an increase in ES100 concentration in the 5FU-ES100 formulation. Due to the low affinity of 5FU towards ES100, 5FU tends to adhere to the surface of ES100 and further dissolves in the organic phase, decreasing the efficiency (E)[229, 431].

6.7 X-RAY DIFFRACTION STUDY

The X-ray diffraction spectrum was obtained for the samples by the procedures described in Chapter-3, Section 3.3.6. 5FU in its pristine form showed high-intensity peaks at 2θ 19.01°, 24.50°, and 28.62° [432, 433] confirming its crystalline phase as shown in Figure 6.31. ES100 exists in the amorphous form with a specific characteristic peak at 2θ :14.5° as shown in Figure 6.32.

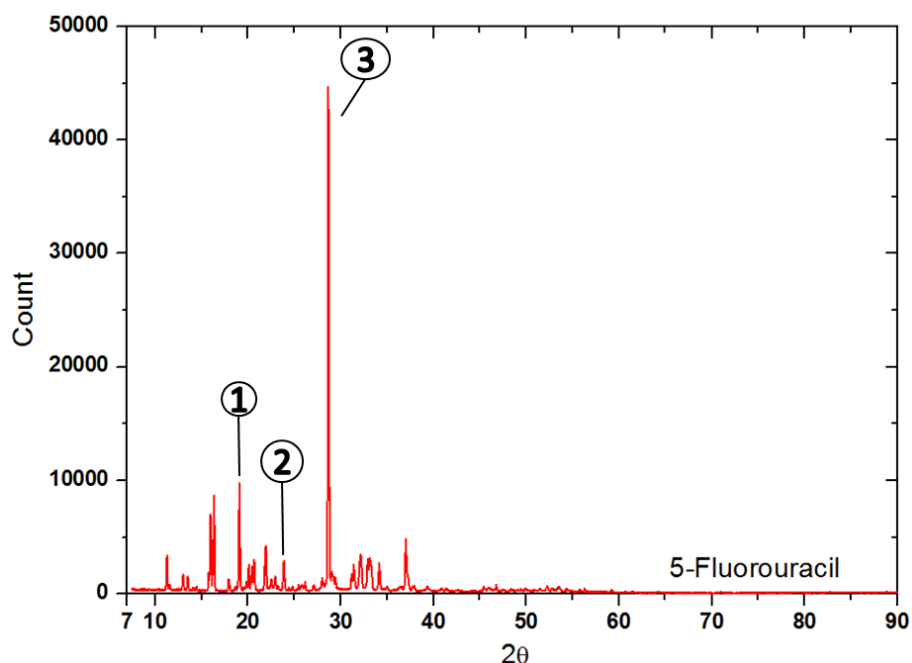


Figure 6.31 XRD pattern of pristine 5FU with crystalline phase at 2θ : (1) 19.01 °, (2) 24.50 °, and (3) 28.62°.

We can observe a systematic decrease in the intensity of crystalline peaks of 5FU with an increase in ES100 concentration. The shift of peaks from 19.01° to 21° 2θ in the encapsulated sample indicates the change in crystallinity from pristine form due to the ARISE processing. The decrease in peak can be attributed to (1) low detection level due to complete dispersion of drug with polymer molecules, or due to the (2) Surface adhesion or absence of drug molecules in the sample [433]. In the current sample, a reduction in peak intensity of the crystalline phase of 5FU is due to the absence of 5FU in the sample. The formation of separate crystals of 5FU and carters due to washing validate the XRD pattern obtained. The systematic decrease in the crystalline phase of 5FU with an increase in ES100 concentration further confirms the argument for low drug loading percentage (0.6 %) at high ES100 concentration (10 %) (Section 6.5).

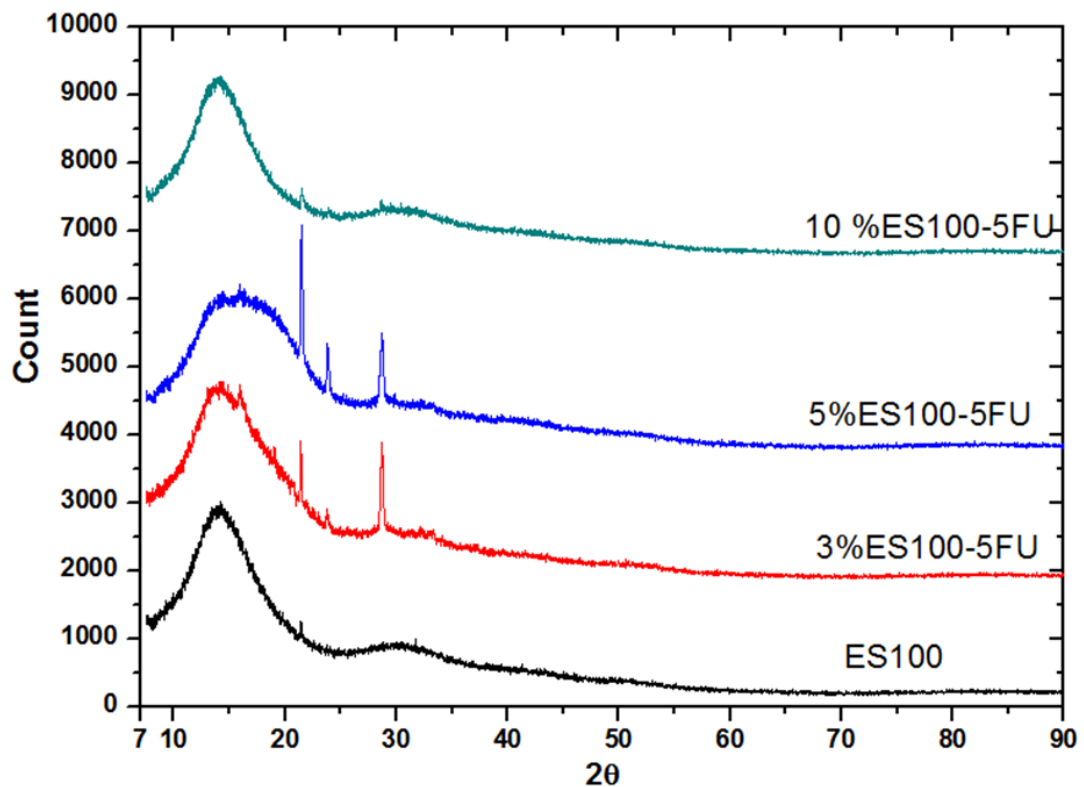


Figure 6.32 XRD patterns of pristine ES100 and 5FU encapsulated ES100 from ARISE process for all concentrations.

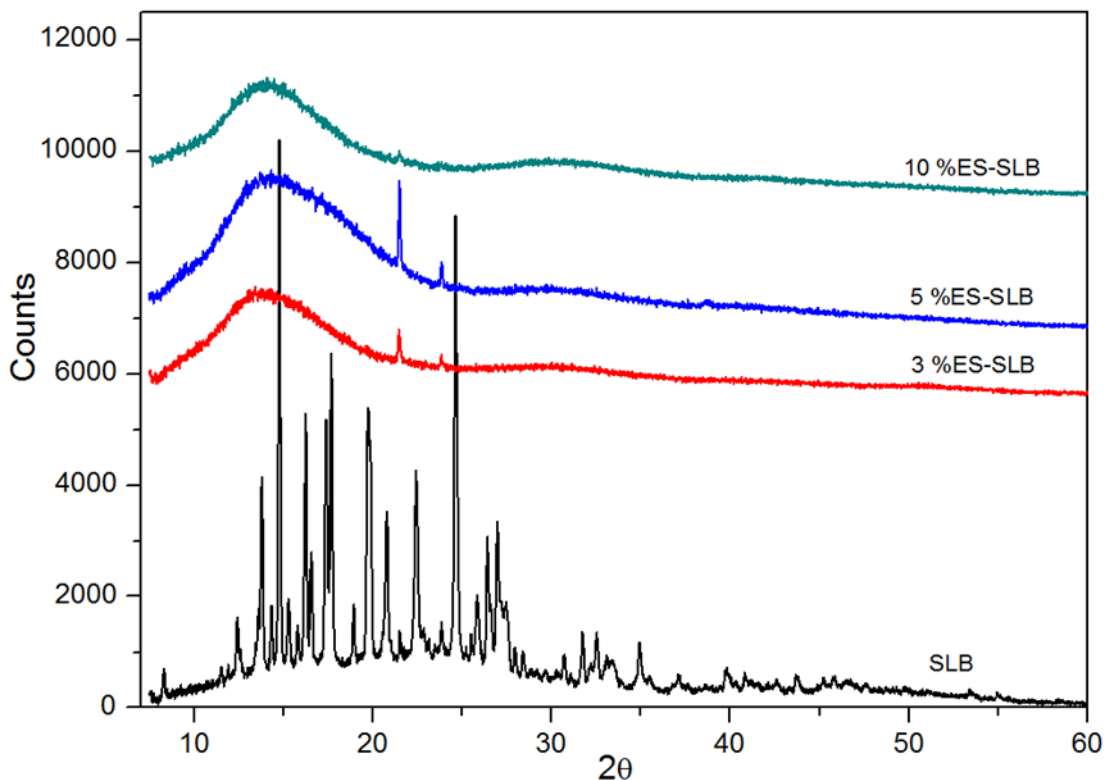


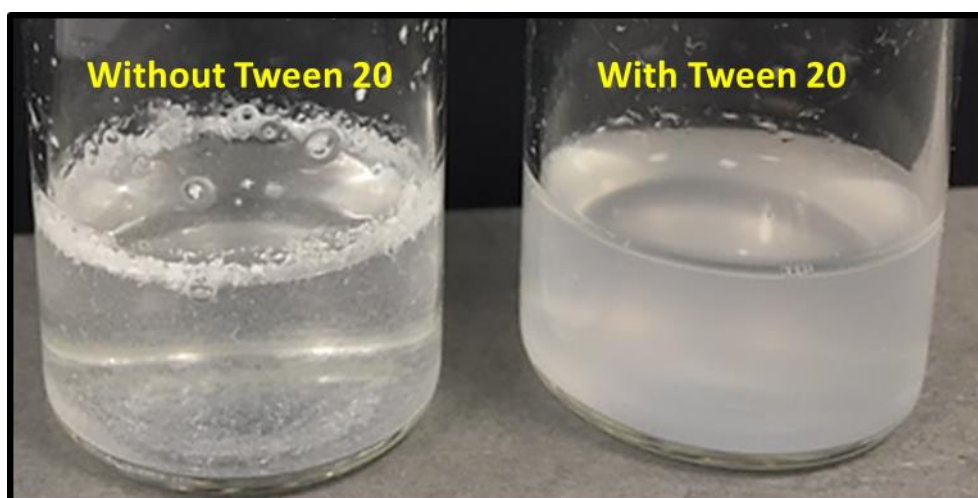
Figure 6.33 XRD pattern of pristine SLB and SLB loaded ES100 samples from ARISE process for all concentrations.

SLB has multiple characteristic peaks at 2θ : 14.7° , 16.1° , 17° , 19.5° , 20° , 21.2° , and 24.9° , as seen from Figure 6.33, confirming the highly crystalline nature of SLB in pristine form. With encapsulation into ES100, the peaks disappear, ensuring that the crystalline nature of SLB is changed to an amorphous form due to the encapsulation [230, 434]. The decrease in intensity of SLB with an increase in the concentration of ES100 may be confused with the pattern observed with 5FU. As indicated in previous discussions, SLB and ES100 are hydrophobic materials and form a homogenous mixture. This high affinity allows the molecular level dispersion of SLB into the polymer matrix, forming an amorphous phase. The absence of crystals of SLB and high loading percentage from the ARISE samples indicate the high molecular level dispersion of SLB with ES100. This observation agreed with other published works [235, 239, 435]. A comparable trend in the XRD pattern of Tamoxifen encapsulated PLLA microspheres was observed by *Alias et al* [136]. The absence of Tamoxifen characteristic peak in the encapsulated microspheres confirmed the complete transition of the crystalline phase to amorphous and loading of drug in the PLLA matrix.

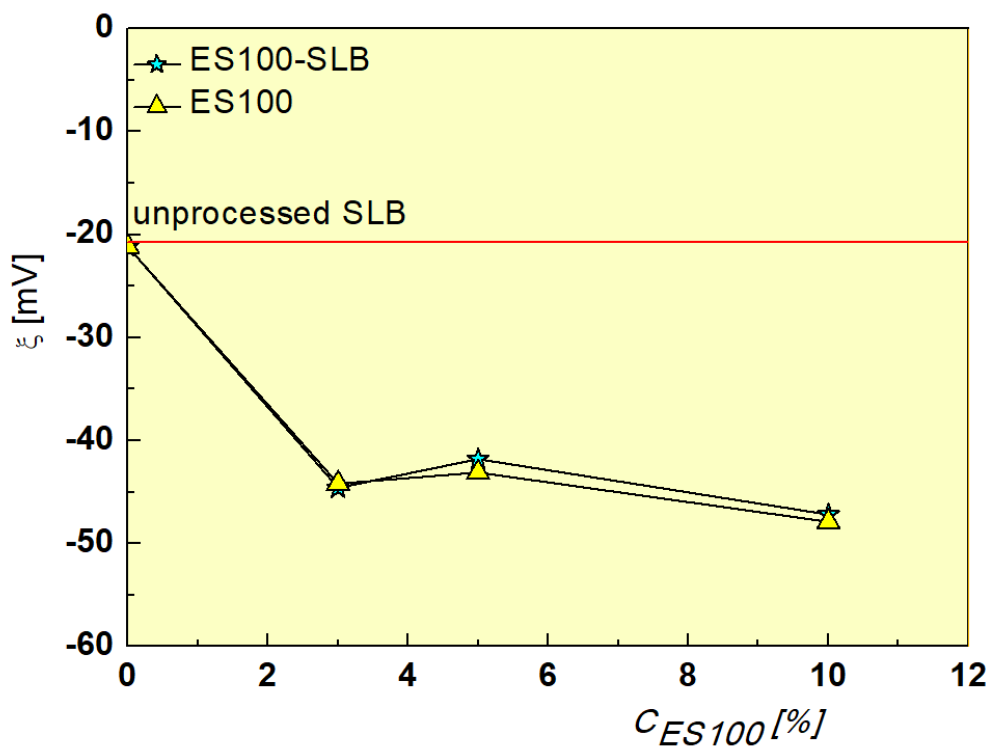
6.8 ZETA POTENTIAL

The procedure for measurement of zeta potential of the samples are explained in Chapter-3, Section 3.3.5. The produce from the ARISE is fluffy particulates. They do not form a homogenous suspension, and the addition of surfactant stabilize the suspension by maintaining the charge balance as shown in Figure 6.34 (a) [419]. ES100 has a zeta potential of -45 mV, which is due to the increase in the ionized fraction at pH 5 (pH >2) causing a net negative charge on the surface of the polymer [436]. The value did not show much variation with the change in concentration as observed by *Barbosa et al.* [436]. Unprocessed SLB showed a zeta potential of -20 mV, indicated by the straight line in Figure 6.34 (b).

SLB and ES100 have similar pKa of 6.63 and 6.66 respectively [436-439] forming weak acids. The similarity in their ionization behaviour facilitates intermolecular binding and uniform dispersion of drug molecules within the polymer matrix. Therefore, the surface charge did not show significant variation between SLB loaded and unloaded samples. Further, a high zeta potential value indicates a high physical stability of the micro/nanoparticles [228, 230, 435] from the ARISE process.



(a)

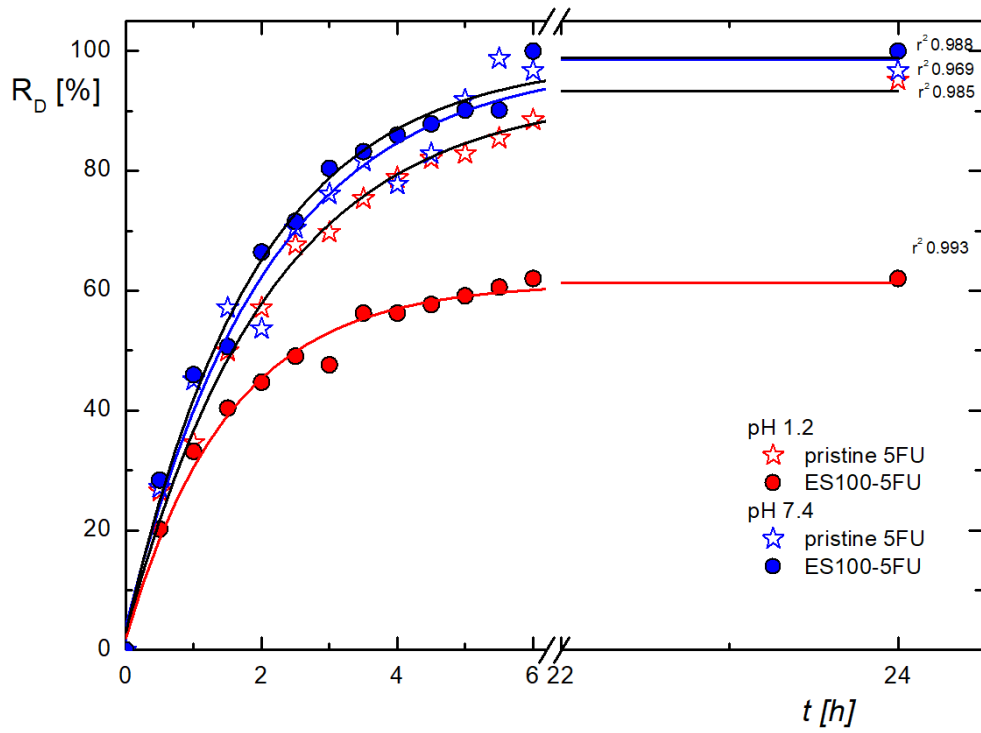


(b)

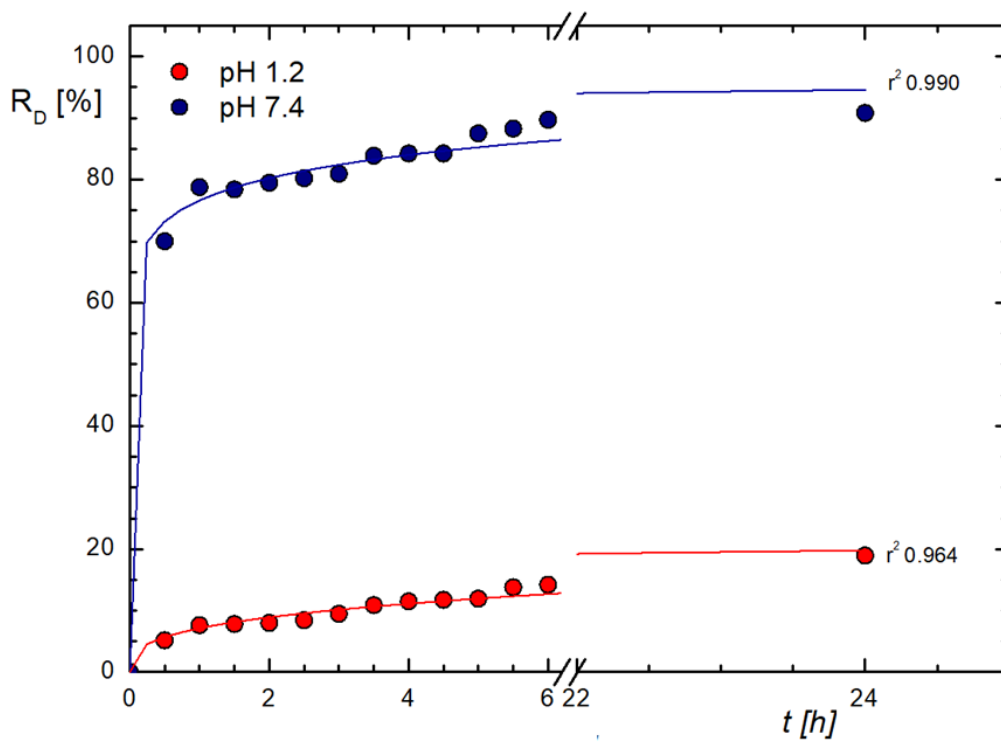
Figure 6.34 (a) The stable suspension formed after the addition of 0.5 % (v/v) Tween 20, (b) Zeta potential of ARISE processed SLB-ES100 sample dispersed in distilled water.

6.9 IN VITRO DRUG RELEASE STUDY

The *in vitro* drug release study was performed in a simulated Gastro-Intestinal environment using the dialysis method detailed in Chapter 3, Section 3.1.7, and 3.3.8. The cumulative release of the drug from the microsphere is plotted in Figure 6.35 (a, b).



(a)



(b)

Figure 6.35 Cumulative release of (a) 5FU from ES100 microsphere, and (b) SLB from ES100 microsphere in simulated gastric pH 1.2 and Intestinal pH 7.4 at 37 °C.

The drug release profile (R_D) of 5FU in Figure 6.35 (a) follows first-order kinetics, relating Cumulative release (R_D), maximum release, $R_D^\infty = R_D$ at $t=\infty$, and release offset y_0 as in Eq 6.2. The release behaviour of 5FU was like the profile exhibited in Chapter 4, Section (4.3).

$$R_D = y_0 + R_D^\infty e^{-\frac{t}{\tau}} \quad (6.2)$$

The release in both the pH (1.2 and 7.4) commenced from the first 30 min of dissolution. Unloaded 5FU released 90 % within 6 h in both the physiological pH. In the ES100-5FU system, about 60% of 5FU was released in gastric pH 1.2 within 6 h and ceased to release further. The release indicates that about 60 % of 5FU starts releasing before reaching the targeted site in the intestine. The release reached 90 % in Intestinal pH 7.4 within 6 h. 5FU is hydrophilic (solubility >10 mg/ml) and molecules of 5FU deprotonate at pH 7.4, and the effective electrostatic repulsive force between 5FU and ES100 molecule is higher, leading to complete dissolution of 5FU into the solution [418, 440-443]. Although a significant fraction of 5FU dissolve into the gastric medium, the remaining fraction of the drug is still retained on the surface of ES100. This is due to the reduction of the electrostatic repulsive force between 5FU and ES100 due to the increase in the ionic strength of the medium. Hence, the overall force between the remaining surface attached 5FU and ES100 is dominated by the net attractive Van der Waals force, lowering further dissolution [418]. The time constant (τ) was observed to be 120 min in both the pH conditions affirming similar observations from Chapter 4, Section (4.3). The ES100-5FU system was not effective in restricting the premature release of drug in the gastric medium. The non-compatibility between 5FU and ES100 could be the cause of using other polysaccharides as encapsulating material for 5FU (Chapter 2, Section 2.4, and Table 2.7).

The release kinetics of the ES100-SLB system followed the Korsmeyer-Peppas model (Equation 6.3), describing the drug release from the polymer matrix [444]. The drug release profile is shown in Figure 6.35 (b)

$$R_D = R_D^\infty [Kt^n] \quad (6.3)$$

Where K is the Korsmeyer-Peppas rate constant, and n is the release exponent. The value of n determines the mechanism of drug release and K , on the formulation characteristics [445]. *Arora et al* [444] described the mechanism of drug release from polymer system based on (i) diffusion, (ii) erosion, and (iii) combined diffusion-erosion

process, which is decided by the value of n . The values of n and K for the ES100-SLB system are tabulated in Table 6.2. The values of n in both the pH conditions were less than 0.45 confirming fickian diffusion mechanism [444, 446, 447]. Pristine SLB exhibited poor aqueous solubility [64, 233]. Micronization and encapsulation of SLB into ES100 improved the aqueous solubility and hence the bioavailability by changing the crystalline phase of SLB to amorphous and increase in surface area due to micronization [230]. The conversion of crystalline SLB to the amorphous phase in the encapsulate improved the dissolution rate in colon conditions due to the increase in Gibbs free energy as mentioned in Chapter 2, Section (2.2) [66]. The release pattern in Figure 6.35 (b) showed a maximum of 20 % in gastric and over 90 % release in intestinal conditions, respectively. Initial burst release was observed within the first 30 min of dissolution, followed by a gradual increment up to 90 % (pH 7.4) and 20 % (pH 1.2) within the first 6 h of dissolution. As stated before, ES100 is highly water-insoluble and ideally, no release of SLB should be found in pH 1.2. However *Varshosaz et al.* [229] observed a lower burst release, which is attributed to the presence of absorbed SLB crystals on the surface of ES100 while encapsulating SLB onto Eudragit RL and PO copolymers. Similar examples of reduction in the release of hydrophobic drugs in gastric medium and their extended release in the colon due to the inclusion of ES100 were discussed in Chapter 2, Section 2.4.

Table 6.2 Correlation coefficient (r^2), Korsmeyer-Peppas rate constant (K), and release exponent (n) of ES100-SLB system at pH 1.2 and 7.4.

pH	Iteration	r^2	K [min^{-1}]	n
1.2	1	0.905	0.285	0.194
	2	0.964	0.112	0.320
7.4	1	0.992	0.626	0.080
	2	0.990	0.649	0.066

It is recollected from Section 6.7 that, ES100 has a pKa of 6.6, meaning that the ion dissociation is restricted in acidic medium, keeping ES100 undissolved (Figure 6.36) [436]. At a pH above its pKa, the carboxyl group ionizes, leading to the maximum release of SLB in the intestine [433]. The low R in pH 1.2 and an instantaneous spike in R, at pH 7.4 attributes to the pH-triggered dissolution of ES100. Metabolic studies

show that the half-life of SLB is approximately 6 h and about 80 % of it is discharged with bile in the urine due to poor bioavailability [439, 448]. In the current work, substantial release in intestinal pH within the half-life period indicates the effective delivery in the colon improving the efficacy.

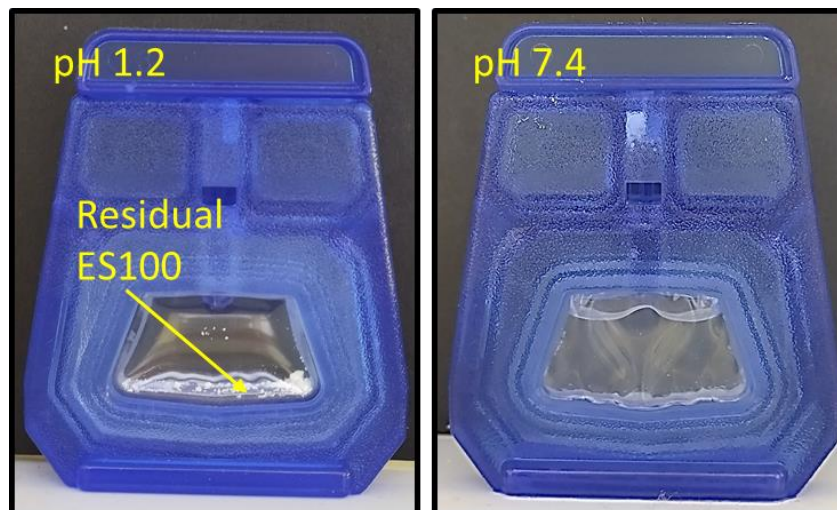


Figure 6.36 Residual suspension of ES100 after 24 h dialysis in pH 1.2, and in pH 7.4.

Several published research works have shown varying release of 5FU and SLB from the polymer matrix. *Gavini et al* encapsulated 5FU into a Gelatin capsule and exhibited a 100 % release over 25 h [449]. 5FU encapsulated in Silkworm bombyx pupal showed 65 % release within the first 2 h of dissolution [450]. 5FU encapsulated in Poly(lactic-co-glycolic acid) displayed complete release in 168 h in the simulated gastrointestinal environment [451]. *Pooja et al* [230] demonstrated R_D of about 50% release at pH 1.2 within the first 3h of dissolution from nanoparticles of SLB encapsulated Chitosan-tripolyphosphate. The value is larger than the R_D achieved in the current work, demonstrating the effectual confinement of SLB in the ES100 matrix.

These varying results between 5FU and SLB system suggest that the difference in release mechanism is not only determined by the encapsulation technique but also on the drug-nano carrier compatibility. In the current work, the cumulative effect of binding affinity of 5FU and SLB with ES100 suggests that the SLB-ES100 combination is advisable compared to 5FU-ES100 [432].

6.10 CONCLUSION

The study demonstrated the capability of the ARISE process to formulate both hydrophilic and hydrophobic drug-loaded ES100 system. The process was performed in a moderate operating condition (ΔP -50 bar, 25°C) suitable for thermally sensitive materials. 5FU and SLB, first-line drugs for colorectal cancer treatment, were used as model drugs in the processes. The ARISE process differentiates from the other DG processing by applying pressure-driven rapid injection into the anti-solvent phase, providing a one-step expansion and precipitation. Micronization and encapsulation take place in single step avoiding process delays that are faced in other DG techniques. The drug loading- L was determined for various concentrations of ES100 by measuring the concentration of 5FU and SLB in the sample through UV-Spectrometry. A detailed analysis of the washing step on the retrieved product was conducted to analyze the free drug content in the sample. The effects of washing conditions and washing time were analyzed to determine an optimal wash condition. It was inferred that harsh washing conditions and an increase in washing time removed about 14 % of the drug from the sample, prompting inaccurate loading estimation. Therefore 1 min of moderate washing is suggested in the current work.

Maximum drug loading of 21.4 % and encapsulation efficiency > 90% were achieved in SLB-ES100 combination, whereas 5FU-ES100 achieved a maximum drug loading of 14.3 % and encapsulation efficiency of 60%. The fraction of drug (5FU) encapsulated decreased with an increase in ES100 concentration.

The ARISE formulation produced uniform spherical morphology particles with individual particle sizes ranging from 200 nm to 700 nm. The average hydrodynamic diameter of the particles varied between 2 μm and 4 μm , which is about 96% reduction in particle size from drugs' and excipients pristine form. The heterogeneity in particle size is attributed to the formation of varying sizes of the droplets of the solution during the transient phase of rapid valve opening. The CO_2 diffusion was higher than the fraction of the solvent extracted from the droplets producing bigger particles. About 90 % of the product was recovered from the process. The product loss was dominant at ES100 concentration above 10 %.

The SEM image analysis revealed that 5FU formed individual crystals on the surface of ES100, and further washing created craters confirming that 5FU was not strongly

encapsulated in ES100. However, SLB showed complete miscibility by forming uniform microspheres at low ES100 concentrations.

The *in vitro* drug release profile was studied in the simulated gastrointestinal environment using the dialysis method. The study revealed that the SLB-ES100 system provides better pH triggered release of 90 % in the colon condition (pH 7.4) and 20 % in the gastric condition (pH 1.2) within 6 h of dissolution compared to unprocessed SLB. The release followed the fickian diffusion mechanism.

The image analysis, drug loading estimation, particle characterization, and drug release complemented one another. The results reveal that SLB-ES100 combinations were favourable with the nano formulation compared to the 5FU-ES100 system.

CHAPTER 7

Evaluation of ARISE process for Hal- loysite nanoclay-5-Fluorouracil for- mulation

RESULTS AND DISCUSSION

The effectiveness of ARISE for processing uniform microparticles and in formulating drug-polymer nano-carriers were discussed in detail in Chapter 5 and 6. In this Chapter, a comparative study on the loading behaviour of 5FU onto HNT between GAS, ARISE, and conventional mechanical loading is detailed. Drug loading onto HNT differs completely from ES100. The former employs porous nanomaterial in suspension, and the latter forms polymer solutions with the APIs used. Also, the mechanism of loading differs between HNT and Eudragit. 5FU molecules get adsorbed onto and into the surface of HNT in their porous sites, as discussed in Chapter 4, whereas the encapsulation in ES100 is achieved by surface adhesion or entrapment into the polymer matrix. The sample preparation and loading procedures were followed, as explained in Chapter 3, Sections 3.4.1 and 3.4.2. The HNT-5FU mass ratio (R) used in the ARISE and mechanical loading was also similar to the GAS process (Chapter 4) for comparison purposes.

7.1 REMOVAL OF CO-PRECIPIRATE

The ARISE product has co-precipitates of 5FU along with encapsulated drug in HNT, similar to the GAS process described in Chapter 4, Section (4.1). The wash procedure was performed for 1 min as per the method described in Chapter 3, Section 3.1.3. The fraction of free drug (α_F) is estimated as the ratio of the mass of free 5FU in the supernatant (m_{5FU}) to the total mass of drug (m_s)-Chapter 4, Section 4.1. The graph in Figure 7.1 shows the variation in α_F with mass ratio, R, for all the processes.

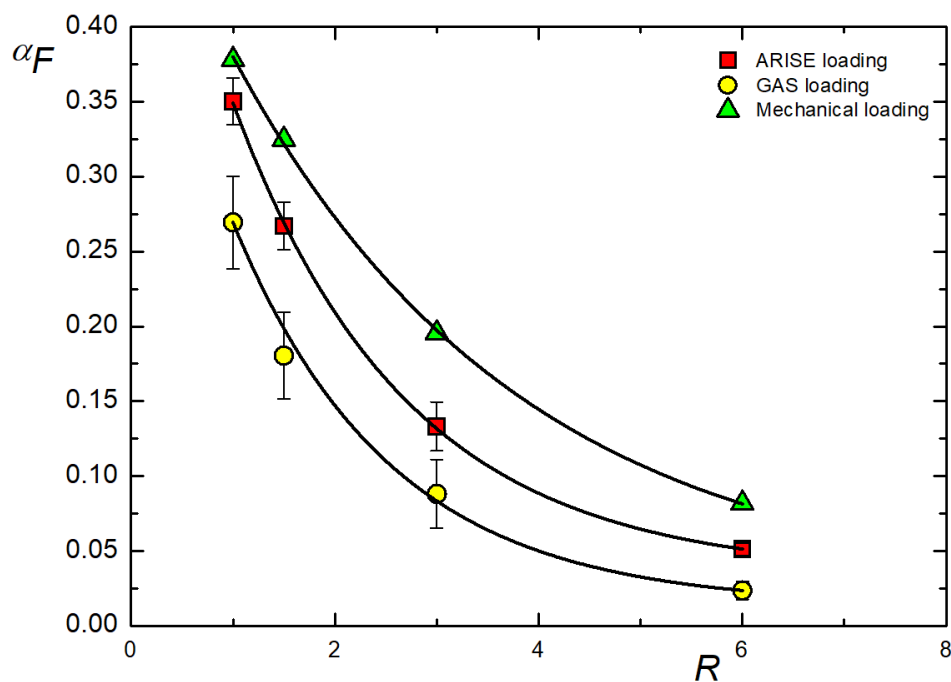
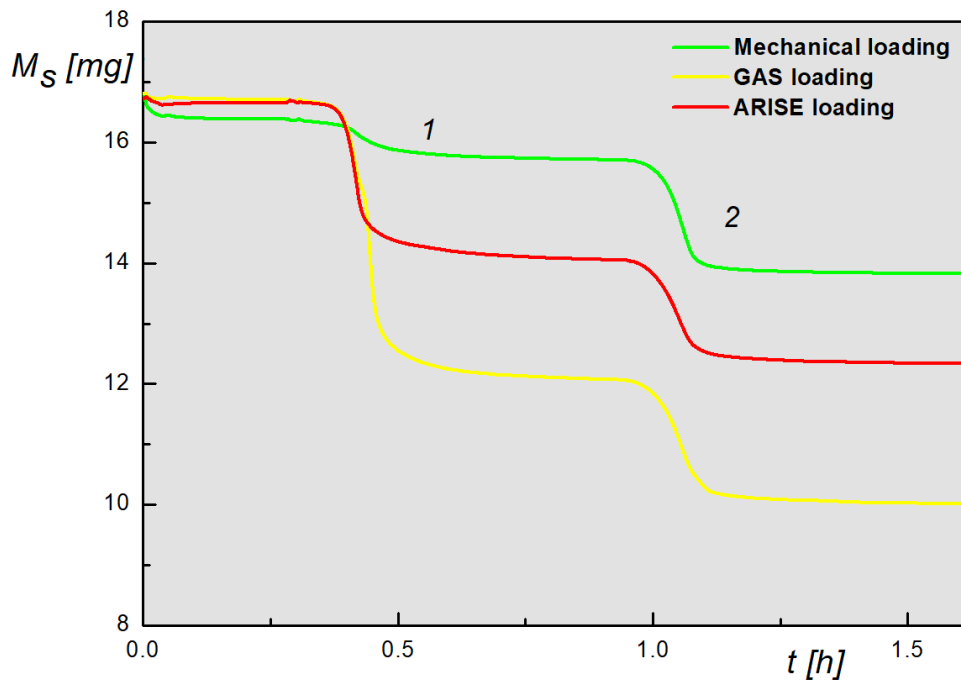


Figure 7.1 Variation in α_F with R for all the processes. (Error are SD of 3 trials).

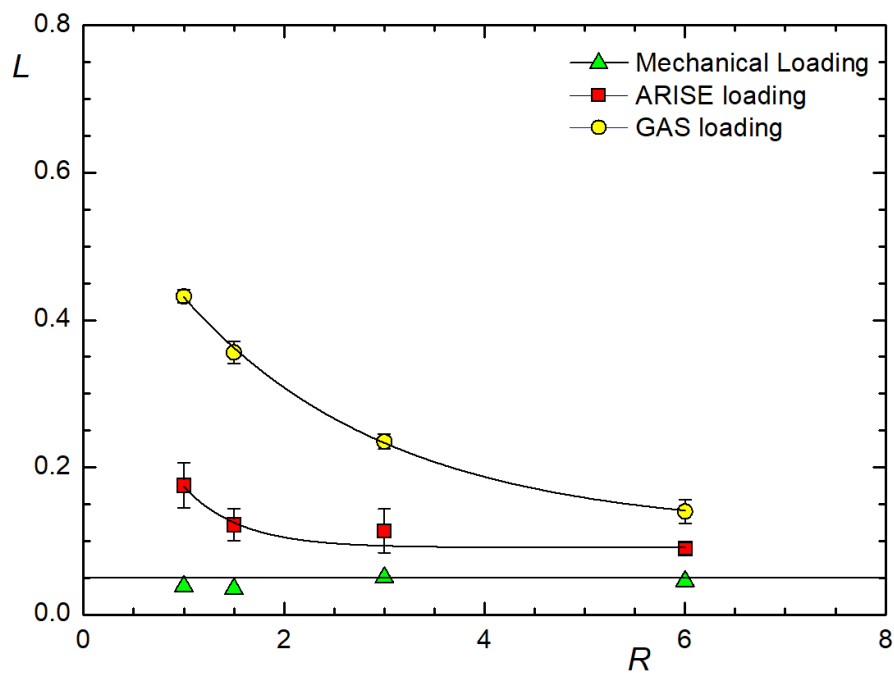
The graph shows exponential decay in α_F with an increase in R, between all the methods. The free drug concentration is high at low R, meaning that the amount of 5FU unadsorbed or co-precipitated is high in low HNT concentration. This is because of the minimal number of active sites available for the excess of 5FU molecules in the solution. However, as the concentration of HNT increases, the number of active HNT sites available for 5FU adsorption increases, thereby resulting in decreasing α_F . The variation in α_F between the encapsulation methods suggest that the GAS process shows a 23 % decrease in free drug concentration compared to the ARISE process and a 27 % decrease compared with mechanical loading. The difference in α_F magnifies to 75 % between mechanical loading and the GAS process at R=6. The data show that 5FU encapsulation in HNT using the GAS process produces a lower fraction of free drug than both the ARISE and mechanical loading techniques. This trend shows that 5FU adsorption onto HNT is more effective with DG processing compared to mechanical loading. The GAS process is effective in retaining the drug onto HNT compared to the other processes, which are explained in the following sections.

7.2 DRUG LOADING

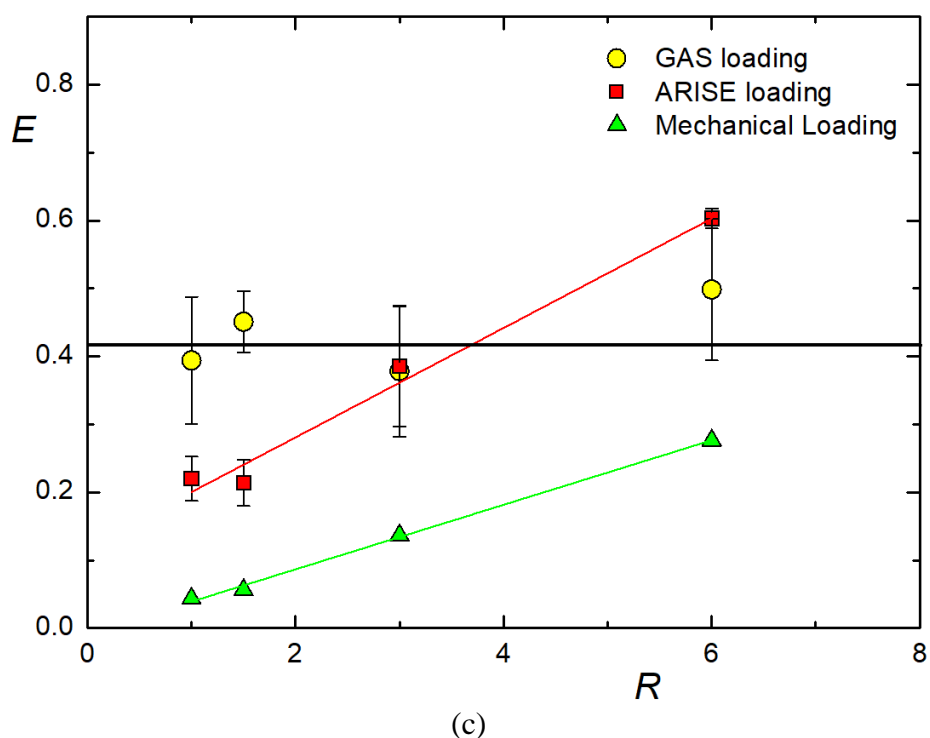
The drug loading estimation was performed based on TGA, as described in Chapter 3, Section 3.1.6. The mass loss curve, drug loading (L), and encapsulation efficiency (E) are presented in Figure 7.2.



(a)



(b)



(c)
 Figure 7.2 (a) Mass loss (vs) time “t” curve from TGA analysis, (1) mass loss due to decomposition of 5FU, (2) mass loss due to decomposition of HNT, comparison graph of (b) Drug loading, L , for different mass ratio R , and (c) Encapsulation efficiency, E . (The individual decomposition curves of HNT and 5FU can be found in Chapter 4, Section 4.2.4, and Figure 4.7).

The drug loading, L , and Encapsulation efficiency, E , were calculated using the Eq 3.1 and 3.2 presented in Chapter 3, Section 3.1.6. The loading of 5FU onto HNT is through adsorption and tubular entrapment [252, 272, 452]. Overall, the loading, L , was higher in the DG process compared to conventional mechanical loading. However, of the DG processes, the GAS technique produced high loading of 43 %, followed by the ARISE with 20 %, whereas the mechanical method produced a loading of 4.2 % on an average for all mass ratios, R as shown in Figure 7.2 (b). The mass loss curve in Figure 7.2 (a) shows the relative difference in the decomposition of 5FU inside the HNT. The region (1) represents the mass loss due to decomposition of 5FU at 340 °C and (2) represents the mass loss due to decomposition of HNT at 510 °C respectively (a reference to Chapter 4, Section 4.2.4, and Figure 4.7). Mechanical loading of similar cancer drugs like curcumin, paclitaxel, and SLB produced loadings in the range of 7-10 %, which agrees with the current work [243, 260, 453, 454]. Table 2.9 in Chapter 2, Section (2.5.1) enlists the drugs loaded onto HNT using the mechanical loading technique. The

loading onto pristine HNT was within 10 %. High loading was achieved only by surface functionalization either with polymer or silane treatment. Contrarily, the DG process effected high loading onto pristine HNT without requiring surface modification. The high loading in the DG processing is due to the use of dense CO₂. The molecular lubricant feature of CO₂ (as explained in previous Chapters 2, and 6) facilitates easier diffusion of the drug into the HNT [102, 422]. The GAS process provides a better loading due to the extended interaction time between 5FU and HNT during the solvent expansion phase. The HNT's larger surface area is made available for a longer time for the drug molecule to diffuse. The interaction between 5FU and HNT in the antisolvent CO₂ phase gradually increases over time while delivering CO₂ inside the pressure chamber. The time-space provides an allowance for maximum adsorption of 5FU into the HNT interlayers as explained by *Harikrishnan et al* [413]. In the ARISE process, the interaction time between 5FU and HNT is limited due to the rapid expansion of the solution. The rapid opening of valve-v3 (process description in Chapter 3, Section 3.2.2) generates high pressure induced nucleation of the solution in the CO₂ continuum. The solvent is extracted from the nucleated droplets into the CO₂ phase, supersaturating the solution (detailed ARISE mechanism is explained in Chapter 2, Section (2.3.2.1)). Hence the chances of 5FU partially re-crystallizing as co-precipitate is higher, resulting in a decrease in loading compared to the GAS process. The variation in loading between R=1 and R=6 with the ARISE process is about 50 %.

On the other hand, mechanical loading does not provide sufficient room for molecular diffusion into the lumen, unlike the DG process, restricting the loading to adsorption on the outer surface of HNT. The loading remains almost unaffected with the change in R. The reason can be attributed to the absence of stronger external forces to facilitate diffusion of drug molecules inside the lumen in HNT. The DG system provides this external force wherein the increased diffusivity in the CO₂ phase facilitates drug molecules to access all adsorption sites in HNT [413]. Apart from the improved loading in the DG process, the decrease in loading with an increase in ratio R is due to the depletion in the free drug concentration available to the unloaded HNT sites, generating more vacant sites in HNT as inferred from Figure 7.2(b).

The encapsulation efficiency, E , is shown in Figure 7.2 (c) as a function of R. The encapsulation efficiency of the GAS process averages 40 %, whereas both the ARISE and mechanical loading showed an increase in E with R. Considering that saturation concentration of 5FU was used in the process, the availability of HNT active sites for

5FU adsorption was low in $R=1$, and 1.5. With an increase in R , more HNT sites are available, providing better absorption of the excess 5FU from the solution resulting in increased efficiency. The efficiency of the ARISE process was observed to be high at $R=6$ ($E=0.6$), implying that the process is efficient in terms of completely utilizing 5FU from the input/feed solution. A significant variation in efficiency was observed at high R between the GAS and ARISE. On the other hand, the maximum efficiency achieved through mechanical loading was about 27 % at $R=6$. The efficiency of mechanical loading was 50-80 % lower than that of the GAS and ARISE processes. The results confirm that the DG techniques provide better encapsulation than the mechanical loading method due to the increased diffusivity of 5FU molecule in the dense CO_2 phase, which promotes encapsulation.

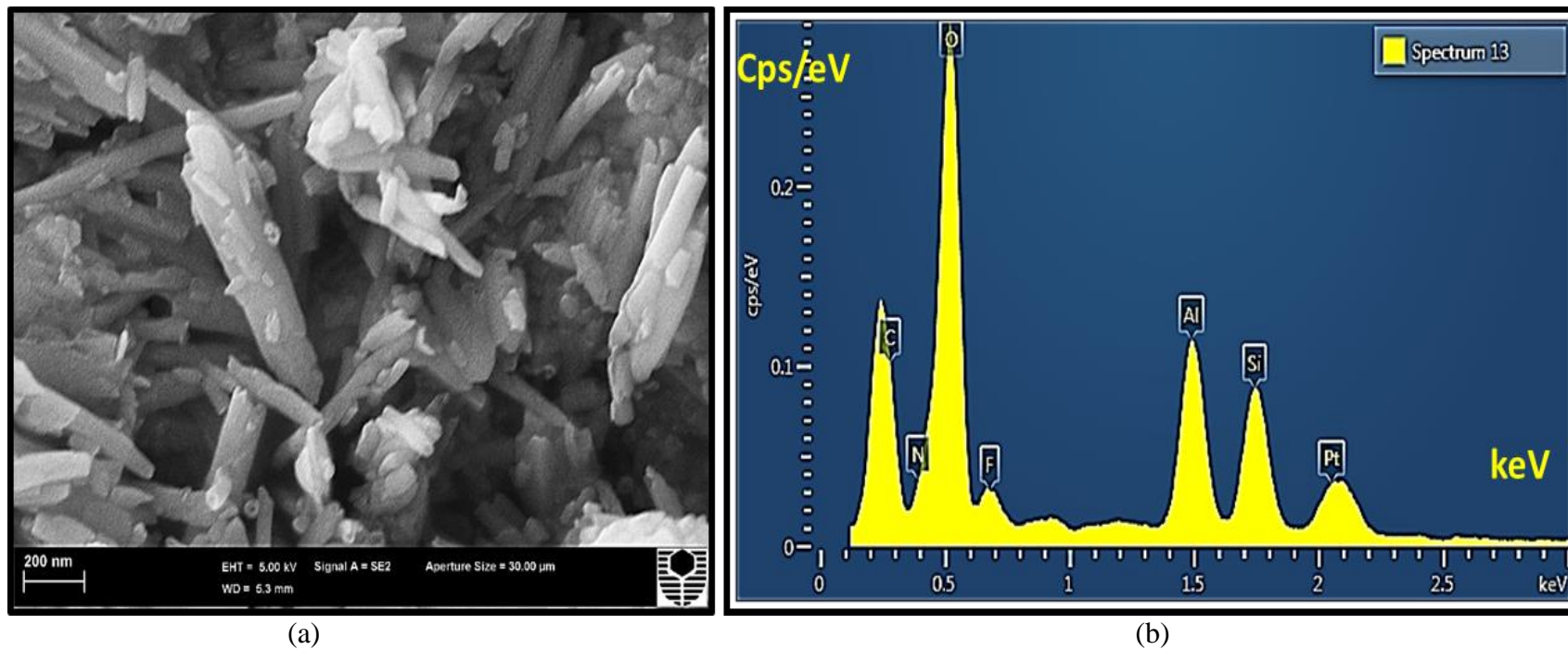
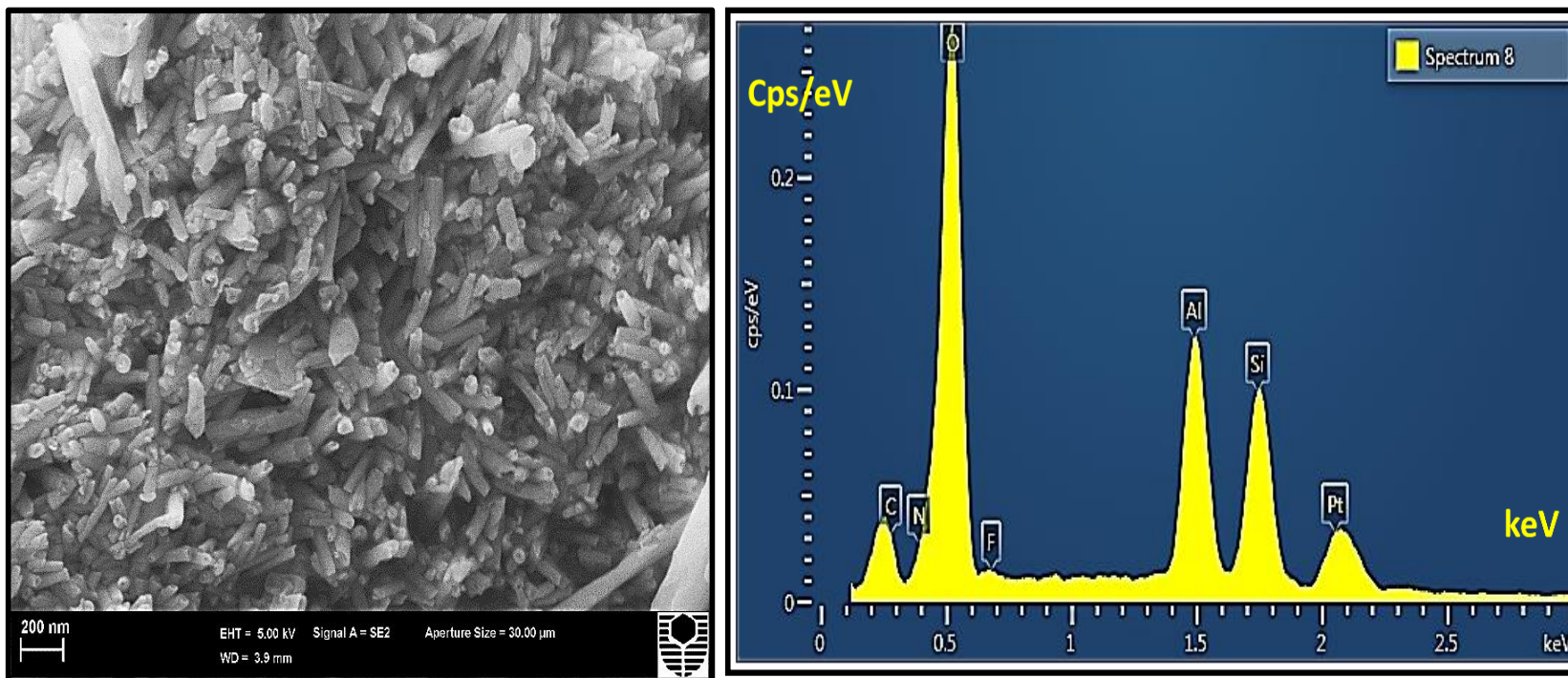


Figure 7.3 (a): SEM image of GAS processed HNT-5FU sample (b): EDS profile of the sample shown in (a).



(a)

(b)

Figure 7.4 (a): SEM image of ARISE processed HNT-5FU sample, (b): EDS profile of the sample shown in (a).

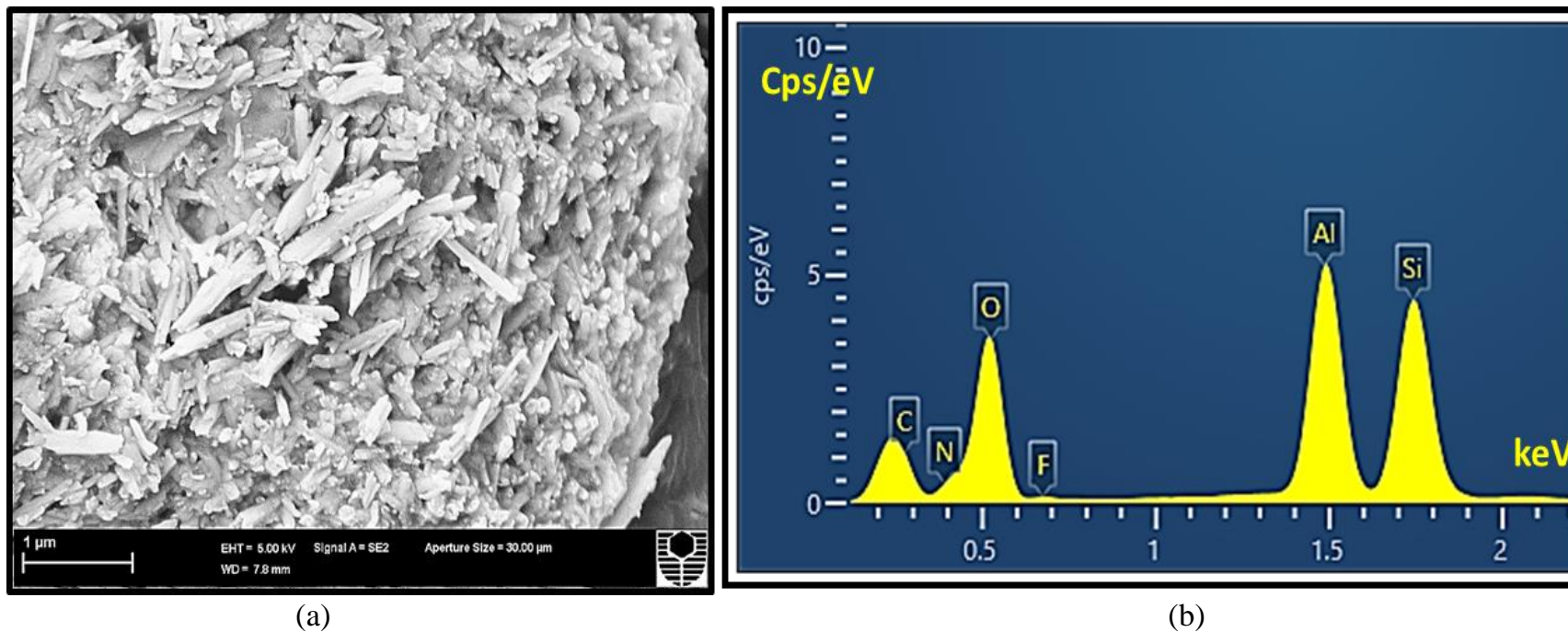


Figure 7.5 (a): SEM image of mechanically processed HNT-5FU sample, (b): EDS profile of the sample shown in (a).

7.3 PARTICLE CHARACTERIZATION

The elemental analysis was performed using Scanning Electron Microscopy (SEM), Energy-dispersive X-ray spectroscopy (EDS), and Fourier transforms infrared spectroscopy (FTIR) as per the procedures explained in Chapter 3, Section 3.1.4, and 3.1.5. The SEM-EDS profiles of the GAS, ARISE, and mechanical loaded samples are shown in Figures 7.3, 7.4, and 7.5, respectively. The EDS profile provides a qualitative and semi-quantitative description of the elemental composition [455]. As mentioned in Chapter 4, Section (4.2.1), the presence of nitrogen and fluorine peaks at a low excitation voltage of 0.2-1 kV confirms the encapsulation of 5FU [445]. The distinct profile of nitrogen is overlapped by the broadening oxygen peak from alumina and silica in HNT. The fluorine peak intensity [456]. The distinct profile of nitrogen is overlapped by the broadening oxygen peak from the oxides of alumina and silica in HNT. The fluorine peak intensity is predominantly seen in the GAS processed sample (Figure 7.3) and decreases in the ARISE and mechanical loaded sample (Figure 7.4, and 7.5). The diminishing of fluorine peak indicates the absence of 5FU in HNT [249].

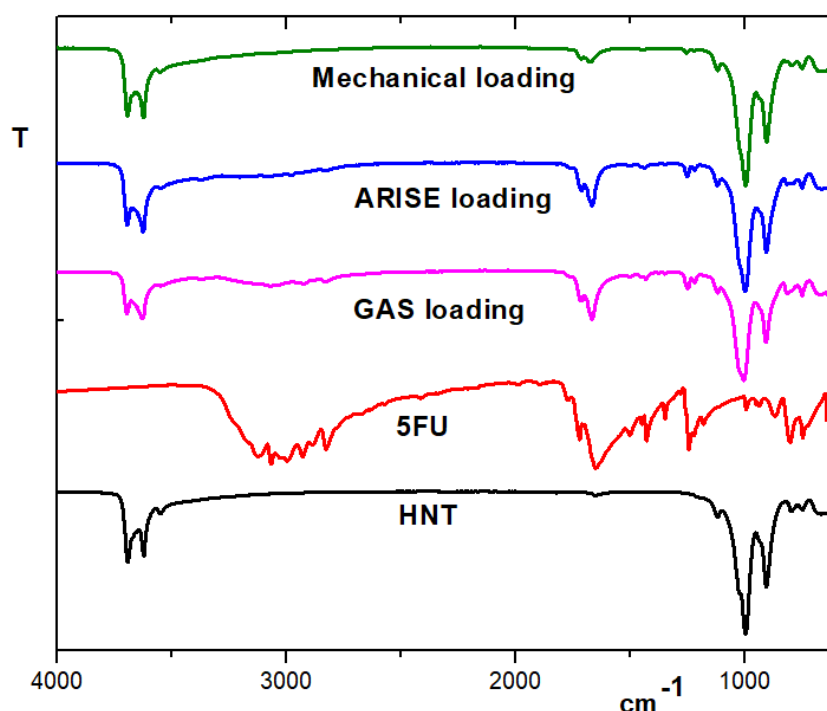


Figure 7.6 FTIR spectrum of unprocessed and DG processed samples. The imprints of 5FU in HNT is seen in all the encapsulated samples.

The FTIR spectrum of the HNT-5FU system is shown in Figure 7.6. The characteristic peak and positions of HNT and 5FU were already discussed in Chapter 4, Section (4.2.2). The imprints of 5FU at 3000 cm^{-1} , 1630 cm^{-1} , 1242 cm^{-1} , and 795 cm^{-1} onto HNT were seen in acquired spectra from all the encapsulation methods, confirming the presence of 5FU encapsulated in HNT. However, the reduction in intensity at 3000 cm^{-1} , 1630 cm^{-1} , and 1242 cm^{-1} from the ARISE and mechanical loading methods indicates depletion of 5FU in HNT sites, validating the decreasing trend in loading, L (%) between processes.

7.4 CONCLUSION

In this chapter, a comparison study of the encapsulation of 5FU onto HNT between DG and conventional mechanical loading processes were discussed. For DG platform, the GAS and ARISE processes were employed, and conventional mechanical loading was performed based on published works [173, 259, 261, 272, 331, 413]. The comparison was drawn based on the estimation of drug loading and encapsulation efficiency. The study revealed that overall drug (5FU) loading with DG processes exhibits a nearly tenfold increase in loading capacity than conventional mechanical loading. The GAS process showed a 43 % average loading, followed by the ARISE process with 17.5 % and 4.5 % with mechanical processing. A common trend of decrease in loading with an increase in the mass ratio R was observed in all the process due to the depletion in 5FU concentration and a relative increase in HNT active sites. The reduction in the fraction of free drug from the samples from mechanical and DG process confirmed that DG processing provides a highly diffusive environment, compared to vacuum cycles for the drug molecules to be effectively adsorbed on the HNT sites. The ability of the drug molecule to access the inner lumen of HNT improved substantially with the use of DG. The increase in encapsulation efficiency with mass ratio, R , validated the findings. The encapsulation efficiency of 60 % was achieved with the ARISE process, 48 % with the GAS process, and 28 % with the mechanical process, respectively. The loading of 5FU onto HNT was confirmed qualitatively through SEM-EDS and FTIR analysis. The DG loading proved to provide efficient loading of the drug (5FU) onto HNT with reduced solvent consumption, thereby reducing the potential for generating chemical wastes.

CHAPTER 8

Green processing of Halloysite nanoclay using Subcritical water treatment

RESULTS AND DISCUSSION

In Chapters 2, 3, and 7, the physiochemical properties and the plausibility of using HNT as drug nanocarrier has been evaluated. Modification of the surface of HNT by altering the adsorption properties can potentially enhance their drug-carrying capacity and mechanical properties. Subsequently, the application profile of HNT is broadened, especially in drug delivery. Modification of HNT can be performed in two ways: Thermal and Chemical methods. The details have been elaborated in Chapter 2, Section (2.5.2). Given the benefits of SCW (Chapter 2, Section (2.6)), their acidic behaviour is utilized in etching HNT and discussed in the current Chapter. Extensive works have been reported earlier on manipulating SCW for formulating hydrophobic drugs and nanocarriers [21, 457-462]. To the best of the author's knowledge, no published work has yet been reported on the treatment of HNT with the SCW process. The current work is an inception study on the possibilities of using SCW as a green alternative to acid etching of HNT's.

As mentioned in Chapter 2, Section (2.5.2.1), though acidic/alkaline etching helps improve the surface area, the purity of HNT is affected due to the retention of toxic solvents in the interlayers. In order to remove the trapped solvents, several washing steps are employed. These steps are time-consuming, expensive, and the process produces massive chemical toxic wastes. Further, the chemical wastes and residues of the process deter the integrity of the material. Acid/alkaline etching causes degradation of material and change in the crystal structure of HNT [291, 463]. The chances of reduction in quality of HNT is high rendering them unsuitable for drug delivery applications. A recent study of the toxic effects of acid-etched HNT was performed by *Barfod et al.* [295]. The toxicological response of acid-etched HNT was performed *in-vitro* in *MutaTMM* Mouse lung epithelial cells. It was observed that, despite the multifold increase in surface area, the use of acid-etched HNT enhanced pulmonary inflammation and toxicity in the epithelial cells and suggested that acid-etched HNT are not ideal candidates for drug delivery from safety design aspects [295]. The use of SCW, on the other hand, is non-toxic with no residual chemical content. The process simply employs deionized water at elevated temperature and pressure as an etchant. The SCW-processed material does not contain acidic residue and the crystallinity of the material is retained without chemical degradation. The SCW process is green and it uses no chemical solvent. Hence it incurs less expense on large-scale production [464].

The sample preparations, experimental, and characterization procedures are detailed in Chapter 3, Section (3.5.1-3.5.6). The inferences of the studies are included in this Chapter.

8.1 BET SURFACE AREA

HNT has a large surface area, which is in the range of 50-64 m²g⁻¹ [240]. Figure 8.1a showed the N₂ adsorption and desorption isotherm of the HNT before and after SCW treatment. The isotherms followed type IV with H3 hysteresis¹ with a slit-shaped pore classified by the International Union of Pure and Applied Chemistry (IUPAC) [466-469]. The hysteresis did not show any significant shift in the adsorption/desorption pattern between untreated and SCW-treated HNT. The specific surface area was determined by calculating the amount of monolayer of gas physically adsorbed on the surface of the nanomaterial. The physical adsorption was accomplished by the weak *Van der Waals* forces between the adsorbent surface and adsorbate gas molecules.

The BET surface area (A_{BET}) was measured from the isotherm by measuring the volume of gas adsorbed at standard temperature and pressure (STP) using the isotherm equation 8.1 and equation 8.2 [466, 470, 471].

$$\frac{1}{V_g \left(\frac{P_0}{P} \right)} = \frac{1}{V_m K} \left[(K-1) \left[\frac{P}{P_0} \right] + 1 \right] \quad (8.1)$$

$$A_{BET} = \frac{6.022 \times 10^{23} V_m}{m \times 22400} \quad (8.2)$$

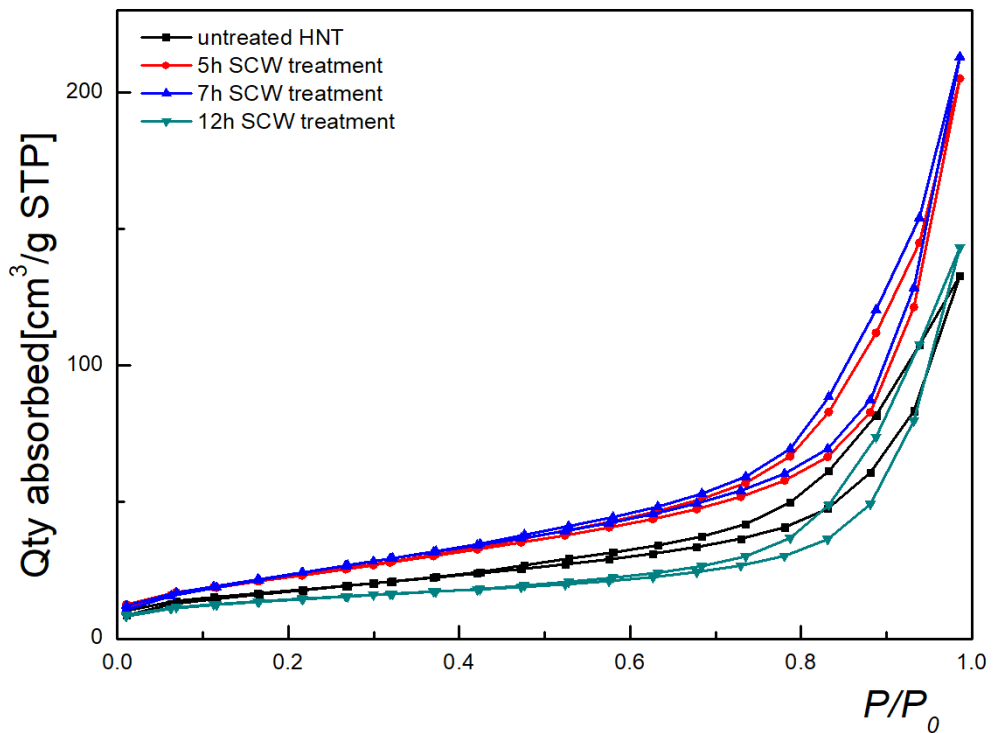
where, V_g is the total volume of gas adsorbed at STP, K is the enthalpy of adsorption

constant, $\frac{P}{P_0}$ is the relative pressure, V_m is the volume of monolayer adsorbed at STP for the sample mass, m .

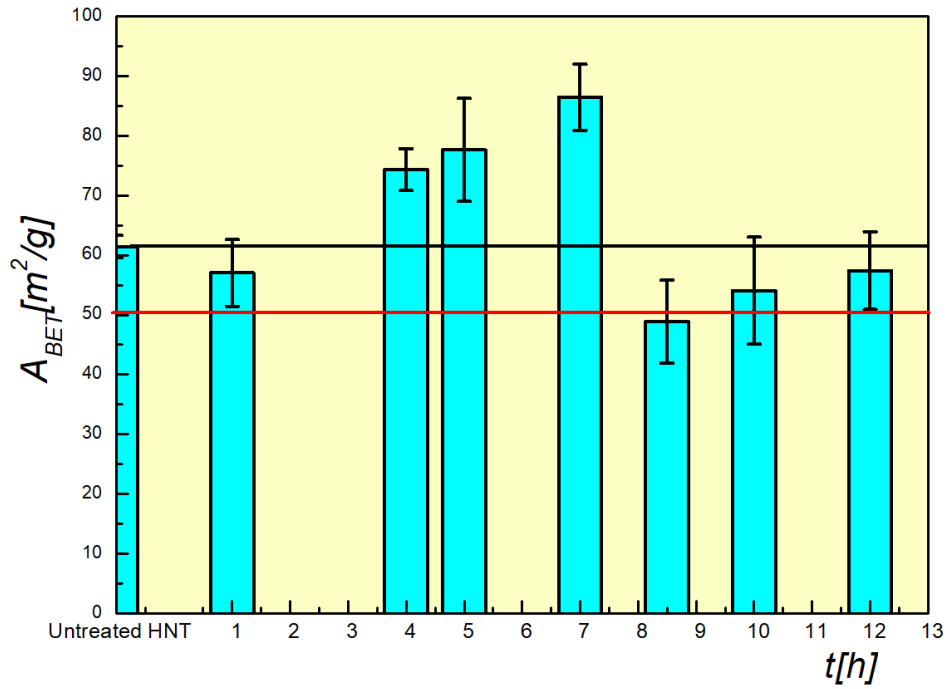
¹ Type IV isotherm represent mono-layer adsorption of mesoporous materials and H3 hysteresis implies the absence of adsorption plateau at high P/P⁰ -more details can be found in *Donohue et al [465] M. Donohue, G. Aranovich, Classification of Gibbs adsorption isotherms, Advances in colloid and interface science 76 (1998) 137-152.*

The BET surface area (A_{BET}) was measured within the linear range of $0.1 \leq \frac{P}{P_0} \leq 0.3$.

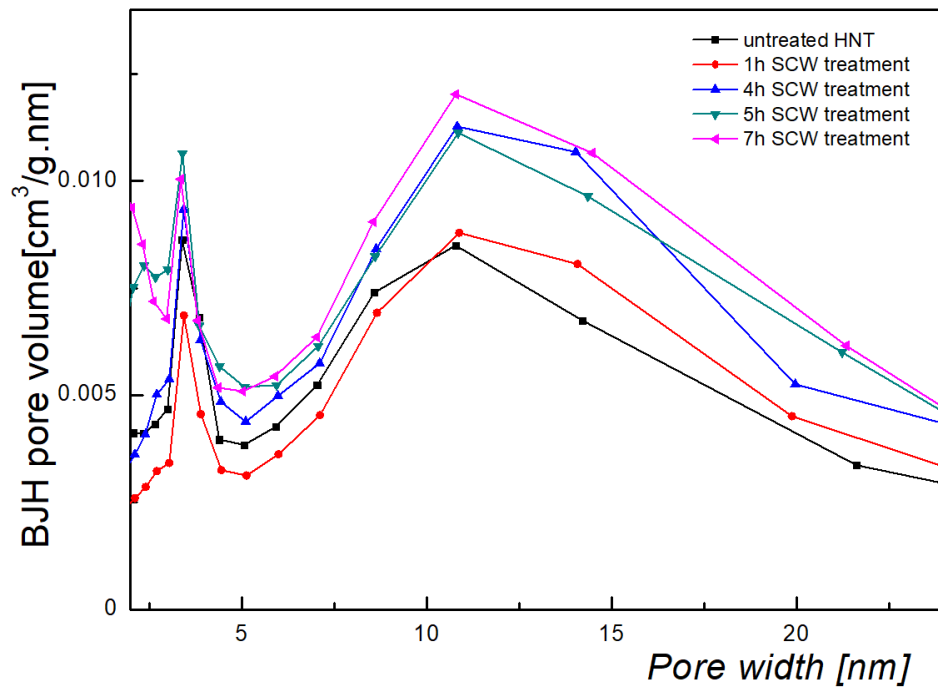
The average BET surface area as a function of treatment time was plotted in Figure 8.1(b). The average surface area of the unprocessed HNT was $62 \text{ m}^2\text{g}^{-1}$. This is in agreement with the supplier specification and other published work [472, 473]. The increase in A_{BET} was about 13% within 4 h of SCW treatment. A similar improvement of 13.4% in surface area was observed by Wang *et al.* [289] by treating HNT with a molten alkali solution. The short treatment time of 1 h did not initiate any significant change in surface area. However, surface area as high as $86.4 \text{ m}^2\text{g}^{-1}$ was achieved after 7 h of SCW treatment. The result reveals a significant 25% increase in A_{BET} from its unprocessed state.



(a)



(b)



(c)

Figure 8.1 (a) Nitrogen absorption-desorption isotherm of HNT for various SCW treatment time (t), P/P_0 is the relative pressure, (b) Graph of BET surface area (A_{BET}) of HNT for various SCW processing time (t), the black and red line are the average BET surface area measured for untreated and thermally treated (at ambient condition) HNT respectively, and (c) Pore size distribution curve of untreated and SCW treated HNT, (Errors are SD of 3 trials).

Consequently, the pore size distribution of the HNT can be determined using the Barrett, Joyner, and Halenda (BJH) method by relating the surface pore radius, r , surface tension of adsorbate, γ , with the volume of gas adsorbed through Kelvin equation—Equation 8.3 [474].

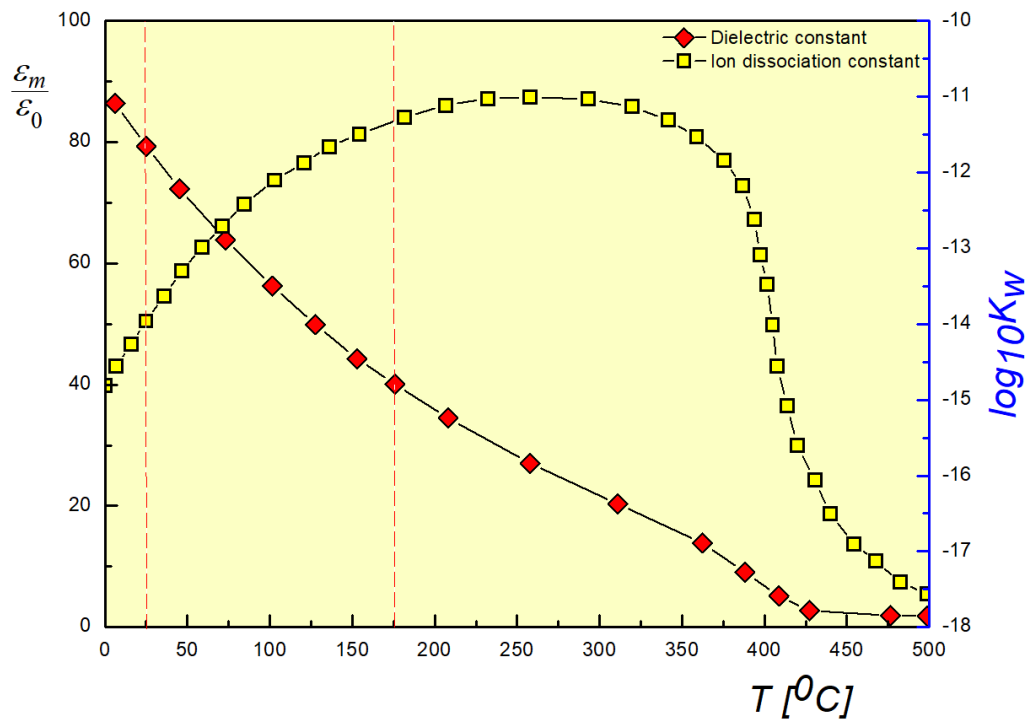
$$\ln\left(\frac{P}{P_0}\right) = \frac{2\gamma V_m}{rRT} \quad (8.3)$$

where R and T are universal gas constant and temperature, respectively. Based on the single point desorption plot from BJH size distribution, HNT is mesoporous material with pore population in the range of 4-13nm, according to IUPAC (Figure 8.1c)[475, 476]. The N_2 adsorption showed a proportional increment in mesopore adsorption with increased treatment time. The adsorption was saturated after 7 h and dropped after 12 h of treatment, suggesting that the dealumination and dissolution of interlayers evenuate with a prolonged treatment time, which was further verified from other characterization methods detailed in the following sections.

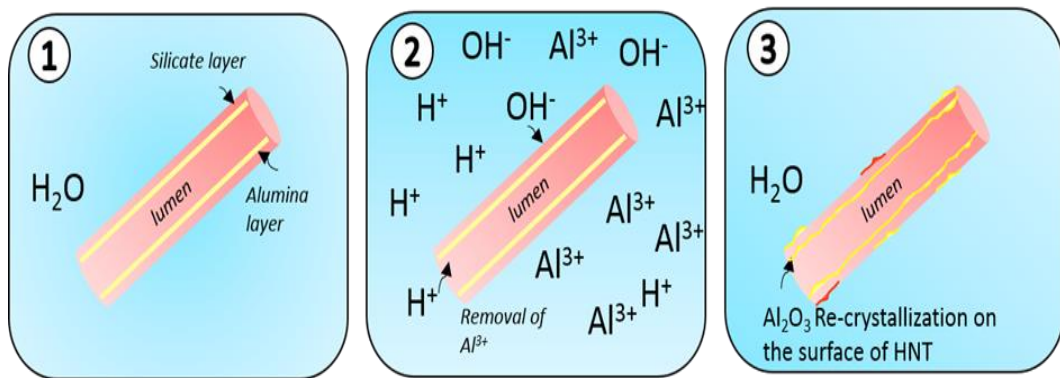
The structure of HNT is constituted with alternating SiO_4 tetrahedron and AlO_6 octahedral layers (Chapter 2, Section 2.5). Research works suggest that the thermal treatment of HNT enhances the reactivity of the aluminosilicate cage structure towards chemical modification[477, 478]. Also, HNT is stable up to 400 °C without alteration in the physicochemical parameters—(Chapter 2, Section 2.5.2) [273, 479]. Hence, treating HNT at 170 °C in SCW provides an environment for calcination and etching at a single step, without causing thermal degradation.

The mesoporous nature of SCW-treated HNT did not alter with treatment time, and the average pore diameter was observed to be 12.5 nm, as explained in the following sections. The BJH pore size distribution of the HNT suggested that the pore width of both untreated and SCW-treated HNT has wide distribution between 2 nm and 40 nm. The mesopore scale of HNT was similar to the single-walled carbon nanotubes as observed by *Hu et al* and others [269, 476, 480]. The peak around the 11 nm pore diameter indicated an increase in BJH pore volume, without a change in pore width distribution (Figure 8.1c). On the contrary, a shift in pore width was observed by *white et al* [300] from 9 nm to 15 nm after etching with 1 mol dm^{-3} of NaOH for 28 days. The increase in BJH pore volume relates to the growth of new crystallite size with an un-

altered pore size distribution, partly indicating that the tubular morphology is preserved during the SCW treatment. The conjecture will be verified by the XRD analysis in the following sections.



(a)



(b)

Figure 8.2 (a) Variation in dielectric constant ($\frac{\epsilon_m}{\epsilon_0}$) and Ion dissociation constant (K_w) of SCW with temperature (T) [481], and (b) Schematic of SCW etching process for HNT.

(1) HNT suspended in water, (2) Etching of alumina layers in protonated SCW, and (3) Formation of new crystallite sites on HNT from saturated SCW.

Water exhibits increased ionic strength at subcritical conditions, behaving as a strong acid. At temperature above 160 °C, the solubility of materials increases remarkably . The strength of the hydrogen bond in the water molecule decreases, causing a reduction in the dielectric constant . The decline in dielectric constant generates an increase in ionic strength in the system. From Figure 8.2a, It can be inferred that the ionic strength increases from -14.5 at 25 °C to -12.7 at 170 °C . The increase in ionic strength of the SCW increases the proton binding ability of HNT and hence increases their solubility in SCW, as observed by *Bretti et al.* . The formation of H⁺ and OH⁻ ions in the subcritical condition induces protonation of the inner alumina layer of the HNT. With increased ionic strength, the imbalance charge between the alumina and silicate layers causes the alumina layer to solubilize faster than the silicate layer .

Further, an increase in treatment time extends the contact time of the HNT with the SCW, thereby inducing greater solubilization of the alumina layer. The system reaches equilibrium once a saturation concentration is achieved in the solution phase. Subsequently, the HNT re-crystallize from the solution phase to form new porous sites. The schematic of this process is shown in Figure 8.2 (b).

The suspension volume in the current work is about 8 mL. With an increase in treatment time, the concentration of alumina in the solution increases by the progressive dissolution of the HNT interlayers into the solution reaching a saturation limit. The saturation limit can be manipulated by altering the suspension volume. However, the re-crystallization plateaus after reaching a particular treatment time. An increase in treatment time beyond 7 h produced a negative effect on the measured A_{BET} . The surface area after 12 h of treatment drops by 33.5%, within the variance of A_{BET} (unprocessed HNT) as seen from Figure 8.1(b).

Besides, a thermal treatment of HNT using the Soxhlet apparatus was performed, as described in Chapter 3, Section 3.5.3. The red line in both Figure 8.1b and Figure. 8.3 represents the average A_{BET} of HNT after thermal treatment at 170°C for 7 h in ambient pressure condition. This measurement was performed to differentiate SCW treatment from equivalent thermal treatment at atmospheric pressure conditions. The A_{BET} of thermally treated HNT did not show improvement from its native form even after 7h, as seen from Figure 8.1(b)-red line. The results agree with the similar work by

Mooinpour et al., wherein the HNT was calcined at 400 °C for 2h. The calcination showed no effect on A_{BET} [273]. The observation ensures that the effective increase in A_{BET} and the resultant change in physicochemical characteristics of HNT are due to the SCW conditions and not on mere calcination/thermal treatment at ambient pressure conditions.

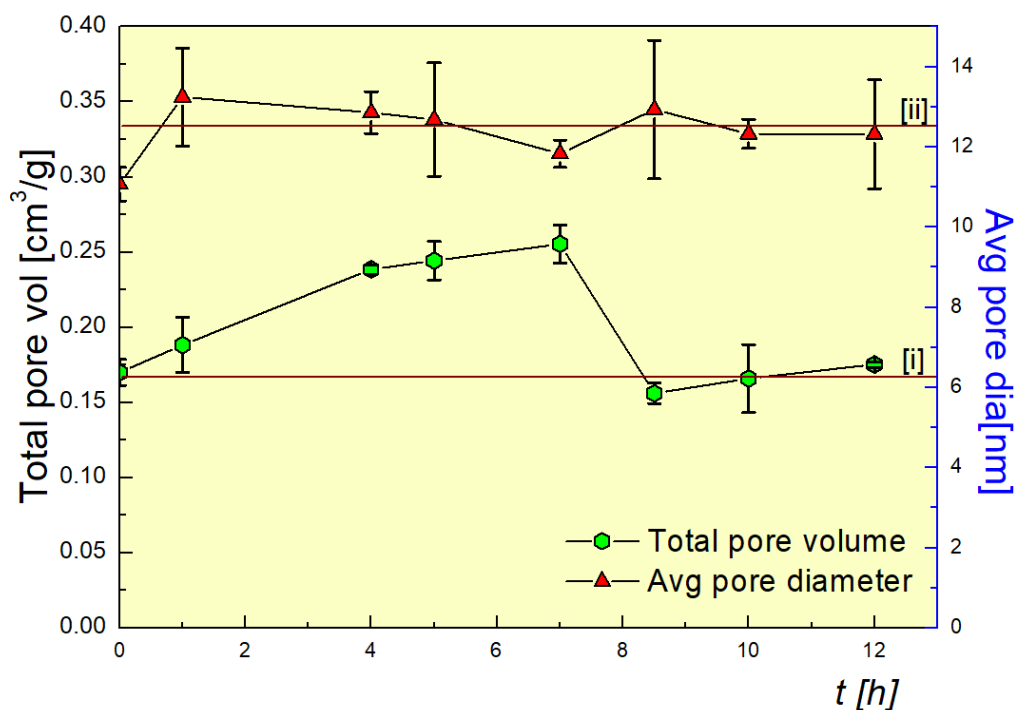


Figure 8.3 A plot of total pore volume and average pore diameter (vs) SCW treatment time for HNT. Line (i) and (ii) represents the total pore volume, and the average pore diameter of HNT after thermal treatment at 170°C for 7 h at ambient pressure condition, respectively. (Errors are SD of 3 trials).

The change in the porosity of HNT with the SCW treatment is shown in Figure. 8.3. The total pore volume increased from 0.17 cm³g⁻¹ at the un-processed state to 0.255 cm³g⁻¹ after 7h of SCW treatment. The increase of 1.5 folds was achieved after the first 7h of treatment. The increase in total pore volume was due to the dehydration of the interlayer, creating longitudinal wide pores, as observed by *Yuan et al* [467]. However, the total pore volume dropped to an average of 0.16 cm³g⁻¹ after 12 h of treatment. The instantaneous decrease in total pore volume with treatment time greater than 7h indicated that the HNT started dissolving irreversibly in the SCW, and the interlayers were etched in the solution alike in acid etching[291]. As described in Chapter 2, Section (2.5.2.1), the effects of acid etching can provide insightfulness about the SCW process.

Treatment with sulphuric acid for 13 h produced a proliferated 458% increase in surface area, as reported by *A-B Zhang et al* [291]. *Garcia et al* [281] detailed a 150.3% increase in surface area after sulphuric acid treatment for 72 h at 50°C. Hydrochloric acid treatment at an elevated temperature of 750 °C -900 °C improved the surface area of HNT from 32 m² g⁻¹ to 414 m² g⁻¹, whereas treatment with NaOH at 950 °C -1150 °C increased the surface area to 159 m² g⁻¹ [482]. The above studies suggested that selective etching of alumina layers can be achieved through acid etching, and silicate layers can be etched in alkaline condition.

The log₁₀ *K_w* of sulphuric acid is between -1.988 to -4.246, within the temperature range of 25 °C to 200 °C, which is a 3-7 order magnitude higher than the ionic strength of the SCW in the same temperature range [483]. The difference indicated that the harsh condition and excessive etching of HNT in the acidic medium led to the severe impact of acids on HNT after treatment. The outer and inner surfaces were destroyed due to the excessive dissolution of Al³⁺ ions in the acidic solution. As a result, HNT was degraded, as illustrated in Figure 8.4. Besides, the acid-treated HNT had high residual acid content in the interlayers despite several washing steps performed in the post-etching procedure rendering it unsuitable for consequent drug loading-Figure 8.4 [292, 484].

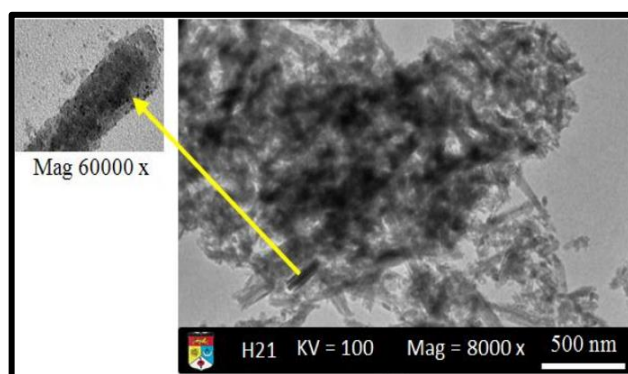
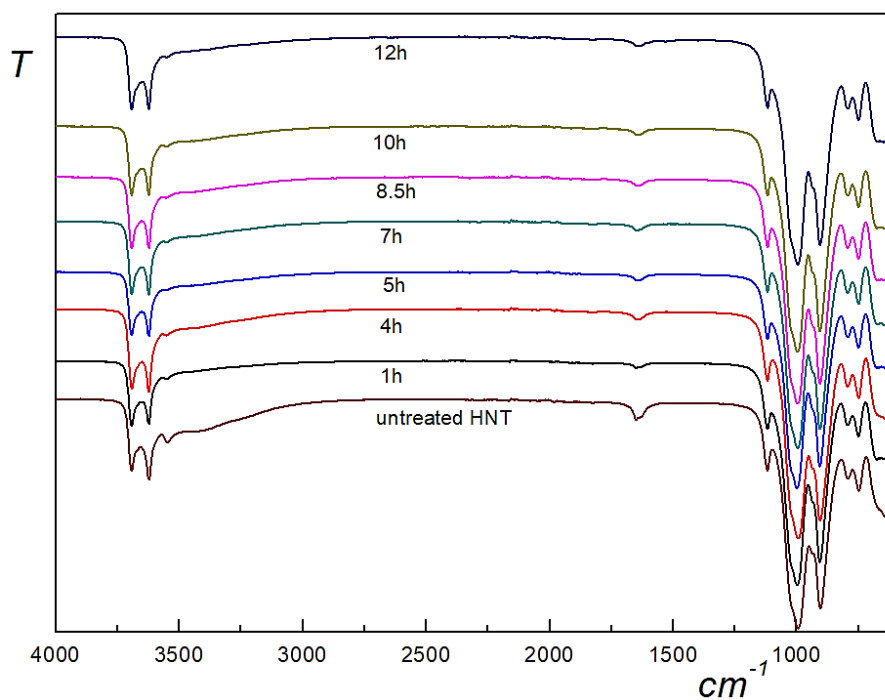


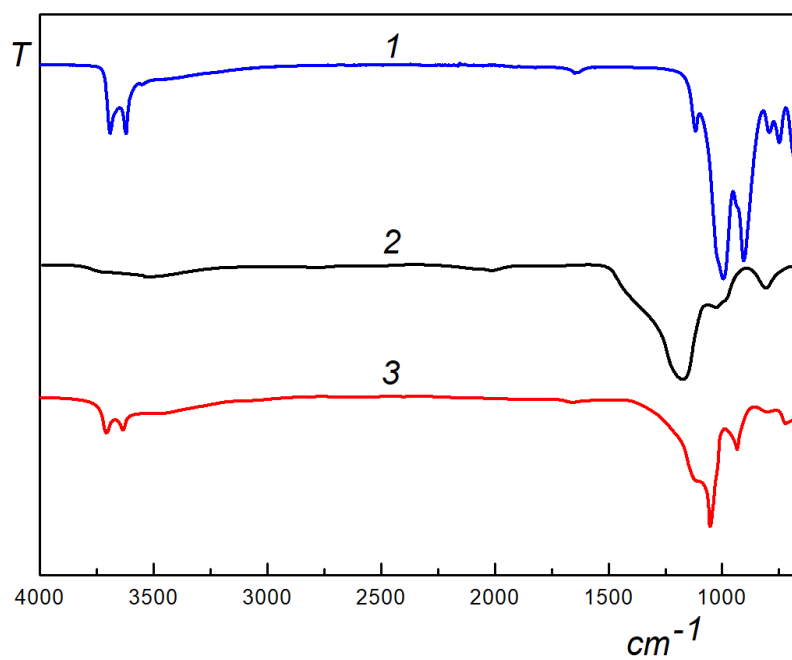
Figure 8.4 Image of severely exfoliated HNT after etching in sulphuric acid. (Image from *Gaaz et al* [292]).

8.2 FTIR SPECTROSCOPY

The characteristic IR spectrum of the untreated and SCW treated HNT is shown in Figure 8.5a and their corresponding spectral bands are tabulated in Table 8.1.



(a)



(b)

Figure 8.5 (a) FTIR spectrum of HNT before and after SCW process at a various treatment time, (b) Comparison of FT-IR spectrum of HNT processed from (1) SCW treatment (7 h), (2) after 21 h H_2SO_4 treatment (adapted from *Gaaz et al* [292]), and (3) after 50 % alumina etching in H_2SO_4 (adapted from *Abdullayev et al*[245]).

Table 8.1 FTIR spectrum of HNT and characteristic peak positions.

Chemical bonding	Wave number [cm ⁻¹]	References
Inner surface OH stretching	3600,3692	[485]
Intermolecular hydrogen O-H stretching	3580	[486]
Water deformation	1648	[487]
Si-OH stretching	1120	[486]
Outer Si-O-Si stretching vibration	995	[486, 488]
Outer Si-O stretching vibration	1050	[485]
Bending vibration of Al-OH	900	[485]
Al-O-OH stretching	750,795	[300]
Out of plane R-OH bending	675	[467]

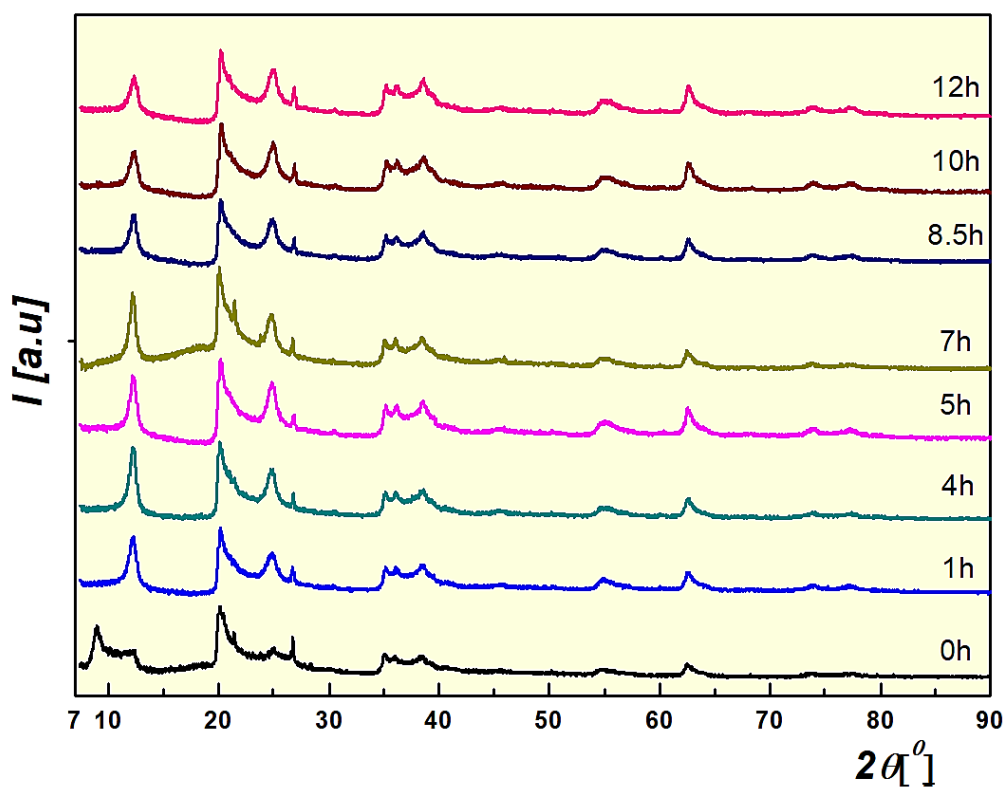
The measured peaks are in accordance with the profile reported in published works (Table 8.1). The inner surface OH stretching at 3692 cm⁻¹ and 3600 cm⁻¹ remains unaltered, and the Si-OH stretching vibration at 1120 cm⁻¹ did not change after SCW treatment. Also, the inner Al-O-OH stretching, and Al-OH bending vibration did not modify. The peak intensity corresponding to the outer silicate layer (3600 cm⁻¹-3692 cm⁻¹) increased marginally. This may be due to the new crystallite formed on the surface of HNT after SCW treatment. However, the intermolecular hydrogen O-H stretching diminished with an increase in treatment time. This is due to the breakage of hydrogen bond in HNT and partial dissolution into SCW. The peak at 1648 cm⁻¹ corresponding to the hydrated interlayer reduced with an increase in treatment time, showing that the HNT interlayers were dehydrated after SCW treatment, forming Halloysite-7Å phase as explained in the following X-ray diffraction analysis.

The diminishing effect of Si-OH and surface O-H bond is significant in sulphuric acid etching, as observed by *Tayser et al.* and *Elshad et al.*, wherein the characteristic peak at 3620 cm⁻¹, 3690 cm⁻¹, and 754 cm⁻¹ disappeared with increasing etch time-Figure 8.5b [245, 292]. Albeit the strong etch rate in a harsh acidic environment, no significant change in spectra was observed below the 50% dealumination of HNT[245]. These observations were consistent with the present study, wherein there were no significant changes in spectral peak position and intensity observed- Figure 8.5b. The SCW treatment has been demonstrated to preserve the chemical composition of HNT

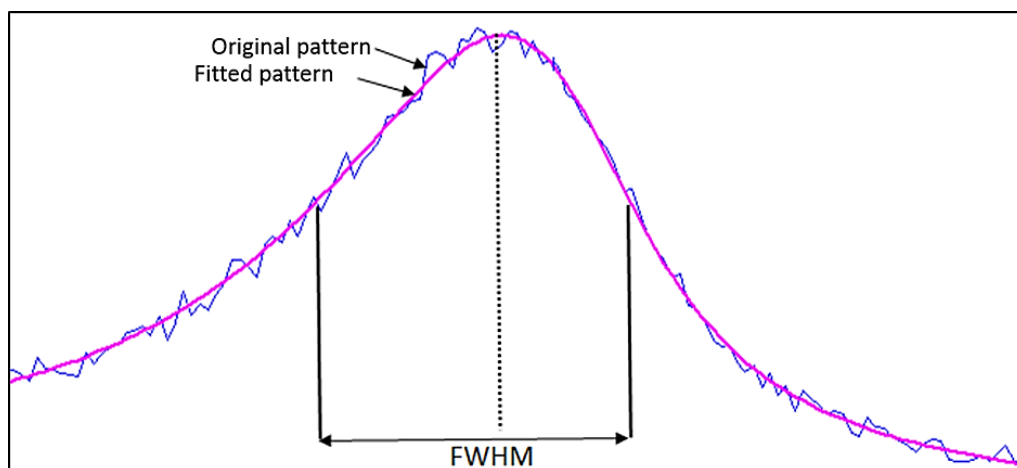
throughout the process without introducing a harsh environment, as strong acids and bases.

8.3 X-RAY DIFFRACTION ANALYSIS

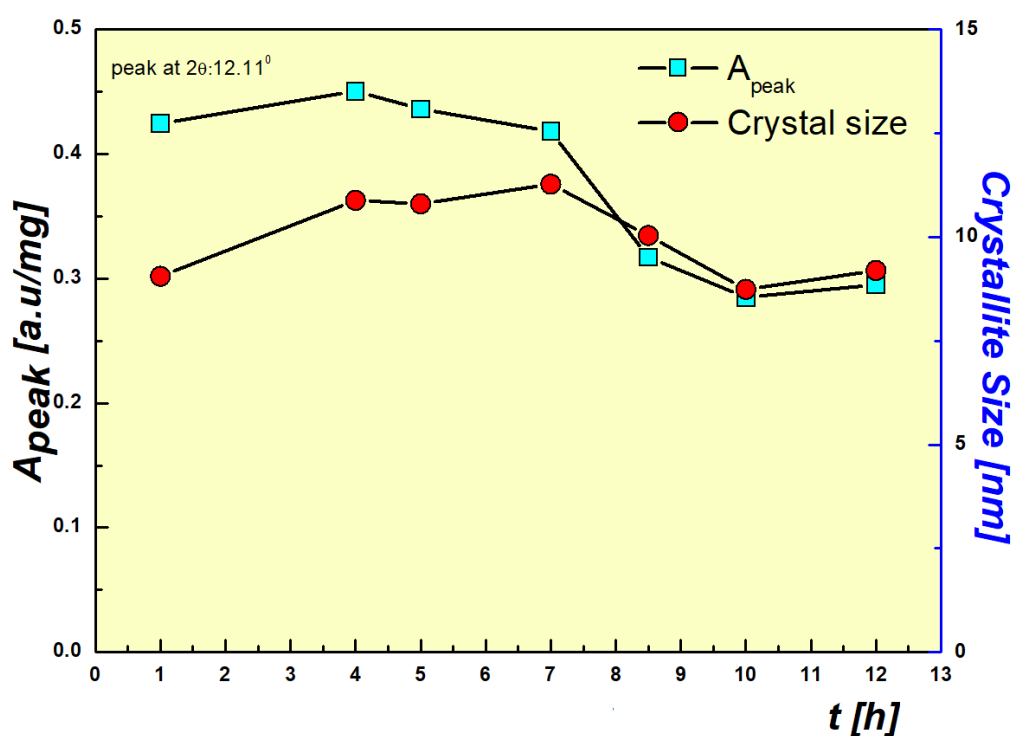
The X-ray diffraction analysis provided information about the material's crystallography and identifies the change in crystal phase behaviour of polycrystalline materials[489]. Figure 8.6(a) shows the X-ray diffraction pattern of the untreated and SCW treated HNT. With untreated HNT, the diffraction peak at $9.13^\circ 2\theta$ corresponds to (001) diffraction plane with a basal spacing of 1.00 nm, which is the characteristic of halloysite-10 Å. After SCW treatment, the peak at $9.13^\circ 2\theta$ disappears and the peak at $12.11^\circ 2\theta$, corresponding to (001) with a basal spacing of 0.730 nm intensifies. The general chemical formula of HNT is, $\text{Al}_2\text{Si}_2\text{O}_5(\text{OH})_4.n\text{H}_2\text{O}$, implying that they naturally exist in hydrated form. The hydration is characterized by quantifying $n\text{H}_2\text{O}$. Untreated HNT exhibit Halloysite-10Å, with $n=4$ and SCW treated HNT in Halloysite-7 Å, with $n=2$. The reduction in (001) spacing from native halloysite-10 Å to 7 Å after SCW treatment indicates dehydration of physically absorbed interlayer water [291, 292, 490]. A similar transformation from Halloysite-10 Å to 7 Å was observed by *Yuan et al* during thermal treatment [467].



(a)



(b)



(c)

Figure 8.6 (a) X-ray diffraction spectrum of untreated and SCW treated HNT at various treatment times (Sample mass and parameters are fixed for comparison reason), (b) Sample of the model fit of the peak at $12.11^\circ 2\theta$ showing peak position and full-width at half maximum (FWHM), and, (c) Plot of change in peak area (A_{peak}) and crystallite size of HNT at various SCW treatment time.

The peak at $24.57^\circ 2\theta$ is due to the (002) diffraction plane with a basal spacing of 0.362nm. The presence of these two peaks indicates the dehydrated HNT structure (halloysite-7 Å) [491]. The diffraction plane (020) at $20^\circ 2\theta$, is attributed to the tubular structure with a basal spacing of 0.443 nm. The peak at $26.6^\circ 2\theta$ corresponds to (011)

SiO₂ plane in HNT [273, 281, 492, 493], and the peak at 21° 2θ, is due to the impurities [273]. The peaks at 35.02°, 37.93°, 54.5°, and 62.6° 2θ, with a basal spacing of 2.56 nm, 2.37 nm, 1.68 nm, and 1.48 nm, respectively, correspond to the γ -Al₂O₃ in accordance to the Powder Diffraction Standards [494].

From the sample's peak profile, one can retrieve information about the crystallite size of the material by deconvoluting the peaks at desired locations. The crystallite growth along (001) plane is quantified by profile modeling of the peak at 12.11° 2θ using Full width at half maximum (FWHM) and integral breadth function as shown in Figure 8.6b. The Scherrer equation used for measuring the crystallite size is defined as in Equation 8.4 [495]:

$$L = \frac{K\lambda}{B\cos\theta} \quad (8.4)$$

Where B = integral breadth in 2θ rad, λ = incident X-ray wavelength, L = Volume-weighted column length in the direction normal to the reflecting plane, and K = Scherrer constant which is 1 for integral breadth function. The crystallite size is estimated from the measured width of the diffraction peak. The pseudo-Voigt function provides an accurate fit, specifically for asymmetric curves of the peaks-Figure 8.6b [496]. It is a linear combination of Gaussian and Lorentzian functions of the FWHM values [497]. *Ida et al* [498] defined the pseudo-Voigt function in terms of the Lorentzian line shape function and the Gaussian function for the peak profile-Equation 8.5-8.7.

$$f_L = \frac{1}{\pi\gamma_L} \left[1 + \frac{p^2}{\gamma_L^2} \right]^{-1} \quad (8.5)$$

Where f_L = Lorentzian function, p = position variable, and γ_L = FWHM value of Lorentzian function.

$$f_G = \frac{1}{\sqrt{\pi}\gamma_G} e^{\left[\frac{-p^2}{\gamma_G^2} \right]} \quad (8.6)$$

Where f_G = Gaussian function, γ_G = FWHM value of Gaussian function, and the Pseudo-Voigt function is defined as:

$$f_{pV}(\theta) = (1-\eta)f_L + \eta f_G \quad (8.7)$$

Where η is the integration constant of the function. The crystallite size derived from the peak fit is shown in Figure 8.6c. It can be observed that the crystallite size increases by 24% from 1 h to 7 h of SCW treatment. The increase within the first 5h was observed to be about 19.3%. Further increase in treatment time decreases the crystallite size by 18%. The increase in intensity and the crystallite size is due to the homogenous nucleation and crystal growth in the SCW environment. Evidence of crystal growth was observed by *Carr et al* [21], in his work wherein, SCW environment induce even growth rate of crystals along the surface of *Griseofulvin* during the particle formation from solution. In the current study, the first 7 h of treatment in subcritical condition dissolves some portion of the alumina layer into the solution. The crystals then re-deposits on the surface of HNT from the water phase, forming new crystallite sites- Figure 8.2b.

An increase in treatment time ensures more contact time between the HNT and SCW. As discussed in Section 8.1, prolonged exposure generates more Al^{3+} into the water phase. Upon reaching the saturation, the Al^{3+} re-crystallizes forming new crystallite sites. A similar trend of forming new crystallite sites was observed by *Hiroshi et al.* while treating silicate glass using SCW [499]. *Karasek et al.* [318] observed formation of re-crystallized silica on the edges of silicon wafers while etching with supercritical water at 400° C.

It is worth mentioning here that the increase in peak area between 1h and 5h of treatment was modest 2.7%. However, when the SCW treatment time exceeds 7h, dealumination of the alumina layer is significant causing a decrease in crystallite size, up to 30% lower than the initial value-Figure 8.6c. The systematic decrease in peak area after 8.5h, 10h, and 12h indicate the loss of HNT interlayers supporting the above argument. Similar dealumination of the alumina layer effect was observed by *Elshad et al* [245], while treating HNT with sulphuric acid.

The (011) silica peak at 26.6° 2 θ , was unaffected by the SCW treatment, implying that the treatment does not significantly affect the outer silicate layer and the effect is less pronounced compared to the inner alumina layer. The peak intensity at 12.11° 2 θ did not shift from its position for all the SCW treated samples, indicating the absence of residual solvent (water in this case) into the interlayers of HNT. Contrarily, the possibility of solvent trapping is high in the case of acid etching and needs several washing steps to ensure removal of residual solvents from the interlayers [245, 269, 289, 296].

Taysler *et al* [292], reported that the sulphuric acid treatment dealuminates the HNT sheets causing a decrease in peak intensities at $35.02^\circ 2\theta$, (110) and $37.93^\circ 2\theta$, at (003). However, these peak intensities did not alter with SCW treatment, indicating the $\gamma - Al_2O_3$ and SiO_2 crystal structure did not completely disintegrate, and the tubular morphology was preserved.

Therefore, the increase in surface area and hence the porosity of SCW treated HNT was significantly influenced by the crystallite growth through partial dissolution and recrystallization of alumina layer and not through complete leaching of aluminosilicate layers, as in the case of acid etching.

Hence, employing SCW as an alternative etchant enables the process to be green, wherein the acidic property of the water dissipates upon depressurizing and cooling, resulting in non-toxic chemical residue, avoiding contamination and preserving sample purity and morphological integrity.

8.4 TRANSMISSION ELECTRON MICROSCOPY

The TEM image in Figure 8.7 (1, 2) reveals that HNT occurs in tubular morphology with the central lumen and ends open. The interlayer spacing has a distance of 15 nm with lumen as large as 20 nm [500].

The crystallinity of HNT can be verified by performing selected area diffraction (SAD) analysis. The SAD pattern generated due to the Bragg reflection from the individual crystallite sites provide brighter spots (due to discrete crystallite sites), and diffused rings/isotropic halo (due to amorphous phase) helps in understanding the effects of SCW treatment [501]. The SAD pattern in Figure 8.7 (3) shows the bright spots indicating the crystalline phase of HNT, confirming the polycrystallinity of the material. Upon exposure to the SCW environment, the tubular morphology remained largely intact, as seen from Figure 8.8 (1), with slight structural distortion and closed tip formation- Figure 8.8 (2). The SAD showed an isotropic halo (diffused rings) at position 1 and a broad diffraction ring at position 2 in Figure 8.8 (3). The isotropic halo indicates the conversion of crystalline phase to amorphous after SCW treatment [467, 501]. The broad diffraction ring indicates the formation of new crystallite sites from the pre-dissolved alumina in the SCW condition [467]. The results of TEM-SAD analysis correlate the findings from XRD patterns discussed in Section 8.3.

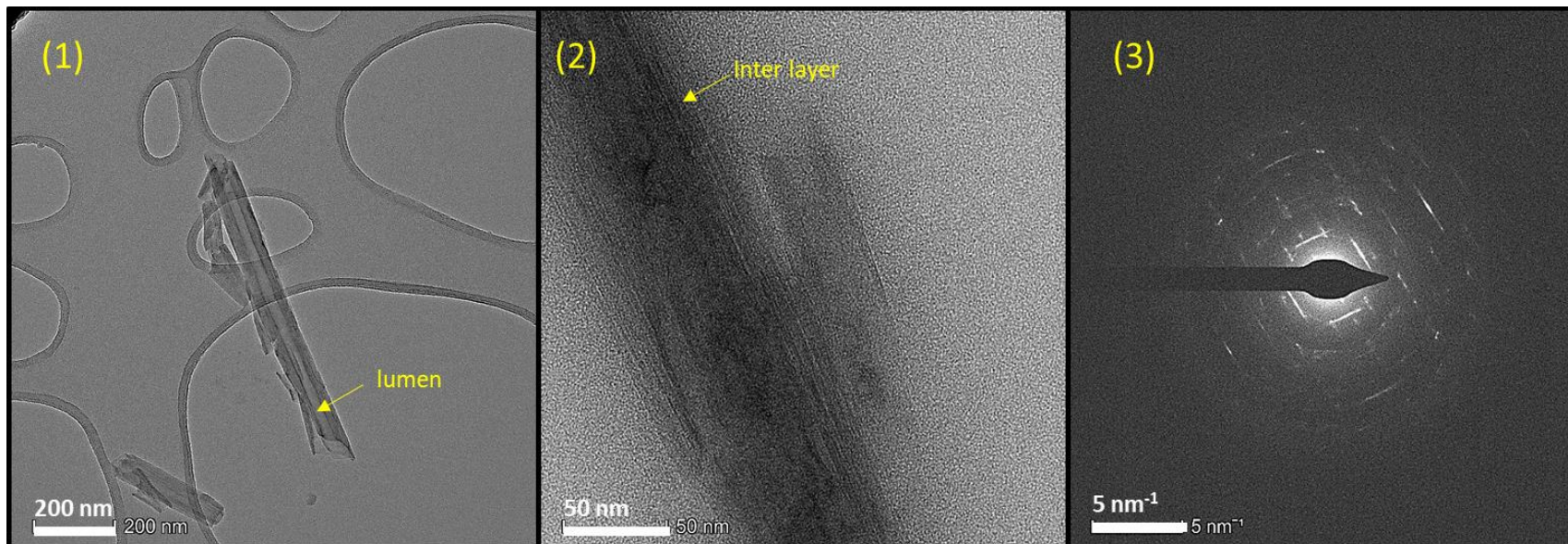


Figure 8.7 Transmission electron microscopy (TEM) image of (1) untreated HNT showing hollow lumen, (2) interlayers of alumina-silicate under magnified view, and (3) SAD patterns of untreated HNT showing the multiple bright spots due to polycrystalline phase.

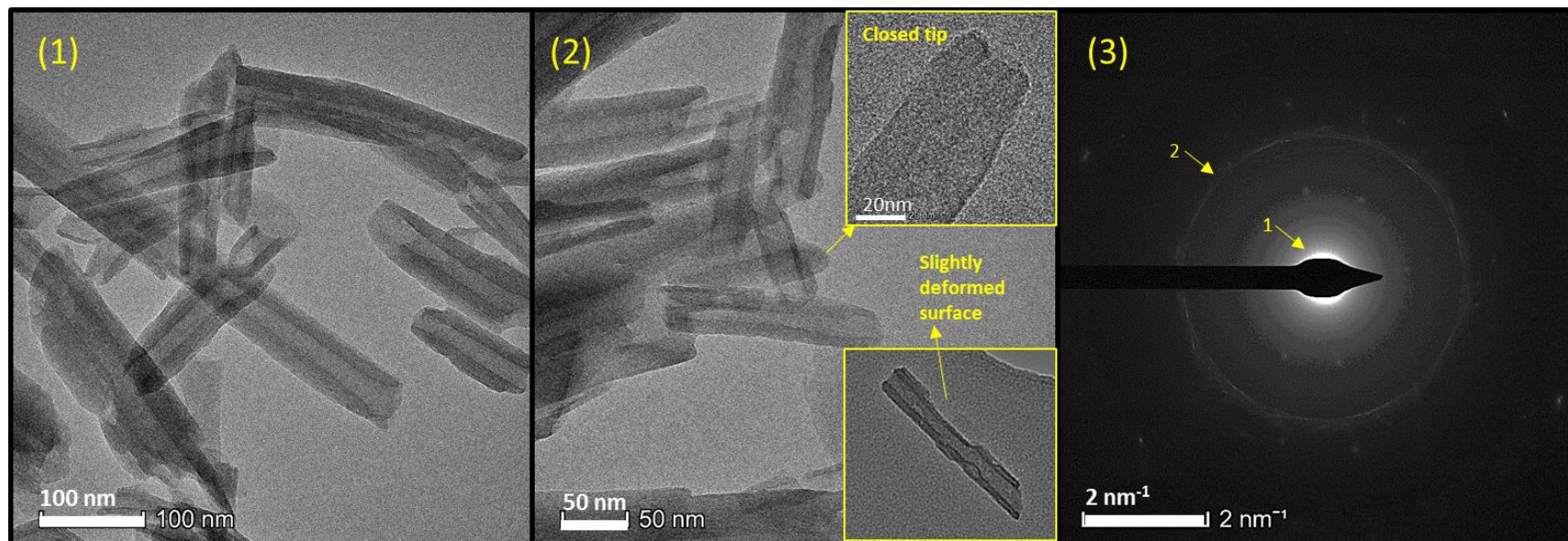
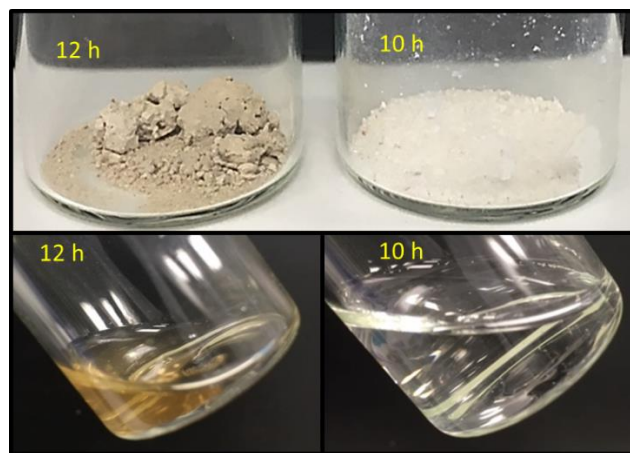
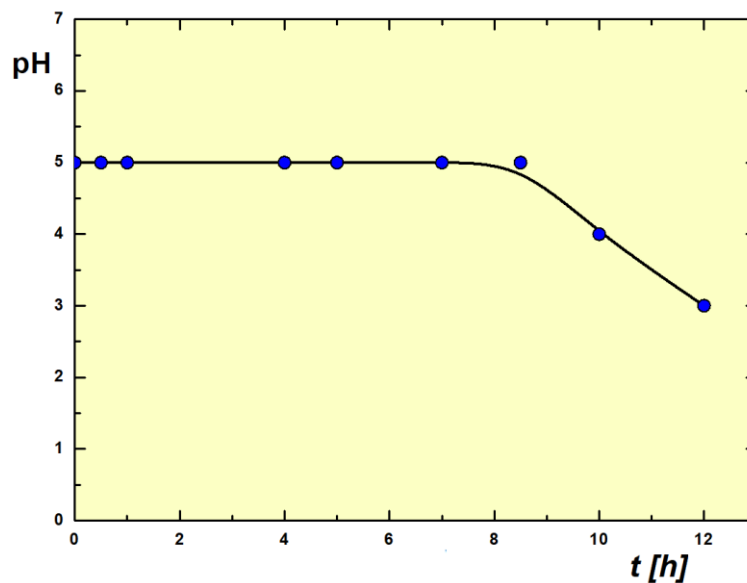


Figure 8.8 Transmission electron microscopy (TEM) image of (1) HNT after 7 h treatment, (2) formation of closed tip and deformed surface after 12 h treatment, and (3) SAD patterns of HNT after 7 h treatment showing formation of isotropic halo at position 1 and 2 indicating the amorphous phase and formation of new crystallite sites.

Apart from the TEM analysis, it was observed that treatment time greater than 10h produced product with pale brown color. The HNT retrieved after 12 h of treatment turned into a dark brown cluster, as seen in Figure 8.9 (a), indicating degradation of the sample. The water collected from the process changed to dark brown color. The pH of the water dropped from pH: 5 to pH: 3, as shown in Figure 8.9 (b). Untreated HNT suspension had a pH in the range of 5-7 [245, 281]. The pH did not change after 7 h, meaning that HNT did not degrade during the first 7 h of treatment. The reduction in pH was observed after 8.5 h. This can be attributed to the irreversible dissolution of HNT in SCW, when HNT was exposed for a long time (>7h).



(a)



(b)

Figure 8.9 (a) TOP-Image of HNT retrieved after 10 h and 12 h of SCW treatment, BOTTOM-water samples collected from the pressure vessel after 10 h and 12 h, (b) Graph of change in pH of the water collected after SCW treatment.

8.5 ZETA POTENTIAL MEASUREMENT

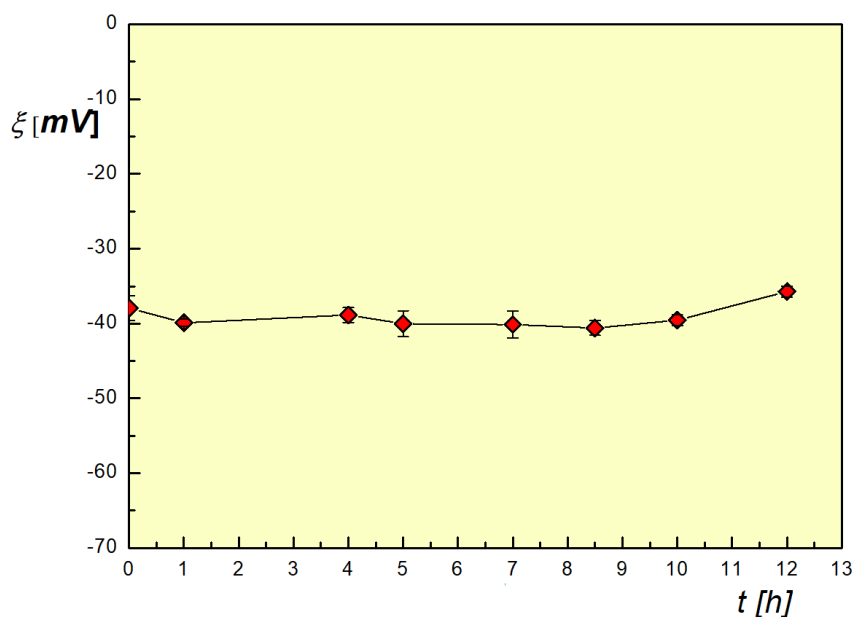


Figure 8.10 Graph showing variation in Zetapotential (ξ) of HNT dispersed in water with treatment time (t), ξ at $t=0$ corresponds to untreated HNT.

The zeta potential (ξ) of HNT is majorly contributed by the outer silicate surface of the material as mentioned in Chapter 4, Section 4.3, and Chapter 2, Section 2.5.1. The outer silicate layer has a large negative surface potential of -35 mV in the pH of 4-8, forming stable suspension [243, 502]. The change in surface potential is influenced by the change in pH of the solution [491, 502]. From Figure 8.9 (b) and Figure 8.10, it can be observed that the surface potential of HNT and pH of the solution did not show significant variation up to 8.5 h of treatment. The pH decreased marginally from 5 to 4, and correspondingly the zeta potential (ξ) increased (Figure 8.10).

Further increase in treatment time to 12 h dropped the solution's pH to 3 with a slight increase in the zeta potential (ξ) [503]. The inner alumina layer shows a positive charge [251]. The increase in zeta potential (ξ) with treatment time can be attributed to the excessive dissolution of the alumina layer in the solution. The dissolution of alumina causes an alteration in the interaction of ions which in turn affects the thickness of the electrical double layer, inducing a slight upward shift in the surface charge in HNT [502, 504]. Hence, prolonged treatment of HNT in SCW generates irreversible dissolution of interlayers affecting the structural integrity and quality of the material.

8.6 CONCLUSION

A novel and non-toxic method of surface modification of HNT using the SCW process was demonstrated. The effects of treatment time on surface properties such as surface area, porosity, morphology, and crystallinity were analyzed. SCW processing of HNT improved the surface area by 25% within 7 h of treatment. Treatment beyond 8.5 h decreased the surface area due to the irreversible dissolution of interlayers in the SCW. The operating temperature and pressure within 7 h of treatment time provided a conducive environment, protecting the structural integrity of the HNT. The improvement in surface area was accomplished by forming new crystallite sites from the partially dissolved alumina interlayers. Processing of SCW is a cheap, green, and non-toxic alternative to the existing acid/alkaline etching. The disadvantages associated with conventional etching, such as retention of toxic solvents, impurities, chemical wastage, and disintegration of particles, have been eliminated by the SCW technique. The SCW process poses scope for large scale (process intensification) implementation of surface modification process for naturally occurring nano-carriers like HNT, which can be consequently used for drug encapsulation and delivery system.

CHAPTER 9

Conclusion and future work

9.1 CONCLUSION

The green techniques such as DG processing and SCW technology provide pathways to produce nanoformulations of API and excipients in a greener way. DG processing provides uniformly spherical particles of size within 5 μm , which are suitable for oral, nasal, and parenteral administration. The shortcomings of conventional nanoformulation techniques such as excessive organic solvent usage, high thermal environment, increased polymorphism is addressed by implementing DG processing.

Elaborate work on the encapsulation of anti-cancer drugs, 5FU, and SLB onto different nanocarriers using DG processes was demonstrated in the current work. The GAS was used to load 5FU onto HNT. The GAS process successfully loaded 5FU onto HNT, with 43% drug loading achieved. The loading using the GAS process demonstrated nearly four-folds increment compared to the conventional mechanical loading process. The assessment of loading performed through *in vitro* drug release showed a 100% release in colonic condition and 30 % in gastric condition, emphasizing the effectiveness of the GAS process towards efficient loading and pH-triggered release.

The formulation of nanoparticles through the in-house conceptualized and designed novel ARISE facilitated in producing ES100 particles of uniformly spherical morphology. The rapid atomization and supersaturation of the ARISE at ambient temperature (25°C) produced particles with an individual particle size of 200 nm and average hydrodynamic diameter of 2.5-3 μm . The ARISE process could produce particles with an ultra-low bulk density (0.02 g/ml), which are suitable for oral and nasal delivery routes. Further, the rapid injection and atomization in the ARISE process were investigated using a simulated spray atomization set-up. The experiments closely simulated the spray pattern and droplet formation inside the precipitation chamber of the ARISE process. The results suggested that the spray is formed in two phases: initial jet and fully developed phases. The time lag between the two phases affects the droplet formation and depends on the rapidity of the valve opening to achieve instantaneous injection of the organic solution.

The viability of the ARISE process for drug encapsulation was demonstrated by loading 5FU and SLB in ES100 at a pressure differential of 50 bar and 25° C. The nanoparticles produced with the ARISE process showed over 96% reduction in size from its pristine form. The study revealed that drug-nanocarrier compatibility played a significant role in drug encapsulation. The SLB-ES100 formulation resulted in a high

loading capacity of about 21% compared to 5FU-ES100 (0.6 %). The results also revealed that the ARISE processed SLB-ES100 nanoparticles showed enhanced pH triggered release at colonic condition (90%) in 24 h, augmenting its application in targeted delivery systems.

The comparative study in the current work between the GAS, ARISE, and conventional mechanical loading processes on HNT revealed that the DG process provided significant enhancement in loading profile compared to the conventional method, confirming the advantage of implementing DG processing in drug formulation.

The green benefits of reduced chemical usage in processing nanomaterials were explored using the SCW system. The surface modification of HNT using the SCW technique provided non-toxic means of achieving increased surface area of HNT. The use of toxic acids and chemicals was wholly avoided, and water at its subcritical state (170° C, 20 bar) was used as an etchant. The surface area of the HNT showed about 25 % improvement within 7 h of treatment with crystallinity and structural integrity retained. The SCW treated HNT contains no acidic residue and can be directly used for further drug loading process.

The above findings demonstrate that green processing techniques such as DG and SCW processing are excellent alternatives to conventional nanoformulation methods. A wide spectrum of drugs and nanocarriers can be processed using DG and SCW techniques to improve their physicochemical and dissolution properties suitable for colon targeted drug delivery systems. The potential application of the ARISE process towards industrial implementation was investigated within a preliminary scale-up study. The study was conducted by micronizing pristine ES100 in 4 stages of operation with increment in the volumetric capacity of the precipitation chamber (60 ml, 150 ml, 300 ml, and 1400 ml). The stage-4 operation was partially automated, implementing a solenoid valve for the rapid injection of the solution. The scale-up system had a nearly 4-fold increase in the anti-solvent volume producing fluffy particles with identical physicochemical properties through all stages. The scale-up study confirmed the reliability of the ARISE process in producing ES100 and ES100-SLB nanoparticles similar to the lab-scale set-up.

9.2. FUTURE WORK

The current work has also outlined possible improvements in terms of process and materials used in DG processing. The ARISE process is relatively new and has immense potential to achieve upscaling and process intensification. The following are recommendations for future work based on the finding of this thesis.

- The core-shell drug delivery vehicles could be produced with the ARISE process in a single step batch processing. The drug can be initially loaded onto the HNT using the prescribed methods in Chapters 4 and 7 and further coated with a protective layer (e.g., ES100 or other biopolymers) to ensure pH-triggered colonic drug release. A preliminary trial of a core-shell system with HNT-ES100 combination is reported in Appendix B. For instance, the HNT-5FU ratio can be selected from the current work. The effect of ES100-HNT ratio on the drug loading and release characteristics can be studied further in-detail and optimized.
- The encapsulation of several drugs in a nanocarrier combination should be explored. Currently, hydrophilic (5FU) and hydrophobic (SLB) drugs were encapsulated in ES100 and HNT separately. Further studies on the simultaneous encapsulation of two or more drugs and nanocarrier combinations can be studied. Encapsulating two drugs in a single nanocarrier creates synergetic therapeutic effects of both drugs as well as processing advantages.
- The spray atomization in the precipitation chamber has been studied in the current work by simulating the spray pattern. However, the precipitation dynamics inside the ARISE processing chamber is highly complex and cannot be observed directly. A detailed multi-physics simulation of the spray patterns and precipitation dynamics would be useful. The simulation would reveal the ARISE process's governing parameters, which can be optimized further to produce fine particle fractions.
- The scale-up of the ARISE process needs parametric optimization. The geometric and parametric variation can affect particle morphology, and parametric optimization must be investigated to ensure particle atomization and size reduction. Automation of the scale-up system can be achieved by implementing automation protocol through LabView and PID control systems in actuating the valves and solution injection systems.

- The scale-up system can be further developed to a pilot plant scale by implementing a parallel operation. The simultaneous ARISE processing would provide continuous production and improved yield that is suitable for industrial mass production. Further, process intensification of the plant can be carried out by performing financial estimation based on production estimation and cost analysis, and detailed market research for the industrial framework.
- The current study focuses on the *in-vitro* release analysis of the formulation to ascertain the efficacy of micronized drugs. The *in-vivo* cell studies can be performed on the (1) colon tissue cultures and (2) animal testing to quantify the drug efficacy. A fluorescence microscopy analysis on the colon cells can be performed to determine the cell viability after the treatment with micronized drugs as a part of the drug screening experiment.

Appendix-A

A1. CALIBRATION CURVES

A1.1 CALIBRATION CURVE OF 5FU IN MEOH

The calibration curve was obtained for a known concentration of the 5FU in MeOH solution before the experimentation and analysis. 25 mg of 5FU was dissolved in 10 ml of MeOH to obtain a test solution of a concentration of 2.5 mg/ml. The calibration curve was obtained for different dilutions of the test solution at a 5FU characteristic wavelength of 266 nm in the UV Spectrometer, and the results were fit with linear interpolation as shown in Figure 10.1.

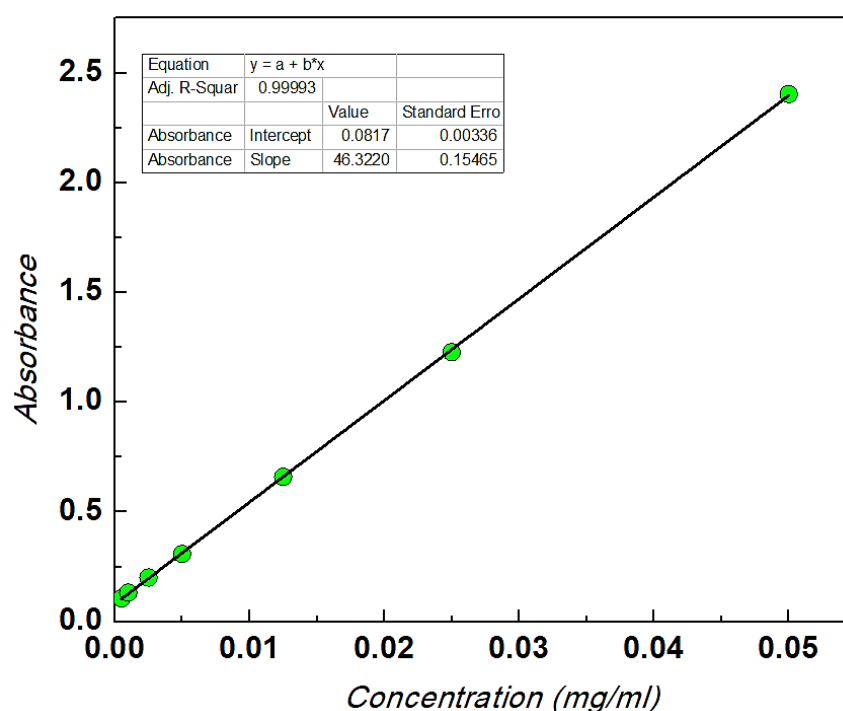


Figure 10.1 Calibration curve of 5FU in MeOH.

A1.2 CALIBRATION CURVE OF 5FU IN PH 7.4-PHOSPHATE BUFFERED SILANE (PBS)

The solution with pH 7.4 was prepared by solubilizing Phosphate buffered silane tablets in deionized water. The calibration curve was obtained for a known concentration of the 5FU in PBS solution before the experimentation and analysis. 12.6 mg of 5FU was dissolved in 10 ml of PBS to get a test solution of a concentration of 1.26 mg/ml. The calibration curve was obtained for different dilutions of the test solution at a 5FU characteristic wavelength of 266 nm in the UV Spectrometer. The results were fit with linear interpolation, as shown in Figure 10.2.

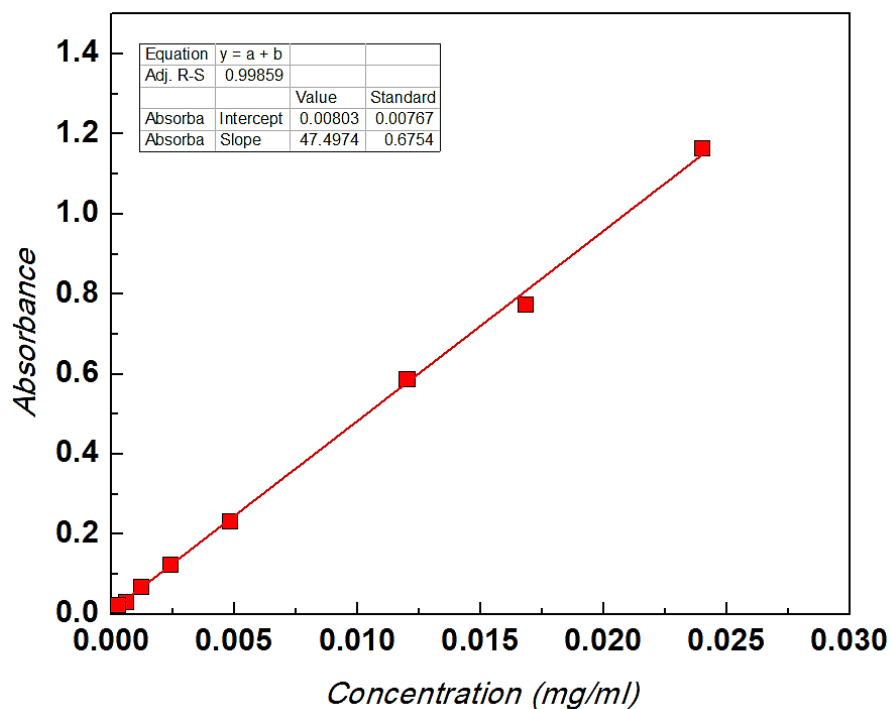


Figure 10.2 Calibration curve of 5FU in PBS.

A1.3 CALIBRATION CURVE OF 5FU IN PH 1.2-0.1M HCL

The 32% w/w HCl was diluted to obtain a 0.1M HCl solution with a pH of 1.2. The calibration curve was obtained for a known concentration of the 5FU in 0.1M HCl solution before the experimentation and analysis. 13 mg of 5FU was dissolved in 10 ml of 0.1M HCl to obtain a test solution of a concentration of 1.3 mg/ml. The calibration curve was obtained for different dilutions of the test solution at a 5FU characteristic wavelength of 266 nm in the UV Spectrometer. The results were fit with linear interpolation as shown in Figure 10.3.

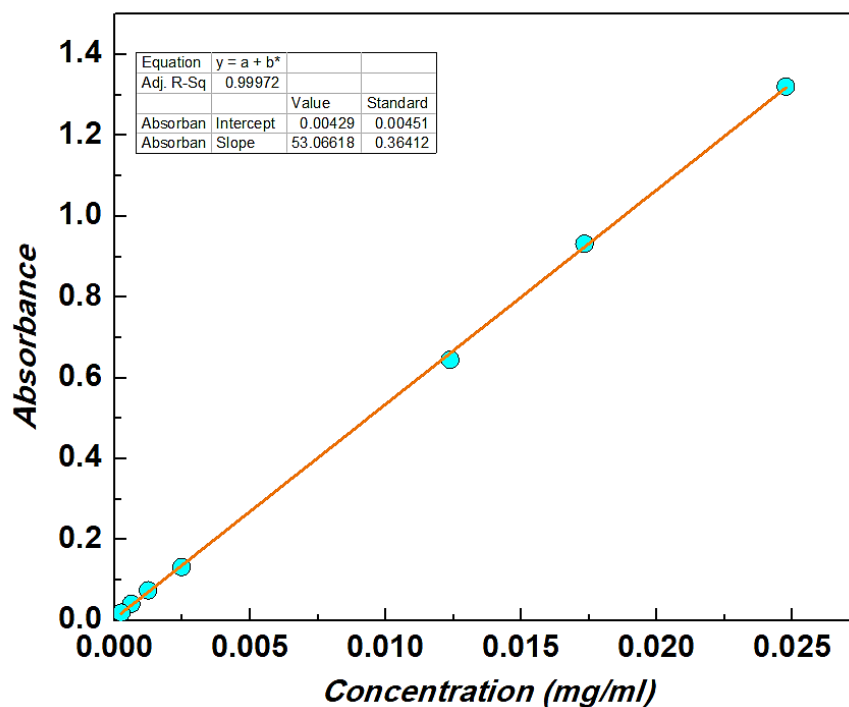


Figure 10.3 Calibration curve of 5FU in 0.1M HCl.

A1.4 CALIBRATION CURVE OF 5FU IN DEIONIZED WATER

The calibration curve was obtained for a known concentration of the 5FU in a deionized water solution before the experimentation and analysis. 14.7 mg of 5FU was dissolved in 10 ml of deionized water to obtain a test solution of a concentration of 1.47 mg/ml. The calibration curve was obtained for different dilutions of the test solution at a 5FU characteristic wavelength of 266 nm in the UV Spectrometer. The results were fit with linear interpolation, as shown in Figure 10.4.

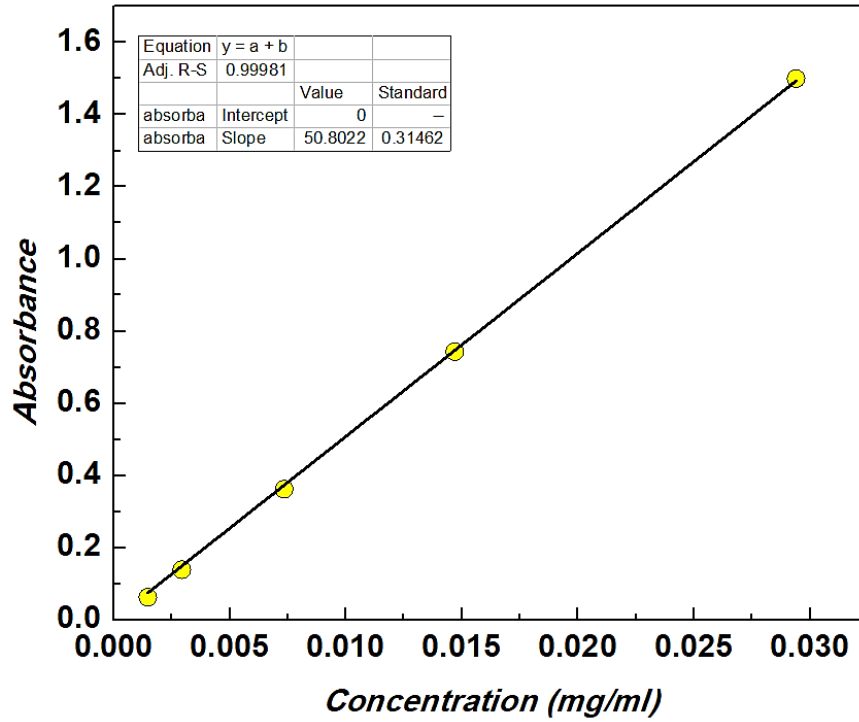


Figure 10.4 Calibration curve of 5FU in deionised water.

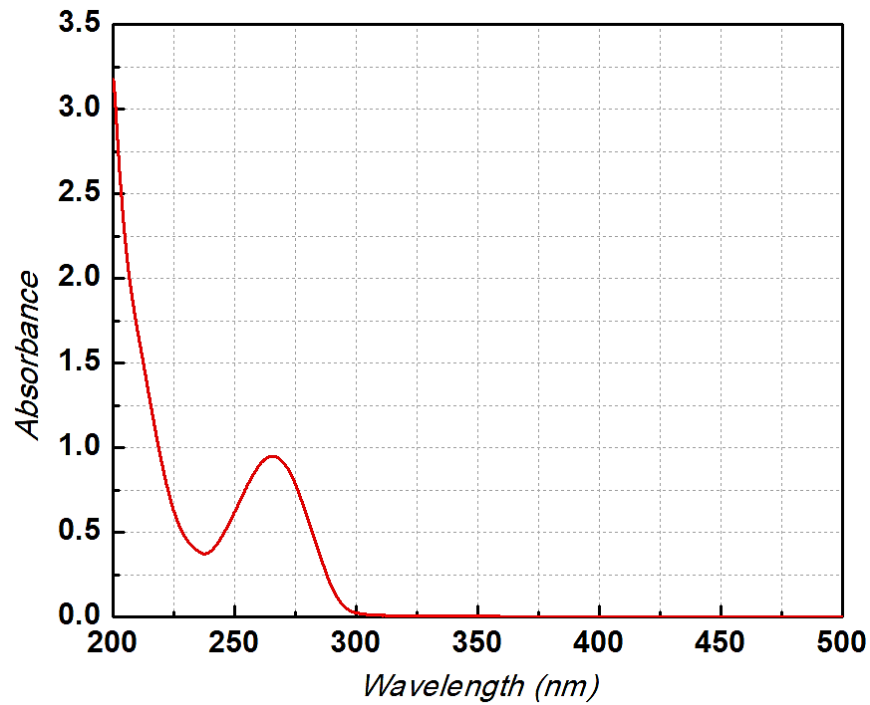


Figure 10.5 Characteristic absorbance peak of 5FU at 266nm.

A1.5 CALIBRATION CURVE OF SLB IN ETHANOL

The calibration curve was obtained for a known concentration of the SLB in the EtOH solution before the experimentation and analysis. 15.3 mg of 5FU was dissolved in 10 ml of EtOH to obtain a test solution of a concentration of 1.53 mg/ml. The calibration curve was obtained for different dilutions of the test solution at a 5FU characteristic wavelength of 288 nm in the UV Spectrometer. The results were fit with linear interpolation, as shown in Figure 10.6.

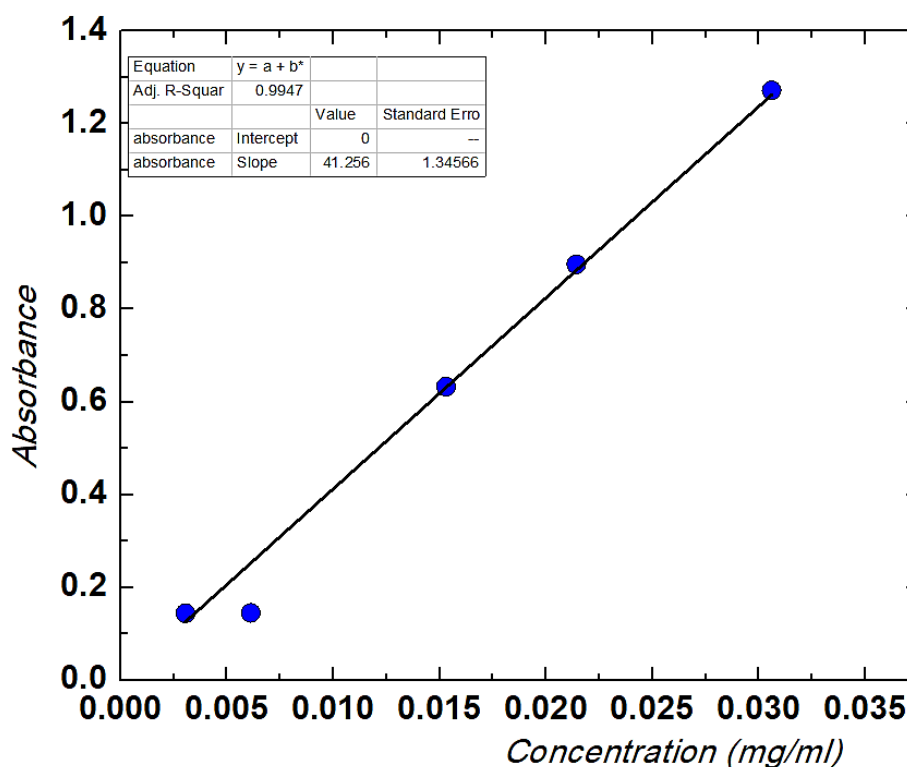


Figure 10.6 Calibration curve of SLB in EtOH.

A1.6 CALIBRATION CURVE OF SLB IN PH 7.4, 1.2, AND DEIONIZED WATER

The preparation of pH 7.4 and pH 1.2 buffers are mentioned in Section 1.2 and 1.3, respectively. SLB has very low solubility in water. Hence a small amount of SLB was solubilized in 10ml MeOH, and 0.5ml from this solution was transferred to 100 ml of deionized water, pH 7.4, and pH 1.2 buffers, respectively to prepare the working solution. The calibration procedures for all the working solutions are similar to Section 1.5, and the curves are plotted for an SLB characteristic wavelength of 288 nm in the UV Spectrometer, as shown in Figure 10.7.

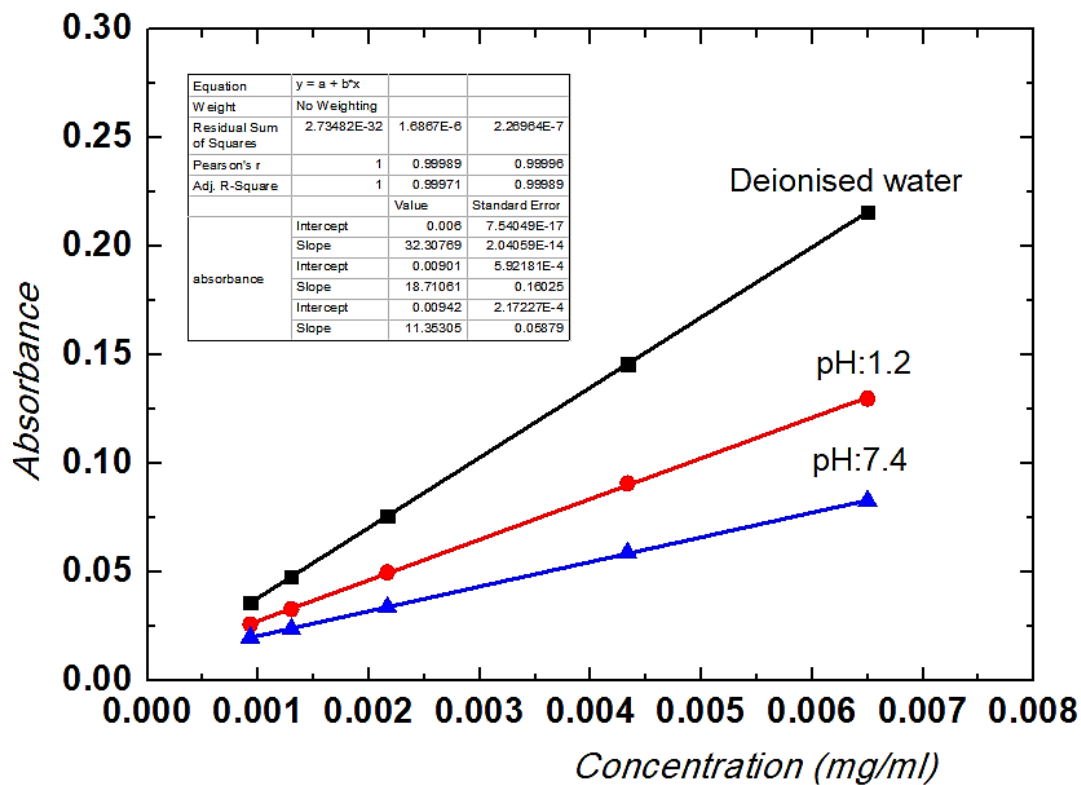


Figure 10.7 Calibration curve of SLB in deionized water, pH:7.4, and pH 1.2 solution. (Concentration of the solutions: 0.0065 mg/ml).

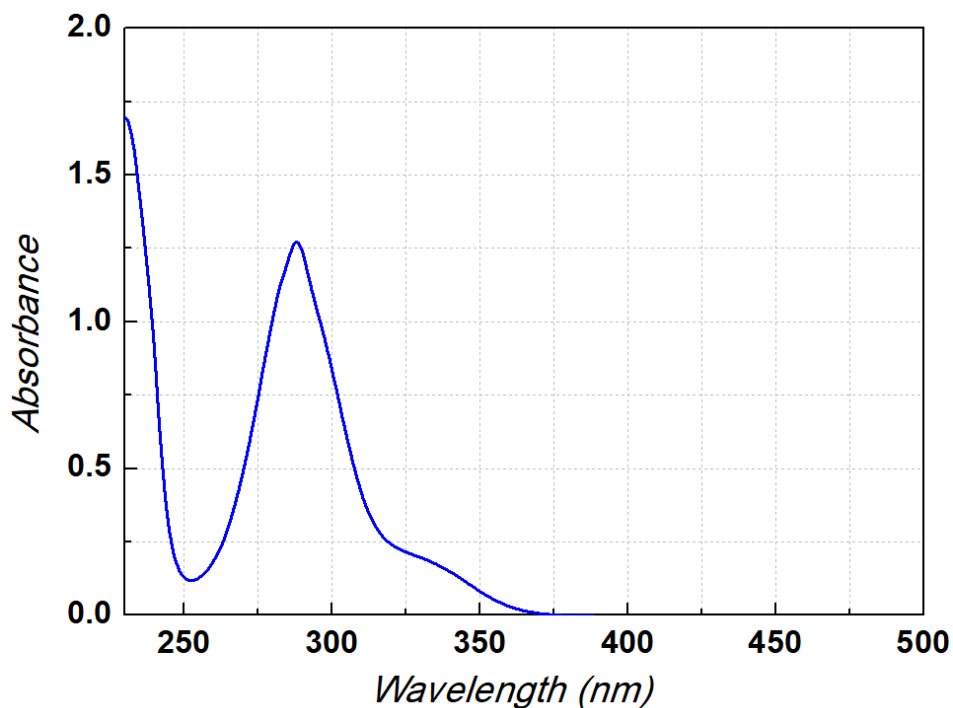


Figure 10.8 Characteristic absorbance peak of SLB at 288nm.

A2. WASHING OF 5FU LOADED IN HNT BY THE GAS PROCESS USING ACETONE

To ascertain the washing step in removing the loosely attached drug from HNT, the 5FU loaded HNT samples were washed for 1 min (as mentioned in Chapter 3, Section 3.1.3) in acetone and MeOH separately. 5FU has low solubility in acetone and is highly soluble in MeOH. The data from Figure 10.9 shows that washing with acetone and MeOH did not show significant variation in the fraction of 5FU (α_F) washed and consequent drug loading (L) measurement from HNT. The observation confirms that: (i) The washing step removed the loosely attached and co-precipitated drug particles, and (ii) The 5FU drug molecule was strongly adsorbed onto the HNT, and the α_F was unaffected by the solvent used. The exhaustive analysis of the washing procedures is detailed in Chapter 4, Section 4.1.

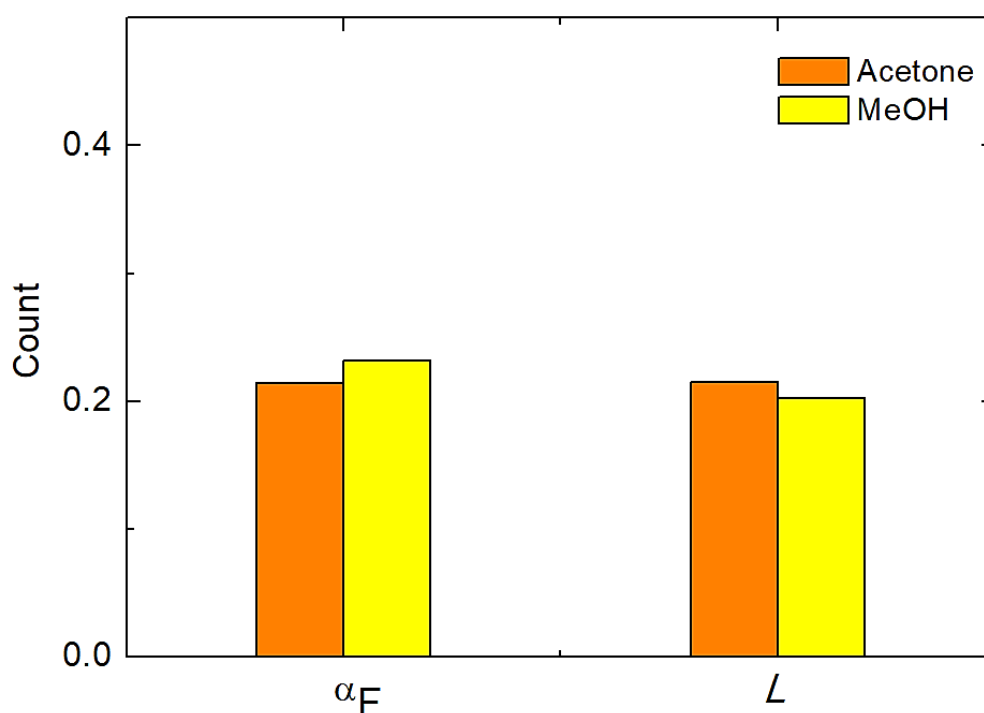


Figure 10.9 Graph of the fraction of 5FU washed (α_F) and Loading (L) of 5FU in HNT after washing with acetone and MeOH.

Appendix B

B1.1. SPRAY ATOMIZATION DUE TO THE GRADUAL OPENING OF THE INJECTION VALVE IN ARISE

The spray pattern and jet propagation due to the rapid opening of the injection valve in the ARISE process were discussed in detail in Chapter 5, Section 5.5. It was inferred that the rapidity of valve opening influences the generation of fine particles due to instantaneous atomization and subsequent supersaturation of solute. On the contrary, when the valve was opened gradually, the time duration of injection was extended by approximately 378 % in air and 980% in water, respectively, during the fully developed jet phase, as shown in Table.B1.1 and Figures 11.1-11.3. The gradual opening of the valve reduces the instantaneous pressure differential across the injection and precipitation chamber. The reduced pressure results in decreased flow velocity (U) and generates a low flow regime near the conduit as described by Eq: 5.4 and Eq: 5.5 in Chapter 5, Section 5.4. The resultant gradual injection of feed solution may cause blockage of the conduit due to partial precipitation of solute due to the expansion of the solvent during the atomization and formation of irregular particles. Therefore, the rapid opening of the injection valve was proposed for obtaining complete atomization and fine particle formation.

Table 11.1 Spray time variation between rapid and gradual valve opening.

Medium	Initial Jet phase		% Increase
	Rapid opening [ms]	Gradual opening [ms]	
Air	63	99	57
water	147	640	335
	Fully developed Jet phase		
	Rapid opening [ms]	Gradual opening [ms]	
Air	500	2392	378
water	650	7021	980

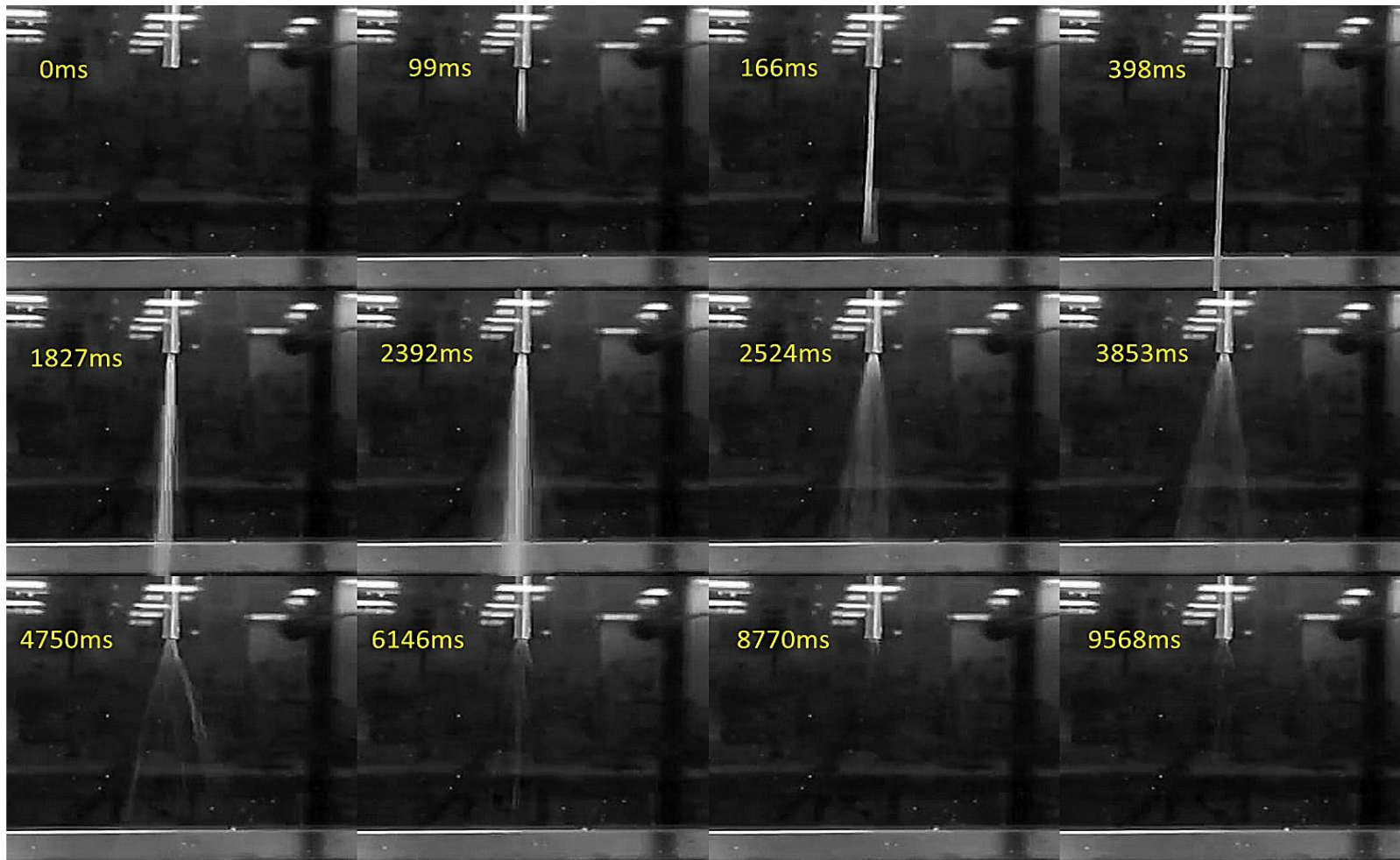


Figure 11.1 Spray propagation of ES100 in air through the gradual opening of the injection valve in the ARISE process.

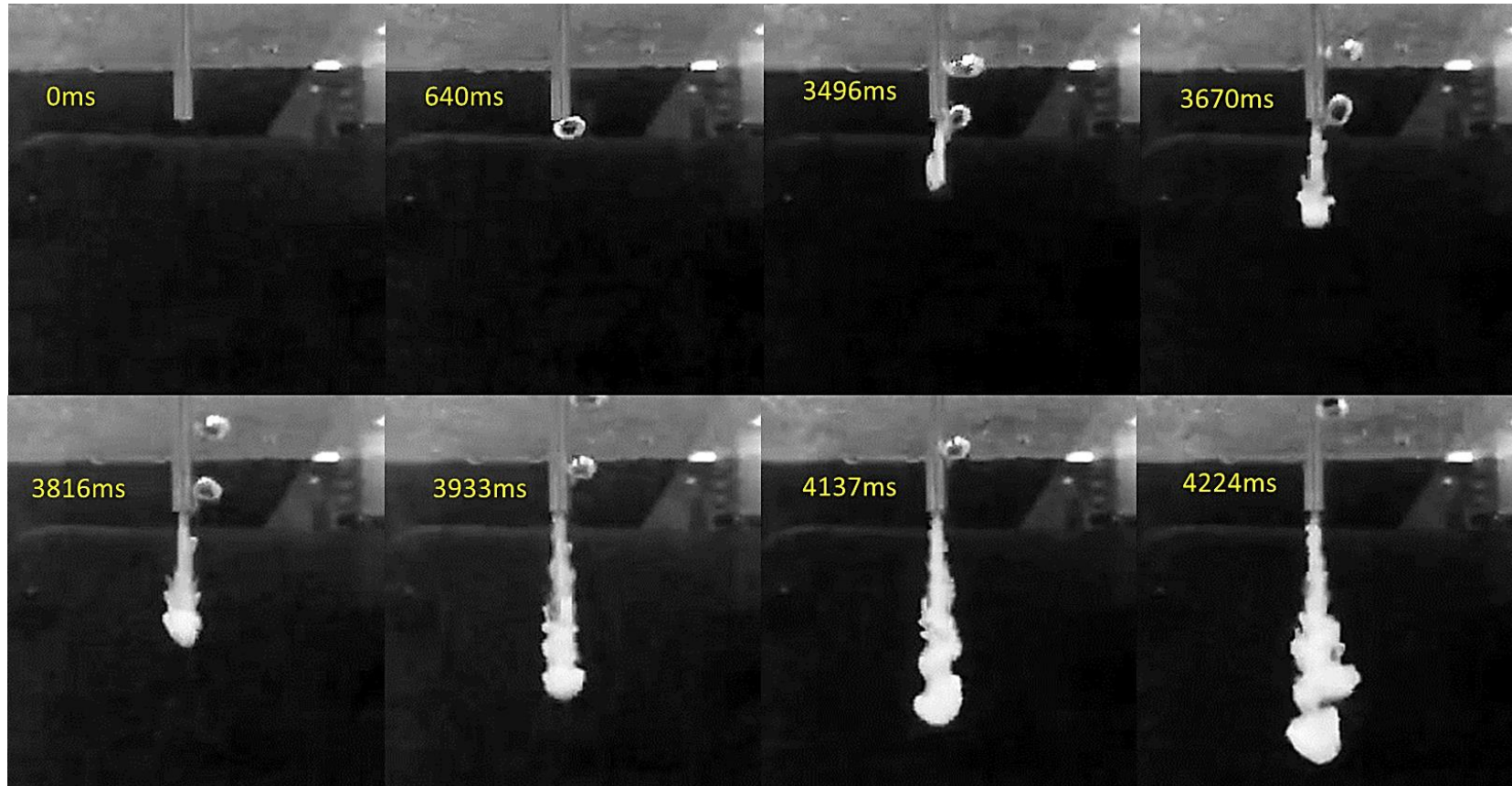


Figure 11.2 Initial jet phase of spray propagation of ES100 in water through the gradual opening of the injection valve in the ARISE process.

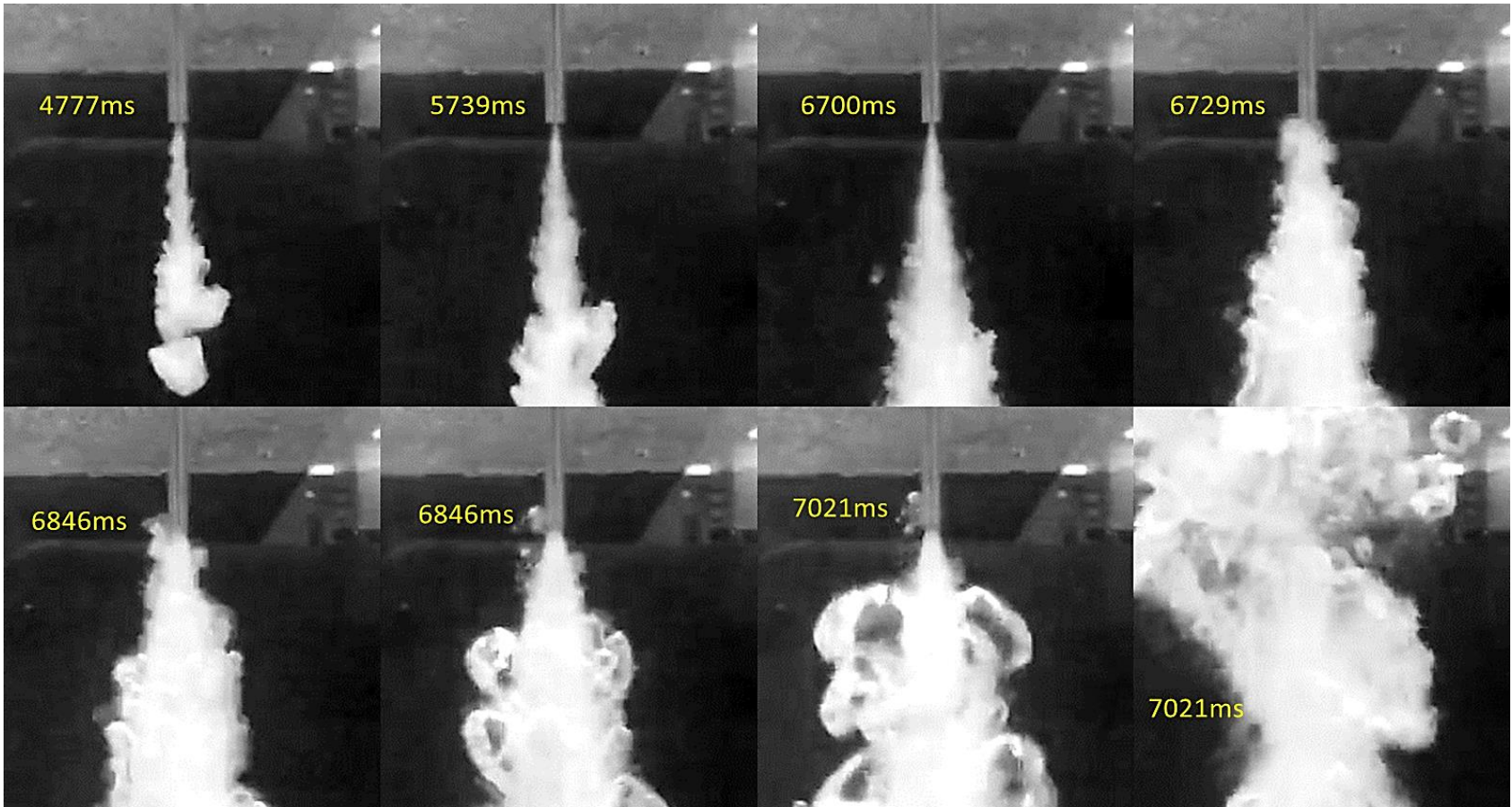


Figure 11.3 Fully developed phase of spray propagation of ES100 in water through the gradual opening of the injection valve in the ARISE process.

B1.2 INFLUENCE OF ADDITIVES IN ES100 ON SPRAY PROFILE

The spray profile analysis of pristine ES100 solution was studied in Chapter 5, Section 5.5. In an inquisitiveness to explore the effect of additives on the spray width of the ES100 solution, a preliminary trial on spray experiment was carried out with a mixture of ES100 and a model drug, p-Coumaric acid (pCA). About 130 mg of pCA was added to 400 mg of ES100 mixed in 10 mL EtOH to prepare the working solution. The spray experiment was carried out similarly, as described in Chapter 3, Section 3.2.3.

It was observed that the inclusion of additives decreased the spray width of the solution in both air and water medium, as seen from Figures 11.4 and Figure 11.5. The spray width reduced by 33% and 42% in the initial jet phase of air and water, respectively, and about 37% and 47% in the fully developed jet phase in air and water, respectively. However, the influence of the decrease in spray width on the particle size and morphology is yet to be studied and is reserved for future work as mentioned in Chapter 9, Section 9.2.

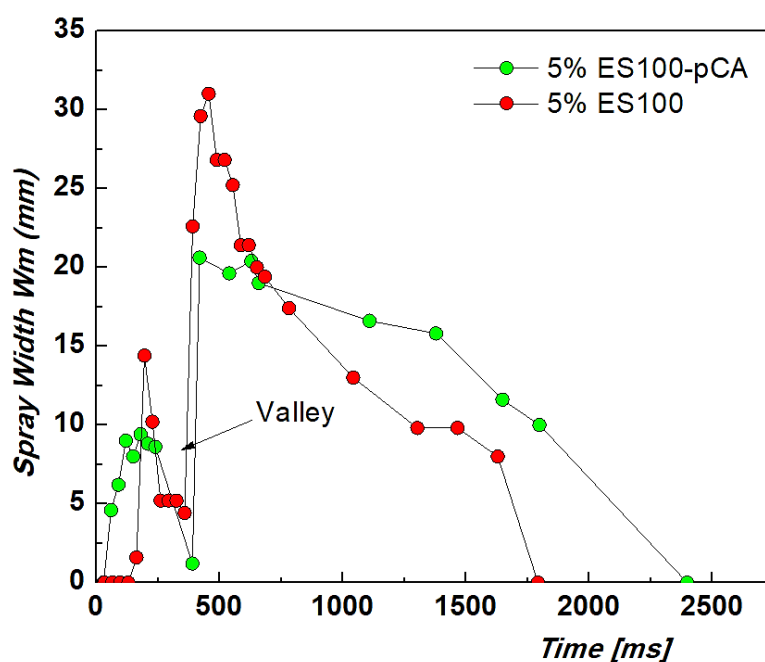


Figure 11.4 Spray width as a function of spray time for 5% w/w pristine ES100 and ES100-pCA combination sprayed in the air.

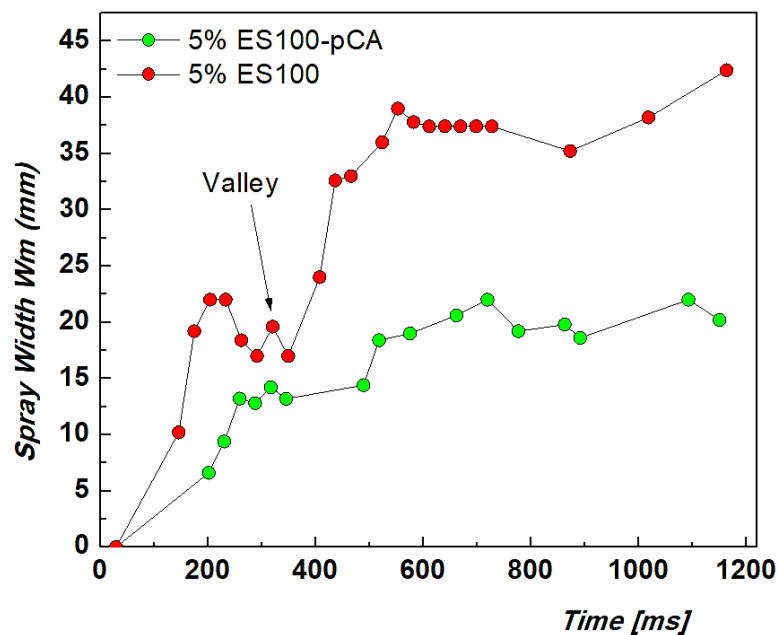


Figure 11.5 Spray width as a function of spray time for 5% w/w pristine ES100 and ES100-pCA combination sprayed in water.

B1.3. ARISE ASSISTED COAT OF ES100 ON HNT

ES100 is widely used as a coating material on nanocarriers. The benefits of ES100 in various formulations was detailed in Chapter 2, Section 2.4. The prospects of coating ES100 on HNT using the ARISE process was initially attempted. The ES100 and HNT were mixed in a 1:1 mass ratio (400 mg of each) to produce a solution-suspension in 10 mL MeOH. The ARISE process parameters were fixed, as described in Chapter 3, Section 3.2.2. The micrographs of the product obtained are shown in Figure 11.6.

The product obtained was fluffy like the pristine ES100 obtained from the ARISE process. The bulk density measured was 72.09 mg/ml, which was 40% higher than the pristine ES100 (51.40 mg/mL from MeOH) obtained from ARISE. It can be noticed from Figure 11.6 that ES100 functioned as a binding material which cemented the individual HNT into a cluster. The ES100 also formed a partial coating on the surface of the HNT cluster, as seen in Figure 11.6 (c, d). By optimizing the ES100-HNT mass ratio, a complete coating of HNT can be achieved, which can further prevent the premature release of drugs from HNT. The study has the potential of formulating a multi-excipient drug delivery system in the future.

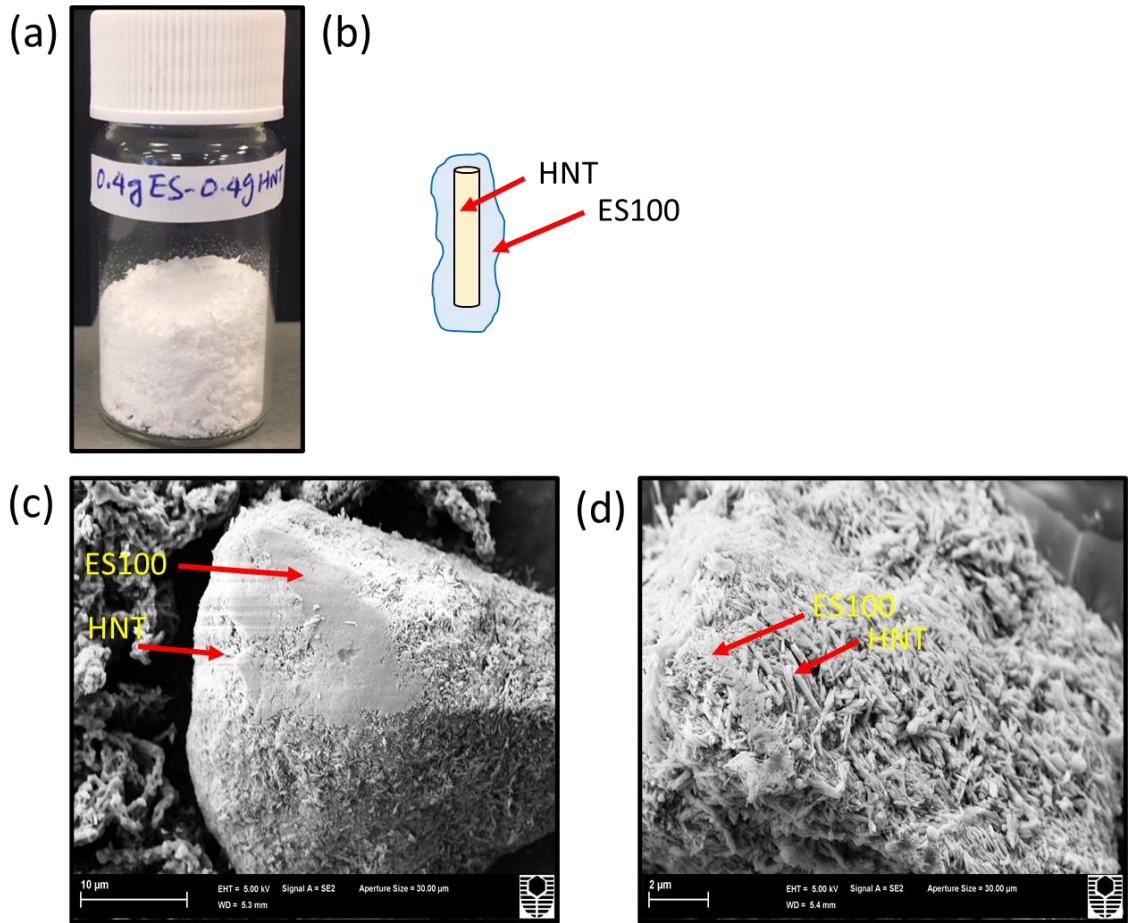


Figure 11.6 (a) ES100-HNT sample retrieved from ARISE process, (b) Illustration of ES100 coating on the HNT surface, (c, d) ES100 coated HNT from ARISE.

Appendix C

C1. PRELIMINARY SCALE-UP STUDY ON ARISE

C1.1 INTRODUCTION

A successful operation of chemical and pharmaceutical industries relies on the effective use of materials to achieve high yield at reduced production cost. The concept of process intensification (PI) imparts sustainable development of processes with the aim of not only reducing the production cost but also towards maintaining green and energy-efficient processing [505].

The term process intensification (PI) is defined as adopting developmental methods that bring on sustainable production with improved product quality, safety operation, cost-effectiveness, cleanliness, and conservativeness [506, 507]. PI in chemical and pharmaceutical systems can be achieved by two means. (i) the production line design, optimization of processing parameters such as heat and mass transfer, and re-engineering plant set-ups, (ii) processing methods to reduce production time, energy consumption, and combine processing steps to a one-step process[508].

In alignment with the current thesis on lab-scale experimentation, PI in the pharmaceutical formulation method culminates with the development of lab-to-industry scale-up systems. As a matter of principle, the reliability of the engineering processes can be harnessed when they are feasible for industrial implementation. Towards achieving these objectives, a preliminary investigation of the scale-up processing of the ARISE was performed. The scale-up processing was performed in 4 operating scales (SC 1-4) with an increasing volume of the precipitation chamber (60 ml, 150 ml, 300 ml, and 1400 ml). The SC-4 operation was designed as a pilot plant with a pneumatic controlled solenoid valve for the rapid injection of the API solution. The processing steps and operation method for the scale-up are explained in the following sections.

C1.2 MATERIALS AND METHODS

The first 3 scales of the ARISE rig consists of a 10 ml high-pressure injection chamber (Sandvik 3R60 ASTM A213-AW /A269), connected to the 60 ml Jegurson cell (Jegurson Gauge R-32 Size 13), 150 ml (Swagelok 316L-50DF4-150 Stainless steel double end DOT-Compliant cylinder), and 300 ml (Swagelok 316L-50DF4-300 Stainless steel double end DOT-Compliant cylinder) precipitation chamber. The SC-4 was custom made with a high-pressure injection chamber (100 mL) (HiP, USA, 304SS HT#0421034-6 TOC1) connected to a 1.4 L precipitation chamber (Hip, USA, 304SS

HT#551235, 405326 REACTOR) via a HiP 10-24AF6 cross taper seal fitting and Sandvik 3R60, ASTM SA213 pipes (OD 13 mm, ID 8 mm). The industrial pressure transducer (Viatran 715-529-3800) was connected to the set-up using Sandvik 3R60, ASTM SA213 pipes (OD 9.33 mm, ID 4.60 mm). The SC-4 incorporated rapid opening through a pneumatically controlled valve (HiP-MINI HIPPO, USA). An automated self-priming high-pressure ISCO pump (Teledyne dual-pump continuous flow system) was used to provide an uninterrupted supply of dense CO₂ during the rinsing step. The parts of the SC-4 ARISE rig, and the scales of operation are shown in Figures 12.1 and 12.2, respectively.

The concentration and the volume of working solutions were fixed to 5% ES100 in 10 mL EtOH, respectively, for all the operating scales. In one of the trials, 77 mg of SLB was loaded in 5% ES100 in the SC-4 scale-up ARISE process. The operating pressure and procedures were based on the method described in Chapter 3, Section 3.2.2. The first 3 scales of operations (SC 1-3) were performed in a water bath at a controlled temperature of 25⁰ C, and the SC-4 stage was performed at ambient condition (approximately 24⁰ C).

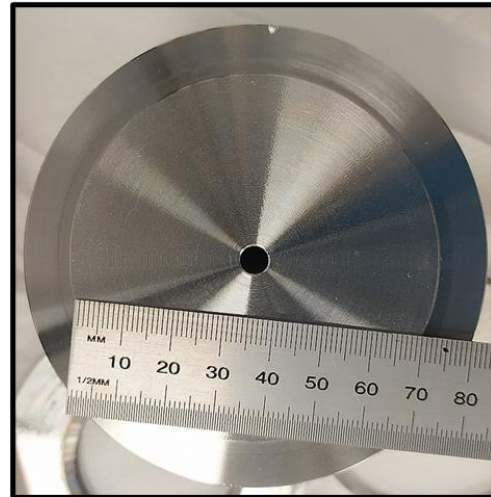
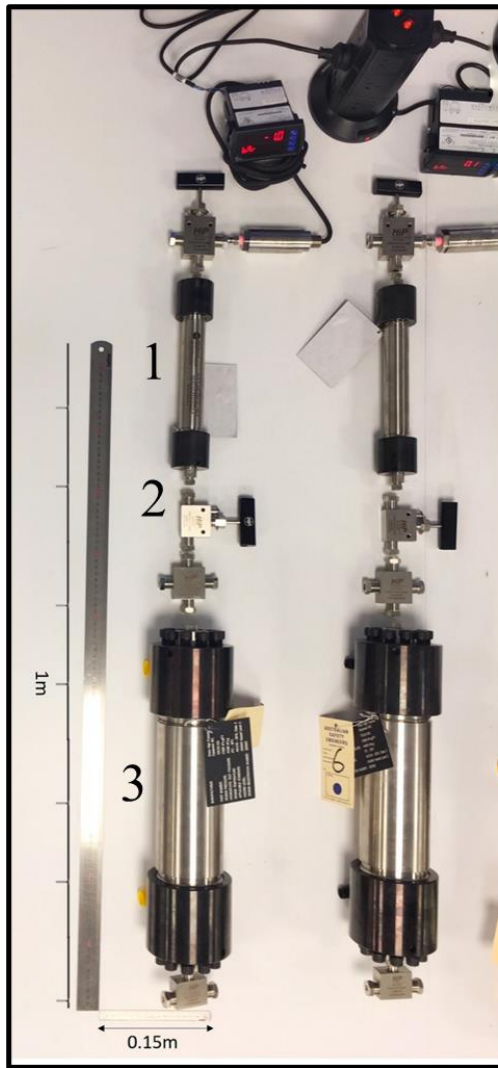


Figure 12.1 Assembly parts of SC-4 ARISE set-up. Left: (1) Injection chamber, (2) Tapper sealed fittings, and (3) Precipitation chamber, Right: integrated conduit in the precipitation chamber (ID 4mm).

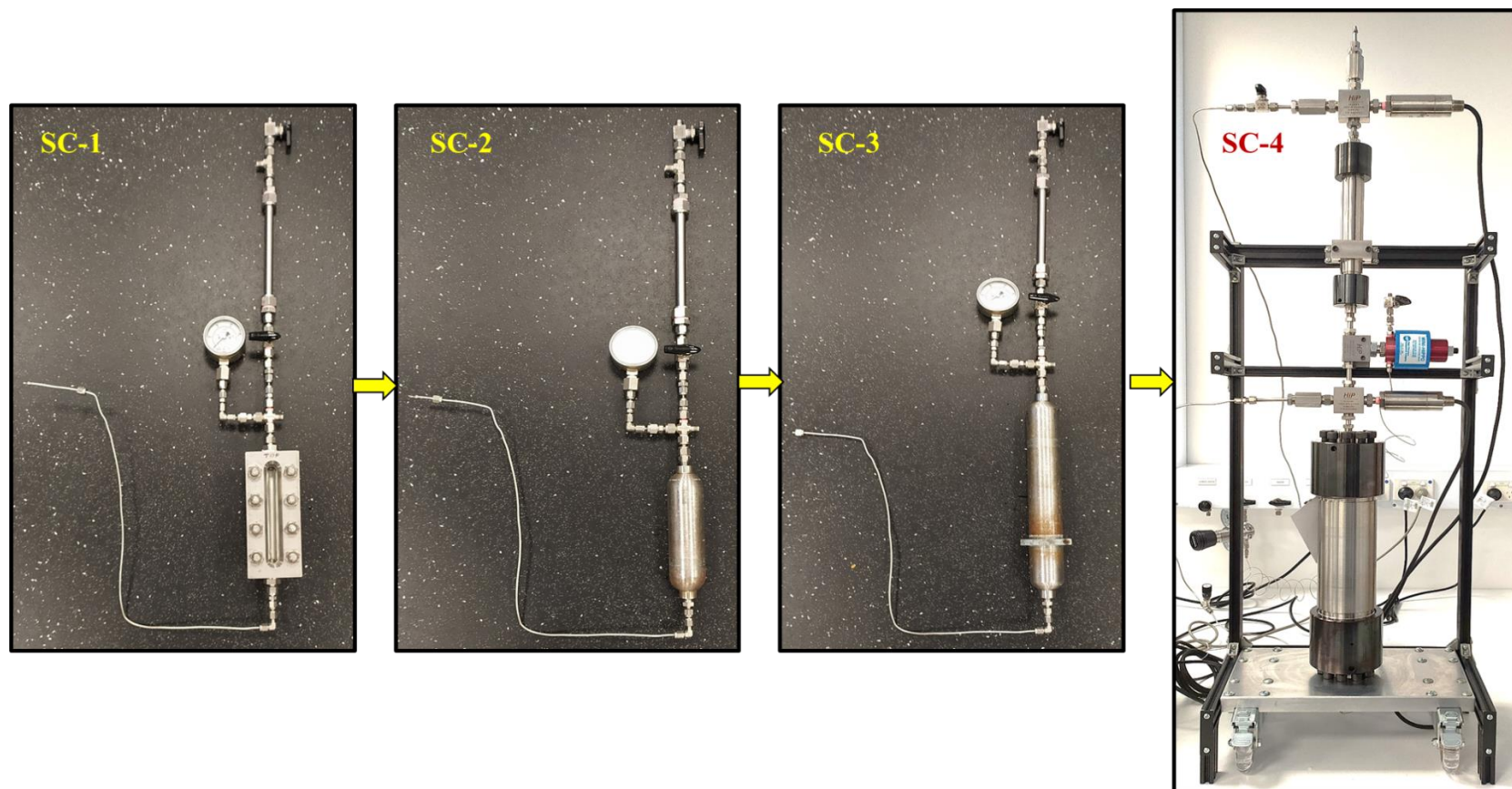


Figure 12.2 Assembly parts of SC-4 ARISE set-up operation with a varying volume of precipitation chamber (V_p), SC-1: 60 mL, SC-2: 150mL, SC-3: 300 mL, and SC-4: 1.4 L).

The evaluation of scale-up was conducted by examining the particle morphology by-SEM (Tescan Clara, Czech Republic) and measuring the particle size distribution using Zetasizer Nano ZS (Malvern).

C1.3. RESULTS AND DISCUSSION.

C1.3.1 ANTISOLVENT EFFECT

The ARISE process is a neoteric process having broad scope for process intensification towards scale-up operations, as explained in Chapter 2, Section 2.3.2.1. *Kurniawansyah* [74] has demonstrated 3 stages of scale-up operations in the ARISE with an increasing volume of the precipitation chambers (0.5 L, 1L, and 2.2 L) and injection through the manual opening of valves. The work demonstrated micronization of APIs such as pCA, and Curcumin, with Hydroxypropyl-beta cyclodextrin (HP β CD) polymer [74, 164]. The current scale-up study focuses on implementing the ARISE process with partial automation of the rapid injection of feed solution. The scale-up incorporates a continuous supply of dense CO₂ using a self-priming high-pressure pump suitable for industrial applications.

In a DG process, the antisolvent-solvent ratio determines the degree of supersaturation and hence the precipitation of the solute [509]. Fig 12.3 shows the trend in the antisolvent-solvent ratio with the scale-up process. The lab-scale ARISE processes reported by *Kurniawansyah* [74] and the ARISE work in the current thesis, were operated within the antisolvent-solvent ratio of 6 to 30 (Fig 12.3). The scale-up rig reported by *Kurniawansyah* was operated in a fixed ratio of 30 for a high volume capacity of precipitation chamber (1L, and 2L) [74]. The current work demonstrated the operability of the ARISE process at a ratio of 140 (Fig 12.3). The exponential increase in the antisolvent concentration over 360% indicates that the supersaturation rate in the current scale-up (SC-4) is higher than the previously reported works which could positively influence the rapid crystallization and solvent extraction.

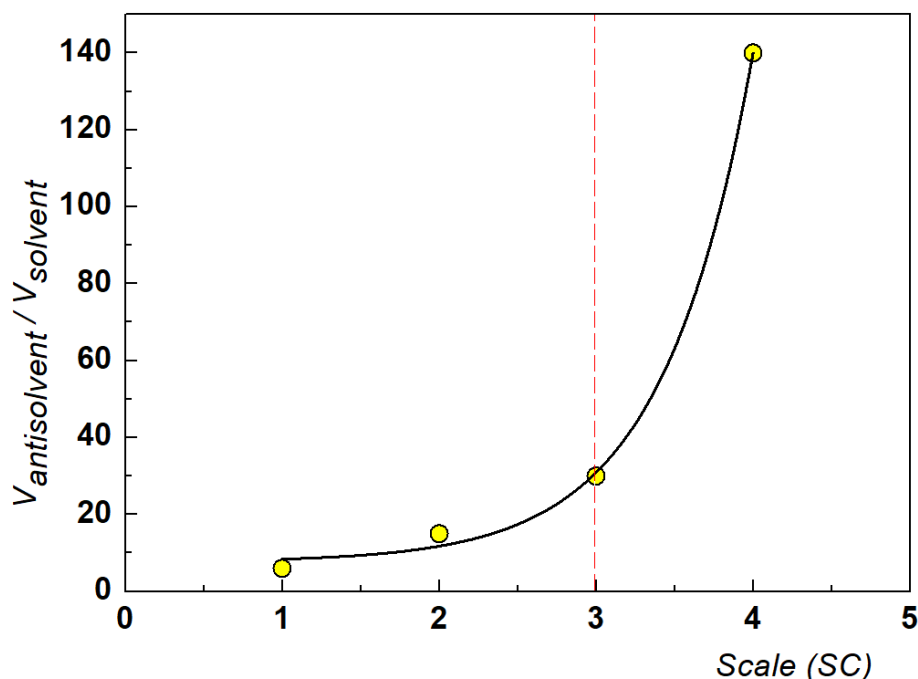


Figure 12.3 The antisolvent-solvent volumetric ratio for different scales of ARISE operation.

C1.3.2. BULK DENSITY

The bulk density (ρ_{bulk}) of the products obtained from the scale-up ARISE is shown in Fig 12.4. The ρ_{bulk} decreased with an increase in the fluffiness of the products in SC-1 to SC-3, indicating that for a fixed concentration of ES100, the increase in the volume of precipitation chamber (V_p) produced fine particles occupying higher volumetric space. The reduction in ρ_{bulk} was systematic from SC-1 to SC-3. In line with the above argument, we may expect a further decrease in ρ_{bulk} in SC-4. However, the preliminary trials showed an increase ($\approx 50\%$) in ρ_{bulk} at SC-4. The reason for the variation is unclear and could be due to the change in operating conditions and dimensions of the SC-4 rig. It is important to note that the conduit ID of the SC-4 was 4 mm (Fig 12.1), which is four folds higher than the SC 1-3 (ID 1mm). The change in conduit diameter has a significant effect on the jet velocity and the Reynolds number, and hence the atomization (Chapter 5, Eq 5.4), which cannot be neglected [510]. Further optimization and process intensification of the SC-4 is required and could reveal the ideal operating parameters suitable for producing low ρ_{bulk} product. Albeit the marginal increase in ρ_{bulk} in SC-4 from SC-3, the ρ_{bulk} of the ARISE product in SC-4 was $\approx 45.5\%$ lower than the pristine ES100 (Fig 12.4).

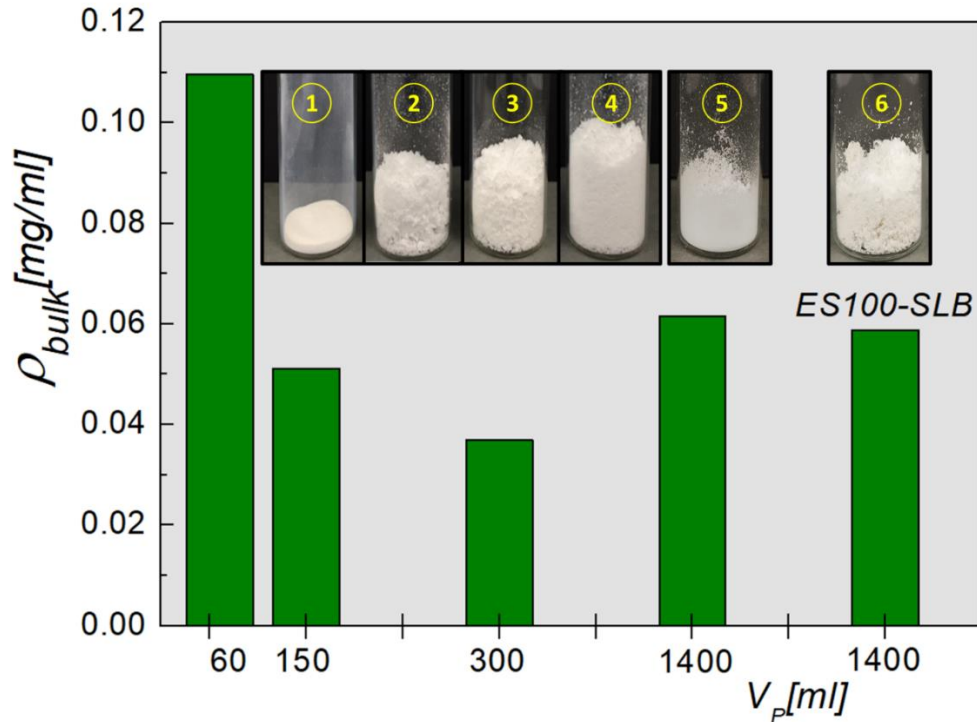


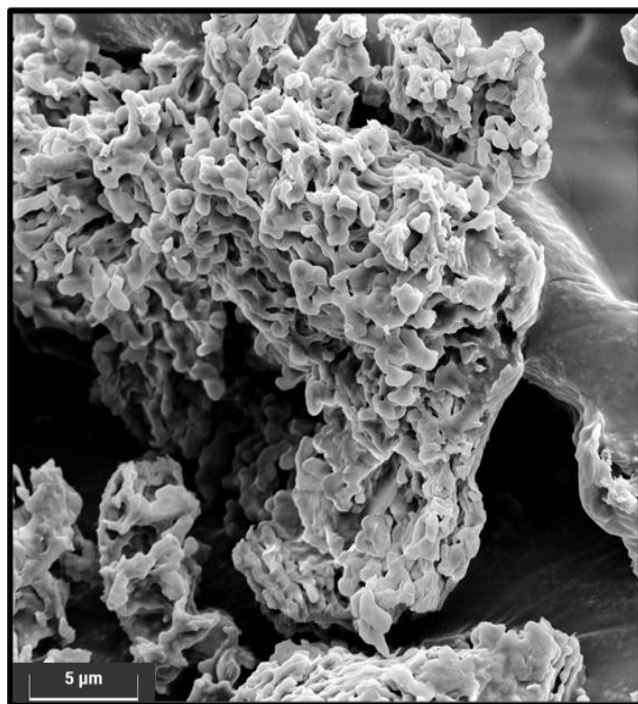
Figure 12.4 Bulk density (ρ_{bulk}) vs volume of precipitation chamber (V_p) for 5% ES100 and 5% ES100-SLB retrieved from scale-up ARISE process. (Inset figure are samples from-1: pristine ES100, 2: SC-1 (60ml), 3: SC-2 (150ml), 4: SC-3 (300ml), 5: SC-4 (1.4L), and 6: SC-4 (ES100-SLB).

C1.3.2 SCANNING ELECTRON MICROSCOPY

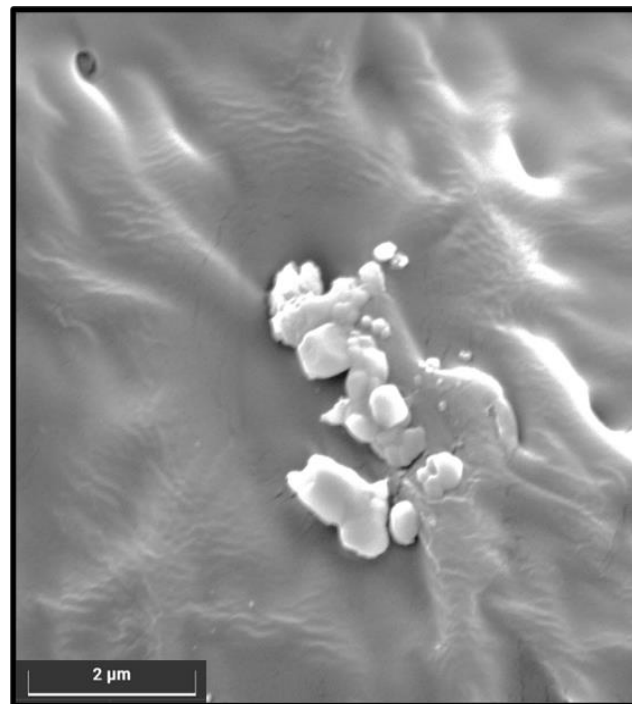
The SEM analysis of particles from the scale-up ARISE indicates that the particles were mostly spherical in morphology, as shown in Figures 12.5-12.10. The SC-1 produced irregular particles with big chunks and flakes (Figure 12.5 a, and b). The SC-2 produced uniformly spherical particles, as discussed in Chapter 5, Section 5.4, Figure 5.8. Similar spherical particles with intermediate bridging were produced in SC-3, as seen from Figure 12.6 a, and b. The reason could be due to the increase in the length-to-diameter (L/D) ratio of the precipitation chamber. SC-3 has an L/D=10.2, which is twice that of SC-2. The increase in L/D implies that the spray jet from the conduit travels longer path length inside the precipitation chamber. The solution may partially crystallize during the jet propagation, forming bridges between the atomized particles (Figure 12.6 a, b). However, a detailed investigation is required to corroborate the findings. The SC-4 produced spherical particles of different sizes, as shown in Figure

12.7 (a,b). The SEM images revealed that the small particles clustered around the bigger spherical particles, as seen from Figure 12.8 (a,b). The ES100-SLB particles from the ARISE process also had a homogenous spherical morphology analogous to the pristine form, as shown in Figures 12.9 and Figure 12.10. The SC-4 has an L/D=6.0, similar to the SC-2 (L/D=5.6, operation scale for the current thesis work), producing similar particle morphology as that of the SC-2 set-up.

The microscopic evidence proves that the particles' spherical morphology was retained in different operating scales of the ARISE, substantiating the reproducibility of the scale-up process, as observed by *Kurniawansyah* [74].

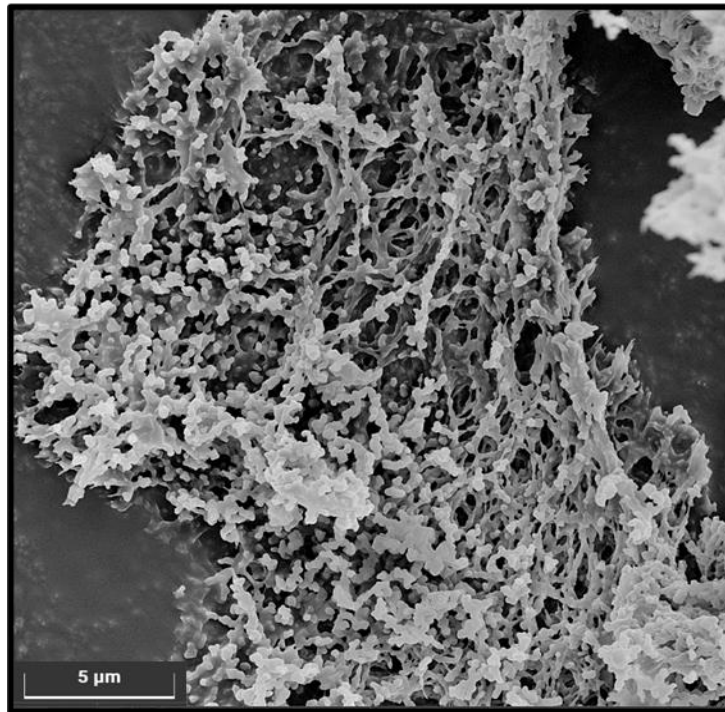


(a)

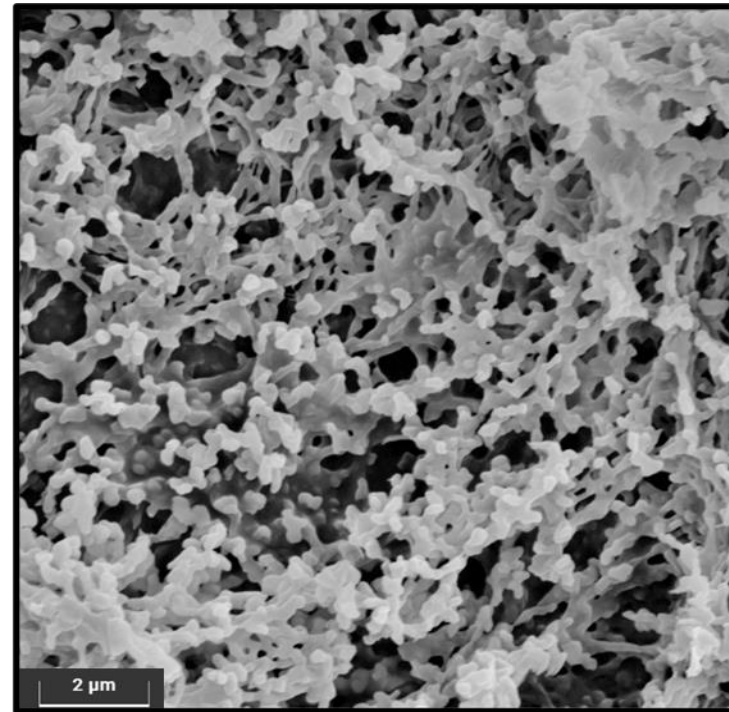


(b)

Figure 12.5 ARISE processed ES100 from SC-1 at, (a): 5 μm scale bar, and (b): 2 μm scale bar-magnified view.

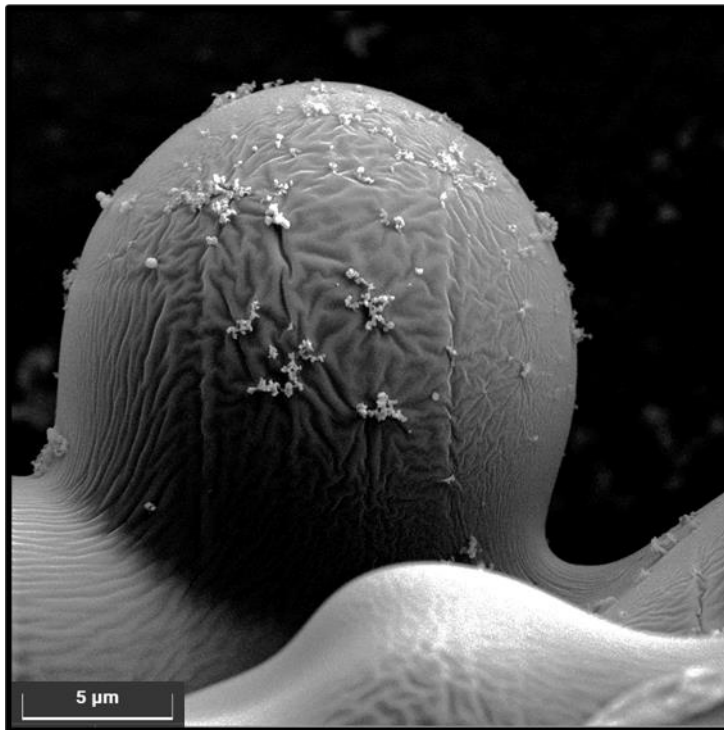


(a)

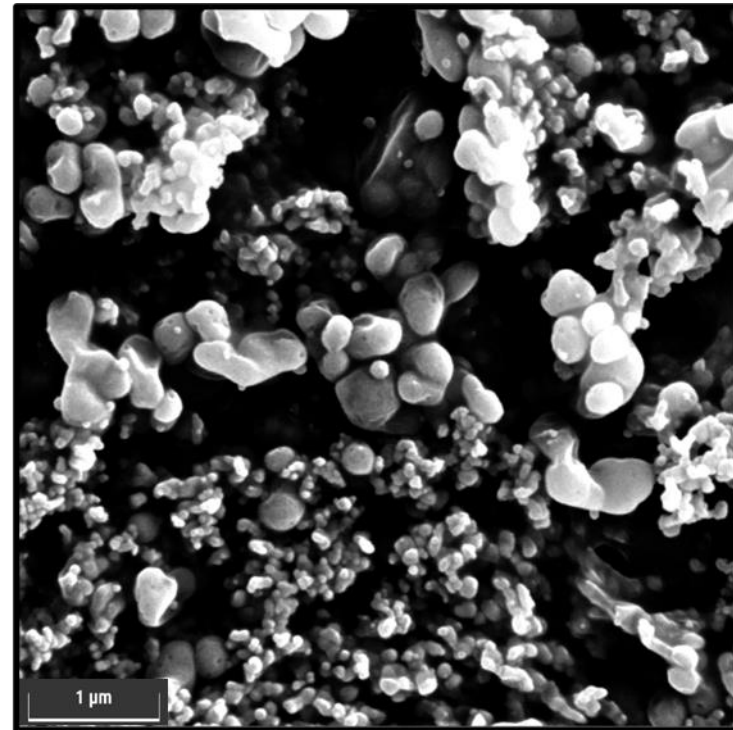


(b)

Figure 12.6 ARISE processed ES100 from SC-3 at, (a): 5 μm scale bar, and (b): 2 μm scale bar-magnified view.

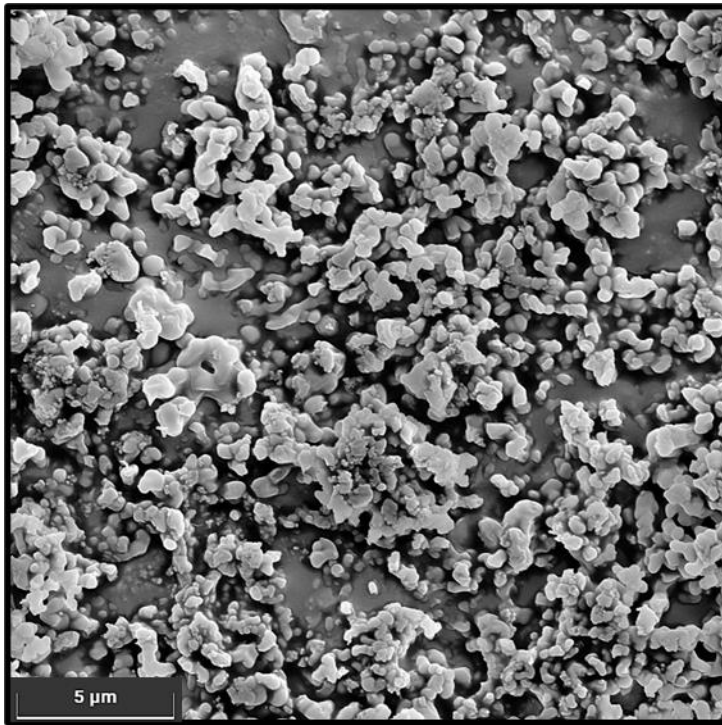


(a)

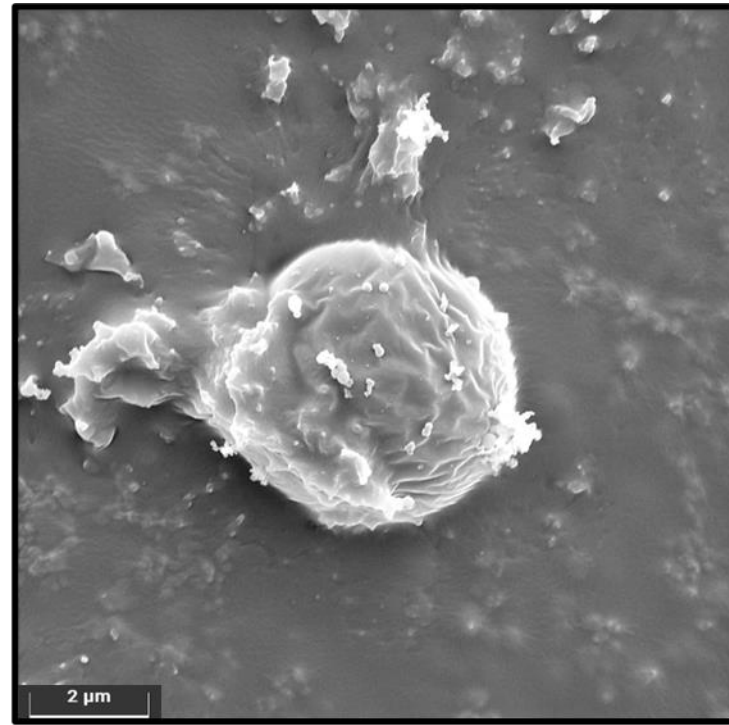


(b)

Figure 12.7 ARISE processed ES100 from SC-4 at, (a): 5 μm scale bar, and (b): 1 μm scale bar-magnified view.

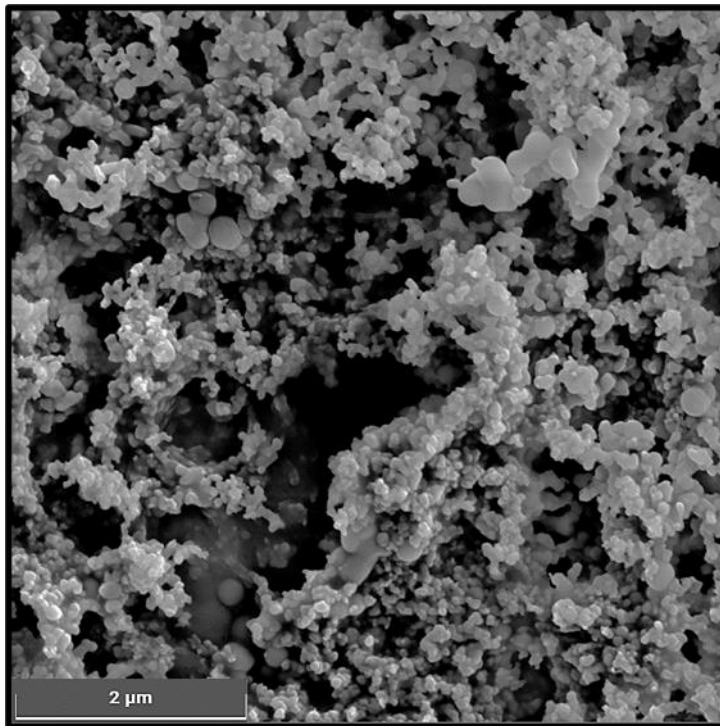


(a)

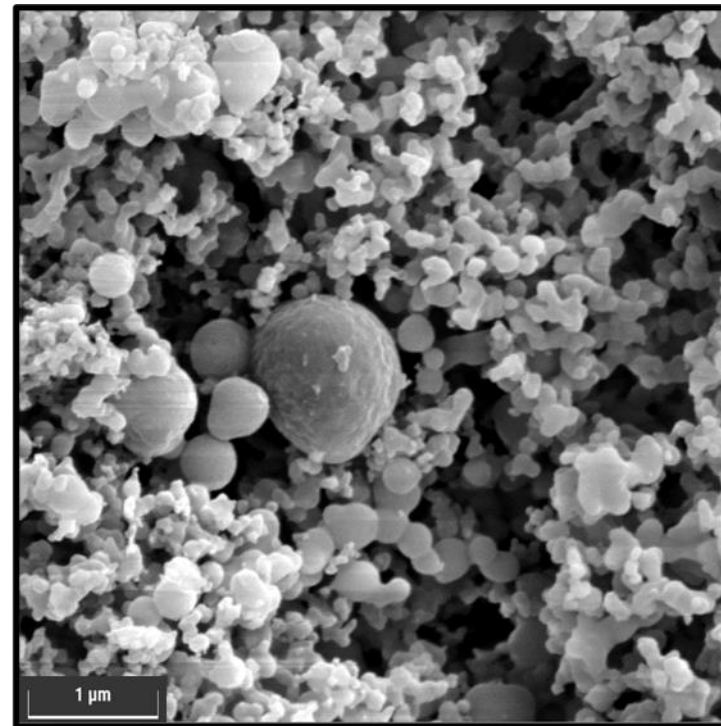


(b)

Figure 12.8 ARISE processed ES100 from SC-4 at, (a): 5 μm scale bar, and (b): 2 μm scale bar-magnified view.

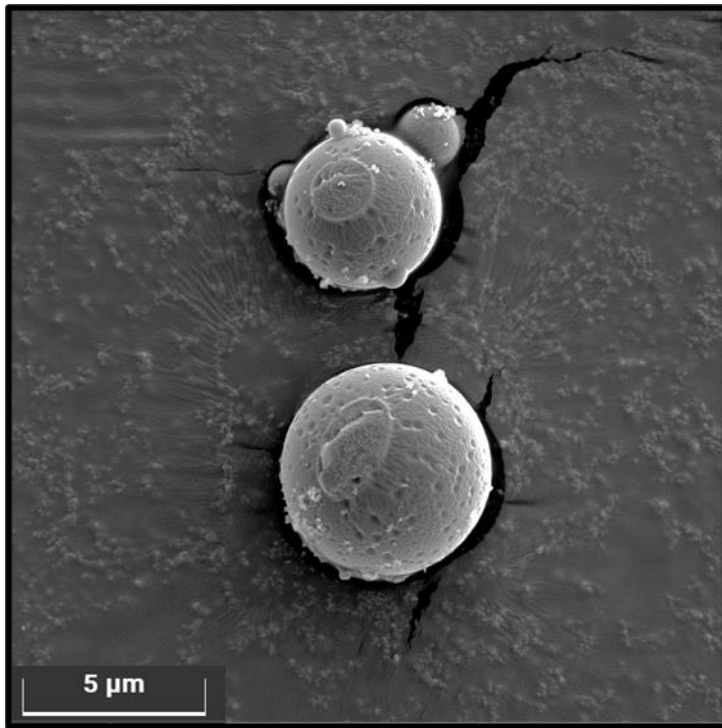


(a)

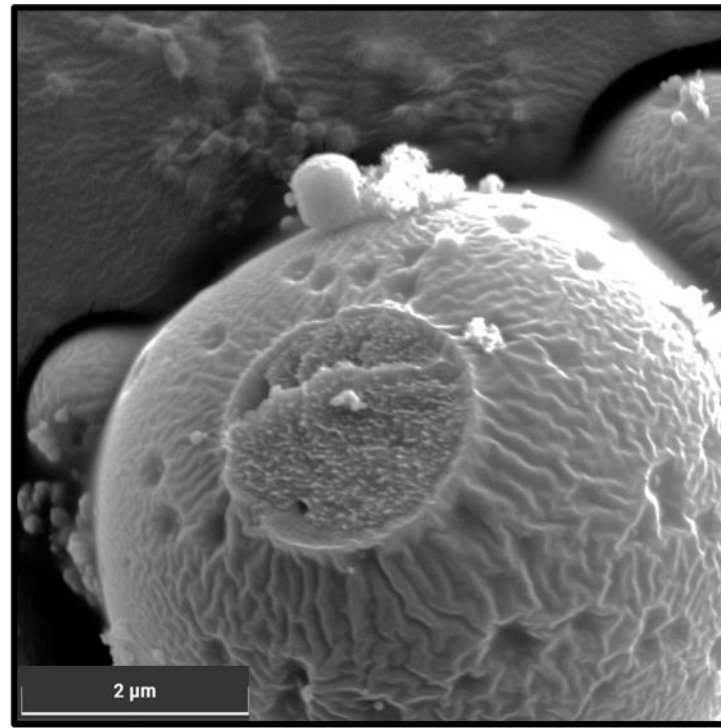


(b)

Figure 12.9 ARISE processed ES100-SLB from SC-4 at, (a): 2 μm scale bar, and (b): 1 μm scale bar-magnified view.



(a)



(b)

Figure 12.10 ARISE processed ES100-SLB from SC-4 at, (c): 5 μm scale bar, and (d): 2 μm scale bar-magnified view.

C1.3.3. PARTICLE SIZE DISTRIBUTION

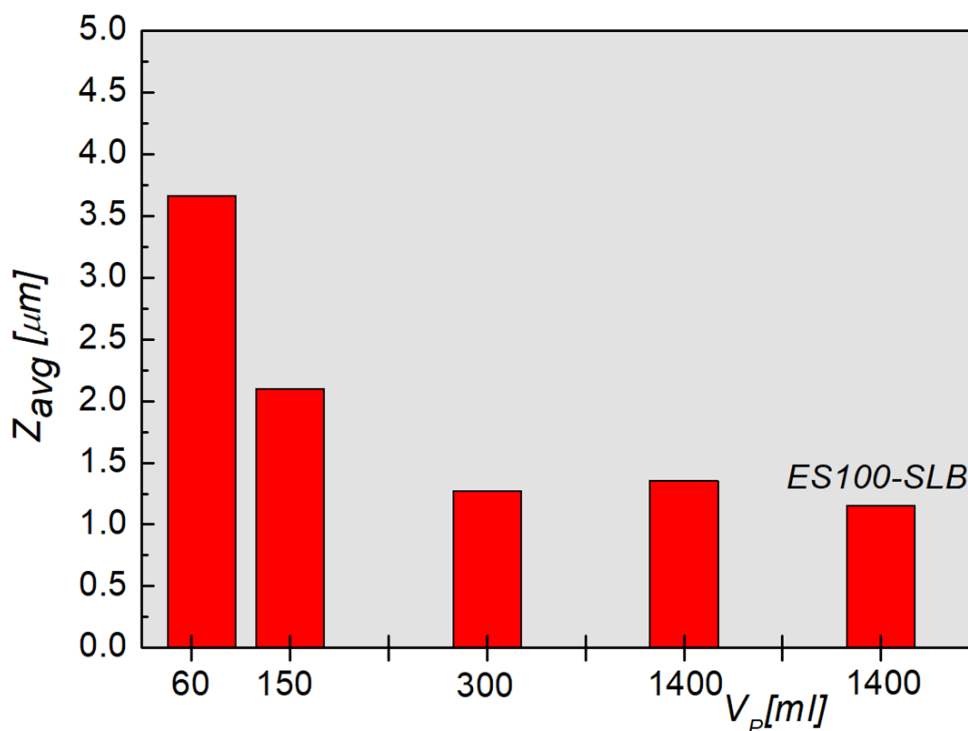


Figure 12.11 Average particle size (Z_{avg}) of ES100 from ARISE scale-up operations. The average size (Z_{avg}) of the particles from the ARISE process systematically decreased with the scale-up operation. The Z_{avg} of the pristine ES100 is 25 μm (Chapter 5, Section 5.4.1). The ARISE processing reduced the particle size by 96%, as seen from Figure 12.11. The different scales of the ARISE operation produced particles within 5 μm size range suitable for oral, nasal, and parenteral drug delivery applications (as explained in Chapter 2, Section 2.2). The reduction in Z_{avg} with an increase in operation scale demonstrates that fine particle production ($\leq 1\mu\text{m}$) is feasible. Further investigation of the SC- operation can enable in production of nano-sized particles in industrial operations.

C1.3.4. PRODUCT YIELD

The product yield or recovery is defined as the amount of product retrieved from the ARISE process as a percentage of the input raw material used. Figure 12.12 indicates the yield for scale-up processing. The results show that about 60%-88% yield was achieved in the scale-up process. The maximum yield ($\approx 90\%$) was achieved in SC-2 (V_p :150 mL). SC-4 (V_p :1400 mL) produced an average yield of 70%, slightly lower

than SC-3 (86.5%) and SC-2. Industrial scale-up involves handling a large volume/mass of raw materials, which may lower the yield due to the handling loss [165]. The yield of HP β CD reported by *Kurniawansyah* [74] was 95.3 % in the 1L precipitation chamber (V_p). On the other hand, the scale-up in the GAS and ARISE processes for the formulation of curcumin reported a low yield of 36% and 60% respectively, which are lower than the present study [164]. The 70% yield in the current work highlights the effectiveness of the design towards product retrieval. The 30% loss in yield could be due to various factors such as reaction selectivity, solvent supersaturation effect, pressure differential, and loss of fine particles during manual retrieval [164, 165]. The drawbacks can be improved by employing solvent combinations and re-engineering the accessibility path inside the precipitation chamber.

Currently, 450 mg/batch of ES100 was processed in 2 h operation. Assuming 2 batch/day, about 900 mg of ES100 can be processed in a day. By implementing 3 simultaneous operations of the scale-up ARISE rig, about 2.7 g of ES100 can be processed in a day with (5 wt% concentration), improving the overall yield.

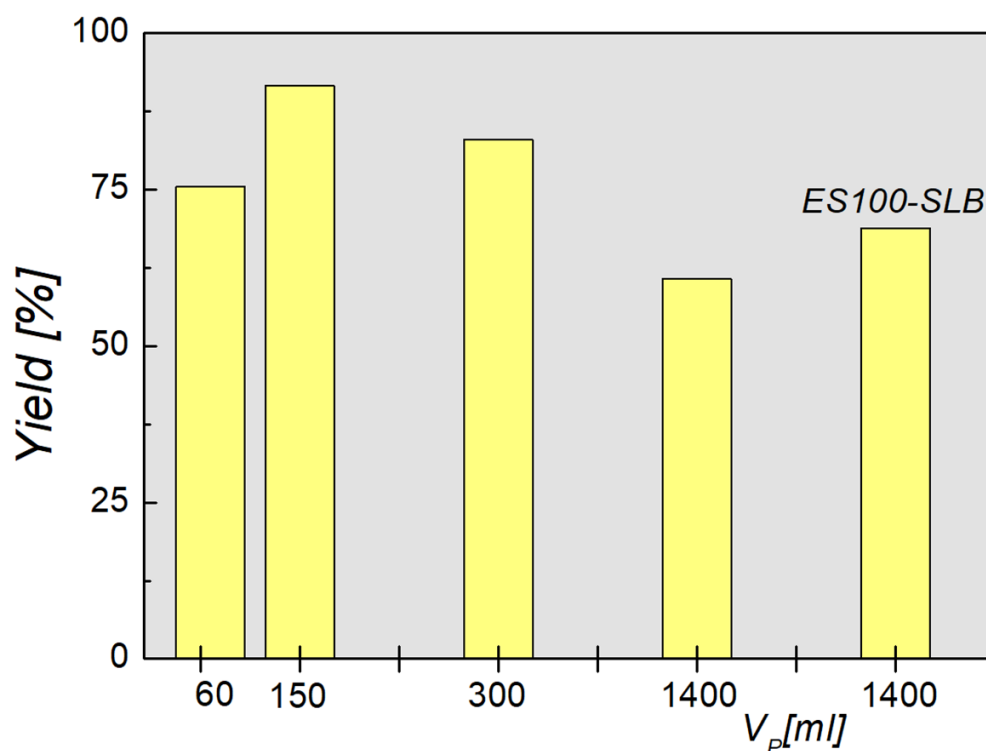


Figure 12.12 The product yield of micronized ES100 and ES100-SLB as a function of the volume of the precipitation chamber (scales of operation).

C1.3.5. LOADING ESTIMATION

Further, the loading of SLB onto ES100 in SC-4 was determined by UV spectroscopy, as mentioned in Chapter 3, Section 3.3.7. The drug loading (L) from the SC-4 was 16.47%, similar to the loading obtained from SC-2 (16.45%). The results suggest that the loading characteristics were unaltered and reproducible with the scale-up operations, advantageous for large production of drug formulations.

C1.4. SCALE-UP CHALLENGES

The ARISE process' transition from lab-to-industry operation requires multi-fold scaling-up in terms of quantity of raw materials, size of the rig, product handling systems, transportation, assembly of components, to site a few.

Apart from the financial and technical aspects (operating parameters, reactor, and conduit dimensions), there is a challenge in increasing production and simultaneously maintaining the quality of the pharmaceutical products during the scale-up process. The product integrity must be maintained by following the FDA's cGMP (current good manufacturing practice), especially the handling procedure of powdered materials. *Clavier et al* [510], detailed safety compliance in scale-up following the GMP based on the mechanical hazard, thermodynamic hazard, chemical hazard, and biological hazard. The choice of material, design, and development of scale-up plants must consider the risk associated with reactor fatigue, tubing leaks, corrosion, and chemical toxin waste handling.

The scale-up protocols have to adhere to the FDA-SUPAC (Food and drug administration- Scale-up and post-approval changes) compliances and suitable special powder transfer systems have to be designed for avoiding pharmaceutical contamination [511]. The ergonomic factors should also be streamlined to improve dexterity while handling raw materials and assembling components. For example, in the ARISE scale-up, the low occurrence of disassembling of the rig alleviates the physical labour and batch operation time. The current ARISE set-up involves customized jigs and fixtures to reduce the complexity of handling. The waste disposal also provides concern during scale-up operations and needs to comply with the EPA (Environmental Protection Agency) standards. The issue associated with waste disposal is minimal in the ARISE system, as the quantity of toxic solvents used is diminutive (eg:30 mL/day in the cur-

rent scale-up). Progressive research and development in addressing the above challenges can eventuate the successful operation of the industrial ARISE scale-up system (Chapter 9, Section 9.2).

C1.5 CONCLUSION

The scalability of the ARISE process was envisaged through conducting preliminary trials on formulating ES100 and ES100-SLB nanoparticles. Four stages of scale-up operations were performed with an increasing volume of precipitation chamber (60 mL, 150 mL, 300 mL, and 1400 mL). The results showed about 95 % decrease in the bulk density of the samples from the ARISE process with an average yield of 70%. All the ARISE process scales demonstrated the capability to produce uniformly spherical morphology with an average particle size between 1 μm to 3.5 μm . The scale-up showed reproducibility in terms of product morphology and loading through all scales of operations, confirming the reliability of the process in industrial application. Further process optimization of SC-4 can substantially improve the drug formulations towards meeting the industrial demands.

REFERENCES

- [1] D. Buckland, New drug treatments for cancer: what the future holds, *Prescriber* 27(1) (2016) 17-21.
- [2] R. Coombes, Cancer drugs: swallowing big pharma's line?, *BMJ* 334(7602) (2007) 1034-1035.
- [3] S. Cassidy, B.A. Syed, *Colorectal cancer drugs market*, Nature Publishing Group, 2017.
- [4] J. Ferlay, I. Soerjomataram, R. Dikshit, S. Eser, C. Mathers, M. Rebelo, D.M. Parkin, D. Forman, F. Bray, Cancer incidence and mortality worldwide: sources, methods and major patterns in GLOBOCAN 2012, *International journal of cancer* 136(5) (2015) E359-E386.
- [5] S. Jaferian, B. Negahdari, A. Eatemadi, Colon cancer targeting using conjugates biomaterial 5-fluorouracil, *Biomedicine & Pharmacotherapy* 84 (2016) 780-788.
- [6] (!!! INVALID CITATION !!! [6-9]).
- [7] C.G. Moertel, Chemotherapy for colorectal cancer, *New England Journal of Medicine* 330(16) (1994) 1136-1142.
- [8] I. Kikic, P. Sist, Applications of supercritical fluids to pharmaceuticals: controlled drug release systems, *Supercritical Fluids*, Springer2000, pp. 291-306.
- [9] C.R. Craig, R.E. Stitzel, *Modern pharmacology with clinical applications*, Lippincott Williams & Wilkins2004.
- [10] P.Y. Muller, M.N. Milton, The determination and interpretation of the therapeutic index in drug development, *Nature reviews Drug discovery* 11(10) (2012) 751-761.
- [11] M. Schachter, M. Pirmohamed, *General pharmacology, Clinical Pharmacology*, Elsevier2012, pp. 74-109.
- [12] D.A. Gewirtz, M.L. Bristol, J.C. Yalowich, *Toxicity issues in cancer drug development*, 2010.
- [13] M.S. Braun, M.T. Seymour, Balancing the efficacy and toxicity of chemotherapy in colorectal cancer, *Therapeutic advances in medical oncology* 3(1) (2011) 43-52.
- [14] J. Jeevanandam, Y. San Chan, M.K. Danquah, Nano-formulations of drugs: recent developments, impact and challenges, *Biochimie* 128 (2016) 99-112.
- [15] J.K. Patra, G. Das, L.F. Fraceto, E.V.R. Campos, M. del Pilar Rodriguez-Torres, L.S. Acosta-Torres, L.A. Diaz-Torres, R. Grillo, M.K. Swamy, S. Sharma, Nano based drug delivery systems: Recent developments and future prospects, *Journal of nanobiotechnology* 16(1) (2018) 71.
- [16] C.G. Knight, *Liposomes, from physical structure to therapeutic applications, sole distributors for the USA and Canada*, Elsevier North-Holland1981.
- [17] D. Shenoy, S. Little, R. Langer, M. Amiji, Poly (ethylene oxide)-modified poly (β -amino ester) nanoparticles as a pH-sensitive system for tumor-targeted delivery of hydrophobic drugs. 1. In vitro evaluations, *Molecular pharmaceutics* 2(5) (2005) 357-366.

- [18] J. Kreuter, Colloidal drug delivery systems, CRC Press 2014.
- [19] A. Glen, The impact of nanotechnology in drug delivery: Global developments, Market Anal. Future Prospects (2005).
- [20] R.R. Stadler, IP Strategies in Fighting Generic Competition in the Pharmaceutical Industry, MAS-IP Diploma Papers & Research Reports (2008) 14.
- [21] A. Carr, Subcritical Water as a Tunable Solvent for Particle Engineering, School of Chemical Engineering (2010).
- [22] M. Bogataj, Z. Kravanja, Z.N. Pintarič, High-Pressure Processing: A Smart Way to Increase Energy Efficiency with Less Toxic Residues, 1st International Conference on Technologies & Business Models for Circular Economy, 2000.
- [23] A.M. Scurto, K. Hutchenson, B. Subramaniam, Gas-expanded liquids: fundamentals and applications, ACS Publications 2009.
- [24] L. Falzone, S. Salomone, M. Libra, Evolution of cancer pharmacological treatments at the turn of the third millennium, Frontiers in Pharmacology 9 (2018) 1300.
- [25] W.H. Organization, Cancer, 2018. <https://www.who.int/news-room/fact-sheets/detail/cancer>.
- [26] V.T. DeVita, E. Chu, A history of cancer chemotherapy, Cancer research 68(21) (2008) 8643-8653.
- [27] M. Arruebo, N. Vilaboa, B. Sáez-Gutierrez, J. Lambea, A. Tres, M. Valladares, Á. González-Fernández, Assessment of the evolution of cancer treatment therapies, Cancers 3(3) (2011) 3279-3330.
- [28] Bowel cancer in Australia statistics, 2019. (Accessed 26/08/2019 2019).
- [29] N.C.C. Indicators, Systemic anti-cancer therapy treatment activity, 2017. (Accessed 22/11/2017 2017).
- [30] S.L. Chen, A.J. Bilchik, More extensive nodal dissection improves survival for stages I to III of colon cancer: a population-based study, Annals of surgery 244(4) (2006) 602.
- [31] F. Tanaka, T. Fukuse, H. Wada, M. Fukushima, The history, mechanism and clinical use of oral 5-fluorouracil derivative chemotherapeutic agents, Current pharmaceutical biotechnology 1(2) (2000) 137-164.
- [32] A.M.C.S. Barrett, F.o.E.U. Engineering, Pharmaceutical processing using dense gas technology, 2008.
- [33] R. Olsen, D. Schwartzmiller, W. Weppner, R. Winandy, Biomedical applications of chitin and its derivatives, Chitin and chitosan (1989) 813-828.
- [34] L. Lu, G. Chen, Y. Qiu, M. Li, D. Liu, D. Hu, X. Gu, Z. Xiao, Nanoparticle-based oral delivery systems for colon targeting: principles and design strategies, Science Bulletin 61(9) (2016) 670-681.
- [35] N. Belali, N. Wathoni, M. Muchtaridi, Advances in orally targeted drug delivery to colon, Journal of advanced pharmaceutical technology & research 10(3) (2019) 100.

- [36] R.M. Goldberg, D.J. Sargent, R.F. Morton, C.S. Fuchs, R.K. Ramanathan, S.K. Williamson, B.P. Findlay, H.C. Pitot, S.R. Alberts, A randomized controlled trial of fluorouracil plus leucovorin, irinotecan, and oxaliplatin combinations in patients with previously untreated metastatic colorectal cancer, *Journal of Clinical Oncology* 22(1) (2004) 23-30.
- [37] C. Tournigand, T. André, E. Achille, G. Lledo, M. Flesh, D. Mery-Mignard, E. Quinaux, C. Couteau, M. Buyse, G. Ganem, FOLFIRI followed by FOLFOX6 or the reverse sequence in advanced colorectal cancer: a randomized GERCOR study, *Journal of Clinical Oncology* 22(2) (2004) 229-237.
- [38] M.W. Saif, A. Choma, S.J. Salamone, E. Chu, Pharmacokinetically Guided Dose Adjustment of 5-Fluorouracil: A Rational Approach to Improving Therapeutic Outcomes, *JNCI: Journal of the National Cancer Institute* 101(22) (2009) 1543-1552.
- [39] C. Heidelberger, R. Duschinsky, E. Plevin, The synthesis of 5-fluoropyrimidines, *J. Amer. Chem. Soc* 79 (1957) 79-4559.
- [40] S.P. Chandran, S.B. Natarajan, S. Chandraseharan, M.S.B.M. Shahimi, Nano drug delivery strategy of 5-fluorouracil for the treatment of colorectal cancer, *Journal of Cancer Research and Practice* 4(2) (2017) 45-48.
- [41] J. Douillard, D. Cunningham, A. Roth, M. Navarro, R. James, P. Karasek, P. Jandik, T. Iveson, J. Carmichael, M. Alakl, Irinotecan combined with fluorouracil compared with fluorouracil alone as first-line treatment for metastatic colorectal cancer: a multicentre randomised trial, *The Lancet* 355(9209) (2000) 1041-1047.
- [42] A. Osol, J.T. Anderson, J.E. Hoover, Remington's pharmaceutical sciences: a treatise on the theory and practice of pharmaceutical sciences, with essential information about pharmaceutical and medicinal agents. Also a guide to the professional responsibilities and services of the pharmacist as a member of the health team... a textbook and reference work for pharmacists, physicians, and other medical scientists, Mack Publishing Company 1975.
- [43] Y. Huang, Y. Wei, H. Yang, C. Pi, H. Liu, Y. Ye, L. Zhao, A 5-fluorouracil-loaded floating gastroretentive hollow microsphere: development, pharmacokinetic in rabbits, and biodistribution in tumor-bearing mice, *Drug design, development and therapy* 10 (2016) 997.
- [44] Y. Ma, Controlled delivery of nanoparticles to the colon for tumour targeting, The University of Queensland, Australia, 2015.
- [45] R.B. Diasio, B.E. Harris, Clinical pharmacology of 5-fluorouracil, *Clinical pharmacokinetics* 16(4) (1989) 215-237.
- [46] I.R. Konings, S. Sleijfer, R.H. Mathijssen, P. de Bruijn, I.M.G. Moghaddam-Helmantel, L.M. van Dam, E.A. Wiemer, J. Verweij, W.J. Loos, Increasing tumoral 5-fluorouracil concentrations during a 5-day continuous infusion: a microdialysis study, *Cancer chemotherapy and pharmacology* 67(5) (2011) 1055-1062.
- [47] H. Matsumoto, H. Okumura, H. Murakami, H. Kubota, M. Higashida, A. Tsuruta, K. Tohyama, T. Hirai, Fluctuation in plasma 5-fluorouracil concentration during continuous 5-fluorouracil infusion for colorectal cancer, *Anticancer research* 35(11) (2015) 6193-6199.
- [48] S. Giacchetti, B. Perpoint, R. Zidani, N. Le Bail, R. Faggiuolo, C. Focan, P. Chollet, J. Llory, Y. Letourneau, B. Coudert, Phase III multicenter randomized trial of oxaliplatin added

to chronomodulated fluorouracil–leucovorin as first-line treatment of metastatic colorectal cancer, *Journal of clinical oncology* 18(1) (2000) 136-136.

[49] C. Wing Ying Cheung, N. Gibbons, D. Wayne Johnson, D. Lawrence Nicol, Silibinin-a promising new treatment for cancer, *Anti-Cancer Agents in Medicinal Chemistry (Formerly Current Medicinal Chemistry-Anti-Cancer Agents)* 10(3) (2010) 186-195.

[50] H. Kohno, T. Tanaka, K. Kawabata, Y. Hirose, S. Sugie, H. Tsuda, H. Mori, Silymarin, a naturally occurring polyphenolic antioxidant flavonoid, inhibits azoxymethane-induced colon carcinogenesis in male F344 rats, *International journal of cancer* 101(5) (2002) 461-468.

[51] R.P. Singh, G. Sharma, S. Dhanalakshmi, C. Agarwal, R. Agarwal, Suppression of advanced human prostate tumor growth in athymic mice by silibinin feeding is associated with reduced cell proliferation, increased apoptosis, and inhibition of angiogenesis, *Cancer Epidemiology and Prevention Biomarkers* 12(9) (2003) 933-939.

[52] K. Ramasamy, R. Agarwal, Multitargeted therapy of cancer by silymarin, *Cancer letters* 269(2) (2008) 352-362.

[53] F.S. Hogan, N.K. Krishnegowda, M. Mikhailova, M.S. Kahlenberg, Flavonoid, silibinin, inhibits proliferation and promotes cell-cycle arrest of human colon cancer, *Journal of Surgical Research* 143(1) (2007) 58-65.

[54] S.-H. Yang, J.-K. Lin, W.-S. Chen, J.-H. Chiu, Anti-angiogenic effect of silymarin on colon cancer LoVo cell line, *Journal of Surgical Research* 113(1) (2003) 133-138.

[55] J. Yang, Y. Liu, Y. Liu, Advances in the pharmaceutical research on the silymarin, *Natural Product Research and Development* 16(2) (2004) 185-187.

[56] A.K. Tyagi, R.P. Singh, C. Agarwal, D.C. Chan, R. Agarwal, Silibinin strongly synergizes human prostate carcinoma DU145 cells to doxorubicin-induced growth Inhibition, G2-M arrest, and apoptosis, *Clinical cancer research* 8(11) (2002) 3512-3519.

[57] P. Morazzoni, E. Bombardelli, *Silybum marianum* (*Carduus marianus*), *Fitoterapia* 66(1) (1995) 3-42.

[58] H. Basaga, G. Poli, C. Tekkaya, I. Aras, Free radical scavenging and antioxidative properties of ‘silibin’ complexes on microsomal lipid peroxidation, *Cell Biochemistry and Function: Cellular biochemistry and its modulation by active agents or disease* 15(1) (1997) 27-33.

[59] R. Leena, M. Vairamani, N. Selvamurugan, Alginate/Gelatin scaffolds incorporated with Silibinin-loaded Chitosan nanoparticles for bone formation in vitro, *Colloids and Surfaces B: Biointerfaces* 158 (2017) 308-318.

[60] C.A. Lipinski, Drug-like properties and the causes of poor solubility and poor permeability, *Journal of pharmacological and toxicological methods* 44(1) (2000) 235-249.

[61] K. Yokogawa, E. Nakashima, J. Ishizaki, H. Maeda, T. Nagano, F. Ichimura, Relationships in the structure–tissue distribution of basic drugs in the rabbit, *Pharmaceutical research* 7(7) (1990) 691-696.

[62] A. Hagelüken, L. Grünbaum, B. Nürnberg, R. Harhammer, W. Schunack, R. Seifert, Lipophilic β -adrenoceptor antagonists and local anesthetics are effective direct activators of G-proteins, *Biochemical pharmacology* 47(10) (1994) 1789-1795.

- [63] P. Kidd, K. Head, A review of the bioavailability and clinical efficacy of milk thistle phytosome: a silybin-phosphatidylcholine complex (Siliphos), *Alternative Medicine Review* 10(3) (2005).
- [64] M. El-Samaly, N. Afifi, E. Mahmoud, Increasing bioavailability of silymarin using a buccal liposomal delivery system: preparation and experimental design investigation, *International journal of pharmaceutics* 308(1-2) (2006) 140-148.
- [65] Y.S. Krishnaiah, Pharmaceutical technologies for enhancing oral bioavailability of poorly soluble drugs, *J Bioequiv Availab* 2(2) (2010) 28-36.
- [66] P. Khadka, J. Ro, H. Kim, I. Kim, J.T. Kim, H. Kim, J.M. Cho, G. Yun, J. Lee, Pharmaceutical particle technologies: An approach to improve drug solubility, dissolution and bioavailability, *Asian journal of pharmaceutical sciences* 9(6) (2014) 304-316.
- [67] G. Kaptay, On the size and shape dependence of the solubility of nano-particles in solutions, *International journal of pharmaceutics* 430(1-2) (2012) 253-257.
- [68] A. Agarwal, Nano-formulation and controlled delivery of low solubility anticancer drugs, (2009).
- [69] M. Rashid, V. Kaur, S.S. Hallan, S. Sharma, N. Mishra, Microparticles as controlled drug delivery carrier for the treatment of ulcerative colitis: A brief review, *Saudi Pharmaceutical Journal* 24(4) (2016) 458-472.
- [70] K. Ståhl, M. Claesson, P. Lilliehorn, H. Lindén, K. Bäckström, The effect of process variables on the degradation and physical properties of spray dried insulin intended for inhalation, *International journal of pharmaceutics* 233(1-2) (2002) 227-237.
- [71] Z. Knez, E. Weidner, Particles formation and particle design using supercritical fluids, *Current opinion in solid state and materials science* 7(4-5) (2003) 353-361.
- [72] K.A. Graeser, J.E. Patterson, J.A. Zeitler, T. Rades, The role of configurational entropy in amorphous systems, *Pharmaceutics* 2(2) (2010) 224-244.
- [73] L. Agüero, D. Zaldivar-Silva, L. Peña, M.L. Dias, Alginate microparticles as oral colon drug delivery device: A review, *Carbohydrate polymers* 168 (2017) 32-43.
- [74] F.C.S. Kurniawansyah, F.o.E.U. Engineering, Phenolic compounds particle engineering and formulation with dense gas technology, in: J.C.S. Zhao, F.o.E.U. Engineering (Eds.) 2016.
- [75] K. Krause, R. Müller, Production and characterisation of highly concentrated nanosuspensions by high pressure homogenisation, *International journal of pharmaceutics* 214(1-2) (2001) 21-24.
- [76] E.L. Parrott, Milling of pharmaceutical solids, *Journal of pharmaceutical Sciences* 63(6) (1974) 813-829.
- [77] Z.H. Loh, A.K. Samanta, P.W. Sia Heng, Overview of milling techniques for improving the solubility of poorly water-soluble drugs, *Asian Journal of Pharmaceutical Sciences* 10(4) (2015) 255-274.
- [78] J. Hu, K.P. Johnston, R.O. Williams III, Nanoparticle engineering processes for enhancing the dissolution rates of poorly water soluble drugs, *Drug development and industrial pharmacy* 30(3) (2004) 233-245.

- [79] A.A. Date, V. Patravale, Current strategies for engineering drug nanoparticles, *Current opinion in colloid & interface science* 9(3-4) (2004) 222-235.
- [80] X. Li, Y. Xu, G. Chen, P. Wei, Q. Ping, PLGA nanoparticles for the oral delivery of 5-Fluorouracil using high pressure homogenization-emulsification as the preparation method and in vitro/in vivo studies, *Drug development and industrial pharmacy* 34(1) (2008) 107-115.
- [81] N. Rasenack, B.W. Müller, Micron-size drug particles: common and novel micronization techniques, *Pharmaceutical development and technology* 9(1) (2004) 1-13.
- [82] P. York, Strategies for particle design using supercritical fluid technologies, *Pharmaceutical science & technology today* 2(11) (1999) 430-440.
- [83] B. Subramaniam, R.A. Rajewski, K. Snavey, Pharmaceutical processing with supercritical carbon dioxide, *Journal of pharmaceutical sciences* 86(8) (1997) 885-890.
- [84] H. Leuenberger, Spray freeze-drying—the process of choice for low water soluble drugs?, *Journal of Nanoparticle Research* 4(1-2) (2002) 111-119.
- [85] E. Weidner, High pressure micronization for food applications, *The Journal of Supercritical Fluids* 47(3) (2009) 556-565.
- [86] N.T. Chi, N.M. Triet, D.M. Chien, Preparation of drug nanoparticles by emulsion evaporation method, *Journal of Physics: conference series*, IOP Publishing, 2009, p. 012047.
- [87] X.-p. Chen, Y. Li, Y. Zhang, G.-w. Li, Formulation, Characterization And Evaluation Of Curcumin-Loaded PLGA-TPGS Nanoparticles For Liver Cancer Treatment, *Drug Design, Development and Therapy* 13 (2019) 3569.
- [88] X. Song, Y. Zhao, S. Hou, F. Xu, R. Zhao, J. He, Z. Cai, Y. Li, Q. Chen, Dual agents loaded PLGA nanoparticles: systematic study of particle size and drug entrapment efficiency, *European journal of pharmaceutics and biopharmaceutics* 69(2) (2008) 445-453.
- [89] T.K. Giri, C. Choudhary, A. Alexander, H. Badwaik, D.K. Tripathi, Prospects of pharmaceuticals and biopharmaceuticals loaded microparticles prepared by double emulsion technique for controlled delivery, *Saudi Pharmaceutical Journal* 21(2) (2013) 125-141.
- [90] M.A. Repka, S. Majumdar, S. Kumar Battu, R. Srirangam, S.B. Upadhye, Applications of hot-melt extrusion for drug delivery, *Expert opinion on drug delivery* 5(12) (2008) 1357-1376.
- [91] J. Jung, M. Perrut, Particle design using supercritical fluids: literature and patent survey, *The Journal of Supercritical Fluids* 20(3) (2001) 179-219.
- [92] M.B. Hicks, W. Farrell, C. Aurigemma, L. Lehmann, L. Weisel, K. Nadeau, H. Lee, C. Moraff, M. Wong, Y. Huang, Making the move towards modernized greener separations: introduction of the analytical method greenness score (AMGS) calculator, *Green chemistry* 21(7) (2019) 1816-1826.
- [93] C.P. Ashcroft, P.J. Dunn, J.D. Hayler, A.S. Wells, Survey of solvent usage in papers published in *Organic Process Research & Development* 1997–2012, *Organic Process Research & Development* 19(7) (2015) 740-747.
- [94] N.R. Foster, R. Mammucari, L.T. Danh, W.H. Teoh, Particle engineering by dense gas technologies applied to pharmaceuticals, *Dense Phase Carbon Dioxide: Food and Pharmaceutical Applications* (2012) 199-226.

- [95] N. Foster, R. Mammucari, F. Dehghani, A. Barrett, K. Bezahehtak, E. Coen, G. Combes, L. Meure, A. Ng, H.L. Regtop, Processing pharmaceutical compounds using dense gas technology, *Industrial & Engineering Chemistry Research* 42(25) (2003) 6476-6493.
- [96] R. Smith, H. Inomata, C. Peters, Introduction to supercritical fluids: a spreadsheet-based approach, Newnes 2013.
- [97] A. Tandy, Dense Gas Particle Processing for Alternative Drug Delivery Formulations, University of New South Wales 2006.
- [98] G. Halder, Introduction to chemical engineering thermodynamics, PHI Learning Pvt. Ltd. 2014.
- [99] H. Rabemanolontsoa, S. Saka, Various pretreatments of lignocellulosics, *Bioresource technology* 199 (2016) 83-91.
- [100] B.E. Poling, J.M. Prausnitz, J.P. O'Connell, The properties of gases and liquids, Mcgraw-hill New York 2001.
- [101] R.C. Reid, J.M. Prausnitz, B.E. Poling, The properties of gases and liquids, (1987).
- [102] P. York, U.B. Kompella, B.Y. Shekunov, Supercritical fluid technology for drug product development, CRC Press 2004.
- [103] C.C. Beh, R. Mammucari, N.R. Foster, Formation of nanocarrier systems by dense gas processing, *Langmuir* 30(37) (2014) 11046-11054.
- [104] A. Teja, R. Lee, D. Rosenthal, M. Anselme, Correlation of the critical properties of alkanes and alkanols, *Fluid Phase Equilibria* 56 (1990) 153-169.
- [105] P.G. Jessop, B. Subramaniam, Gas-expanded liquids, *Chem. Rev.* 107(6) (2007) 2666-2694.
- [106] U. Hintermair, W. Leitner, P. Jessop, Expanded Liquid Phases in Catalysis: Gas-expanded Liquids and Liquid-Supercritical Fluid Biphasic Systems, *Handbook of Green Chemistry: Online* (2010) 101-187.
- [107] G.A. Sacha, W.J. Schmitt, S.L. Nail, Identification of critical process variables affecting particle size following precipitation using a supercritical fluid, *Pharmaceutical development and technology* 11(2) (2006) 187-194.
- [108] F.G. Denardina, S.A.V. de Melob, R. Mammucari, N.R. Foster, Phase transition and volume expansion in CO₂-expanded liquid systems, *CHEMICAL ENGINEERING* 32 (2013).
- [109] V.T. Wyatt, D. Bush, J. Lu, J.P. Hallett, C.L. Liotta, C.A. Eckert, Determination of solvatochromic solvent parameters for the characterization of gas-expanded liquids, *The Journal of supercritical fluids* 36(1) (2005) 16-22.
- [110] R. Sih, New process development of dense gas technology for the processing of pharmaceuticals, *School of Chemical Sciences and Engineering* (2008) 274.
- [111] A. Tandy, R. Mammucari, F. Dehghani, N.R. Foster, Dense gas processing of polymeric controlled release formulations, *International journal of pharmaceutics* 328(1) (2007) 1-11.

- [112] P.G. Debenedetti, J.W. Tom, X. Kwauk, S.-D. Yeo, Rapid expansion of supercritical solutions (RESS): fundamentals and applications, *Fluid Phase Equilibria* 82 (1993) 311-321.
- [113] J.W. Tom, G.-B. Lim, P.G. Debenedetti, R.K. Prud'Homme, Applications of supercritical fluids in the controlled release of drugs, ACS Publications 1993.
- [114] E. Reverchon, Supercritical antisolvent precipitation of micro-and nano-particles, *The journal of supercritical fluids* 15(1) (1999) 1-21.
- [115] S.K. Sharma, S. Al Hosani, M. Kalmouni, A.R. Nair, L. Palanikumar, R. Pasricha, K.C. Sadler, M. Magzoub, R. Jagannathan, Supercritical CO₂ Processing Generates Aqueous Cisplatin Solutions with Enhanced Cancer Specificity, *ACS omega* 5(9) (2020) 4558-4567.
- [116] M. Gadermann, S. Kular, A.H. Al-Marzouqi, R. Signorell, Formation of naproxen-poly(lactic acid) nanoparticles from supercritical solutions and their characterization in the aerosol phase, *Physical Chemistry Chemical Physics* 11(36) (2009) 7861-7868.
- [117] M. Zayed, M. Hawash, M. El-Desawy, A.M. El-Gizouli, Investigation of naproxen drug using mass spectrometry, thermal analyses and semi-empirical molecular orbital calculation, *Arabian Journal of Chemistry* 10(3) (2017) 351-359.
- [118] G. Sodeifian, S.A. Sajadian, Solubility measurement and preparation of nanoparticles of an anticancer drug (Letrozole) using rapid expansion of supercritical solutions with solid cosolvent (RESS-SC), *The Journal of Supercritical Fluids* 133 (2018) 239-252.
- [119] G. Sodeifian, S.A. Sajadian, S. Daneshyan, Preparation of Aprepitant nanoparticles (efficient drug for coping with the effects of cancer treatment) by rapid expansion of supercritical solution with solid cosolvent (RESS-SC), *The Journal of Supercritical Fluids* 140 (2018) 72-84.
- [120] M. Fraile, D. Deodato, S. Rodriguez-Rojo, I. Nogueira, A. Simplicio, M. Cocero, C. Duarte, Production of new hybrid systems for drug delivery by PGSS (Particles from Gas Saturated Solutions) process, *The Journal of Supercritical Fluids* 81 (2013) 226-235.
- [121] S. Palakodaty, P. York, Phase behavioral effects on particle formation processes using supercritical fluids, *Pharmaceutical research* 16(7) (1999) 976-985.
- [122] S.-D. Yeo, E. Kiran, Formation of polymer particles with supercritical fluids: a review, *The Journal of Supercritical Fluids* 34(3) (2005) 287-308.
- [123] L. Padrela, M.A. Rodrigues, A. Duarte, A.M. Dias, M.E. Braga, H.C. de Sousa, Supercritical carbon dioxide-based technologies for the production of drug nanoparticles/nanocrystals—a comprehensive review, *Advanced drug delivery reviews* 131 (2018) 22-78.
- [124] A.Z. Chen, X.M. Pu, Y.Q. Kang, L. Liao, Y.D. Yao, G.F. Yin, Preparation of 5-Fluorouracil-Poly (L-lactide) Microparticles Using Solution-Enhanced Dispersion by Supercritical CO₂, *Macromolecular Rapid Communications* 27(15) (2006) 1254-1259.
- [125] S. Naik, D. Patel, N. Surti, A. Misra, Preparation of PEGylated liposomes of docetaxel using supercritical fluid technology, *The Journal of Supercritical Fluids* 54(1) (2010) 110-119.
- [126] G. Liu, W. Wang, H. Wang, Y. Jiang, Preparation of 10-hydroxycamptothecin proliposomes by the supercritical CO₂ anti-solvent process, *Chemical Engineering Journal* 243 (2014) 289-296.

- [127] I.A. Cuadra, F. Zahran, D. Martín, A. Cabañas, C. Pando, Preparation of 5-fluorouracil microparticles and 5-fluorouracil/poly (l-lactide) composites by a supercritical CO₂ antisolvent process, *The Journal of Supercritical Fluids* 143 (2019) 64-71.
- [128] P. Kalantarian, I. Haririan, A.R. Najafabadi, M.A. Shokrgozar, A. Vatanara, Entrapment of 5-fluorouracil into PLGA matrices using supercritical antisolvent processes, *Journal of Pharmacy and Pharmacology* 63(4) (2011) 500-506.
- [129] E. De Paz, A. Martin, H. Every, M.J. Cocero, Production of water-soluble quercetin formulations by antisolvent precipitation and supercritical drying, *The Journal of Supercritical Fluids* 104 (2015) 281-290.
- [130] S. Li, Y. Liu, T. Liu, L. Zhao, J. Zhao, N. Feng, Development and in-vivo assessment of the bioavailability of oridonin solid dispersions by the gas anti-solvent technique, *International journal of pharmaceutics* 411(1-2) (2011) 172-177.
- [131] H. Hong, Q. Suo, F. Li, X. Wei, J. Zhang, Precipitation and characterization of chelerythrine microparticles by the supercritical antisolvent process, *Chemical Engineering & Technology: Industrial Chemistry-Plant Equipment-Process Engineering-Biotechnology* 31(7) (2008) 1051-1055.
- [132] M. Xie, D. Fan, Z. Zhao, Z. Li, G. Li, Y. Chen, X. He, A. Chen, J. Li, X. Lin, Nano-curcumin prepared via supercritical: Improved anti-bacterial, anti-oxidant and anti-cancer efficacy, *International journal of pharmaceutics* 496(2) (2015) 732-740.
- [133] D.P. Nesta, J.S. Elliott, J.P. Warr, Supercritical fluid precipitation of recombinant human immunoglobulin from aqueous solutions, *Biotechnology and bioengineering* 67(4) (2000) 457-464.
- [134] O. Yesil-Celiktas, E.O. Cetin-Uyanikgil, In vitro release kinetics of polycaprolactone encapsulated plant extract fabricated by supercritical antisolvent process and solvent evaporation method, *The Journal of Supercritical Fluids* 62 (2012) 219-225.
- [135] J.-E. Lee, I.-I. Jung, G.-B. Lim, J.-H. Ryu, BP-P5 Preparation of gemcitabine-loaded mPEG-PLLA microparticles using supercritical carbon dioxide and their characterization (Section II Biopharmaceuticals Production), *Journal of bioscience and bioengineering* 108(1) (2009) S25-S26.
- [136] D. Alias, R. Yunus, G.H. Chong, C.A.C. Abdullah, Single step encapsulation process of tamoxifen in biodegradable polymer using supercritical anti-solvent (SAS) process, *Powder Technology* 309 (2017) 89-94.
- [137] M. Fraile, R. Buratto, B. Gómez, A.n. Martín, M.a.J. Cocero, Enhanced delivery of quercetin by encapsulation in poloxamers by supercritical antisolvent process, *Industrial & Engineering Chemistry Research* 53(11) (2014) 4318-4327.
- [138] M. Hua, X. Hua, Polymer nanoparticles prepared by supercritical carbon dioxide for in vivo anti-cancer drug delivery, *Nano-Micro Letters* 6(1) (2014) 20-23.
- [139] K. Chhouk, H. Kanda, S.-I. Kawasaki, M. Goto, Micronization of curcumin with biodegradable polymer by supercritical anti-solvent using micro swirl mixer, *Frontiers of Chemical Science and Engineering* 12(1) (2018) 184-193.

- [140] F. Zabihi, N. Xin, J. Jia, T. Chen, Y. Zhao, High yield and high loading preparation of curcumin–PLGA nanoparticles using a modified supercritical antisolvent technique, *Industrial & Engineering Chemistry Research* 53(15) (2014) 6569-6574.
- [141] L.Y. Lee, C.H. Wang, K.A. Smith, Supercritical antisolvent production of biodegradable micro-and nanoparticles for controlled delivery of paclitaxel, *Journal of Controlled Release* 125(2) (2008) 96-106.
- [142] I. Akbari, S. Ghoreishi, N. Habibi, Generation and precipitation of paclitaxel nanoparticles in basil seed mucilage via combination of supercritical gas antisolvent and phase inversion techniques, *The Journal of Supercritical Fluids* 94 (2014) 182-188.
- [143] Y. Cheng, W. Xu, Z. Chen, Z. Wang, D. Huang, Micronization of etoposide using solution-enhanced dispersion by supercritical CO₂, *The Journal of Supercritical Fluids* 115 (2016) 10-16.
- [144] Y. Huang, H. Wang, G. Liu, Y. Jiang, New polymorphs of 9-nitro-camptothecin prepared using a supercritical anti-solvent process, *International journal of pharmaceutics* 496(2) (2015) 551-560.
- [145] G. Liu, Q. Lin, Y. Huang, G. Guan, Y. Jiang, Tailoring the particle microstructures of gefitinib by supercritical CO₂ anti-solvent process, *Journal of CO₂ Utilization* 20 (2017) 43-51.
- [146] I.A. Cuadra, A. Cabañas, J.A. Cheda, M. Türk, C. Pando, Cocrystallization of the anticancer drug 5-fluorouracil and cofomers urea, thiourea or pyrazinamide using supercritical CO₂ as an antisolvent (SAS) and as a solvent (CSS), *The Journal of Supercritical Fluids* (2020) 104813.
- [147] O. Guney, A. Akgerman, Synthesis of controlled-release products in supercritical medium, *AIChE Journal* 48(4) (2002) 856-866.
- [148] L. Cabezas, I. Gracia, M. García, A. De Lucas, J. Rodríguez, Production of biodegradable porous scaffolds impregnated with 5-fluorouracil in supercritical CO₂, *The Journal of Supercritical Fluids* 80 (2013) 1-8.
- [149] A. Dias, M. Braga, I. Seabra, P. Ferreira, M. Gil, H. De Sousa, Development of natural-based wound dressings impregnated with bioactive compounds and using supercritical carbon dioxide, *International journal of pharmaceutics* 408(1-2) (2011) 9-19.
- [150] S. Yoda, K. Sato, H.T. Oyama, Impregnation of paclitaxel into poly (DL-lactic acid) using high pressure mixture of ethanol and carbon dioxide, *RSC advances* 1(1) (2011) 156-162.
- [151] M. Champeau, J.-M. Thomassin, T. Tassaing, C. Jérôme, Drug loading of polymer implants by supercritical CO₂ assisted impregnation: a review, *Journal of Controlled Release* 209 (2015) 248-259.
- [152] Z. Zhao, Y. Li, Y. Zhang, Preparation and characterization of Paclitaxel loaded SF/PLLA-PEG-PLLA nanoparticles via solution-enhanced dispersion by supercritical CO₂, *Journal of Nanomaterials* 2015 (2015).
- [153] Q. Lin, G. Liu, Z. Zhao, D. Wei, J. Pang, Y. Jiang, Design of gefitinib-loaded poly (l-lactic acid) microspheres via a supercritical anti-solvent process for dry powder inhalation, *International journal of pharmaceutics* 532(1) (2017) 573-580.

- [154] R.L. Matos, T. Lu, V. Prosapio, C. McConville, G. Leeke, A. Ingram, Coprecipitation of curcumin/PVP with enhanced dissolution properties by the supercritical antisolvent process, *Journal of CO2 Utilization* 30 (2019) 48-62.
- [155] A. Martín, M.J. Cocero, Micronization processes with supercritical fluids: fundamentals and mechanisms, *Advanced Drug Delivery Reviews* 60(3) (2008) 339-350.
- [156] (!!! INVALID CITATION !!! [158, 160]).
- [157] X. Zhao, Y. Zu, Q. Li, M. Wang, B. Zu, X. Zhang, R. Jiang, C. Zu, Preparation and characterization of camptothecin powder micronized by a supercritical antisolvent (SAS) process, *The Journal of Supercritical Fluids* 51(3) (2010) 412-419.
- [158] M.V. Sosa, S. Rodríguez-Rojo, F. Mattea, M. Cismondi, M.J. Cocero, Green tea encapsulation by means of high pressure antisolvent coprecipitation, *The Journal of Supercritical Fluids* 56(3) (2011) 304-311.
- [159] N.R. Foster, R.P.T. Sih, Process for producing particles via atomized rapid injection for solvent extraction, Google Patents, 2013.
- [160] S.D. Yeo, G.B. Lim, P.G. Debendetti, H. Bernstein, Formation of microparticulate protein powder using a supercritical fluid antisolvent, *Biotechnology and Bioengineering* 41(3) (1993) 341-346.
- [161] S. Mawson, S. Kanakia, K.P. Johnston, Coaxial nozzle for control of particle morphology in precipitation with a compressed fluid antisolvent, *Journal of applied polymer science* 64(11) (1997) 2105-2118.
- [162] M. Türk, P. Hils, B. Helfgen, K. Schaber, H.-J. Martin, M.A. Wahl, Micronization of pharmaceutical substances by the rapid expansion of supercritical solutions (RESS): a promising method to improve bioavailability of poorly soluble pharmaceutical agents, *The Journal of supercritical fluids* 22(1) (2002) 75-84.
- [163] U.T. Lam, *Bioparticle Engineering Using Dense Gas Technologies*, (2009).
- [164] F. Kurniawansyah, R. Mammucari, N.R. Foster, Polymorphism of curcumin from dense gas antisolvent precipitation, *Powder Technology* 305 (2017) 748-756.
- [165] D.J.A. Ende, *Chemical engineering in the pharmaceutical industry: R & D to manufacturing*, John Wiley & Sons 2011.
- [166] N.A. Mitchell, P.J. Frawley, Nucleation kinetics of paracetamol–ethanol solutions from metastable zone widths, *J. Cryst. Growth* 312(19) (2010) 2740-2746.
- [167] K. Sangwal, Recent developments in understanding of the metastable zone width of different solute– solvent systems, *J. Cryst. Growth* 318(1) (2011) 103-109.
- [168] N. Deora, N. Misra, A. Deswal, H. Mishra, P. Cullen, B. Tiwari, Ultrasound for improved crystallisation in food processing, *Food Engineering Reviews* 5(1) (2013) 36-44.
- [169] in: P.M. Doran (Ed.), *Bioprocess Engineering Principles (Second Edition)*, Academic Press, London, 2013, pp. 899-919.
- [170] F. Kurniawansyah, H.T. Duong, T.D. Luu, R. Mammucari, O. Vittorio, C. Boyer, N. Foster, Inhalable curcumin formulations: Micronization and bioassay, *Chemical Engineering Journal* 279 (2015) 799-808.

- [171] A. Aguiar-Ricardo, Building dry powder formulations using supercritical CO₂ spray drying, *Current Opinion in Green and Sustainable Chemistry* 5 (2017) 12-16.
- [172] N.R. Foster, F. Kurniawansyah, A. Tandya, C. Delgado, R. Mammucari, Particle processing by dense gas antisolvent precipitation: ARISE scale-up, *Chemical Engineering Journal* 308 (2017) 535-543.
- [173] W. Lam, L.T. Danh, R. Mammucari, N.R. Foster, Formulation of 5-fluorouracil by the atomized rapid injection solvent extraction (arise) process, *Chemeca 2011: Engineering a Better World: Sydney Hilton Hotel, NSW, Australia, 18-21 September 2011* (2011) 1862.
- [174] F. Kurniawansyah, R. Mammucari, N.R. Foster, Inhalable curcumin formulations by supercritical technology, *Powder Technology* 284 (2015) 289-298.
- [175] N.R. Foster, R. Sih, Development of a novel precipitation technique for the production of highly respirable powders: the atomized rapid injection for solvent extraction process, *ACS Publications* 2009.
- [176] S.V. de Melo, L. Danh, R. Mammucari, N. Foster, Dense CO₂ antisolvent precipitation of levothyroxine sodium: A comparative study of GAS and ARISE techniques based on morphology and particle size distributions, *The Journal of Supercritical Fluids* 93 (2014) 112-120.
- [177] N. Ventosa, S. Sala, J. Veciana, J. Torres, J. Llibre, Depressurization of an expanded liquid organic solution (DELOS): a new procedure for obtaining submicron-or micron-sized crystalline particles, *Crystal Growth & Design* 1(4) (2001) 299-303.
- [178] Y. Hakuta, H. Hayashi, K. Arai, Fine particle formation using supercritical fluids, *Current Opinion in Solid State & Materials Science* 7(4-5) (2003) 341-351.
- [179] M.J. Cocero, Á. Martín, F. Mattea, S. Varona, Encapsulation and co-precipitation processes with supercritical fluids: fundamentals and applications, *The Journal of Supercritical Fluids* 47(3) (2009) 546-555.
- [180] V. Andonova, G.C. Sekhar, Supercritical fluid technology: a promising approach for preparation of nano-scale drug delivery systems, *Journal of Applied Science and Engineering Methodologies* 2(1) (2016) 239-242.
- [181] A. Di Capua, R. Adami, E. Reverchon, Production of luteolin/biopolymer microspheres by supercritical assisted atomization, *Industrial & Engineering Chemistry Research* 56(15) (2017) 4334-4340.
- [182] R. Adami, A. Di Capua, E. Reverchon, Supercritical Assisted Atomization for the production of curcumin-biopolymer microspheres, *Powder Technology* 305 (2017) 455-461.
- [183] H.-H. Peng, D.-X. Hong, Y.-X. Guan, S.-J. Yao, Preparation of pH-responsive DOX-loaded chitosan nanoparticles using supercritical assisted atomization with an enhanced mixer, *International journal of pharmaceutics* 558 (2019) 82-90.
- [184] R.D. Smith, *Supercritical fluid molecular spray film deposition and powder formation*, Google Patents, 1986.
- [185] K.L. Hoy, K.A. Nielsen, *Electrostatic liquid spray application of coatings with supercritical fluids as diluents and spraying from an orifice*, Google Patents, 1993.

- [186] A.D. Shine, J. Gelb Jr, Microencapsulation process using supercritical fluids, Google Patents, 1998.
- [187] R.E. Sievers, B.M. Hybertson, B.N. Hansen, Methods and apparatus for drug delivery using supercritical solutions, Google Patents, 1994.
- [188] R.E. Sievers, S.P. Sellers, J.F. Carpenter, Supercritical fluid-assisted nebulization and bubble drying, Google Patents, 2003.
- [189] M. Hanna, P. York, Method and apparatus for the formation of particles, Google Patents, 2002.
- [190] R.B. Gupta, P. Chattopadhyay, Method of forming nanoparticles and microparticles of controllable size using supercritical fluids with enhanced mass transfer, Google Patents, 2003.
- [191] P.P.C. Avontuur, D.R. Merrifield, A.R. Souter, C.E. Valder, J.P. Warr, Process and apparatus for producing particles using a supercritical fluid, Google Patents, 2004.
- [192] M. Gentile, C. Di Palma, M.C. Cesta, Supercritical fluids processing: preparation of protein microparticles and their stabilisation, Google Patents, 2007.
- [193] E. Reverchon, Process for the production of micro and/or nano particles, Google Patents, 2007.
- [194] N.R. Foster, H.L. Regtop, F. Dehghani, A. Tandya, Formulation of fine particles using liquefield or dense gases, Google Patents, 2011.
- [195] P. Chattopadhyay, B.Y. Shekunov, J.S. Seitzinger, Method and apparatus for supercritical fluid assisted particle production, Google Patents, 2012.
- [196] S.F.A. Hossainy, Y. Tang, H. Askaryar, Q. Lin, T. Glauser, Methods of forming coatings with a crystalline or partially crystalline drug for implantable medical devices using supercritical fluid assisted sorption, Google Patents, 2013.
- [197] H. Lochard, B. Freiss, Method for impregnation with supercritical CO₂, Google Patents, 2015.
- [198] S.P. Dunuweera, R.M.S.I. Rajapakse, R.B.S.D. Rajapakshe, S.H.D.P. Wijekoon, N. Thilakarathna, M.G.G. Sasanka, R.M. Rajapakse, Review on Targeted Drug Delivery Carriers Used in Nanobiomedical Applications, *Current Nanoscience* 15(4) (2019) 382-397.
- [199] S. Svenson, Carrier-based drug delivery, ACS Publications 2004.
- [200] M. Wei, Y. Gao, X. Li, M.J. Serpe, Stimuli-responsive polymers and their applications, *Polymer Chemistry* 8(1) (2017) 127-143.
- [201] L. Zhang, Y. Sang, J. Feng, Z. Li, A. Zhao, Polysaccharide-based micro/nanocarriers for oral colon-targeted drug delivery, *Journal of drug targeting* 24(7) (2016) 579-589.
- [202] S.H. Lee, R. Bajracharya, J.Y. Min, J.-W. Han, B.J. Park, H.-K. Han, Strategic Approaches for Colon Targeted Drug Delivery: An Overview of Recent Advancements, *Pharmaceutics* 12(1) (2020) 68.
- [203] C.N. Patra, R. Priya, S. Swain, G.K. Jena, K.C. Panigrahi, D. Ghose, Pharmaceutical significance of Eudragit: A review, *Future Journal of Pharmaceutical Sciences* (2017).

[204] B. Skalsky, Eudragit Application Guidelines, in: E. Industries (Ed.) Evonik Nutrition & Care GmbH.

[205] S.S. Kadian, S. Harikumar, Eudragit and its pharmaceutical significance, Eudragit Pharm. Signif (2009).

[206] J.-W. Yoo, N. Giri, C.H. Lee, pH-sensitive Eudragit nanoparticles for mucosal drug delivery, International journal of Pharmaceutics 403(1-2) (2011) 262-267.

[207] P. Li, Z. Yang, Y. Wang, Z. Peng, S. Li, L. Kong, Q. Wang, Microencapsulation of coupled folate and chitosan nanoparticles for targeted delivery of combination drugs to colon, Journal of microencapsulation 32(1) (2015) 40-45.

[208] G. Rai, A.K. Yadav, N.K. Jain, G.P. Agrawal, Eudragit-coated dextran microspheres of 5-fluorouracil for site-specific delivery to colon, Drug delivery 23(1) (2016) 328-337.

[209] I. Tariq, A.M. Yousaf, S.A. Raza, Y. Shahzad, T. Hussain, I.U. Khan, T. Mahmood, M. Jamshaid, Cellulosic and acrylic polymers based composites for controlled drug release, Iranian Polymer Journal 28(9) (2019) 769-776.

[210] U.E. Illangakoon, D.-G. Yu, B.S. Ahmad, N.P. Chatterton, G.R. Williams, 5-Fluorouracil loaded Eudragit fibers prepared by electrospinning, International journal of pharmaceutics 495(2) (2015) 895-902.

[211] A. Kumari, A. Jain, P. Hurkat, A. Tiwari, S.K. Jain, Eudragit S100 coated microsponges for Colon targeting of prednisolone, Drug development and industrial pharmacy 44(6) (2018) 902-913.

[212] M.B. Subudhi, A. Jain, A. Jain, P. Hurkat, S. Shilpi, A. Gulbake, S.K. Jain, Eudragit S100 coated citrus pectin nanoparticles for colon targeting of 5-fluorouracil, Materials 8(3) (2015) 832-849.

[213] S. Guo, G. Wang, T. Wu, F. Bai, J. Xu, X. Zhang, Solid dispersion of berberine hydrochloride and Eudragit® S100: formulation, physicochemical characterization and cytotoxicity evaluation, Journal of Drug Delivery Science and Technology 40 (2017) 21-27.

[214] M. Mahalingam, K. Krishnamoorthy, Fabrication and optimization of camptothecin loaded Eudragit S 100 nanoparticles by Taguchi L4 orthogonal array design, International journal of pharmaceutical investigation 5(3) (2015) 147.

[215] J. Yin, C. Xiang, X. Song, Nanoencapsulation of psoralidin via chitosan and Eudragit S100 for enhancement of oral bioavailability, International journal of pharmaceutics 510(1) (2016) 203-209.

[216] N.V. Patel, N.R. Sheth, B. Mohddesi, Formulation and Evaluation of Genistein—A Novel Isoflavone Loaded Chitosan and Eudragit® Nanoparticles for Cancer Therapy, Materials Today: Proceedings 2(9) (2015) 4477-4482.

[217] R. Jat, Formulation and In Vitro-In Vivo Evaluation of Quercetin Loaded Eudragit S100 Microspheres, Asian Journal of Pharmaceutics (AJP): Free full text articles from Asian J Pharm 12(01) (2018).

[218] H. Duan, S. Lü, C. Gao, X. Bai, H. Qin, Y. Wei, X.a. Wu, M. Liu, Mucoadhesive microparticulates based on polysaccharide for target dual drug delivery of 5-aminosalicylic

acid and curcumin to inflamed colon, *Colloids and Surfaces B: Biointerfaces* 145 (2016) 510-519.

[219] P. Rajasree, W. Paul, C.P. Sharma, R.A.M. Osmani, U. Hani, A. Srivastava, Eudragit encapsulated cationic poly (lactic-co-glycolic acid) nanoparticles in targeted delivery of capecitabine for augmented colon carcinoma therapy, *Journal of Drug Delivery Science and Technology* 46 (2018) 302-311.

[220] M.M. Patel, Formulation and development of di-dependent microparticulate system for colon-specific drug delivery, *Drug Deliv Transl Res* 7(2) (2017) 312-324.

[221] A. Jain, S. Jain, R. Jain, D.V. Kohli, Coated chitosan nanoparticles encapsulating caspase 3 activator for effective treatment of colorectal cancer, *Drug Deliv Transl Res* 5(6) (2015) 596-610.

[222] R. Sareen, N. Jain, A. Rajkumari, K. Dhar, pH triggered delivery of curcumin from Eudragit-coated chitosan microspheres for inflammatory bowel disease: characterization and pharmacodynamic evaluation, *Drug delivery* 23(1) (2016) 55-62.

[223] L.E. Aguilar, A.R. Unnithan, A. Amarjargal, A.P. Tiwari, S.T. Hong, C.H. Park, C.S. Kim, Electrospun polyurethane/Eudragit® L100-55 composite mats for the pH dependent release of paclitaxel on duodenal stent cover application, *International journal of pharmaceutics* 478(1) (2015) 1-8.

[224] F. Maestrelli, M. Cirri, G. Corti, N. Mennini, P. Mura, Development of enteric-coated calcium pectinate microspheres intended for colonic drug delivery, *European journal of pharmaceutics and biopharmaceutics* 69(2) (2008) 508-518.

[225] A. Sood, A. Dev, S.J. Mohanbhai, N. Shrimali, M. Kapasiya, A.C. Kushwaha, S. Roy Choudhury, P. Guchhait, S. Karmakar, Disulfide-Bridged Chitosan-Eudragit S-100 Nanoparticles for Colorectal Cancer, *ACS Applied Nano Materials* 2(10) (2019) 6409-6417.

[226] P.K. Pawar, C. Gautam, Design, optimization and evaluation of mesalamine matrix tablet for colon drug delivery system, *Journal of Pharmaceutical Investigation* 46(1) (2016) 67-78.

[227] V. Bansal, Pharmacokinetic and Biodistribution Analysis of 5-Fluorouracil-and Celecoxib-loaded Eudragit S100-coated Chitosan Microspheres Intended for Colon-specific Delivery, *Asian Journal of Pharmaceutics (AJP): Free full text articles from Asian J Pharm* 12(04) (2019).

[228] S. Mahira, N. Kommineni, G.M. Husain, W. Khan, Cabazitaxel and silibinin co-encapsulated cationic liposomes for CD44 targeted delivery: A new insight into nanomedicine based combinational chemotherapy for prostate cancer, *Biomedicine & Pharmacotherapy* 110 (2019) 803-817.

[229] J. Varshosaz, M. Minaiyan, N. Khaleghi, Eudragit nanoparticles loaded with silybin: a detailed study of preparation, freeze-drying condition and in vitro/in vivo evaluation, *Journal of microencapsulation* 32(3) (2015) 211-223.

[230] D. Pooja, D.J.B. Bikkina, H. Kulhari, N. Nikhila, S. Chinde, Y. Raghavendra, B. Sreedhar, A.K. Tiwari, Fabrication, characterization and bioevaluation of silibinin loaded chitosan nanoparticles, *International journal of biological macromolecules* 69 (2014) 267-273.

- [231] R. Garg, G. Gupta, Gastroretentive floating microspheres of silymarin: preparation and in vitro evaluation, *Tropical journal of pharmaceutical research* 9(1) (2010).
- [232] S. Hossainzadeh, N. Ranji, A. Naderi Sohi, F. Najafi, Silibinin encapsulation in polymersome: A promising anticancer nanoparticle for inducing apoptosis and decreasing the expression level of miR-125b/miR-182 in human breast cancer cells, *Journal of cellular physiology* (2019).
- [233] J.M. Tan, G. Karthivashan, P. Arulselvan, S. Fakurazi, M.Z. Hussein, Characterization and in vitro sustained release of silibinin from pH responsive carbon nanotube-based drug delivery system, *Journal of Nanomaterials* 2014 (2014) 1.
- [234] Y. Li, D. Yang, Y. Wang, Z. Li, C. Zhu, Co-delivery doxorubicin and silybin for antihepatoma via enhanced oral hepatic-targeted efficiency, *International Journal of Nanomedicine* 14 (2019) 301-315.
- [235] M. Gohulkumar, K. Gurushankar, N.R. Prasad, N. Krishnakumar, Enhanced cytotoxicity and apoptosis-induced anticancer effect of silibinin-loaded nanoparticles in oral carcinoma (KB) cells, *Materials Science and Engineering: C* 41 (2014) 274-282.
- [236] M.C.L. Marchiori, C. Rigon, P.M. Copetti, M.R. Sagrillo, L. Cruz, Nanoencapsulation Improves Scavenging Capacity and Decreases Cytotoxicity of Silibinin and Pomegranate Oil Association, *AAPS PharmSciTech* 18(8) (2017) 3236-3246.
- [237] C.H. Campos, C.F. Díaz, J.L. Guzmán, J.B. Alderete, C.C. Torres, V.A. Jiménez, PAMAM-Conjugated Alumina Nanotubes as Novel Noncytotoxic Nanocarriers with Enhanced Drug Loading and Releasing Performances, *Macromolecular Chemistry and Physics* 217(15) (2016) 1712-1722.
- [238] X. Zhou, Z. Chen, Preparation and performance evaluation of emulsomes as a drug delivery system for silybin, *Archives of pharmacological research* 38(12) (2015) 2193-2200.
- [239] P. Gogoi, M.K. Das, A. Ramteke, T.K. Maji, Soy flour–ZnO nanoparticles for controlled release of silibinin: Effect of ZnO nanoparticle, surfactant, and cross-linker, *International Journal of Polymeric Materials and Polymeric Biomaterials* 67(9) (2018) 543-552.
- [240] E. Joussein, S. Petit, J. Churchman, B. Theng, D. Righi, B. Delvaux, Halloysite clay minerals—a review, *De Gruyter*, 2005.
- [241] M. Massaro, G. Lazzara, R. Noto, S. Riela, Halloysite nanotubes: a green resource for materials and life sciences, *Rendiconti Lincei. Scienze Fisiche e Naturali* (2020) 1-9.
- [242] E. Joussein, S. Petit, J. Churchman, B. Theng, D. Righi, B. Delvaux, Halloysite clay minerals—a review, *Clay minerals* 40(4) (2005) 383-426.
- [243] S. Leporatti, Halloysite Clay Nanotubes as Nano-Bazookas for Drug Delivery, *Polymer International* (2017).
- [244] Y.M. Lvov, M.M. DeVilliers, R.F. Fakhruddin, The application of halloysite tubule nanoclay in drug delivery, *Expert opinion on drug delivery* 13(7) (2016) 977-986.
- [245] E. Abdullayev, A. Joshi, W. Wei, Y. Zhao, Y. Lvov, Enlargement of halloysite clay nanotube lumen by selective etching of aluminum oxide, *ACS nano* 6(8) (2012) 7216-7226.
- [246] S. Satish, M. Tharmavaram, D. Rawtani, Halloysite nanotubes as a nature's boon for biomedical applications, *Nanobiomedicine* 6 (2019) 1849543519863625.

- [247] T.S. Gaaz, A.B. Sulong, A.A.H. Kadhum, M.H. Nassir, A.A. Al-Amiery, Surface improvement of halloysite nanotubes, *Applied Sciences* 7(3) (2017) 291.
- [248] M.S. Nazir, M.H.M. Kassim, L. Mohapatra, M.A. Gilani, M.R. Raza, K. Majeed, Characteristic properties of nanoclays and characterization of nanoparticulates and nanocomposites, *Nanoclay reinforced polymer composites*, Springer 2016, pp. 35-55.
- [249] E.G. Bediako, E. Nyankson, D. Dodoo-Arhin, B. Agyei-Tuffour, D. Łukowiec, B. Tomiczek, A. Yaya, J.K. Efavi, Modified halloysite nanoclay as a vehicle for sustained drug delivery, *Heliyon* 4(7) (2018) e00689.
- [250] H. Zhang, Selective modification of inner surface of halloysite nanotubes: a review, *Nanotechnology Reviews* 6(6) (2017) 573-581.
- [251] S. Levis, P. Deasy, Characterisation of halloysite for use as a microtubular drug delivery system, *International Journal of Pharmaceutics* 243(1) (2002) 125-134.
- [252] B.G. R. Price, Y. Lvov, R. In-vitro release characteristics of tetracycline HCl, khellin and nicotinamide adenine dincucleotide from halloysite; a cylindrical mineral, *Journal of microencapsulation* 18(6) (2001) 713-722.
- [253] V. Vergaro, E. Abdullayev, Y.M. Lvov, A. Zeitoun, R. Cingolani, R. Rinaldi, S. Leporatti, Cytocompatibility and uptake of halloysite clay nanotubes, *Biomacromolecules* 11(3) (2010) 820-826.
- [254] X. Lai, M. Agarwal, Y.M. Lvov, C. Pachpande, K. Varahramyan, F.A. Witzmann, Proteomic profiling of halloysite clay nanotube exposure in intestinal cell co-culture, *Journal of Applied Toxicology* 33(11) (2013) 1316-1329.
- [255] G.I. Fakhrollina, F.S. Akhatova, Y.M. Lvov, R.F. Fakhrollin, Toxicity of halloysite clay nanotubes in vivo: a *Caenorhabditis elegans* study, *Environmental Science: Nano* 2(1) (2015) 54-59.
- [256] R. Kamble, M. Ghag, S. Gaikawad, B.K. Panda, Halloysite Nanotubes and Applications: A Review, *Journal of Advanced Scientific Research* 3(2) (2012).
- [257] H. Hemmatpour, V. Haddadi-Asl, H. Roghani-Mamaqani, Synthesis of pH-sensitive poly (N,N-dimethylaminoethyl methacrylate)-grafted halloysite nanotubes for adsorption and controlled release of DPH and DS drugs, *Polymer* 65(Supplement C) (2015) 143-153.
- [258] E. Gianni, K. Avgoustakis, M. Pšenička, M. Pospíšil, D. Papoulis, Halloysite nanotubes as carriers for irinotecan: Synthesis and characterization by experimental and molecular simulation methods, *Journal of Drug Delivery Science and Technology* 52 (2019) 568-576.
- [259] C. Dionisi, N. Hanafy, C. Nobile, M.L. De Giorgi, R. Rinaldi, S. Casciaro, Y.M. Lvov, S. Leporatti, Halloysite clay nanotubes as carriers for curcumin: characterization and application, *IEEE Transactions on Nanotechnology* 15(5) (2016) 720-724.
- [260] R. Yendluri, Y. Lvov, M.M. de Villiers, V. Vinokurov, E. Naumenko, E. Tarasova, R. Fakhrollin, Paclitaxel encapsulated in halloysite clay nanotubes for intestinal and intracellular delivery, *Journal of Pharmaceutical Sciences* 106(10) (2017) 3131-3139.
- [261] W. Wei, R. Minullina, E. Abdullayev, R. Fakhrollin, D. Mills, Y. Lvov, Enhanced efficiency of antiseptics with sustained release from clay nanotubes, *RSC Advances* 4(1) (2014) 488-494.

- [262] K. Sudhakar, S.J. Moloi, K. Madhusudhana Rao, Green Synthesis and Characterization of Halloysite Nanoclay/Curcumin/Ag Hybrid Nano Materials for Antibacterial Applications, *Journal of Inorganic and Organometallic Polymers and Materials* (2017).
- [263] P. Yuan, P.D. Southon, Z. Liu, C.J. Kepert, Organosilane functionalization of halloysite nanotubes for enhanced loading and controlled release, *Nanotechnology* 23(37) (2012) 375705.
- [264] Y. Lvov, W. Wang, L. Zhang, R. Fakhrullin, Halloysite clay nanotubes for loading and sustained release of functional compounds, *Advanced Materials* 28(6) (2016) 1227-1250.
- [265] D. Tan, P. Yuan, F. Annabi-Bergaya, H. Yu, D. Liu, H. Liu, H. He, Natural halloysite nanotubes as mesoporous carriers for the loading of ibuprofen, *Microporous and Mesoporous Materials* 179 (2013) 89-98.
- [266] G. Biddeci, G. Cavallaro, F. Di Blasi, G. Lazzara, M. Massaro, S. Milioto, F. Parisi, S. Riela, G. Spinelli, Halloysite nanotubes loaded with peppermint essential oil as filler for functional biopolymer film, *Carbohydrate polymers* 152 (2016) 548-557.
- [267] R. Qi, R. Guo, F. Zheng, H. Liu, J. Yu, X. Shi, Controlled release and antibacterial activity of antibiotic-loaded electrospun halloysite/poly (lactic-co-glycolic acid) composite nanofibers, *Colloids and Surfaces B: Biointerfaces* 110 (2013) 148-155.
- [268] X. Li, QianYang, J. Ouyang, H. Yang, S. Chang, Chitosan modified halloysite nanotubes as emerging porous microspheres for drug carrier, *Applied Clay Science* 126(Supplement C) (2016) 306-312.
- [269] Q. Wang, J. Zhang, A. Wang, Alkali activation of halloysite for adsorption and release of ofloxacin, *Applied Surface Science* 287(Supplement C) (2013) 54-61.
- [270] M. Massaro, S. Piana, C. Colletti, R. Noto, S. Riela, C. Baiamonte, C. Giordano, G. Pizzolanti, G. Cavallaro, S. Milioto, Multicavity halloysite–amphiphilic cyclodextrin hybrids for co-delivery of natural drugs into thyroid cancer cells, *Journal of Materials Chemistry B* 3(19) (2015) 4074-4081.
- [271] M. Massaro, C.G. Colletti, R. Noto, S. Riela, P. Poma, S. Guernelli, F. Parisi, S. Milioto, G. Lazzara, Pharmaceutical properties of supramolecular assembly of co-loaded cardanol/triazole-halloysite systems, *International Journal of Pharmaceutics* 478(2) (2015) 476-485.
- [272] N.G. Veerabadran, R.R. Price, Y.M. Lvov, Clay nanotubes for encapsulation and sustained release of drugs, *Nano* 2(02) (2007) 115-120.
- [273] F. Moeinpour, F. Soofivand, F.S. Mohseni-Shahri, Controlled release of losartan from acid-and heat-treated halloysite nanotubes, *Medicinal Chemistry Research* 28(2) (2019) 160-168.
- [274] M.R. Abukhadra, A.F. Allah, Synthesis and characterization of kaolinite nanotubes (KNTs) as a novel carrier for 5-fluorouracil of high encapsulation properties and controlled release, *Inorganic Chemistry Communications* 103 (2019) 30-36.
- [275] M. Fizir, P. Dramou, K. Zhang, C. Sun, C. Pham-Huy, H. He, Polymer grafted-magnetic halloysite nanotube for controlled and sustained release of cationic drug, *Journal of colloid and interface science* 505 (2017) 476-488.

- [276] B. Huang, M. Liu, C. Zhou, Cellulose–halloysite nanotube composite hydrogels for curcumin delivery, *Cellulose* 24(7) (2017) 2861-2875.
- [277] A. Czyrski, Determination of the Lipophilicity of Ibuprofen, Naproxen, Ketoprofen, and Flurbiprofen with Thin-Layer Chromatography, *Journal of Chemistry* 2019 (2019) 3407091.
- [278] W. Li, D. Liu, H. Zhang, A. Correia, E. Mäkilä, J. Salonen, J. Hirvonen, H.A. Santos, Microfluidic assembly of a nano-in-micro dual drug delivery platform composed of halloysite nanotubes and a pH-responsive polymer for colon cancer therapy, *Acta biomaterialia* 48 (2017) 238-246.
- [279] K.M. Rao, S. Nagappan, D.J. Seo, C.-S. Ha, pH sensitive halloysite-sodium hyaluronate/poly (hydroxyethyl methacrylate) nanocomposites for colon cancer drug delivery, *Applied clay science* 97 (2014) 33-42.
- [280] D. Tan, P. Yuan, F. Dong, H. He, S. Sun, Z. Liu, Selective loading of 5-fluorouracil in the interlayer space of methoxy-modified kaolinite for controlled release, *Applied Clay Science* 159 (2018) 102-106.
- [281] D. Garcia-Garcia, J.M. Ferri, L. Ripoll, M. Hidalgo, J. Lopez-Martinez, R. Balart, Characterization of selectively etched halloysite nanotubes by acid treatment, *Applied Surface Science* 422 (2017) 616-625.
- [282] Y. Sarikaya, M. Önal, B. Baran, T. Alemdaroğlu, The effect of thermal treatment on some of the physicochemical properties of a bentonite, *Clays and Clay Minerals* 48(5) (2000) 557-562.
- [283] F. Hussin, M.K. Aroua, W.M.A.W. Daud, Textural characteristics, surface chemistry and activation of bleaching earth: A review, *Chemical Engineering Journal* 170(1) (2011) 90-106.
- [284] M. Tharmavaram, G. Pandey, D. Rawtani, Surface modified halloysite nanotubes: A flexible interface for biological, environmental and catalytic applications, *Advances in colloid and interface science* 261 (2018) 82-101.
- [285] Y. Liu, M. Liu, Conductive carboxylated styrene butadiene rubber composites by incorporation of polypyrrole-wrapped halloysite nanotubes, *Composites Science and Technology* 143 (2017) 56-66.
- [286] G. Pandey, D.M. Munguambe, M. Tharmavaram, D. Rawtani, Y. Agrawal, Halloysite nanotubes-An efficient ‘nano-support’ for the immobilization of α -amylase, *Applied Clay Science* 136 (2017) 184-191.
- [287] H. Li, X. Zhu, H. Zhou, S. Zhong, Functionalization of halloysite nanotubes by enlargement and hydrophobicity for sustained release of analgesic, *Colloids and Surfaces A: Physicochemical and Engineering Aspects* 487 (2015) 154-161.
- [288] M. Massaro, A. Campofelice, C.G. Colletti, G. Lazzara, R. Noto, S. Riela, Functionalized halloysite nanotubes: Efficient carrier systems for antifungine drugs, *Applied Clay Science* 160 (2018) 186-192.
- [289] Q. Wang, Y. Wang, Y. Zhao, B. Zhang, N. Yunyin, X. Xiang, R. Chen, Fabricating roughened surfaces on halloysite nanotubes via alkali etching for deposition of high-efficiency Pt nanocatalysts, *CrystEngComm* 17(16) (2015) 3110-3116.

- [290] L. Ge, R. Lin, L. Wang, T.E. Rufford, B. Villacorta, S. Liu, L.X. Liu, Z. Zhu, Surface-etched halloysite nanotubes in mixed matrix membranes for efficient gas separation, *Separation and Purification Technology* 173 (2017) 63-71.
- [291] A.-B. Zhang, L. Pan, H.-Y. Zhang, S.-T. Liu, Y. Ye, M.-S. Xia, X.-G. Chen, Effects of acid treatment on the physico-chemical and pore characteristics of halloysite, *Colloids and Surfaces A: Physicochemical and Engineering Aspects* 396 (2012) 182-188.
- [292] T. Gaaz, A. Sulong, A. Kadhum, M. Nassir, A. Al-Amiery, Impact of sulfuric acid treatment of halloysite on physico-chemic property modification, *Materials* 9(8) (2016) 620.
- [293] S. Chaudhari, M. Baek, Y. Kwon, M. Shon, S. Nam, Y. Park, Surface-modified halloysite nanotube-embedded polyvinyl alcohol/polyvinyl amine blended membranes for pervaporation dehydration of water/isopropanol mixtures, *Applied Surface Science* 493 (2019) 193-201.
- [294] H. Xiang, J. Zhou, Y. Zhang, M.T. Innocent, M. Zhu, Polyethylene glycol infused acid-etched halloysite nanotubes for melt-spun polyamide-based composite phase change fibers, *Applied Clay Science* 182 (2019) 105249.
- [295] K.K. Barfod, K.M. Bendtsen, T. Berthing, A.J. Koivisto, S.S. Poulsen, E. Segal, E. Verleysen, J. Mast, A. Holländer, K.A. Jensen, Increased surface area of halloysite nanotubes due to surface modification predicts lung inflammation and acute phase response after pulmonary exposure in mice, *Environmental Toxicology and Pharmacology* (2019) 103266.
- [296] Y. Zhao, X. Quan, C. Li, Facile preparation of etched halloysite@ polyaniline nanorods and their enhanced electrochemical capacitance performance, *Electrochimica Acta* 321 (2019) 134715.
- [297] S. Zeng, C. Reyes, J. Liu, P.A. Rodgers, S.H. Wentworth, L. Sun, Facile hydroxylation of halloysite nanotubes for epoxy nanocomposite applications, *Polymer* 55(25) (2014) 6519-6528.
- [298] O. Tamada, G.V. Gibbs, M.B. Boisen Jr, J.D. Rimstidt, Silica dissolution catalyzed by NaOH: Reaction kinetics and energy barriers simulated by quantum mechanical strategies, *Journal of Mineralogical and Petrological Sciences* 107(2) (2012) 87-98.
- [299] J.M. Rimsza, R.E. Jones, L.J. Criscenti, Interaction of NaOH solutions with silica surfaces, *Journal of colloid and interface science* 516 (2018) 128-137.
- [300] R.D. White, D.V. Bavykin, F.C. Walsh, The stability of halloysite nanotubes in acidic and alkaline aqueous suspensions, *Nanotechnology* 23(6) (2012) 065705.
- [301] A.H. Asl, M. Khajenoori, Subcritical water extraction, *Mass Transfer-Advances in sustainable energy and environment oriented numerical modeling* (2013) 459-487.
- [302] A.G. Carr, R. Mammucari, N. Foster, A review of subcritical water as a solvent and its utilisation for the processing of hydrophobic organic compounds, *Chemical Engineering Journal* 172(1) (2011) 1-17.
- [303] R. Fernandez-Prini, *High-temperature aqueous solutions: thermodynamic properties*, CRC Press 1991.
- [304] E.R. Caffarena, J.R. Grigera, On the hydrogen bond structure of water at different densities, *Physica A: Statistical Mechanics and its Applications* 342(1-2) (2004) 34-39.

- [305] I. Okajima, T. Sako, Energy conversion of biomass with supercritical and subcritical water using large-scale plants, *Journal of Bioscience and Bioengineering* 117(1) (2014) 1-9.
- [306] D.J. Miller, S.B. Hawthorne, Method for determining the solubilities of hydrophobic organics in subcritical water, *Anal. Chem.* 70(8) (1998) 1618-1621.
- [307] J.W. King, R.D. Grabiell, Isolation of polyphenolic compounds from fruits or vegetables utilizing sub-critical water extraction, Google Patents, 2007.
- [308] E. Priego-López, M.L. de Castro, Demetalisation of soils by continuous acidified subcritical water extraction, *Talanta* 58(2) (2002) 377-385.
- [309] V. Fernández-Pérez, M. Jiménez-Carmona, M.L. de Castro, Continuous liquid-liquid extraction using modified subcritical water for the demetalisation of used industrial oils, *Analytica chimica acta* 433(1) (2001) 47-52.
- [310] A. Kubátová, A.J. Lagadec, D.J. Miller, S.B. Hawthorne, Selective extraction of oxygenates from savory and peppermint using subcritical water, *Flavour and Fragrance Journal* 16(1) (2001) 64-73.
- [311] J. Cacace, G. Mazza, Pressurized low polarity water extraction of lignans from whole flaxseed, *Journal of Food Engineering* 77(4) (2006) 1087-1095.
- [312] W.-J. Kim, J. Kim, B. Veriansyah, J.-D. Kim, Y.-W. Lee, S.-G. Oh, R.R. Tjandrawinata, Extraction of bioactive components from *Centella asiatica* using subcritical water, *The Journal of Supercritical Fluids* 48(3) (2009) 211-216.
- [313] H. Yoshida, S. Izhar, E. Nishio, Y. Utsumi, N. Kakimori, S.A. Feridoun, Recovery of indium from TFT and CF glasses in LCD panel wastes using sub-critical water, *Solar energy materials and solar cells* 125 (2014) 14-19.
- [314] K. Liu, F.-S. Zhang, Innovative leaching of cobalt and lithium from spent lithium-ion batteries and simultaneous dechlorination of polyvinyl chloride in subcritical water, *Journal of hazardous materials* 316 (2016) 19-25.
- [315] K. Morita, K. Ohnaka, Novel selective etching method for silicon nitride films on silicon substrates by means of subcritical water, *Industrial & engineering chemistry research* 39(12) (2000) 4684-4688.
- [316] N.s.G. González-Pereyra, W. Glasgow, A. Parenzan, J.L. Sharp, O.T. Mefford, Investigation of the etching of silicon under subcritical water conditions, *Industrial & Engineering Chemistry Research* 53(1) (2014) 173-181.
- [317] V. Bagratashvili, A. Konovalov, A. Novitskiy, M. Poliakoff, S. Tsypina, Reflectometric studies of the etching of a silica fiber with a germanium silicate core in sub-and supercritical water, *Russian Journal of Physical Chemistry B* 3(8) (2009) 1154-1164.
- [318] P. Karásek, J. Grym, M. Roth, J. Planeta, F. Foret, Etching of glass microchips with supercritical water, *Lab on a Chip* 15(1) (2015) 311-318.
- [319] K. Dixit, R.B. Athawale, S. Singh, Quality control of residual solvent content in polymeric microparticles, *Journal of microencapsulation* 32(2) (2015) 107-122.
- [320] J. Chalmers, P. Griffiths, *Handbook of Vibrational Spectroscopy*, 5 volumes set, Wiley 2002.

- [321] Q.-y. Liu, Y.-l. Bei, G.-b. Qi, Y.-j. Ding, Thermal decomposition kinetics of 5-fluorouracil from thermogravimetric analysis, *Korean Journal of Chemical Engineering* 25(5) (2008) 980-981.
- [322] Y. Chen, Y. Zhang, J. Liu, H. Zhang, K. Wang, Preparation and antibacterial property of polyethersulfone ultrafiltration hybrid membrane containing halloysite nanotubes loaded with copper ions, *Chemical Engineering Journal* 210 (2012) 298-308.
- [323] M. Du, B. Guo, D. Jia, Thermal stability and flame retardant effects of halloysite nanotubes on poly (propylene), *European Polymer Journal* 42(6) (2006) 1362-1369.
- [324] P. Singh, G. Tyagi, R. Mehrotra, A. Bakhshi, Thermal stability studies of 5-fluorouracil using diffuse reflectance infrared spectroscopy, *Drug testing and analysis* 1(5) (2009) 240-244.
- [325] V. Venkateswarlu, K. Manjunath, Preparation, characterization and in vitro release kinetics of clozapine solid lipid nanoparticles, *Journal of controlled release* 95(3) (2004) 627-638.
- [326] W. Liu, H. Pan, C. Zhang, L. Zhao, R. Zhao, Y. Zhu, W. Pan, Developments in methods for measuring the intestinal absorption of nanoparticle-bound drugs, *International journal of molecular sciences* 17(7) (2016) 1171.
- [327] V.S. Shenoy, R.P. Gude, R.S.R. Murthy, In vitro anticancer evaluation of 5-fluorouracil lipid nanoparticles using B16F10 melanoma cell lines, *International Nano Letters* 3(1) (2013) 36.
- [328] S. D'Souza, A review of in vitro drug release test methods for nano-sized dosage forms, *Advances in Pharmaceutics* 2014 (2014).
- [329] J. Linnankoski, J. Mäkelä, J. Palmgren, T. Mauriala, C. Vedin, A.L. Ungell, L. Lazorova, P. Artursson, A. Urtti, M. Yliperttula, Paracellular porosity and pore size of the human intestinal epithelium in tissue and cell culture models, *Journal of pharmaceutical sciences* 99(4) (2010) 2166-2175.
- [330] R.J. Crawford, J.L. Throne, *Rotational molding technology*, William Andrew 2001.
- [331] J. Kurczewska, P. Pecyna, M. Ratajczak, M. Gajęcka, G. Schroeder, Halloysite nanotubes as carriers of vancomycin in alginate-based wound dressing, *Saudi pharmaceutical journal* 25(6) (2017) 911-920.
- [332] F.J. Sotomayor, K.A. Cychosz, M. Thommes, Characterization of micro/mesoporous materials by physisorption: concepts and case studies, *Acc. Mater. Surf. Res* 3 (2018) 34-50.
- [333] J.A.G. Balanay, C.T. Lungu, Morphologic and surface characterization of different types of activated carbon fibres, *Adsorption Science & Technology* 30(4) (2012) 355-367.
- [334] S.J. Lee, S. Kim, B. Seo, Y.-W. Lee, J.M. Lee, Batch-Wise Nonlinear Model Predictive Control of a Gas Antisolvent Recrystallization Process for the Uniform Production of Micronized HMX with Carbon Dioxide as the Antisolvent, *Ind. Eng. Chem. Res.* 54(47) (2015) 11894-11902.
- [335] S. Dodds, J.A. Wood, P.A. Charpentier, Modeling of the Gas– Antisolvent (GAS) Process for Crystallization of Beclomethasone Dipropionate Using Carbon Dioxide, *Industrial & Engineering Chemistry Research* 46(24) (2007) 8009-8017.

- [336] D. Suleiman, L.A. Estévez, J.C. Pulido, J.E. García, C. Mojica, Solubility of anti-inflammatory, anti-cancer, and anti-HIV drugs in supercritical carbon dioxide, *Journal of Chemical & Engineering Data* 50(4) (2005) 1234-1241.
- [337] A.M. Scurto, K. Hutchenson, B. Subramaniam, Gas-expanded liquids: Fundamentals and applications, in: K. Hutchenson, A.M. Scurto, B. Subramaniam (Eds.), *Gas-Expanded Liquids and Near-Critical Media Green Chemistry and Engineering*, ACS, Washington DC, 2009, pp. 3-37.
- [338] G.R. Akien, M. Poliakoff, A critical look at reactions in class I and II gas-expanded liquids using CO₂ and other gases, *Green Chem.* 11(8) (2009) 1083-1100.
- [339] M. Müller, U. Meier, A. Kessler, M. Mazzotti, Experimental Study of the Effect of Process Parameters in the Recrystallization of an Organic Compound Using Compressed Carbon Dioxide as Antisolvent, *Ind. Eng. Chem. Res.* 39(7) (2000) 2260-2268.
- [340] N. Foster, R. Mammucari, F. Dehghani, A. Barrett, K. Bezanehtak, E. Coen, G. Combes, L. Meure, A. Ng, H.L. Regtop, A. Tandy, Processing Pharmaceutical Compounds Using Dense Gas Technology, *Ind. Eng. Chem. Res.* 42(25) (2003) 6476-6493.
- [341] K. Dixit, R.B. Athawale, S. Singh, Quality control of residual solvent content in polymeric microparticles, *J. Microencapsul.* 32(2) (2015) 107-122.
- [342] J.B. Parker, J.T. Stivers, Dynamics of Uracil and 5-Fluorouracil in DNA, *Biochem.* 50(5) (2011) 612-617.
- [343] O.E. Almersjö, B.G. Gustavsson, C.-G. Regårdh, P. Wåhlén, Pharmacokinetic Studies of 5-Fluorouracil after Oral and Intravenous Administration in Man, *Acta Pharmacologica et Toxicologica* 46(5) (1980) 329-336.
- [344] R.J. Fraile, L.H. Baker, T.R. Buroker, J. Horwitz, V.K. Vaitkevicius, Pharmacokinetics of 5-Fluorouracil Administered Orally, by Rapid Intravenous and by Slow Infusion, *Cancer Res.* 40(7) (1980) 2223-2228.
- [345] S. Tummala, M.N. Satish Kumar, A. Prakash, Formulation and characterization of 5-Fluorouracil enteric coated nanoparticles for sustained and localized release in treating colorectal cancer, *Saudi Pharm. J.* 23(3) (2015) 308-314.
- [346] K.M. Rao, S. Nagappan, D.J. Seo, C.-S. Ha, pH sensitive halloysite-sodium hyaluronate/poly(hydroxyethyl methacrylate) nanocomposites for colon cancer drug delivery, *Appl. Clay Sci.* 97-98 (2014) 33-42.
- [347] Y. Lvov, W. Wang, L. Zhang, R. Fakhrullin, Halloysite Clay Nanotubes for Loading and Sustained Release of Functional Compounds, *Adv. Mater.* 28(6) (2016) 1227-1250.
- [348] C.J. Ward, M. DeWitt, E.W. Davis, Halloysite Nanoclay for Controlled Release Applications, in: R. Nagarajan (Ed.), *Nanomaterials for Biomedicine*, ACS, Washington, DC, 2012.
- [349] P. Komadel, Acid activated clays: Materials in continuous demand, *App. Clay Sci.* 131 (2016) 84-99.
- [350] P. Kalantarian, A.R. Najafabadi, I. Haririan, A. Vatanara, Y. Yamini, M. Darabi, K. Gilani, Preparation of 5-fluorouracil nanoparticles by supercritical antisolvents for pulmonary delivery, *Int. J. Nanomed.* 5 (2010) 763-70.

- [351] N. Esfandiari, S.M. Ghoreishi, Synthesis of 5-Fluorouracil nanoparticles via supercritical gas antisolvent process, *J. Supercrit. Fluids* 84 (2013) 205-210.
- [352] L.I. Cabezas, V. Fernández, R. Mazarro, I. Gracia, A. de Lucas, J.F. Rodríguez, Production of biodegradable porous scaffolds impregnated with indomethacin in supercritical CO₂, *J. Supercrit. Fluids* 63 (2012) 155-160.
- [353] D. Tan, P. Yuan, F. Dong, H. He, S. Sun, Z. Liu, Selective loading of 5-fluorouracil in the interlayer space of methoxy-modified kaolinite for controlled release, *Appl. Clay Sci.* 159 (2018) 102-106.
- [354] Halloysite and Kaolinite, The James Hutton Institute (2019) <https://www.claysandminerals.com/halloysite-and-kaolinite>.
- [355] G. Cavallaro, G. Lazzara, S. Milioto, F. Parisi, Hydrophobically modified halloysite nanotubes as reverse micelles for water-in-oil emulsion, *Langmuir* 31(27) (2015) 7472-7478.
- [356] R.D. White, D.V. Bavykin, F.C. Walsh, The stability of halloysite nanotubes in acidic and alkaline aqueous suspensions, *Nanotechnol.* 23(6) (2012) 065705.
- [357] H. Zhu, M. Du, M. Zou, C. Xu, Y. Fu, Green synthesis of Au nanoparticles immobilized on halloysite nanotubes for surface-enhanced Raman scattering substrates, *Dalton transactions* (Cambridge, England : 2003) 41(34) (2012) 10465-71.
- [358] X. Zhang, M. Cresswell, Inorganic controlled release technology, *Inorg. Control. Release Technol.* (2016).
- [359] R. Sih, F. Dehghani, N.R. Foster, Viscosity measurements on gas expanded liquid systems - Methanol and carbon dioxide, *J. Supercrit. Fluids* 41(1) (2007) 148-157.
- [360] V.T. Wyatt, D. Bush, J. Lu, J.P. Hallett, C.L. Liotta, C.A. Eckert, Determination of solvatochromic solvent parameters for the characterization of gas-expanded liquids, *J. Supercrit. Fluids* 36(1) (2005) 16-22.
- [361] F.H. Lin, Y.H. Lee, C.H. Jian, J.-M. Wong, M.-J. Shieh, C.-Y. Wang, A study of purified montmorillonite intercalated with 5-fluorouracil as drug carrier, *Biomater.* 23(9) (2002) 1981-1987.
- [362] S.A. Gârea, A.I. Mihai, A. Ghebaure, C. Nistor, A. Sârbu, Porous clay heterostructures: A new inorganic host for 5-fluorouracil encapsulation, *Int. J. Pharmaceut.* 491(1) (2015) 299-309.
- [363] D. Tan, P. Yuan, F. Annabi-Bergaya, D. Liu, H. He, High-capacity loading of 5-fluorouracil on the methoxy-modified kaolinite, *Appl. Clay Sci.* 100 (2014) 60-65.
- [364] T. Loftsson, *Essential Pharmacokinetics*, Elsevier, Amsterdam, 2015.
- [365] N.W. Read, M.N. Al-Janabi, A.M. Holgate, D.C. Barber, C.A. Edwards, Simultaneous measurement of gastric emptying, small bowel residence and colonic filling of a solid meal by the use of the gamma camera, *Gut* 27(3) (1986) 300-308.
- [366] G. Tari, I. Bobos, C.S.F. Gomes, J.M.F. Ferreira, Modification of surface charge properties during kaolinite to halloysite-7Å transformation, *J. Colloid Interface Sci.* 210(2) (1999) 360-366.

[367] A. Buur, H. Bundgaard, Prodrugs of 5-fluorouracil. III. Hydrolysis kinetics in aqueous solution and biological media, lipophilicity and solubility of various 1-carbamoyl derivatives of 5-fluorouracil, *Int. J. Pharmaceut.* 23(2) (1985) 209-222.

[368] R.J. Hunter, *Zeta potential in colloid science: principles and applications*, Academic Press, London, 1981.

[369] M. Chorom, P. Rengasamy, Dispersion and zeta potential of pure clays as related to net particle charge under varying pH, electrolyte concentration and cation type, *Eur. J. Soil Sci.* 46(4) (1995) 657-665.

[370] G.S. Abdrakhimova, M.Y. Ovchinnikov, A.N. Lobov, L.V. Spirikhin, S.P. Ivanov, S.L. Khursan, 5-Fluorouracil solutions: NMR study of acid–base equilibrium in water and DMSO, *J. Phys. Org. Chem.* 27(11) (2014) 876-883.

[371] N. Şanlı, S. Şanlı, G. Alsancak, Determination of dissociation constants of folic acid (Leucovorin), 5-fluorouracil, and Irinotecan in hydro-organic media by a spectrophotometric method, *J. Chem. Eng. Data* 55(8) (2010) 2695-2699.

[372] S. Mutalik, P.K. Shetty, A. Kumar, R. Kalra, H.S. Parekh, Enhancement in deposition and permeation of 5-fluorouracil through human epidermis assisted by peptide dendrimers, *Drug Deliv.* 21(1) (2014) 44-54.

[373] D. Li, *Microencapsulation of protein with EUDRAGIT S 100 polymer*, 2005.

[374] M.L. Huggins, The viscosity of dilute solutions of long-chain molecules. IV. Dependence on concentration, *J. Am. Chem. Soc.* 64(11) (1942) 2716-2718.

[375] M. Rao, Viscosity of dilute to moderately concentrated polymer solutions, *Polymer* 34(3) (1993) 592-596.

[376] S. Matsuoka, M. Cowman, Equation of state for polymer solution, *Polymer* 43(12) (2002) 3447-3453.

[377] S.I. Shah, G.H. Jaffari, E. Yassitepe, B. Ali, Evaporation: Processes, bulk microstructures, and mechanical properties, *Handbook of Deposition Technologies for Films and Coatings*, Elsevier 2010, pp. 135-252.

[378] R. Thiering, F. Dehghani, N.R. Foster, Current issues relating to anti-solvent micronisation techniques and their extension to industrial scales, *The Journal of Supercritical Fluids* 21(2) (2001) 159-177.

[379] A.H. Lefebvre, V.G. McDonell, *Atomization and Sprays*, 2 ed. 2017.

[380] S. Al-Hamimi, A.c. Abellan Mayoral, L.P. Cunico, C. Turner, Carbon dioxide expanded ethanol extraction: Solubility and extraction kinetics of α -pinene and cis-verbenol, *Anal. Chem.* 88(8) (2016) 4336-4345.

[381] D.J. Dixon, K.P. Johnston, Formation of microporous polymer fibers and oriented fibrils by precipitation with a compressed fluid antisolvent, *Journal of Applied Polymer Science* 50(11) (1993) 1929-1942.

[382] J.M. Smith, *Introduction to chemical engineering thermodynamics* / J.M. Smith, H.C. Van Ness, M.M. Abbott, 5th ed., International ed., New York

Singapore : McGraw-Hill, New York

Singapore, 1996.

[383] C. Lengsfeld, J. Delplanque, V. Barocas, T. Randolph, Mechanism governing microparticle morphology during precipitation by a compressed antisolvent: atomization vs nucleation and growth, *The Journal of Physical Chemistry B* 104(12) (2000) 2725-2735.

[384] A. Lefebvre, *Atomization and Sprays*"Hemisphere Publishing Corp, New York (1989).

[385] T.J. Young, K.P. Johnston, K. Mishima, H. Tanaka, Encapsulation of lysozyme in a biodegradable polymer by precipitation with a vapor-over-liquid antisolvent, *Journal of pharmaceutical sciences* 88(6) (1999) 640-650.

[386] J. Nývlt, *Industrial crystallisation from solutions*, Butterworths 1971.

[387] I. De Marco, E. Reverchon, Influence of pressure, temperature and concentration on the mechanisms of particle precipitation in supercritical antisolvent micronization, *The Journal of Supercritical Fluids* 58(2) (2011) 295-302.

[388] S.A. Rizvi, A.M. Saleh, Applications of nanoparticle systems in drug delivery technology, *Saudi Pharmaceutical Journal* 26(1) (2018) 64-70.

[389] M. Kumar, R. Awasthi, Development of Metronidazole-Loaded Colon-Targeted Microparticulate Drug Delivery System, *Polim. Med* 45(2) (2015) 57-65.

[390] M.A. Hadi, N.R. Rao, A.S. Rao, Formulation and evaluation of pH-responsive mini-tablets for ileo-colonic targeted drug delivery, *Tropical Journal of Pharmaceutical Research* 13(7) (2014) 1021-1029.

[391] H. Uchida, A. Manaka, M. Matsuoka, H. Takiyama, Growth phenomena of single crystals of naphthalene in supercritical carbon dioxide, *Crystal growth & design* 4(5) (2004) 937-942.

[392] W. Bachalo, *Spray diagnostics for the twenty-first century*, *Atomization and Sprays* 10(3-5) (2000) 439-474.

[393] O. Klüsener, The injection process in compressorless diesel engines, *VDI Z* 77(7) (1933) 107-110.

[394] J. Lewis, J. ARGYROPOULOS, K. NIELSON, Supercritical carbon dioxide spray systems, *Metal Finishing. Guidebook-directory* 100(6A) (2002) 301-309.

[395] B. Helfgen, M. Türk, K. Schaber, Hydrodynamic and aerosol modelling of the rapid expansion of supercritical solutions (RESS-process), *The Journal of supercritical fluids* 26(3) (2003) 225-242.

[396] P. Li, Y. Wang, Z. Peng, M.F. She, L. Kong, Physicochemical property and morphology of 5-fluorouracil loaded chitosan nanoparticles, 2010 International Conference on Nanoscience and Nanotechnology, IEEE, 2010, pp. 248-250.

[397] P. Li, Y. Wang, Z. Peng, F. She, L. Kong, Development of chitosan nanoparticles as drug delivery systems for 5-fluorouracil and leucovorin blends, *Carbohydrate polymers* 85(3) (2011) 698-704.

[398] B. Zhang, Y. Song, T. Wang, S. Yang, J. Zhang, Y. Liu, N. Zhang, S. Garg, Efficient co-delivery of immiscible hydrophilic/hydrophobic chemotherapeutics by lipid emulsions for improved treatment of cancer, *International journal of nanomedicine* 12 (2017) 2871.

- [399] S. Arpicco, L. Battaglia, P. Brusa, R. Cavalli, D. Chirio, F. Dosio, M. Gallarate, P. Milla, E. Peira, F. Rocco, Recent studies on the delivery of hydrophilic drugs in nanoparticulate systems, *Journal of Drug Delivery Science and Technology* 32 (2016) 298-312.
- [400] S. Shen, Y. Wu, Y. Liu, D. Wu, High drug-loading nanomedicines: progress, current status, and prospects, *International journal of nanomedicine* 12 (2017) 4085.
- [401] N. Onetto, R. Canetta, B. Winograd, R. Catane, M. Dougan, J. Grechko, J. Burroughs, M. Rozenzweig, Overview of Taxol safety, *Journal of the National Cancer Institute Monographs* 15 (1993) 131-139.
- [402] D.R. Luke, B.L. Kasiske, G.R. Matzke, W.M. Awni, W.F. Keane, Effects of cyclosporine on the isolated perfused rat kidney, *Transplantation* 43(6) (1987) 795-799.
- [403] P. Franco, I. De Marco, Eudragit: A Novel Carrier for Controlled Drug Delivery in Supercritical Antisolvent Coprecipitation, *Polymers* 12(1) (2020) 234.
- [404] N.Y. Chew, H.-K. Chan, Use of solid corrugated particles to enhance powder aerosol performance, *Pharmaceutical Research* 18(11) (2001) 1570-1577.
- [405] H.-K. Chan, Dry powder aerosol delivery systems: current and future research directions, *Journal of aerosol medicine* 19(1) (2006) 21-27.
- [406] D.J. Kroll, H.S. Shaw, N.H. Oberlies, Milk thistle nomenclature: why it matters in cancer research and pharmacokinetic studies, *Integrative cancer therapies* 6(2) (2007) 110-119.
- [407] R. Mehta, A. Chawla, P. Sharma, P. Pawar, Formulation and in vitro evaluation of Eudragit S-100 coated naproxen matrix tablets for colon-targeted drug delivery system, *Journal of advanced pharmaceutical technology & research* 4(1) (2013) 31.
- [408] M. Sharma, V. Sharma, A.K. Panda, D.K. Majumdar, Development of enteric submicron particle formulation of papain for oral delivery, *International journal of nanomedicine* 6 (2011) 2097.
- [409] M.Z.I. Khan, H.P. Štedul, N. Kurjaković, A pH-dependent colon-targeted oral drug delivery system using methacrylic acid copolymers. II. Manipulation of drug release using Eudragit® L100 and Eudragit S100 combinations, *Drug Development and industrial pharmacy* 26(5) (2000) 549-554.
- [410] M. Barea, M. Jenkins, Y. Lee, P. Johnson, R. Bridson, Encapsulation of liposomes within pH responsive microspheres for oral colonic drug delivery, *International journal of biomaterials* 2012 (2012).
- [411] F. Ansari, H. Pourjafar, V. Jodat, J. Sahebi, A. Ataei, Effect of Eudragit S100 nanoparticles and alginate chitosan encapsulation on the viability of *Lactobacillus acidophilus* and *Lactobacillus rhamnosus*, *AMB Express* 7(1) (2017) 144.
- [412] P.A. McCARRON, A.D. WOOLFSON, S.M. KEATING, Sustained release of 5-fluorouracil from polymeric nanoparticles, *Journal of pharmacy and pharmacology* 52(12) (2000) 1451-1459.
- [413] S. Harikrishnan, R. Sedev, C.C. Beh, C. Priest, N.R. Foster, Loading of 5-fluorouracil onto Halloysite nanotubes for targeted drug delivery using a subcritical gas antisolvent process (GAS), *The Journal of Supercritical Fluids* 159 (2020) 104756.

- [414] N. Esfandiari, S.M. Ghoreishi, Synthesis of 5-fluorouracil nanoparticles via supercritical gas antisolvent process, *The Journal of Supercritical Fluids* 84 (2013) 205-210.
- [415] A. Lamprecht, H. Yamamoto, H. Takeuchi, Y. Kawashima, Observations in simultaneous microencapsulation of 5-fluorouracil and leucovorin for combined pH-dependent release, *European Journal of Pharmaceutics and Biopharmaceutics* 59(2) (2005) 367-371.
- [416] Z.-B. Zhang, Z.-G. Shen, J.-X. Wang, H.-X. Zhang, H. Zhao, J.-F. Chen, J. Yun, Micronization of silybin by the emulsion solvent diffusion method, *International journal of pharmaceutics* 376(1-2) (2009) 116-122.
- [417] S.-H. Kim, H.-J. Kim, S.-D. Yeo, Crystallization of silibinin from organic solutions using supercritical and aqueous antisolvents, *The Journal of Supercritical Fluids* 85 (2014) 102-109.
- [418] F. Giorgi, D. Coglitore, J.M. Curran, D. Gilliland, P. Macko, M. Whelan, A. Worth, E.A. Patterson, The influence of inter-particle forces on diffusion at the nanoscale, *Scientific reports* 9(1) (2019) 1-6.
- [419] T. Sato, S. Kohnosu, Effect of surfactant concentration on the stability of aqueous titanium dioxide suspensions, *Journal of colloid and interface science* 143(2) (1991) 434-439.
- [420] S.G. Kazarian, M.F. Vincent, F.V. Bright, C.L. Liotta, C.A. Eckert, Specific intermolecular interaction of carbon dioxide with polymers, *J. Am. Chem. Soc.* 118(7) (1996) 1729-1736.
- [421] D.L. Tomasko, H. Li, D. Liu, X. Han, M.J. Wingert, L.J. Lee, K.W. Koelling, A review of CO₂ applications in the processing of polymers, *Industrial & Engineering Chemistry Research* 42(25) (2003) 6431-6456.
- [422] S.G. Kazarian, N.H. Brantley, B.L. West, M.F. Vincent, C.A. Eckert, In situ spectroscopy of polymers subjected to supercritical CO₂: plasticization and dye impregnation, *Appl. Spectrosc.* 51(4) (1997) 491-494.
- [423] S.G. Kazarian, Supercritical fluid impregnation of polymers for drug delivery, *Supercritical fluid technology for drug product development*, CRC Press 2004, pp. 343-364.
- [424] M. Champeau, J.-M. Thomassin, T. Tassaing, C. Jérôme, Drug loading of polymer implants by supercritical CO₂ assisted impregnation: A review, *Journal of controlled release* 209 (2015) 248-259.
- [425] B.L. Karger, L.R. Snyder, C. Eon, Expanded solubility parameter treatment for classification and use of chromatographic solvents and adsorbents, *Anal. Chem.* 50(14) (1978) 2126-2136.
- [426] S. Kazarian, G. Martirosyan, Spectroscopy of polymer/drug formulations processed with supercritical fluids: in situ ATR-IR and Raman study of impregnation of ibuprofen into PVP, *International Journal of Pharmaceutics* 232(1-2) (2002) 81-90.
- [427] J. Liu, Y. Xiao, C. Allen, Polymer-drug compatibility: a guide to the development of delivery systems for the anticancer agent, ellipticine, *Journal of pharmaceutical sciences* 93(1) (2004) 132-143.

- [428] R. Falk, T.W. Randolph, J.D. Meyer, R.M. Kelly, M.C. Manning, Controlled release of ionic compounds from poly (L-lactide) microspheres produced by precipitation with a compressed antisolvent, *Journal of controlled release* 44(1) (1997) 77-85.
- [429] M. Whelehan, I.W. Marison, Microencapsulation using vibrating technology, *Journal of microencapsulation* 28(8) (2011) 669-688.
- [430] R. Adami, S. Liparoti, A. Di Capua, M. Scognamiglio, E. Reverchon, Production of PEA composite microparticles with polyvinylpyrrolidone and luteolin using supercritical assisted atomization, *The Journal of Supercritical Fluids* 143 (2019) 82-89.
- [431] M. Cetin, A. Atila, Y. Kadioglu, Formulation and in vitro characterization of Eudragit® L100 and Eudragit® L100-PLGA nanoparticles containing diclofenac sodium, *Aaps Pharmscitech* 11(3) (2010) 1250-1256.
- [432] E.C. Sekhar, K.K. Rao, R.R. Raju, Chitosan/guargum-g-acrylamide semi IPN microspheres for controlled release studies of 5-Fluorouracil, *Journal of Applied Pharmaceutical Science* 1(8) (2011) 199.
- [433] S. Tummala, M.S. Kumar, A. Prakash, Formulation and characterization of 5-Fluorouracil enteric coated nanoparticles for sustained and localized release in treating colorectal cancer, *Saudi Pharmaceutical Journal* 23(3) (2015) 308-314.
- [434] A. Patel, Y. Hu, J.K. Tiwari, K.P. Velikov, Synthesis and characterisation of zein–curcumin colloidal particles, *Soft Matter* 6(24) (2010) 6192-6199.
- [435] A. Patel, P. Heussen, J. Hazekamp, K.P. Velikov, Stabilisation and controlled release of silibinin from pH responsive shellac colloidal particles, *Soft Matter* 7(18) (2011) 8549-8555.
- [436] J.A. Barbosa, M.S. Abdelsadig, B.R. Conway, H.A. Merchant, Using zeta potential to study the ionisation behaviour of polymers employed in modified-release dosage forms and estimating their pKa, *International journal of pharmaceutics: X* 1 (2019) 100024.
- [437] T.-C. Bai, J.-J. Zhu, J. Hu, H.-L. Zhang, C.-G. Huang, Solubility of silybin in aqueous hydrochloric acid solution, *Fluid phase equilibria* 254(1-2) (2007) 204-210.
- [438] E. van Wenum, R. Jurczakowski, G. Litwinienko, Media effects on the mechanism of antioxidant action of silybin and 2, 3-dehydrosilybin: Role of the enol group, *The Journal of organic chemistry* 78(18) (2013) 9102-9112.
- [439] M. Bijak, Silybin, a major bioactive component of milk thistle (*Silybum marianum* L. Gaernt.)—Chemistry, bioavailability, and metabolism, *Molecules* 22(11) (2017) 1942.
- [440] A. Buur, H. Bundgaard, Prodrugs of 5-fluorouracil. III. Hydrolysis kinetics in aqueous solution and biological media, lipophilicity and solubility of various 1-carbamoyl derivatives of 5-fluorouracil, *International journal of pharmaceutics* 23(2) (1985) 209-222.
- [441] G.S. Abdrakhimova, M.Y. Ovchinnikov, A.N. Lobov, L.V. Spirikhin, S.P. Ivanov, S.L. Khursan, 5-Fluorouracil solutions: NMR study of acid–base equilibrium in water and DMSO, *Journal of Physical Organic Chemistry* 27(11) (2014) 876-883.
- [442] N. Şanlı, S. Şanlı, G.I. Alsancak, Determination of dissociation constants of folic acid (leucovorin), 5-fluorouracil, and irinotecan in hydro-organic media by a spectrophotometric method, *Journal of Chemical & Engineering Data* 55(8) (2010) 2695-2699.

- [443] S. Mutalik, P.K. Shetty, A. Kumar, R. Kalra, H.S. Parekh, Enhancement in deposition and permeation of 5-fluorouracil through human epidermis assisted by peptide dendrimers, *Drug delivery* 21(1) (2014) 44-54.
- [444] G. Arora, K. Malik, I. Singh, Formulation and evaluation of mucoadhesive matrix tablets of taro gum: Optimization using response surface methodology, *Polimery w medycynie* 41(2) (2011) 23-34.
- [445] I.Y. Wu, S. Bala, N. Škalko-Basnet, M.P. di Cagno, Interpreting non-linear drug diffusion data: Utilizing Korsmeyer-Peppas model to study drug release from liposomes, *European Journal of Pharmaceutical Sciences* 138 (2019) 105026.
- [446] P.L. Ritger, N.A. Peppas, A simple equation for description of solute release I. Fickian and non-fickian release from non-swellable devices in the form of slabs, spheres, cylinders or discs, *Journal of controlled release* 5(1) (1987) 23-36.
- [447] S. Dash, P.N. Murthy, L. Nath, P. Chowdhury, Kinetic modeling on drug release from controlled drug delivery systems, *Acta Pol Pharm* 67(3) (2010) 217-23.
- [448] R. Weyhenmeyer, H. Mascher, J. Birkmayer, Study on dose-linearity of the pharmacokinetics of silibinin diastereomers using a new stereospecific assay, *International journal of clinical pharmacology, therapy, and toxicology* 30(4) (1992) 134-138.
- [449] V. Gavini, M.S. Murthy, P.K. Kumar, Formulation and Invitro Evaluation of Nanoparticulate Drug Delivery System Loaded With 5-Fluorouracil, *Research Journal of Pharmaceutical Dosage Forms and Technology* 6(4) (2014) 243-248.
- [450] N.P. Reneeta, B. Thiyonila, V.S. Aathmanathan, T. Ramya, P. Chandrasekar, N. Subramanian, V.K. Prajapati, M. Krishnan, Encapsulation and Systemic Delivery of 5-Fluorouracil Conjugated with Silkworm Pupa Derived Protein Nanoparticles for Experimental Lymphoma Cancer, *Bioconjugate chemistry* 29(9) (2018) 2994-3009.
- [451] Y.A. Haggag, M.A. Osman, S.A. El-Gizawy, A.E. Goda, M.M. Shamloula, A.M. Faheem, P.A. McCarron, Polymeric nano-encapsulation of 5-fluorouracil enhances anti-cancer activity and ameliorates side effects in solid Ehrlich Carcinoma-bearing mice, *Biomedicine & Pharmacotherapy* 105 (2018) 215-224.
- [452] M. Hanif, F. Jabbar, S. Sharif, G. Abbas, A. Farooq, M. Aziz, Halloysite nanotubes as a new drug-delivery system: a review, *Clay Minerals* 51(3) (2016) 469-477.
- [453] G. Cavallaro, G. Lazzara, M. Massaro, S. Milioto, R. Noto, F. Parisi, S. Riela, Biocompatible poly (N-isopropylacrylamide)-halloysite nanotubes for thermoresponsive curcumin release, *The Journal of Physical Chemistry C* 119(16) (2015) 8944-8951.
- [454] M. Massaro, R. Amorati, G. Cavallaro, S. Guernelli, G. Lazzara, S. Milioto, R. Noto, P. Poma, S. Riela, Direct chemical grafted curcumin on halloysite nanotubes as dual-responsive prodrug for pharmacological applications, *Colloids and Surfaces B: Biointerfaces* 140 (2016) 505-513.
- [455] S. Nasrazadani, S. Hassani, Modern analytical techniques in failure analysis of aerospace, chemical, and oil and gas industries, *Handbook of Materials Failure Analysis with Case Studies from the Oil and Gas Industry*, Elsevier 2016, pp. 39-54.

- [456] S. Iqbal, M.H. Rashid, A.S. Arbab, M. Khan, Encapsulation of anticancer drugs (5-fluorouracil and paclitaxel) into polycaprolactone (PCL) nanofibers and in vitro testing for sustained and targeted therapy, *Journal of biomedical nanotechnology* 13(4) (2017) 355-366.
- [457] Z. Sayyar, H. Jafarizadeh-Malmiri, Preparation of Curcumin Nanodispersions Using Subcritical Water–Screening of Different Emulsifiers, *Chemical Engineering & Technology* 43(2) (2020) 263-272.
- [458] Y. Pu, X. Wen, Y. Li, D. Wang, N.R. Foster, J.-F. Chen, Ultrafine clarithromycin nanoparticles via anti-solvent precipitation in subcritical water: Effect of operating parameters, *Powder Technology* 305 (2017) 125-131.
- [459] Y. Pu, J. Lu, D. Wang, F. Cai, J.-X. Wang, N.R. Foster, J.-F. Chen, Nanonization of ciprofloxacin using subcritical water-ethanol mixture as the solvent: Solubility and precipitation parameters, *Powder Technology* 321 (2017) 197-203.
- [460] Y. Pu, J.-X. Wang, D. Wang, N.R. Foster, J.-F. Chen, Subcritical water processing for nanopharmaceuticals, *Chemical Engineering and Processing-Process Intensification* 140 (2019) 36-42.
- [461] P. Richter, M.I. Toral, C. Toledo, Subcritical Water Extraction and Determination of Nifedipine in Pharmaceutical Formulations, *Journal of AOAC International* 89(2) (2006) 365-368.
- [462] A.G. Carr, R. Mammucari, N.R. Foster, Particle formation of budesonide from alcohol-modified subcritical water solutions, *International journal of pharmaceutics* 405(1-2) (2011) 169-180.
- [463] M. Fizir, P. Dramou, N.S. Dahiru, W. Ruya, T. Huang, H. He, Halloysite nanotubes in analytical sciences and in drug delivery: A review, *Microchimica Acta* 185(8) (2018) 389.
- [464] M.S. Curren, J.W. King, Solubility of triazine pesticides in pure and modified subcritical water, *Anal. Chem.* 73(4) (2001) 740-745.
- [465] M. Donohue, G. Aranovich, Classification of Gibbs adsorption isotherms, *Advances in colloid and interface science* 76 (1998) 137-152.
- [466] S. Gregg, K. Sing, W. Adsorption, surface area and porosity, London: Academic Press (1982) 195-197.
- [467] P. Yuan, D. Tan, F. Annabi-Bergaya, W. Yan, M. Fan, D. Liu, H. He, Changes in structure, morphology, porosity, and surface activity of mesoporous halloysite nanotubes under heating, *Clays and Clay Minerals* 60(6) (2012) 561-573.
- [468] S. Lowell, J.E. Shields, M.A. Thomas, M. Thommes, Characterization of porous solids and powders: surface area, pore size and density, Springer Science & Business Media 2012.
- [469] Z. AlOthman, A review: fundamental aspects of silicate mesoporous materials, *Materials* 5(12) (2012) 2874-2902.
- [470] S. Lowell, J.E. Shields, J.E. Morral, Powder Surface Area and Porosity, 2nd Edition, *Journal of Engineering Materials and Technology* 107(2) (1985) 180-180.
- [471] E.G.N. Marsden, Surface area determination, *Proceedings of the Society for Analytical Chemistry* 7(8) (1970) 142-144.




- [472] M.S. Saharudin, J. Wei, I. Shyha, F. Inam, Flexural Properties of Halloysite Nanotubes-Polyester Nanocomposites Exposed to Aggressive Environment, *Int. J. Chem. Mol. Nucl. Mater. Metall. Eng* 11 (2017) 292-296.
- [473] J. Alberton, S. Martelli, F. Fakhouri, V. Soldi, Mechanical and moisture barrier properties of titanium dioxide nanoparticles and halloysite nanotubes reinforced polylactic acid (PLA), *IOP Conference Series: Materials Science and Engineering*, IOP Publishing, 2014, p. 012010.
- [474] R. Bardestani, G.S. Patience, S. Kaliaguine, Experimental methods in chemical engineering: specific surface area and pore size distribution measurements—BET, BJH, and DFT, *The Canadian Journal of Chemical Engineering* 97(11) (2019) 2781-2791.
- [475] X.S. Zhao, G. Lu, G.J. Millar, Advances in mesoporous molecular sieve MCM-41, *Industrial & Engineering Chemistry Research* 35(7) (1996) 2075-2090.
- [476] G. Churchman, T. Davy, L. Aylmore, R. Gilkes, P. Self, Characteristics of fine pores in some halloysites, *Clay Minerals* 30(2) (1995) 89-98.
- [477] K. Okada, H. Kawashima, Y. Saito, S. Hayashi, A. Yasumori, New preparation method for mesoporous γ -alumina by selective leaching of calcined kaolin minerals, *Journal of Materials Chemistry* 5(8) (1995) 1241-1244.
- [478] M. Lenarda, L. Storaro, A. Talon, E. Moretti, P. Riello, Solid acid catalysts from clays: Preparation of mesoporous catalysts by chemical activation of metakaolin under acid conditions, *Journal of colloid and interface science* 311(2) (2007) 537-543.
- [479] Q. Wang, J. Zhang, Y. Zheng, A. Wang, Adsorption and release of ofloxacin from acid- and heat-treated halloysite, *Colloids and Surfaces B: Biointerfaces* 113 (2014) 51-58.
- [480] Y.H. Hu, E. Ruckenstein, Pore size distribution of single-walled carbon nanotubes, *Industrial & engineering chemistry research* 43(3) (2004) 708-711.
- [481] A.A. Peterson, F. Vogel, R.P. Lachance, M. Fröling, M.J. Antal Jr, J.W. Tester, Thermochemical biofuel production in hydrothermal media: a review of sub- and supercritical water technologies, *Energy & Environmental Science* 1(1) (2008) 32-65.
- [482] Z. Shu, Y. Chen, J. Zhou, T. Li, D. Yu, Y. Wang, Nanoporous-walled silica and alumina nanotubes derived from halloysite: controllable preparation and their dye adsorption applications, *Applied Clay Science* 112 (2015) 17-24.
- [483] W.L. Marshall, E.V. Jones, Second dissociation constant of sulfuric acid from 25 to 350 evaluated from solubilities of calcium sulfate in sulfuric acid solutions, *The Journal of Physical Chemistry* 70(12) (1966) 4028-4040.
- [484] A.K. Panda, B.G. Mishra, D.K. Mishra, R.K. Singh, Effect of sulphuric acid treatment on the physico-chemical characteristics of kaolin clay, *Colloids and Surfaces A: Physicochemical and Engineering Aspects* 363(1) (2010) 98-104.
- [485] W. Jinhua, Z. Xiang, Z. Bing, Z. Yafei, Z. Rui, L. Jindun, C. Rongfeng, Rapid adsorption of Cr (VI) on modified halloysite nanotubes, *Desalination* 259(1-3) (2010) 22-28.
- [486] P. Luo, Y. Zhao, B. Zhang, J. Liu, Y. Yang, J. Liu, Study on the adsorption of Neutral Red from aqueous solution onto halloysite nanotubes, *Water research* 44(5) (2010) 1489-1497.


- [487] H. Zhu, M. Du, M. Zou, C. Xu, Y. Fu, Green synthesis of Au nanoparticles immobilized on halloysite nanotubes for surface-enhanced Raman scattering substrates, *Dalton Transactions* 41(34) (2012) 10465-10471.
- [488] C. Bretti, S. Cataldo, A. Gianguzza, G. Lando, G. Lazzara, A. Pettignano, S. Sammartano, Thermodynamics of proton binding of halloysite nanotubes, *The Journal of Physical Chemistry C* 120(14) (2016) 7849-7859.
- [489] S.T. Mixture, R.L. Snyder, X-ray Diffraction, in: K.H.J. Buschow, R.W. Cahn, M.C. Flemings, B. Ilschner, E.J. Kramer, S. Mahajan, P. Veysseyre (Eds.), *Encyclopedia of Materials: Science and Technology*, Elsevier, Oxford, 2001, pp. 9799-9808.
- [490] E. Joussein, S. Petit, C.-I. Fialips, P. Vieillard, D. Righi, Differences in the dehydration-rehydration behavior of halloysites: new evidence and interpretations, *Clays and Clay Minerals* 54(4) (2006) 473-484.
- [491] H. Chen, H. Yan, Z. Pei, J. Wu, R. Li, Y. Jin, J. Zhao, Trapping characteristic of halloysite lumen for methyl orange, *Applied Surface Science* 347 (2015) 769-776.
- [492] S. Sahnoun, M. Boutahala, H. Zaghouane-Boudiaf, L. Zerroual, Trichlorophenol removal from aqueous solutions by modified halloysite: kinetic and equilibrium studies, *Desalination and Water Treatment* 57(34) (2016) 15941-15951.
- [493] X. Wu, C. Liu, H. Qi, X. Zhang, J. Dai, Q. Zhang, L. Zhang, Y. Wu, X. Peng, Synthesis and adsorption properties of halloysite/carbon nanocomposites and halloysite-derived carbon nanotubes, *Applied Clay Science* 119 (2016) 284-293.
- [494] P.D. File, Joint Committee on Powder Diffraction Standards (JCPDS), ASTM, Philadelphia, PA (1997).
- [495] B.D. Cullity, S.R. Stock, *Elements of X-ray Diffraction*, Prentice hall New Jersey 2001.
- [496] D. Balzar, H. Ledbetter, Voigt-function modeling in Fourier analysis of size-and strain-broadened X-ray diffraction peaks, *J. Appl. Crystallogr.* 26(1) (1993) 97-103.
- [497] G. Wertheim, M. Butler, K. West, D. Buchanan, Determination of the Gaussian and Lorentzian content of experimental line shapes, *Rev. Sci. Instrum.* 45(11) (1974) 1369-1371.
- [498] T. Ida, M. Ando, H. Toraya, Extended pseudo-Voigt function for approximating the Voigt profile, *J. Appl. Crystallogr.* 33(6) (2000) 1311-1316.
- [499] H. Miyoshi, D. Chen, T. Akai, A novel process utilizing subcritical water to remove lead from wasted lead silicate glass, *Chemistry Letters* 33(8) (2004) 956-957.
- [500] J. Tully, R. Yendluri, Y. Lvov, Halloysite clay nanotubes for enzyme immobilization, *Biomacromolecules* 17(2) (2016) 615-621.
- [501] R.F. Egerton, *Physical principles of electron microscopy*, Springer 2005.
- [502] P. Pasbakhsh, G.J. Churchman, J.L. Keeling, Characterisation of properties of various halloysites relevant to their use as nanotubes and microfibre fillers, *Applied Clay Science* 74 (2013) 47-57.
- [503] M. Robinson, J. Pask, D. Fuerstenau, Surface charge of alumina and magnesia in aqueous media, *J. Am. Ceram. Soc.* 47(10) (1964) 516-520.

- [504] G. Tari, I. Bobos, C.S. Gomes, J.M. Ferreira, Modification of surface charge properties during kaolinite to halloysite-7Å transformation, *Journal of Colloid and Interface Science* 210(2) (1999) 360-366.
- [505] Z. Qian, Q. Chen, I.E. Grossmann, Optimal synthesis of rotating packed bed and packed bed: a case illustrating the integration of PI and PSE, *Computer Aided Chemical Engineering*, Elsevier 2018, pp. 2377-2382.
- [506] C.C. Beh, R. Mammucari, N. Foster, Process intensification and sustainability in chemical engineering, *Chemeca 2016: Chemical Engineering-Regeneration, Recovery and Reinvention* (2016) 453.
- [507] D. Reay, C. Ramshaw, A. Harvey, *Process Intensification: Engineering for efficiency, sustainability and flexibility*, Butterworth-Heinemann 2013.
- [508] A.I. Stankiewicz, J.A. Moulijn, Process intensification: transforming chemical engineering, *Chemical engineering progress* 96(1) (2000) 22-34.
- [509] F. Dehghani, N. Foster, Dense gas anti-solvent processes for pharmaceutical formulation, *Current Opinion in Solid State and Materials Science* 7(4-5) (2003) 363-369.
- [510] J.-Y. Clavier, M. Perrut, Scale-up issues for supercritical fluid processing in compliance with GMP, *Supercritical Fluid Technology for Drug Product Development*, CRC Press 2004, pp. 586-618.
- [511] M. Yelvigi, W.G. Chambliss, T. Sam, Scale-Up and Post Approval Changes (SUPAC), *Encyclopedia of Pharmaceutical Science and Technology*, Six Volume Set (Print), CRC Press 2013, pp. 3052-3055.

Statement of attribution

“S. Harikrishnan, R. Sedev, C.C. Beh, C. Priest, N.R. Foster, **Loading of 5-fluorouracil onto Halloysite nanotubes for targeted drug delivery using a subcritical gas antisolvent process (GAS)**, The Journal of Supercritical Fluids 159 (2020) 104756.”

	Concep- tion and design	Acquisi- tion of data & method	Data con- ditioning & manipu- lation	Analysis & statis- tical method	Interpreta- tion & dis- cussion	Final ap- proval
Emeritus Prof. Neil. R Foster	<input checked="" type="checkbox"/>	<input type="checkbox"/>	<input type="checkbox"/>	<input type="checkbox"/>	<input checked="" type="checkbox"/>	<input checked="" type="checkbox"/>
I acknowledge that these represent my contribution to the above research output. Signature:  Date: 27 Jan 2021						
Dr. Rossen Sedev	<input checked="" type="checkbox"/>	<input checked="" type="checkbox"/>	<input checked="" type="checkbox"/>	<input checked="" type="checkbox"/>	<input checked="" type="checkbox"/>	<input checked="" type="checkbox"/>
I acknowledge that these represent my contribution to the above research output. Signature:  Date: 14 Dec 2020						
Dr.Chau Chun Beh (Jane)	<input checked="" type="checkbox"/>	<input checked="" type="checkbox"/>	<input type="checkbox"/>	<input type="checkbox"/>	<input checked="" type="checkbox"/>	<input checked="" type="checkbox"/>
I acknowledge that these represent my contribution to the above research output. Signature:  Date: 11 Jan 2021						

Dr. Craig Priest	<input type="checkbox"/>	<input type="checkbox"/>	<input type="checkbox"/>	<input type="checkbox"/>	<input checked="" type="checkbox"/>	<input checked="" type="checkbox"/>
I acknowledge that these represent my contribution to the above research output.						
Signature: 						
Date: 11/12/2020						

Every reasonable effort has been made to acknowledge the owners of copyright material. I would be pleased to hear from any copyright owner who has been omitted or incorrectly acknowledged.

Harikrishnan Sekar

28/01/2021